THE UNIVERSITY OF CHICAGO

REDUCED DENSITY MATRIX METHODS FOR THE RESOLUTION OF ELECTRON CORRELATION AND THEIR APPLICATIONS TO BIMETALLIC COMPLEXES

A DISSERTATION SUBMITTED TO
THE FACULTY OF THE DIVISION OF THE PHYSICAL SCIENCES
IN CANDIDACY FOR THE DEGREE OF
DOCTOR OF PHILOSOPHY

DEPARTMENT OF CHEMISTRY

BY
JAN-NIKLAS BOYN

CHICAGO, ILLINOIS
JUNE 2022

To Isabel.

TABLE OF CONTENTS

LIST OF FIGURES

LIST OF TABLES

ACKNOWLEDGMENTS

First, I would like to thank David Mazziotti for his great mentorship over the course of my studies. I really appreciate all the support, including for the various ideas I have been able to pursue over the years, and without which this work would not have been possible. I would also like to thank John Anderson and Laura Gagliardi for having given me the chance to work on so many collaborative projects. Particularly the chemical insight from the many discussions with John has played a major role in the conception, as well as successful completion of many of the projects in this dissertation. I am also particularly thankful for the students and postdocs that I have had the pleasure to work with on the many collaborations over the years: Jiaze Xie, Airi Kawamura, Lauren McNamara and Maia Czaikowski who carried out the many experiments that formed a major part of many of my projects, and Scott Smart, Daniel Gibney, Simon Ewing and Aleksandr Lykhin, who contributed significantly to several theoretical projects. Thanks also goes to all the other members of the Mazziotti group who have created such a great working environment: Anthony, Kade, Manas, Ali, Olivia, Shayan, Shiva, LeeAnn, Guan, Anna, Sam, Jordan, Amatullah, Irma and Tori.

Additionally, I would like to thank the many great people in the Chemistry Department and James Franck Institute that are so determined in making the University of Chicago such a wonderful place. Especially the work carried out by Vera and Melinda has been invaluable. I would also again like to thank David, John and Laura for their invaluable career advice and help during the last few months in my search for a postdoc position, and their general encouragement.

Finally, a huge thanks to all the great friends I have made throughout my PhD, including those in the chemistry department, as well as those I met in Chicago, and especially my wife Isabel, whom I would have never met if it weren't for me pursuing this degree, and her wonderful family, all of whom have been so supportive of my research and ambitions. The same thank you goes to my parents and grandparents, who while having been a few thousand miles away, have always been supportive and encouraging throughout the last 5 years.

ABSTRACT

The most fundamental struggle of modern electronic structure theory is the accurate description of electron correlation, which is commonly divided into its dynamic and multireference or strong parts. The former is readily captured with various modern electronic structure methods at polynomial computational cost, while the latter exhibits exponential scaling in traditional wave function based theories. For the precise and tractable computation of molecular electronic properties and processes it is essential to develop methods that capture both dynamic and strong correlation effects at affordable computational cost. Reduced density matrix (RDM) based theories, which exploit the fact that fermions interact pairwise to express the electronic energy as a linear functional of the two electron RDM (2-RDM), provide a promising path towards achieving this goal. In the first part of this dissertation several theoretical developments based on the anti-Hermitian contracted Schrödinger equation are detailed, which enable the computation of all-electron correlation. This includes the introduction of a spin-averaging scheme allowing for the efficient calculation of non-singlet spin states, the elucidation of its orbital dependence, as well as the use of a hybrid quantum-classical algorithm to calculate the multi-reference correlation on a quantum computer. Additionally, it is demonstrated that pure N-representability conditions imposed on the 2-RDM may yield sparse non-orthogonal wave function expansions, which may serve as a sparse ansatz in the development of RDM functional theories. In the second part of this dissertation RDM methods are applied to resolve the electronic structures and properties of several bimetallic complexes. Binuclear transition metal complexes exhibit significant multi-reference character arising from the degenerate d-orbital manifolds and their complex and tunable electronic structures make them prime candidates in development of single molecule magnets (SMMs), molecular switches, molecular conductors, as well as in the fields of spintronics and quantum information storage. The magnetic exchange interaction in a cobalt quinoid dimer is investigated, as well as the biradical character and electronic properties, including the excited states and singlet-triplet gaps, of a series of tetrathiafulvalene-2,3,6,7-tetrathiolate bridged bimetallic complexes.

CHAPTER 1

INTRODUCTION

1.1 Electron Correlation

The foremost goal of research undertaken in modern electronic structure theory is the accurate and computationally efficient capture of electron correlation. Here, the electron correlation energy is generally defined as the difference between the Hartree-Fock (HF)[1] solution, which only considers a single electronic configuration, and the full configuration interaction (FCI)[2] limit, which includes all possible electronic configurations in a specified basis set, $E_C = E_{FCI} - E_{HF}$. It is commonly divided into two different components: dynamic correlation and strong correlation[3]. We note that the HF formalism already includes correlations between electrons of parallel spins which is not commonly included in the traditional definition of E_C.

Dynamic electron correlation arises from the correlated movement of electrons within molecules, i.e. the correlation of electronic spatial distributions[4]. As such it is characterized by wave function expansions containing large numbers of Slater determinants with small CI coefficients, which results in it being readily approximated at non-exponential computational cost. Common methods for the approximate recovery of dynamic correlation effects include n-th order Møller-Plesset Perturbation theory (MPn)[5], coupled cluster theory (CC)[6] or density functional theory (DFT)[7].

Strong correlation on the other hand arises in systems with degenerate or near-degenerate orbitals, requiring the use of a multi-configurational wave function for its accurate treatment. Consequently, the capture of strong correlation requires the use of a reference wave function containing several Slater determinants with large CI coefficients, leading to strong correlation also being commonly referred to as multi-reference correlation. Singlet biradicals provide a common example of such a system[8], and this is illustrated with the case of para-benzyne in Figure 1.1, which displays

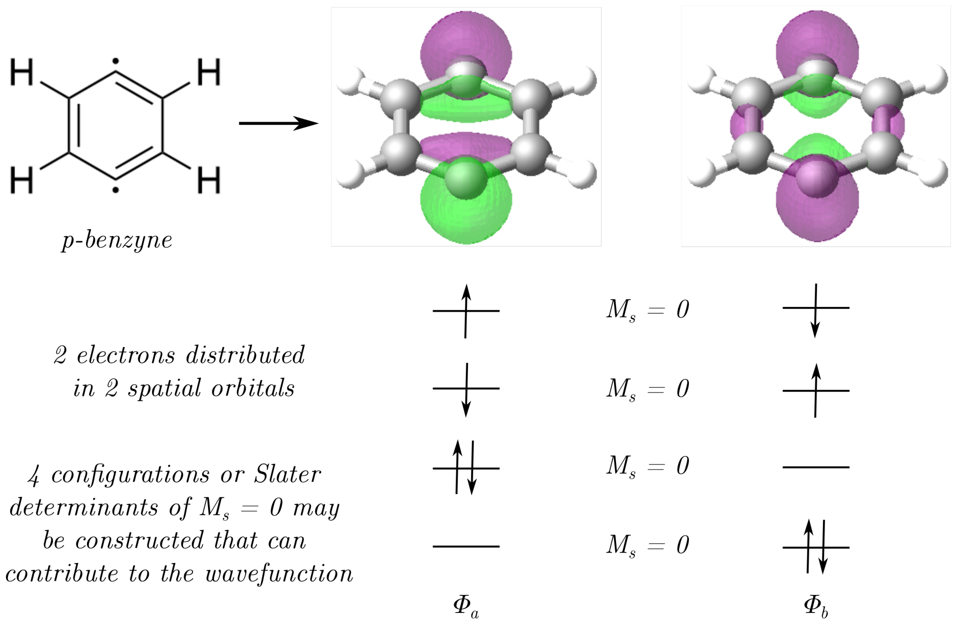

Figure 1.1: Multireference or strong correlation illustrated with para-benzyne. Abstraction of two hydrogen atoms from benzene yields two radical electrons localized in two (near)degenerate orbitals perpendicular to the π system, displayed as Φ_a and Φ_b. There are four distinct configurations or Slater determinants with the correct projection of the total spin, $M_s = 0$, that may contribute to a singlet wave function.

the electronic configurations required to accurately describe the distributions of the two biradical electrons in the degenerate frontier orbitals. Unlike dynamic correlation, multi-reference correlation is not readily described at polynomial scaling, with the go-to method being complete active space self-consistent field (CASSCF)[9, 10], which scales exponentially with respect to the number of basis functions. This effectively limits its use to active spaces containing no more than 18 electrons distributed in 18 spatial orbitals on commonly available modern computing clusters, while massively parallel calculations performed on a supercomputer have reached active spaces of up to 22 electrons distributed in 22 orbitals[11].

The precise capture of electron correlation effects is essential for the successful computational description of many physical and electronic properties in molecular and extended systems[12]. This includes intermolecular van-der-Waals interactions, which arise from dynamic correlation effects[13, 14], while strong correlation plays an important role in the chemistry of radicals[15, 16], transition metal complexes[17, 18] and excited states[19], and as such needs to be accounted for in the computation of experimentally relevant properties such as exchange coupling constants J or electronic spectra.

1.2 Wave Function Methods

In electronic structure theory we aim to solve the N-electron Schrödinger equation:

$$\hat{H}\Psi(r,R) = E\Psi(r,R), \tag{1.1}$$

where $\hat{H}$ is the Hamiltonian operator:

$$\hat{H} = -\frac{\hbar^2}{2}\sum_{i=1}^{N}\frac{1}{m_i}\nabla_i^2 + V(r,R), \tag{1.2}$$

and $\Psi(r,R)$ is the wave function, E is the energy and r and R are the electronic and nuclear coordinates, respectively. The N-electron Schrödinger equation may only be solved exactly for the simplest of systems, i.e. those containing one electron, and applications to systems of physical and chemical interest require the use of approximations. The most common of these is the Born-Oppenheimer approximation (BOA), which assumes that as a result of their significant greater mass the atomic nuclei are stationary on the time-scale of electronic motion. Further commonly made approximations are solving the non-relativistic Schrödinger equation, as well as the use of approximate Hamiltonians and the use of finite basis functions[20].

Hartree-Fock theory (HF) presents the simplest commonly used approximation to the N-electron problem, relying on a mean-field approximation, which assumes an uniform charge density around each electron[1, 21]. While HF theory recovers the Fermi part of the dynamic correlation arising from the interaction between same spins, the dynamic correlation between electrons of opposite spins is not captured. Additionally, the HF wave function is based on a single electronic configuration, or Slater determinant, and as such no multi-reference correlation effects are resolved. While the lack of electron correlation in the HF solution places severe limitations on its applicability to problems of current chemical interest, it has, nonetheless, established itself as an important method in modern electronic structure theory, with the HF solution serving as a starting point in many state-of-the-art computational methods[22].

Full configuration interaction (FCI) presents the opposite of HF on the spectrum of approximations, yielding the exact solution of the non-relativistic time-independent Schrödinger equation within a specified finite basis set[2]. It presents a special case of the configuration interaction (CI) method which expands the N-electron wave function as a linear combination of electronic configurations[23]:

$$\Psi = \sum_{i}^{N} c_i \, |\Phi_i\rangle \ , \tag{1.3}$$

where c_i are the expansion or CI coefficients, and Φ_i are Slater determinants:

$$|\Phi_i\rangle = \frac{1}{\sqrt{N!}} \begin{vmatrix} \chi_1(1) & \cdots & \chi_N(1) \\ \vdots & \ddots & \vdots \\ \chi_1(N) & \cdots & \chi_N(N) \end{vmatrix} \ , \tag{1.4}$$

with χ being the molecular spin orbitals. CI methods commonly use the variational principle to obtain the expansion coefficients and solve for the N-electron energy[24, 25]. The inclusion of all configurations within a specified finite basis set as in the FCI case, however, scales exponentially with the number of basis functions and hence it is limited to all but the smallest chemical systems, with the currently largest calculation carried out comprising 22 electrons distributed in 22 spatial orbitals[11]. Nonetheless, CI provides an important framework for the resolution of multi-reference or strong electron correlation in the complete active space CI and SCF (CASCI and CASSCF) methods, which play an important role in modern quantum chemistry, particularly in the treatment of in transition metal and extended π systems[3, 26, 27].

A variety of methods falling onto the spectrum of accuracy defined by the HF and FCI limits have been developed over the recent decades following the advent of modern computing in the 1950's with the aim of striking a compromise between computational costs and the degree of electron correlation recovered. The most successful of these methods include n-th order many-body perturbation theories, also known as Møller-Plesset perturbation theories (MPn)[5] and coupled cluster (CC) theories[6]. In MPn perturbative corrections to n-th order are applied to the Hartree-Fock reference Hamiltonian, with MP2 providing a cost-effective way of resolving dynamic correlation at $\mathscr{O}(r^4)$ scaling, where r is the number of basis functions. CC theory on the other hand uses the cluster operator to act on the HF reference wave function to generate a wave function expansion of excited determinants. The excitations included in the cluster operator are truncated at a certain order, with CC with single and double excitations (CCSD) and CC with single, double and perturbative triple excitations (CCSD(T)) yielding computational scalings of $\mathscr{O}(r^6)$ and $\mathscr{O}(r^7)$, respectively. CCSD(T) presents an often-used method, being termed the "gold standard" of quantum chemistry, however, it still fails to accurately describe systems exhibiting multi-reference correlation[28].

1.3 Density Functional Theory

Since its conception by Walter Kohn in 1965 Kohn-Sham density functional theory (DFT) has become one of the foremost computational methods in chemistry, solid state physics and materials science[29, 30]. Unlike wave function based approaches DFT uses the electron density ρ as its fundamental variable. The objective of the Kohn-Sham equations is finding the electron density that minimizes the ground state energy[31, 32]:

$$E[\rho] = T_S[\rho] + E_{Ne}[\rho] + J[\rho] + E_{XC}[\rho], \tag{1.5}$$

where T_S is the kinetic energy functional, E_{Ne} is the classical Coulomb nuclear-electron energy, J is the classical Coulomb repulsion and E_{XC} is the exchange-correlation energy[33, 34]. As a result of the fact that the exact exchange-correlation functional is not known, E_{XC}, which accounts for non-classical exchange and correlation interactions, cannot be calculated exactly[35, 36].

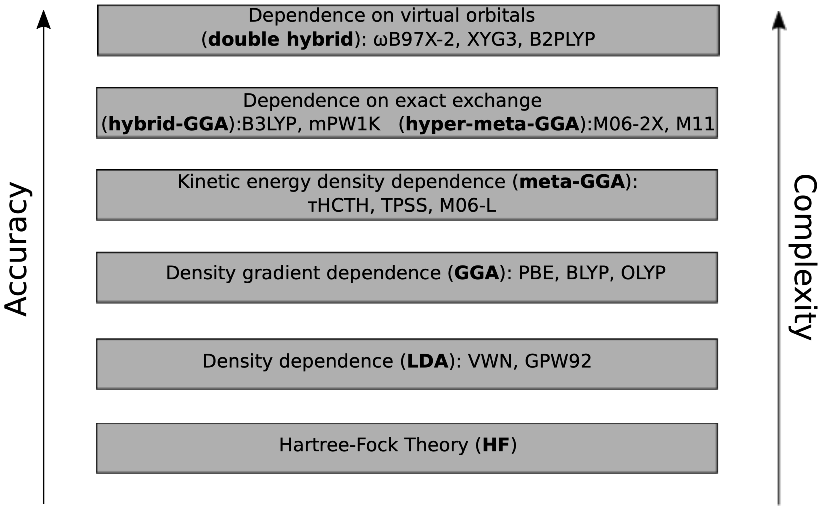

Figure 1.2: Jacob's Ladder of DFT exchange-correlation functionals, illustrating their evolution in terms of accuracy and complexity.

Consequently, modern DFT relies on approximate exchange-correlation functionals for the calculation of E_{XC}, with significant research efforts having been extended to the development of such functionals over the last half century, giving rise to today's so-called ”functional zoo”[37, 38]. Functional development generally relies on parametrization and the use of known theoretical constraints of the exact functional, aiming to recover electronic and chemical properties with experimental accuracy[39]. A range of different approximations have been used, including the use of spin-densities, magnitudes of their gradients, spin-specfic kinetic-energy densities or non-local exchange and correlation[38, 40]. These give rise to functionals of varying degrees of accuracy and complexity and leading to them being commonly categorized according to ”Jacob’s Ladder” as perceived by Perdew[41], which is displayed in Figure 1.2. Notwithstanding the significant progress in the development of functionals, DFT, being inherently a single-reference method, continues to struggle with the description of strong correlation[42, 43]. Additionally, as there currently exists no universally applicable functional, the choice of functional is critical to yield the most accurate description of the specific system and electronic property to be calculated[38, 40]. Nonetheless, owing to its ease-of-use as a black-box method and its favorable computational scaling, allowing its application to systems of chemical interest that are otherwise not readily treated with wave function based methods, DFT has established itself as the go-to method in modern computational chemistry and materials science[29, 38, 44, 45].

An extension of DFT has also been developed to allow for the modeling of electronically excited states – time-depedent density functional theory (TD-DFT). It is based on the Runge-Gross theorem which maps the time-dependent N-electron wave function onto the time-dependent electronic density[46] and modern implementations utilize an effective linear-response formalism developed by Casida[47]. While TD-DFT still struggles with the description of multi-reference systems and double excitations, its low computational costs and black-box usability in line with DFT has made it the method of choice for the modeling of experimentally important light-matter interactions such as the simulation of emission and absorption spectra[48, 49].

1.4 Reduced Density Matrix Methods

In contrast to wave function based methods, reduced density matrix theory utilizes n-particle reduced density matrices (p-RDMs, ${}^{p}D$) to express the Schrödinger equation. A general p-RDM is obtained from the N-electron density matrix, ${}^{N}D = \Psi\Psi^{*}$, by integrating over the coordinates of all but p electrons:

$$^{p}D = \int \Psi\Psi^{*} dp_{+1}...dN \,. \tag{1.6}$$

RDM theory traces its roots to the 1950's when Coleman realized that the fact that fermions interact pairwise allows us to express the ground state energy of an electronic system as a linear functional of the 2-electron RDM (2-RDM)[50]:

$$E = Tr[^{2}K\,^{2}D]\,, \tag{1.7}$$

where ^{2}K is the 2-electron reduced Hamiltonian with its elements given by:

$$^{2}K^{ij}_{kl} = \frac{1}{N-1}(^{1}K^{i}_{k}\delta^{j}_{l} + {}^{1}K^{j}_{l}\delta^{i}_{k}) + {}^{2}V^{ij}_{kl}\,, \tag{1.8}$$

and ^{1}K and ^{2}V contain the 1- and 2-electron integrals, respectively. In second quantization the elements of the 2-RDM are given by:

$$^{2}D^{ij}_{kl} = \langle\Psi|\,\hat{a}^{\dagger}_{i}\hat{a}^{\dagger}_{j}\hat{a}_{l}\hat{a}_{k}\,|\Psi\rangle\,. \tag{1.9}$$

While the use of the 2-RDM as the basic variable in electronic structure theory provides a viable, cost-effective alternative to wave function based approaches, it requires the use of so-called N-representability conditions which ensure that the 2-RDM corresponds to a physically valid N-electron wave function[51].

While complete pure N-representability constraints form a hierarchy of conditions that remains intractable for all but the smallest of problems[52], sets of sufficient N-representability constraints have proven successful for the variational determination of CAS ground and excited state energies in multi-reference systems, with accuracy rivaling that of high-level wave function CAS methods[53, 54]. Additionally, methods for the direct computation of 2-RDMs from approximate solutions to the contracted Schrödinger equation such as the anti-Hermitian contracted Schrödinger equation[55] have been established and demonstrated to successfully resolve both dynamic and multi-reference correlation[56]. Furthermore, in recent years RDM methods have gained prominence in the realm of quantum computing algorithms due to the fact that RDMs – unlike the N-electron wave function – may be readily measured on quantum devices, and as such a variety of RDM-based quantum and quantum-classical hybrid algorithms have been proposed[57–61].

1.5 Quantum and Quantum Classical Algorithms

Quantum computing has risen to significant prominence in recent years, driven by remarkable progress in the development of many-qubit quantum devices[60–62]. While applications of quantum computations to entire systems of chemical interest that pose intractable problems to modern classical computers would require quantum devices of hundreds of thousands of qubits and thus will likely remain out of reach for quantum devices for decades to come[63, 64], the use of quantum algorithms for the simulation strongly correlated quantum systems provides a particularly viable near-term application for noisy intermediate-scale quantum (NISQ) devices[60–62]. Here, the exponential scaling of the CASCI and CASSCF methods limits their applications to active space sizes of 18 electrons distributed in 18 orbitals, meaning that simulations on quantum devices with only hundreds or thousands of qubits may yield an advantage over classical methods, assuming sufficient error mitigation[63, 64].

A large variety of quantum and quantum-classical hybrid algorithms have been introduced in the last five years, attempting to allow for the resolution of correlated electronic structure on quantum devices. Of these, variational quantum eigensolvers (VQEs)[65–67], which minimize the energy of a parametrizable ansatz, such as unitary coupled cluster (UCC)[68–71] against the Schrödinger equation, and contracted quantum eigensolvers (CQEs)[58, 72], which minimize the contraction of the Schrödinger equation onto the space of two electrons, have proven to be particularly promising and been demonstrated to successfully resolve strong correlation in model systems and small molecules[60–62].

The accurate resolution of experimentally relevant electronic properties may often not be resolved to within chemical accuracy without the inclusion of dynamic correlation, even in systems exhibiting strong correlation[3]. As such, the development of quantum-classical hybrid algorithms, which perform the CAS multi-reference calculation on a quantum device and resolve the remaining dynamic correlation on a classical computer, is an active area of research aiming to provide near-term applications of quantum computing to systems of chemical interest[62, 73–76].

References

(1) Slater, J. C. *Phys. Rev.* **1951**, *81*, 385–390.

(2) Knowles, P.; Handy, N. *Chem. Phys. Lett.* **1984**, *111*, 315–321.

(3) Stein, C. J.; von Burg, V.; Reiher, M. *J. Chem. Theory Comput.* **2016**, *12*, 3764–3773.

(4) Cohen, A. J.; Handy, N. C. *Mol. Phys.* **2001**, *99*, 607–615.

(5) Cremer, D. *Wiley Interdiscip. Rev. Comput. Mol. Sci.* **2011**, *1*, 509–530.

(6) Bartlett, R. J.; Musiał, M. *Rev. Mod. Phys.* **2007**, *79*, 291–352.

(7) Cremer, D. *Mol. Phys.* **2001**, *99*, 1899–1940.

(8) Abe, M. *Chem. Rev.* **2013**, *113*, 7011–7088.

(9) Roos, B. O.; Taylor, P. R.; Sigbahn, P. E. *Chem. Phys.* **1980**, *48*, 157–173.

(10) Olsen, J. *Int. J. Quantum Chem.* **2011**, *111*, 3267–3272.

(11) Vogiatzis, K. D.; Ma, D.; Olsen, J.; Gagliardi, L.; de Jong, W. A. *J. Chem. Phys.* **2017**, *147*, 184111.

(12) Raghavachari, K.; Anderson, J. B. *J. Phys. Chem.* **1996**, *100*, 12960–12973.

(13) Stöhr, M.; Van Voorhis, T.; Tkatchenko, A. *Chem. Soc. Rev.* **2019**, *48*, 4118–4154.

(14) Grimme, S. *Chem. Eur. J.* **2004**, *10*, 3423–3429.

(15) Doehnert, D.; Koutecky, J. *J. Am. Chem. Soc.* **1980**, *102*, 1789–1796.

(16) Crawford, T. D.; Kraka, E.; Stanton, J. F.; Cremer, D. *J. Chem. Phys.* **2001**, *114*, 10638–10650.

(17) Hait, D.; Tubman, N. M.; Levine, D. S.; Whaley, K. B.; Head-Gordon, M. *J. Chem. Theory Comput.* **2019**, *15*, 5370–5385.

(18) Marti, K. H.; Reiher, M. *Phys. Chem. Chem. Phys.* **2011**, *13*, 6750–6759.

(19) Lischka, H.; Nachtigallová, D.; Aquino, A. J. A.; Szalay, P. G.; Plasser, F.; Machado, F. B. C.; Barbatti, M. *Chem. Rev.* **2018**, *118*, 7293–7361.

(20) Helgaker, T.; Jorgensen, P.; Olsen, J., *Molecular electronic-structure theory*; John Wiley & Sons: 2014.

(21) Baerends, E.; Ellis, D.; Ros, P. *Chem. Phys.* **1973**, *2*, 41–51.

(22) Bao, J. J.; Truhlar, D. G. *J. Chem. Theory Comput.* **2019**, *15*, 5308–5318.

(23) Shavitt, I. In *Methods of Electronic Structure Theory*, Schaefer, H. F., Ed.; Springer US: Boston, MA, 1977, pp 189–275.

(24) Knowles, P.; Handy, N. *Chem. Phys. Lett.* **1984**, *111*, 315–321.

(25) Pople, J. A.; Head-Gordon, M.; Raghavachari, K. *J. Chem. Phys.* **1987**, *87*, 5968–5975.

(26) Pelzer, K.; Greenman, L.; Gidofalvi, G.; Mazziotti, D. A. *J. Phys. Chem. A* **2011**, *115*, 5632–5640.

(27) Khedkar, A.; Roemelt, M. *Phys. Chem. Chem. Phys.* **2021**, *23*, 17097–17112.

(28) Cársky, P.; Paldus, J.; Pittner, J. **2010**.

(29) Burke, K. *J. Chem. Phys.* **2012**, *136*, 150901.

(30) Koch, W.; Holthausen, M. C., *A chemist's guide to density functional theory*; John Wiley & Sons: 2015.

(31) Hohenberg, P.; Kohn, W. *Phys. Rev.* **1964**, *136*, B864–B871.

(32) Kohn, W.; Sham, L. J. *Phys. Rev.* **1965**, *140*, A1133–A1138.

(33) Pople, J. A.; Gill, P. M.; Johnson, B. G. *Chem. Phys. Lett.* **1992**, *199*, 557–560.

(34) Marques, M. A.; Oliveira, M. J.; Burnus, T. *Comput. Phys. Commun.* **2012**, *183*, 2272–2281.

(35) Von Barth, U.; Hedin, L. *J. Phys. C Solid State Phys.* **1972**, *5*, 1629–1642.

(36) Hedin, L.; Lundqvist, B. I. *J. Phys. C Solid State Phys.* **1971**, *4*, 2064–2083.

(37) Korth, M.; Grimme, S. *J. Chem. Theory Comput.* **2009**, *5*, 993–1003.

(38) Mardirossian, N.; Head-Gordon, M. *Mol. Phys.* **2017**, *115*, 2315–2372.

(39) Medvedev, M. G.; Bushmarinov, I. S.; Sun, J.; Perdew, J. P.; Lyssenko, K. A. *Science* **2017**, *355*, 49–52.

(40) Cohen, A. J.; Mori-Sánchez, P.; Yang, W. *Chem. Rev.* **2012**, *112*, 289–320.

(41) Perdew, J. P.; Schmidt, K. *AIP Conf. Proc.* **2001**, *577*, 1–20.

(42) Duboc, C.; Ganyushin, D.; Sivalingam, K.; Collomb, M.-N.; Neese, F. *J. Phys. Chem. A* **2010**, *114*, 10750–10758.

(43) Cohen, A. J.; Mori-Sánchez, P.; Yang, W. *Science* **2008**, *321*, 792–794.

(44) Becke, A. D. *J. Chem. Phys.* **2014**, *140*, 18A301.

(45) Neugebauer, J.; Hickel, T. *Wiley Interdiscip. Rev. Comput. Mol. Sci.* **2013**, *3*, 438–448.

(46) Runge, E.; Gross, E. K. U. *Phys. Rev. Lett.* **1984**, *52*, 997–1000.

(47) Casida, M. E. In *Recent Advances in Density Functional Methods*, 1995, pp 155–192.

(48) Adamo, C.; Jacquemin, D. *Chem. Soc. Rev.* **2013**, *42*, 845–856.

(49) Burke, K.; Werschnik, J.; Gross, E. K. U. *J. Chem. Phys.* **2005**, *123*, 062206.

(50) Coleman A. J.and Yukalov, V. I., *Reduced Density Matrices: Coulson's Challenge*; Springer-Verlag: New York: 2000.

(51) Coleman, A. J. *Rev. Mod. Phys.* **1963**, *35*, 668–686.

(52) Mazziotti, D. A. *Phys. Rev. Lett.* **2012**, *108*, 263002.

(53) Mazziotti, D. A. *Chem. Rev.* **2012**, *112*, 244–262.

(54) Mazziotti, D. A. *Acc. Chem. Res.* **2006**, *39*, 207–215.

(55) Mazziotti, D. A. *Phys. Rev. Lett.* **2006**, *97*, 143002.

(56) Mazziotti, D. A. *Phys. Rev. A* **2007**, *76*, 052502.

(57) Head-Marsden, K.; Flick, J.; Ciccarino, C. J.; Narang, P. *Chem. Rev.* **2021**, *121*, 3061–3120.

(58) Smart, S. E.; Mazziotti, D. A. *Phys. Rev. Lett.* **2021**, *126*, 070504.

(59) Boyn, J.-N.; Lykhin, A. O.; Smart, S. E.; Gagliardi, L.; Mazziotti, D. A. *J. Chem. Phys.* **2021**, *155*, 244106.

(60) Bauer, B.; Bravyi, S.; Motta, M.; Chan, G. K.-L. *Chem. Rev.* **2020**, *120*, 12685–12717.

(61) McArdle, S.; Endo, S.; Aspuru-Guzik, A.; Benjamin, S. C.; Yuan, X. *Rev. Mod. Phys.* **2020**, *92*, 015003.

(62) Motta, M.; Rice, J. E. *Wiley Interdiscip. Rev. Comput. Mol. Sci.* **2021**, e1580.

(63) Reiher, M.; Wiebe, N.; Svore, K. M.; Wecker, D.; Troyer, M. *Proc. Natl. Acad. Sci. U.S.A.* **2017**, *114*, 7555–7560.

(64) Elfving, V. E.; Broer, B. W.; Webber, M.; Gavartin, J.; Halls, M. D.; Lorton, K. P.; Bochevarov, A. *arXiv:2009.12472* **2020**.

(65) Kandala, A.; Mezzacapo, A.; Temme, K.; Takita, M.; Brink, M.; Chow, J. M.; Gambetta, J. M. *Nature* **2017**, *549*, 242–246.

(66) Peruzzo, A.; McClean, J.; Shadbolt, P.; Yung, M.-H.; Zhou, X.-Q.; Love, P. J.; Aspuru-Guzik, A.; O'Brien, J. L. *Nat. Comm.* **2014**, *5*, 4213.

(67) McClean, J. R.; Romero, J.; Babbush, R.; Aspuru-Guzik, A. *New J. Phys* **2016**, *18*, 023023.

(68) *Chem. Phys. Lett.* **1989**, *155*, 133–140.

(69) Romero, J.; Babbush, R.; McClean, J. R.; Hempel, C.; Love, P. J.; Aspuru-Guzik, A. *Quantum Sci. Technol.* **2018**, *4*, 014008.

(70) Shen, Y.; Zhang, X.; Zhang, S.; Zhang, J.-N.; Yung, M.-H.; Kim, K. *Phys. Rev. A* **2017**, *95*, 020501.

(71) Lee, J.; Huggins, W. J.; Head-Gordon, M.; Whaley, K. B. *J. Chem. Theory Comput.* **2019**, *15*, 311–324.

(72) Mazziotti, D. A.; Smart, S. E.; Mazziotti, A. R. *New J. Phys.* **2021**, *23*, 113037.

(73) Bauer, B.; Wecker, D.; Millis, A. J.; Hastings, M. B.; Troyer, M. *Phys. Rev. X* **2016**, *6*, 031045.

(74) Yamazaki, T.; Matsuura, S.; Narimani, A.; Saidmuradov, A.; Zaribafiyan, A. *arXiv:1806.01305* **2018**.

(75) Kowalski, K.; Bauman, N. P. *J. Chem. Phys.* **2020**, *152*, 244127.

(76) Urbanek, M.; Camps, D.; Van Beeumen, R.; de Jong, W. A. *J. Chem. Theory Comput.* **2020**, *16*, 5425–5431.

CHAPTER 2

REDUCED DENSITY MATRIX METHODS FOR THE RESOLUTION OF ELECTRON CORRELATION

2.1 Variational 2-RDM

The variational 2-RDM method makes use of the fact that the ground state energy of a N-electron system may be expressed as a linear functional of the 2-RDM[1–3]:

$$E = Tr[{}^2K\,{}^2D]\,. \tag{2.1}$$

However, first trials to obtain the ground state energy via variational minimization of the 2-RDM in the 1950's quickly showed that without imposing constraints the optimization will result in solutions that lie well below the true electronic ground state energy of the studied system[4, 5]. Understanding that this error was the result of the 2-RDM not corresponding to a physically valid wave function, Coleman realized that so-called N-representability conditions need to be imposed on the 2-RDM during the variational minimization to ensure that the final ground-state 2-RDM may be integrated from a N-electron wave function[4].

While four of these conditions were known and imposed by Coleman during his first calculations, namely that the 2-RDM remain Hermitian, antisymmetric with respect to the exchange of electrons, and positive semidefinite, as well as that its trace, which relates to the number of electrons in the system, stays constant, proved to be insufficient to ensure sufficient N-representability for a chemically accurate calculation[4]. It was not until the 1990's that further N-representability conditions were discovered that allowed 2-RDM methods to resolve electronic properties with accuracy comparable to those obtained with traditional wave function based methods[3, 6–10]. These so-called p-positivity constraints form a hierarchy of constraints that may be derived from the action of p-particle operators on the ground state wave function[11]:

$$ {}^{p}M^{i_1..i_p}_{i_1..i_p} = \langle\Psi|\hat{C}_{i_1..i_p}\hat{C}^{\dagger}_{i_1..i_p}|\Psi\rangle \,, \tag{2.2} $$

where

$$ \hat{C}_{i_1..i_p} = \hat{a}^{\dagger}_{i_1}..\hat{a}^{\dagger}_{i_p} \,, \tag{2.3} $$

and the ${}^{p}M^{i_1..i_p}_{i_1..i_p}$ matrices need to be positive-semidefinite, ${}^{p}M^{i_1..i_p}_{i_1..i_p} \succeq 0$, meaning their eigenvalues are non-negative. These constraints are readily imposed on the 2-RDM during variational minimization using a so-called semi-definite programming (SDP) algorithm[12–16].

As higher-order p-positivity conditions quickly become computationally intractable, modern variational 2-RDM implementations generally restrict themselves to the use of 2- and 3-positivity constraints, avoiding the computation of 4- and higher-order particle matrices[17–23]. Of these the 2-positivity conditions are the most commonly imposed set of N-representability conditions and they are also commonly referred to as the DGQ conditions, where:

$$ {}^{2}D^{ij}_{kl} = \langle\Psi|\hat{a}^{\dagger}_{i}\hat{a}^{\dagger}_{j}\hat{a}_{l}\hat{a}_{k}|\Psi\rangle \succeq 0 \tag{2.4} $$

$$ {}^{2}Q^{kl}_{ij} = \langle\Psi|\hat{a}_{k}\hat{a}_{l}\hat{a}^{\dagger}_{j}\hat{a}^{\dagger}_{i}|\Psi\rangle \succeq 0, \tag{2.5} $$

$$ {}^{2}G^{il}_{kj} = \langle\Psi|\hat{a}^{\dagger}_{i}\hat{a}_{l}\hat{a}^{\dagger}_{j}\hat{a}_{k}|\Psi\rangle \succeq 0\,, \tag{2.6} $$

and ${}^{2}D$ is the 2-RDM, ${}^{2}Q$ is the particle-hole RDM and ${}^{2}G$ is the 2-hole RDM. Additionally, the 2-positivity constraints imply 1-positivity. Implementation of the DQG conditions in a SDP minimization of the ground state energy yields favorable computational scaling of $\mathscr{O}(r^6)$[15]. The full 3-positivity conditions give rise to four metric matrices of rank six that result in significant computational cost when imposed on the variational 2-RDM method. Instead, only a subset of the full conditions, the so-called T_1 and T_2 conditions, are applied when a more accurate lower bound to the true ground state energy compared to the DGQ conditions is desired, which, however, comes at a higher computational cost[19, 20].

The V2RDM method has found most success when implemented in a CASSCF procedure[17, 18]. Here, the V2RDM replaces the CI solver in the traditional CASSCF algorithm, reducing its computational scaling from $\mathscr{O}(r^N)$, where N is the number of electrons, to $\mathscr{O}(r^6)$ with DQG constraints. The more favorable scaling in the V2RDM CASSCF allows for the resolution of multi-reference correlation in significantly larger active spaces than wave function based CASSCF which is limited to active spaces of [18,18]. Indeed, V2RDM CASSCF calculations have been carried out with active spaces as large as [50,50][18], allowing their application to the resolution of the electronic structure of large acene chains[18, 24] or complexes containing multiple metal centers such as the nitrogenase cofactor FeMoCo[25].

2.2 Anti-Hermitian Contracted Schrödinger Equation

A different approach to calculate ground state 2-RDMs and energies is the use of the contracted Schrödinger equation (CSE), which is the Schrödinger equation contracted onto the space of all two-particle transitions[26, 27]. The CSE is given by:

$$\langle\Psi|\,\hat{a}_i^\dagger\hat{a}_j^\dagger\hat{a}_l\hat{a}_k\hat{H}\,|\Psi\rangle = E\;{}^2D^{ij}_{kl}\,, \tag{2.7}$$

where $\hat{H}$ is the Hamiltonian operator

$$\hat{H} = \sum_{ij}{}^1K^i_j\hat{a}_i^\dagger\hat{a}_j + \sum_{ijkl}{}^2V^{ij}_{kl}\hat{a}_i^\dagger\hat{a}_j^\dagger\hat{a}_l\hat{a}_k\,, \tag{2.8}$$

and ${}^{1}K^{i}_{j}$ and ${}^{2}V^{ij}_{kl}$ contain the 1- and 2-electron integrals, respectively. As the CSE depends on the 2-, 3- and 4-RDMs it is not solved at feasible computational cost, however, it can be expanded into its Hermitian and anti-Hermitian parts, with selection of the latter yielding the anti-Hermitian contracted Schrödinger equation (ACSE)[28, 29]:

$$\langle \Psi | [\hat{a}^{\dagger}_{i} \hat{a}^{\dagger}_{j} \hat{a}_{l} \hat{a}_{k}, \hat{H}] | \Psi \rangle = 0 \,, \tag{2.9}$$

where [] denotes a commutator. Unlike the CSE and its Hermitian part, the ACSE only depends on the 2- and 3-RDMs and the dependence on the latter may be further resolved by the use of an approximate reconstruction of its in elements in terms of the 2-RDM[30]. This allows the ACSE to be solved via a series of differential equations and with a computational scaling of $\mathscr{O}(r^6)$. When seeded with a HF guess the ACSE computes dynamic correlation with accuracy comparable to CCSD(T)[31]. However, it may also be seeded with a strongly correlated guess 2-RDM from a CAS calculation, in which case the on-top dynamic correlation will be resolved with significantly greater accuracy than that of CASPT2, the most common-place method for the resolution of all-electron correlation in multi-reference systems[32, 33].

2.3 Pure N-representability Conditions

In addition to the necessary and sufficient p-positivity conditions imposed on the 2-RDM in the V2RDM method, which ensure ensemble N-representability, a further class of N-representability conditions exists that assures that a RDM corresponds to a pure state[34]. These were first discovered by Borland and Dennis at IBM in the 1970s for the specific case of the 1-RDM of a system comprising three electrons distributed in six spin orbitals, showing them to take the form of linear constraints on the natural occupations numbers $\{\lambda\}$[35]:

$$\lambda_1+\lambda_6=\lambda_2+\lambda_5=\lambda_3+\lambda_4=1\,, \tag{2.10}$$

$$2-(\lambda_1+\lambda_2+\lambda_4)\geq 0\,. \tag{2.11}$$

Pure N-representability conditions are also known as generalized Pauli conditions, or GPC, and they were further enumerated by Klyachko in 2008 through the use of Schubert calculus for systems comprising up to 10 spin orbitals[36, 37] and later extended to the 2-RDM by Mazziotti in 2016[34, 38]. A special case termed ”pinning” is observed when a system saturates its GPC, which is observed in the case of three electrons[39–42] and has been demonstrated experimentally on a quantum device[43]. However, ”pinning” is not necessarily observed in higher odd numbered systems and never observed in the case of even numbered systems. The GPC can yield insight into the quantum state of fermionic systems[44, 45], as well as provide a valuable basis for the development of reduced density matrix functionals and quantum algorithms utilizing a GPC defined sparse ansatz[41, 46–49].

References

(1) Coleman A. J.and Yukalov, V. I., *Reduced Density Matrices: Coulson's Challenge*; Springer-Verlag: New York: 2000.

(2) Löwdin, P.-O. *Phys. Rev.* **1955**, *97*, 1474–1489.

(3) Mazziotti, D. A. *Phys. Rev. A* **2002**, *65*, 062511.

(4) Coleman, A. J. *Rev. Mod. Phys.* **1963**, *35*, 668–686.

(5) Tredgold, R. H. *Phys. Rev.* **1957**, *105*, 1421–1423.

(6) Colmenero, F.; Valdemoro, C. *Phys. Rev. A* **1993**, *47*, 979–985.

(7) Colmenero, F.; Valdemoro, C. *Int. J. Quantum Chem.* **1994**, *51*, 369–388.

(8) Mazziotti, D. A. *Phys. Rev. A* **1998**, *57*, 4219–4234.

(9) Nakatsuji, H.; Yasuda, K. *Phys. Rev. Lett.* **1996**, *76*, 1039–1042.

(10) Yasuda, K.; Nakatsuji, H. *Phys. Rev. A* **1997**, *56*, 2648–2657.

(11) Mazziotti, D. A. *Phys. Rev. Lett.* **2012**, *108*, 263002.

(12) Nakata, M.; Nakatsuji, H.; Ehara, M.; Fukuda, M.; Nakata, K.; Fujisawa, K. *J. Chem. Phys.* **2001**, *114*, 8282–8292.

(13) Mazziotti, D. A. *Phys. Rev. Lett.* **2004**, *93*, 213001.

(14) Nakata, M.; Braams, B. J.; Fujisawa, K.; Fukuda, M.; Percus, J. K.; Yamashita, M.; Zhao, Z. *J. Chem. Phys.* **2008**, *128*, 164113.

(15) Mazziotti, D. A. *Phys. Rev. Lett.* **2011**, *106*, 083001.

(16) Mazziotti, D. A. *Phys. Rev. A* **2020**, *102*, 052819.

(17) Gidofalvi, G.; Mazziotti, D. A. *J. Chem. Phys.* **2008**, *129*, 134108.

(18) Fosso-Tande, J.; Nguyen, T.-S.; Gidofalvi, G.; DePrince, A. E. *J. Chem. Theory Comput.* **2016**, *12*, 2260–2271.

(19) Mazziotti, D. A. *Phys. Rev. A* **2005**, *72*, 032510.

(20) Mazziotti, D. A. *Phys. Rev. A* **2006**, *74*, 032501.

(21) Gidofalvi, G.; Mazziotti, D. A. *J. Chem. Phys.* **2007**, *126*, 024105.

(22) Fosso-Tande, J.; Nascimento, D. R.; III, A. E. D. *Mol. Phys.* **2016**, *114*, 423–430.

(23) Li, R. R.; Liebenthal, M. D.; DePrince, A. E. *J. Chem. Phys.* **2021**, *155*, 174110.

(24) Pelzer, K.; Greenman, L.; Gidofalvi, G.; Mazziotti, D. A. *J. Phys. Chem. A* **2011**, *115*, 5632–5640.

(25) Montgomery, J. M.; Mazziotti, D. A. *J. Phys. Chem. A* **2018**, *122*, 4988–4996.

(26) Mazziotti, D. A. *Phys. Rev. A* **1998**, *57*, 4219–4234.

(27) Mazziotti, D. A. *Chem. Phys. Lett.* **1998**, *289*, 419–427.

(28) Mazziotti, D. A. *Phys. Rev. Lett.* **2006**, *97*, 143002.

(29) Mazziotti, D. A. *Phys. Rev. A* **2007**, *75*, 022505.

(30) DePrince, A. E.; Mazziotti, D. A. *J. Chem. Phys.* **2007**, *127*, 104104.

(31) Mazziotti, D. A. *Phys. Rev. A* **1999**, *60*, 4396.

(32) Mazziotti, D. A. *Phys. Rev. A* **2007**, *76*, 052502.

(33) Greenman, L.; Mazziotti, D. A. *J. Chem. Phys.* **2011**, *134*, 174110.

(34) Mazziotti, D. A. *Phys. Rev. A* **2016**, *94*, 032516.

(35) Borland, R. E.; Dennis, K. *J. Phys. B* **1972**, *5*, 7–15.

(36) Klyachko, A. A. *J. Phys. Conf. Ser.* **2006**, *36*, 72–86.

(37) Altunbulak, M.; Klyachko, A. *Commun. Math. Phys.* **2008**, *282*, 287–322.

(38) DePrince, A. E. *J. Chem. Phys.* **2016**, *145*, 164109.

(39) Schilling, C.; Gross, D.; Christandl, M. *Phys. Rev. Lett.* **2013**, *110*, 040404.

(40) Tennie, F.; Ebler, D.; Vedral, V.; Schilling, C. *Phys. Rev. A* **2016**, *93*, 042126.

(41) Theophilou, I.; Lathiotakis, N. N.; Marques, M. A. L.; Helbig, N. *J. Chem. Phys.* **2015**, *142*, 154108.

(42) Schilling, C. *Phys. Rev. A* **2015**, *91*, 022105.

(43) Smart, S. E.; Schuster, D. I.; Mazziotti, D. A. *Commun. Phys.* **2019**, *2*, 11.

(44) Chakraborty, R.; Mazziotti, D. A. *Phys. Rev. A* **2015**, *91*, 010101.

(45) Chakraborty, R.; Mazziotti, D. A. *Int. J. Quantum Chem.* **2016**, *116*, 784–790.

(46) Boyn, J.-N.; Mazziotti, D. A. *J. Chem. Phys.* **2019**, *150*, 144102.

(47) Chakraborty, R.; Mazziotti, D. A. *J. Chem. Phys.* **2018**, *148*, 054106.

(48) Rubin, N. C.; Babbush, R.; McClean, J. *New J. Phys.* **2018**, *20*, 053020.

(49) Schilling, C. *J. Chem. Phys.* **2018**, *149*, 231102.

CHAPTER 3

EXTENSION OF THE GENERALIZED PAULI CONSTRAINTS TO THE TWO-ELECTRON REDUCED DENSITY MATRIX

Reprinted with permission from J.-N. Boyn and D.A. Mazziotti, *Journal of Chemical Physics* **150**, 144102 (2019). Copyright 2019 American Institute of Physics.

3.1 Introduction

Quantum states are restricted to be physically realistic by the Pauli exclusion principle, which dictates that electron occupation numbers must lie between 0 and 1. This was later extended to 1-RDMs by Coleman, who in 1963 [1] proved that the Pauli exclusion principle is necessary and sufficient for the 1-RDM to be derivable from an N-electron ensemble system. However, pure quantum states levy further restrictions on the electronic occupation numbers[2–6].

It was first shown in the 1970s that global antisymmetry leads to linear constraints on the natural occupation numbers for 3 electron systems[5]. The so-called Borland-Dennis setting of 3 electrons in 6 spin orbitals ($\mathscr{H} = \wedge^3[\mathscr{H}_1^{(6)}]$, where $\mathscr{H}_1^{(6)}$ denotes the dimension of the 1-particle Hilbert space and $\wedge^3$ denotes the number of fermions), discovered by Borland and Dennis at IBM in 1972, has 4 well known constraints on the natural orbital occupation numbers $\{\lambda\}$:

$$\lambda_1 + \lambda_6 = \lambda_2 + \lambda_5 = \lambda_3 + \lambda_4 = 1 \tag{3.1}$$

$$2 - (\lambda_1 + \lambda_2 + \lambda_4) \geq 0. \tag{3.2}$$

These generalized Pauli constraints (GPC), also known as pure N-representability conditions, ensure that the 1-RDM is representable by a N-fermion wave function[1]. Altunbulak and Klyachko developed an algorithm in 2008 that derives the GPC for systems up to a maximum size of 10 spin orbitals [2, 3]. The effect of these constraints has been computationally explored for various electronic ground and excited states of atoms and molecules[7–11]. The ground states of systems of 3 electrons tend to saturate one of their GPC, which is termed *pinning*. Odd numbered systems of 5 or more electrons may be pinned, however, they are not necessarily so, and the ground states of even-numbered electronic systems never saturate the GPC derived by Klyachko[12]. Saturation of the GPC implies a reduction in complexity of the wave function, decreasing the number of electronic configurations needed to fully describe the system. This can have significant implications for the treatment of systems exhibiting strong correlations.

Recent work has included the study of the Hubbard model[13, 14], as well as open and time-dependent quantum systems[15, 16]. Furthermore, the GPC have proven to be promising in the development of density matrix functionals, where Benavides-Riveros has recently used the pinned solution of the Borland-Dennis setting to create a functional yielding significantly improved results over traditional DFT and RDMFs when applied to a Hubbard model[14]. The GPCs for systems of 3 electrons in 6 spin orbitals have been thoroughly studied in the literature, using various atoms and molecules such as Li or H_3, and families of interacting fermions in a harmonic potential[7–9, 11, 17–19].

In our present work we will explore the sparsity of the wave function of 4 electrons in 8 spin orbitals ($\mathscr{H} = \wedge^4[\mathscr{H}_1^{(8)}]$) based on the pure N-representability conditions of the 2-RDM previously derived by Mazziotti, which extend the GPC to the 2-RDM[20]. Previous work has shown systems of 4 electrons in 8 spin orbitals to saturate these 2-RDM constraints[20]. This pinning has two remarkable consequences in the emergence of: (i) sparsity in the wave function, which is seen in the 3-electron case and (ii) non-orthogonal spin orbitals in the wave function, which only appears for the first time in the 4-electron case. Non-orthogonal orbitals are typically used in an *ad hoc* fashion due to empirical observations of rapid convergence[21–26]. Saturation of a pure representability condition of the 2-RDM in the case of the 4-electron wave function provides a rigorous foundation for the introduction of non-orthogonal orbitals for a compact representation of the wave function. This relates to recent work aiming to exploit sparse wave function representations using non-orthogonal CI (NOCI), which is commonly implemented using Monte Carlo or stochastic sampling of determinants[21, 27–34].

We validate our approach with complete active space calculations on the isoelectronic series of the carbon atom and calculations on the dissociation of the linear hydrogen chain H_4, comparing against results from Hartree Fock (HF), Møller-Plesset perturbation theory (MP2), full configuration interaction (FCI) and complete active space configuration interaction (CASCI) calculations. This work provides a basis for the development of *sparse Ansatz* methods for even numbered electronic systems and further improvement of RDM functionals based on pinned solutions. Furthermore, we elucidate a fundamental physical basis for the emergence of non-orthogonal bases in electronic systems of 4 or more electrons.

3.2 Theory

Density matrices are useful tools to describe quantum systems. A p-electron reduced density matrix of an N-electron system is obtained by integrating the total density matrix over the coordinates of all but p electrons. For the 1-RDM and 2-RDM this may be achieved in second quantization as follows:

$$ {}^1D^i_k = \langle\Psi|\hat{a}^\dagger_i \hat{a}_k|\Psi\rangle \tag{3.3}$$

$$ {}^2D^{ij}_{kl} = \langle\Psi|\hat{a}^\dagger_i \hat{a}^\dagger_j \hat{a}_l \hat{a}_k|\Psi\rangle \,. \tag{3.4}$$

The energy of a system can be expressed exactly in terms of its 1-RDM and 2-RDM:

$$ E = \mathrm{Tr}\,({}^1K\,{}^1D) + \frac{1}{2}\mathrm{Tr}\,({}^2V\,{}^2D) \tag{3.5}$$

where ${}^1K$ and ${}^2V$ are the one and two electron integral matrices respectively. The eigenvectors of the 1-RDM are termed natural orbitals and its eigenvalues are the natural occupation numbers $\{\lambda_i\}$, corresponding to the probability of finding an electron in natural spin orbital i for all possible configuration of the other $N-1$ electrons.

Generalized Pauli constraints (GPC), also known as pure N-representability conditions, ensure that the 1-RDM is representable by a N-fermion wave function[1, 15]. Recently, the GPC have been shown to obey the following general form:

$$D_j(\vec{\lambda}) = \kappa_j^{(0)} + \sum_{i=0}^{d} \kappa_j^{(i)} \lambda_i \geq 0 \tag{3.6}$$

where $\kappa_j^{(i)} \in \mathbb{Z}$, $j = 1, 2, ..., \nu_{N,d} < \infty$, d is the dimension of the 1-particle Hilbert space and the natural occupation numbers are in decreasing order. The GPC provide necessary and sufficient conditions for the pure N-representability of 1-RDMs and Klyachko has developed an algorithm that derives these GPC up to a setting of $d \leq 10$ [2, 3]. Together with the ordering and normalization constraints on the natural occupation numbers, they form a polytope $\mathscr{P}_{N,r}^1$ of pure N-representable 1-RDMs. This set contains all 1-RDMs that can be derived from an N-electron wave function.
An N-electron wave function may be a expressed as a linear combination of Slater determinants

$$|\Psi\rangle = \sum_i c_i |\Phi_i\rangle \tag{3.7}$$

where $\{|\Phi_i\rangle\}$ is the set of all possible electronic configurations, e.g. $|123\rangle$ would denote a Slater determinant for an electron configuration with spin orbitals 1 through 3 filled and the rest unfilled. If one or more of the GPC is saturated the system can be considered *pinned* (or *quasi-pinned* if a GPC is nearly saturated), meaning it lies on the boundary of $\mathscr{P}_{N,r}^1$, which implies a simplification of the many-electron wave function as the number of allowed Slater determinants is reduced[7–9, 12, 35, 36]. The fact that only pinned Slater determinants contribute to a pinned N-electron wave function is termed the selection rule[37].

While saturation of the GPC has been studied for various systems it has only been shown to occur consistently for odd-N fermionic systems with $N \leq 5$[9, 12, 17]. For even-N fermion singlet ground states, e.g. a $\mathscr{H} = \wedge^4[\mathscr{H}_1^{(8)}]$ space, it has been shown that the 1-RDM spectrum

Boundary	Operator
1	${}^1\hat{O}_1 = 2 - \hat{a}_2^\dagger\hat{a}_2 - \hat{a}_3^\dagger\hat{a}_3 - \hat{a}_4^\dagger\hat{a}_4 - \hat{a}_5^\dagger\hat{a}_5$
2	${}^1\hat{O}_2 = 2 - \hat{a}_1^\dagger\hat{a}_1 - \hat{a}_3^\dagger\hat{a}_3 - \hat{a}_4^\dagger\hat{a}_4 - \hat{a}_6^\dagger\hat{a}_6$
3	${}^1\hat{O}_3 = 2 - \hat{a}_1^\dagger\hat{a}_1 - \hat{a}_2^\dagger\hat{a}_2 - \hat{a}_4^\dagger\hat{a}_4 - \hat{a}_7^\dagger\hat{a}_7$
4	${}^1\hat{O}_4 = 2 - \hat{a}_1^\dagger\hat{a}_1 - \hat{a}_2^\dagger\hat{a}_2 - \hat{a}_5^\dagger\hat{a}_5 - \hat{a}_6^\dagger\hat{a}_6$

Table 3.1: Operators that expose the GPC in the natural orbital basis of the $\mathscr{H} = \wedge^3[\mathscr{H}_1^{(7)}]$ setting, where $\hat{a}^\dagger$ and $\hat{a}$ are the creation and annihilation operators respectively.

is not pinned to the polytope defined by the GPC derived by Klyachko[9, 17, 20] as time-reversal symmetry reduces the Klyachko GPC to the conventional Pauli conditions[20]. Recently, one of the authors (Mazziotti) has shown that the GPC can be extended to generate constraints defining the set of pure *N*-representable 2-RDMs[20]. Calculations show that the wave functions of 4-electron atoms and molecules in 8 spin orbitals non-trivially saturate one of these GPC-like constraints on the 2-RDM.

Here we exploit this observed pinning in 4-electron systems to derive a sparse parameterization of the 4-electron wave function. The form of the GPC-like constraints of the 2-RDM suggests that the 4-electron wave function can be parameterized efficiently by considering the one-electron ionization and one-electron attachment of the 4-electron wave function. Such consideration yields two effective odd-*N* systems, which possess non-trivial GPC which the wave function may saturate. The set of operators that expose the GPC in the natural orbital basis for the $\mathscr{H} = \wedge^3[\mathscr{H}_1^{(7)}]$ space are shown in Table 3.1.

Consider the action of the identity operator $\hat{I}$ on a wave function $|\Psi_{4,8}\rangle$ lying in the $\mathscr{H} = \wedge^4[\mathscr{H}_1^{(8)}]$ space:

$$|\tilde{\Psi}_{4,8}\rangle = (\hat{a}_j\hat{a}_j^\dagger + \hat{a}_j^\dagger\hat{a}_j)\,|\Psi_{4,8}\rangle \tag{3.8}$$

where $\hat{a}_j$ and $\hat{a}_j^\dagger$ are effective annihilation and creation operators running over all spin orbitals:

$$\hat{a}_j = \sum_i c_i\hat{a}_i. \tag{3.9}$$

Hence,

$$|\tilde{\Psi}_{4,8}\rangle = (\sum_i c_i\hat{a}_i \sum_i c_i\hat{a}_i^\dagger + \sum_i c_i\hat{a}_i^\dagger \sum_i c_i\hat{a}_i)\,|\Psi_{4,8}\rangle\,. \tag{3.10}$$

This yields two composite wave functions which we will now consider separately. Action of $\sum_i c_i\hat{a}_i$ first yields a system with 3 electrons in 8 spin orbitals, one of which is always unoccupied, an effective wave function $|\Psi_{3,7}\rangle$ lying in the space $\mathscr{H} = \wedge^3[\mathscr{H}_1^{(7)}]$:

$$\sum_i c_i\hat{a}_i^\dagger \sum_i c_i\hat{a}_i\,|\Psi_{N,r}\rangle = \sum_i c_i\hat{a}_i^\dagger\,|\Psi_{3,7}\rangle\,. \tag{3.11}$$

The choice of parameter c_i determines the removed spin orbital. Conversely, action of $\sum_i c_i a_i^\dagger$ on $|\Psi_{4,8}\rangle$ yields a wave function of 5 electrons in 8 spin orbitals, one of which is always occupied. This wave function can be related to the $\mathscr{H} = \wedge^3[\mathscr{H}_1^{(7)}]$ space and its GPC via particle-hole symmetry:

$$\sum_i c_i\hat{a}_i \sum_i c_i\hat{a}_i^\dagger\,|\Psi_{4,8}\rangle = \sum_i c_i\hat{a}_i\,|\Psi_{5,8}\rangle \tag{3.12}$$

where $|\Psi_{5,8}\rangle = |\Psi'_{3,7}\rangle$ via particle-hole symmetry. Action of the conjugate operators on each of the constituent wave functions recovers the $|\Psi_{4,8}\rangle$ wave function parametrized in terms of two $\mathscr{H} = \wedge^3[\mathscr{H}_1^{(7)}]$ systems, which have been demonstrated to be pinned to the boundary of one of their GPC[9].

If a pure wave function saturates one of the GPC then it must satisfy a constraint of the following form:

$$\mathrm{Tr}({}^1\hat{O}_m\,{}^1D) = 0 \tag{3.13}$$

where ${}^1\hat{O}_m$ is an operator of the set that exposes the boundary of $P^1_{N,r}$, the set of all permissible wave functions of N fermions in r spin orbitals , shown in table 3.1. This leads to a decrease in the degrees of freedom in the representation of the wave function, a reduction in the set of permissible Slater determinants. To fully describe the $\mathscr{H} = \wedge^4[\mathscr{H}_1^{(8)}]$ space 70 Slater determinants are needed[9]. A wave function lying in the $\mathscr{H} = \wedge^3[\mathscr{H}_1^{(7)}]$ space requires 36 Slater determinants to

	Energy (a.u.)			
Species	HF	CASCI	2RDM-GPC	%
B^-	-24.105841	-24.126046	-24.126046	**100.00**
C	-37.572364	-37.592804	-37.592803	**100.00**
N^+	-53.765204	-53.785867	-53.785860	**99.97**
O^{2+}	-72.799360	-72.821142	-72.821137	**99.98**
F^{3+}	-94.703887	-94.726615	-94.726613	**99.99**

Table 3.2: Energies (in Hartree) for HF, CASCI and our pinned wave function Ansatz for the isoelectronic series of carbon. CASCI calculations use an active space of the 2s and 2p orbitals. The energy for the pinned solution represents the solution arising from the 1-RDMs pinned to the set of GPC delivering the lowest upper bound of the CASCI energy. In all cases the correlation energy is recovered to μHartree accuracy.

be fully characterized, however, the wave function should saturate one of its GPC, reducing the set of permissible Slater determinants from 36 to 18. Consequently, the present approach reduced 70 Slater determinants to 36 Slater determinants (18 for each of the composite wave functions) in the parametrized $\mathscr{H} = \wedge^4[\mathscr{H}_1^{(8)}]$ space. If the $\mathscr{H} = \wedge^4[\mathscr{H}_1^{(8)}]$ wave function can, indeed, be constructed from two parameterized, $\mathscr{H} = \wedge^3[\mathscr{H}_1^{(7)}]$ wave functions as theorized, a significant decrease in computational complexity will be observed as the number Slater determinants required to the fully describe the system is reduced.

3.3 Applications

We apply the pinned Ansatz to some chosen systems of four electrons in eight spin orbitals: the isoelectronic series of the carbon atom (B^-, C, N^+, O^{2+}, F^{3+}) and the dissociation of linear H_4. The results are compared against HF, MP2, FCI, or CASCI calculations. All calculations were executed with the GAMESS software package [38] using a minimal STO-6G basis set[39]. Pinned energies are obtained starting from the full CI wave function and using one- and two-electron integrals obtained from a GAMESS full CI calculation. The energies associated with each pinned wave function was obtained via minimization subject to the constraint that the two constituent 1-RDMs lying in the $\wedge^3[\mathscr{H}_1^{(7)}]$ space saturate to a set of chosen GPC, and the total system remains

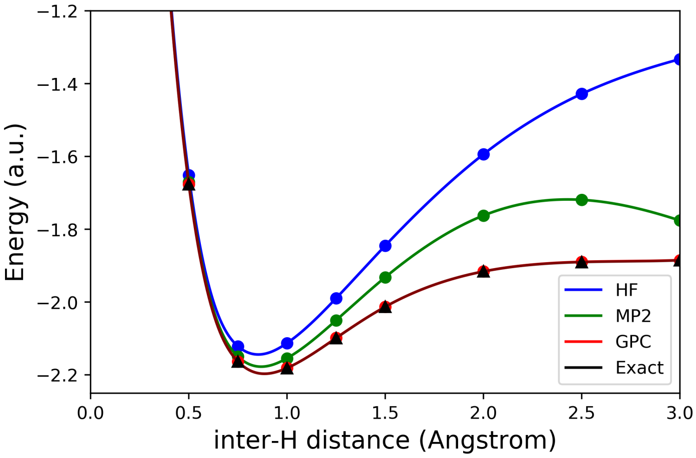

Figure 3.1: Dissociation curve for the linear, equally spaced H_4 chain, showing results for HF, MP2, FCI and our pinned Ansatz. The pinned Ansatz successfully describes the system at all bond distances and recovers the correct dissociation limit, recovering 99.19% to 99.99% of the correlation energy.

normalized. The constrained minimization was achieved using the interior point algorithm as implemented in the MATLAB R2018a optimization toolbox with a constraint tolerance of 10^{-10} assumed to be sufficient for the constraint to be saturated. The set of GPC that gave the best upper bound to the full CI or CASCI energy was selected as the optimal structure of the pinned wave function.

For the isoelectronic series of the carbon atom an $\mathscr{H} = \wedge^4[\mathscr{H}_1^{(8)}]$ active space of the 2s and 2p orbitals was used. The 1s core orbitals were excluded for a setting of four electrons in eight spin orbitals. The electronic ground state energy arising from the wave function saturating the optimal set of GPC is compared to the HF and CASCI results in Table 3.2, where the percentage of recovered correlation energy is defined as

$$\%E_{rec}^{cor} = \frac{E_{pin} - E_{\text{HF}}}{E_{\text{CASCI}} - E_{\text{HF}}} \tag{3.14}$$

In all cases the CASCI correlation energy was recovered with micro Hartree (μE_h) accuracy, with the largest deviation being $5\mu E_h$ in the case of O^{2+}, and errors for B^- and C being in the sub μE_h

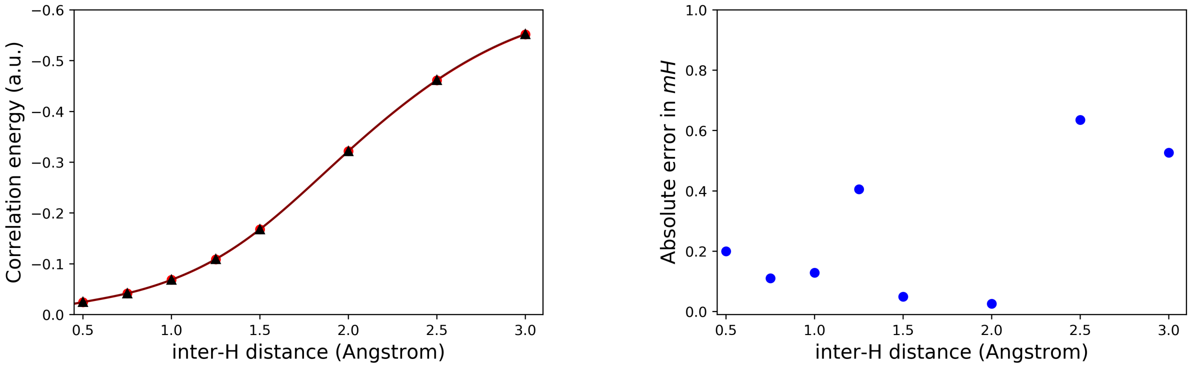

(a) (b)

Figure 3.2: (a): Magnitude of the correlation energy for different inter-H distances in H_4 for CASCI (black) and the pinned Ansatz (red). The two lines coincide and cannot easily be visually distinguished. The magnitude of the correlation energy increases with inter-H distance as electronic configurations become more degenerate. (b): Absolute errors in the correlation energy for the dissociation of the linear, equally spaces H_4 chain. Chemical accuracy of $\Delta E \leq 1$ kcal/mol is achieved for all geometries. Higher absolute errors are observed in the dissociated regime where the magnitude of the correlation energy is largest.

range.

The dissociation of H_4 was investigated as linear hydrogen chains show large correlation contributions to the electronic energy in the dissociative limit, owing to the high degeneracy of the system[40]. Figure 3.1 shows the dissociation curve for H_4, dissociating into four equally spaced H atoms, from our pinned Ansatz, as well as, HF, MP2 and FCI, and the absolute error of the pinned energy. Figure 3.2 shows the value of the correlation energy as a function of inter-H separation for CASCI and the pinned Ansatz and the magnitude of the error of the pinned Ansatz. Pinning recovers between 99.19% and 99.99% of the correlation energies with errors ranging from $0.026\mathrm{m}E_h$ to $0.635\mathrm{m}E_h$. The energy was minimized across all possible sets of saturated GPC and the set that minimized the energy varied across the inter-H distances. The pinned results are compared to those from HF, MP2 and FCI. The pinned Ansatz significantly outperforms HF and MP2, reproducing the FCI results to chemical accuracy for all geometries, and yielding the correct behavior in the dissociation regime.

3.4 Conclusions

Based on the pure N-representability conditions for the 2-RDM, derived previously by Mazziotti, we have extended saturation of the GPC to the $\mathscr{H} = \wedge^4[\mathscr{H}_1^{(8)}]$, demonstrating a sparse wave function Ansatz for an even-N electron system. Pinning is achieved through parameterization of the four electron wave function in terms of two 3 electrons wave functions via one electron attachment and ionization. Computationally, the Ansatz is explored via constrained optimization, forcing the two constituent 3 electron wave functions to saturate the GPC in their respective natural orbitals basis. The Ansatz leads to the emergence of not only sparsity but also non-orthogonality in the CI expansion. We demonstrated the validity of the pinned Ansatz for the $\mathscr{H} = \wedge^4[\mathscr{H}_1^{(8)}]$ space via calculations of the isoelectronic series of the carbon atom and the dissociation of the linear H_4 chain, where saturation of the GPC recovered the FCI or CASCI result to well within chemical accuracy.

This work provides new insights into the generalization of the Pauli exclusion principle as well as the physical basis of non-orthogonal CI expansions. The results can have significant applications in the development of computational methods for the treatment of strong electronic correlations in quantum chemistry and physics where expressing an electronic wave function with fewer degrees of freedom results in significant reduction of the computational complexity. Applications include the improvement of methodologies including the variational 2-RDM method[20, 41–45], natural-orbital functional theory (NOFT)[46–48], and NOCI[21, 23, 26–30] as well as the treatment of correlation in atoms, molecules or other fermionic systems.

References

(1) Coleman A. J.and Yukalov, V. I., *Reduced Density Matrices: Coulson's Challenge*; Springer-Verlag: New York: 2000.

(2) Klyachko, A. A. *J. Phys. Conf. Ser.* **2006**, *36*, 72.

(3) Altunbulak, M.; Klyachko, A. *Comm. Math. Phys.* **2008**, *282*, 287–322.

(4) Smith, D. W. *Phys. Rev.* **1966**, *147*, 896–898.

(5) Borland, R.; Dennis, K. *J. Phys. B.* **1972**, *5*, 7.

(6) Ruskai, M. B. *J. Phys. A*, *40*, F961.

(7) Benavides-Riveros, C. L.; Schilling, C. *Z. Phys. Chem.* **2016**, *230*, 703–717.

(8) Schilling, C.; Gross, D.; Christandl, M. *Phys. Rev. Lett.* **2013**, *110*, 040404.

(9) Chakraborty, R.; Mazziotti, D. A. *J. Chem. Phys.* **2018**, *148*, 054106.

(10) Chakraborty, R.; Mazziotti, D. A. *Int. J. Quantum Chem.* **2016**, *116*, 784–790.

(11) Schilling, C.; Altunbulak, M.; Knecht, S.; Lopes, A.; Whitfield, J. D.; Christandl, M.; Gross, D.; Reiher, M. *Phys. Rev. A* **2018**, *97*, 052503.

(12) Chakraborty, R.; Mazziotti, D. A. *Phys. Rev. A* **2014**, *89*, 042505.

(13) Schilling, C. *Phys. Rev. B* **2015**, *92*, 155149.

(14) Benavides-Riveros, Carlos L.; Marques, Miguel A.L. *Eur. Phys. J. B* **2018**, *91*, 133.

(15) Chakraborty, R.; Mazziotti, D. A. *Phys. Rev. A* **2015**, *91*, 010101.

(16) Chakraborty, R.; Mazziotti, D. A. *J. Chem. Phys.* **2017**, *146*, 184101.

(17) Tennie, F.; Vedral, V.; Schilling, C. *Phys. Rev. A* **2016**, *94*, 012120.

(18) Tennie, F.; Vedral, V.; Schilling, C. *Phys. Rev. A* **2017**, *95*, 022336.

(19) Legeza, Ö.; Schilling, C. *Phys. Rev. A* **2018**, *97*, 052105.

(20) Mazziotti, D. A. *Phys. Rev. A* **2016**, *94*, 032516.

(21) Olsen, J. *J. Chem. Phys.* **2015**, *143*, 114102.

(22) McClean, J. R.; Aspuru-Guzik, A. *RSC Adv.* **2015**, *5*, 102277–102283.

(23) Goto, H.; Kojo, M.; Sasaki, A.; Hirose, K. *Nanoscale Res. Lett.* **2013**, *8*, 200.

(24) Jiménez-Hoyos, C. A.; Rodríguez-Guzmán, R.; Scuseria, G. E. *J. Chem. Phys.* **2013**, *139*, 204102.

(25) Head-Gordon, M.; Maslen, P. E.; White, C. A. *J. Chem. Phys.* **1998**, *108*, 616–625.

(26) Koch, H.; Dalgaard, E. *Chem. Phys. Lett.* **1993**, *212*, 193–200.

(27) Ayala, P. Y.; Schlegel, H. B. *J. Chem. Phys.* **1998**, *108*, 7560–7567.

(28) Josué Landinez Borda, E.; Gomez, J. A.; Morales, M. A. *ArXiv e-prints* **2018**, arXiv:1801.10307, arXiv:1801.10307.

(29) Thom, A. J. W.; Head-Gordon, M. *J. Chem. Phys.* **2009**, *131*, 124113.

(30) Paulus, B.; Rosciszewski, K.; Stoll, H.; Birkenheuer, U. *Phys. Chem. Chem. Phys.* **2003**, *5*, 5523–5529.

(31) Knecht, S.; Keller, S.; Autschbach, J.; Reiher, M. *J. Chem. Theory Comput.* **2016**, *12*, 5881–5894.

(32) Sundstrom, E. J.; Head-Gordon, M. *J. Chem. Phys.* **2014**, *140*, 114103.

(33) Greer, J. C. *J. Chem. Phys.* **1995**, *103*, 1821–1828.

(34) Zhang, T.; Evangelista, F. A. *J. Chem. Theory Comput.* **2016**, *12*, 4326–4337.

(35) Benavides-Riveros, C. L.; Lathiotakis, N. N.; Marques, M. A. L. *Phys. Chem. Chem. Phys.* **2017**, *19*, 12655–12664.

(36) Schilling, C. *Phys. Rev. A* **2015**, *91*, 022105.

(37) Schilling, C.; Benavides-Riveros, C. L.; Vrana, P. *Phys. Rev. A* **2017**, *96*, 052312.

(38) Schmidt, M. W.; Baldridge, K. K.; Boatz, J. A.; Elbert, S. T.; Gordon, M. S.; Jensen, J. H.; Koseki, S.; Matsunaga, N.; Nguyen, K. A.; Su, S.; Windus, T. L.; Dupuis, M.; Montgomery, J. A. *J. Comput. Chem.* **1993**, *14*, 1347–1363.

(39) Hehre, W. J.; Stewart, R. F.; Pople, J. A. *J. Chem. Phys.* **1969**, *51*, 2657–2664.

(40) El Khatib, M.; Brea, O.; Fertitta, E.; Bendazzoli, G. L.; Evangelisti, S.; Leininger, T. *J. Chem. Phys.* **2015**, *142*, 094113.

(41) Mazziotti, D. A. *Phys. Rev. A* **1998**, *57*, 4219–4234.

(42) Mazziotti, D. A. *Phys. Rev. Lett.* **2016**, *117*, 153001.

(43) Mazziotti, D. A. *Phys. Rev. A* **2005**, *72*, 032510.

(44) Gidofalvi, G.; Mazziotti, D. A. *J. Chem. Phys.* **2008**, *129*, 134108.

(45) DePrince, A. E. *J. Chem. Phys.* **2016**, *145*, 164109.

(46) Piris, M.; Ugalde, J. M. *Int. J. Quantum Chem.* **2014**, *114*, 1169–1175.

(47) Piris, M.; Matxain, J. M.; Lopez, X.; Ugalde, J. M. *J. Chem. Phys.* **2009**, *131*, 021102.

(48) Piris, M.; Matxain, J. M.; Lopez, X. *J. Chem. Phys.* **2013**, *139*, 234109.

CHAPTER 4

THE SPIN AVERAGED ACSE

Reprinted with permission from J.-N. Boyn and D.A. Mazziotti, *Journal of Chemical Physics* **154**, 134103 (2021). Copyright 2021 American Institute of Physics.

4.1 Introduction

The accurate theoretical description of open-shell and biradical systems is quintessential in the understanding of chemical processes and properties in various areas of modern chemistry. Not only are biradicals fundamental to chemical reactions, where the breaking and formation of chemical bonds passes through a transition state via the unpairing of electrons[1], they also play roles in catalysis, e.g. as carbene species which have recently garnered significant research interest[2, 3], or in solid state and materials application such as molecular magnets, qubits or photochemical devices[4–6]. While modern developments in electronic structure theory have made great advances in the treatment of closed shell molecular systems, allowing common black-box methods such as DFT to be used in the calculation of various electronic properties by chemists from all disciplines with great accuracy, the treatment of biradicals and open-shell systems continues to pose major challenges[7–10].

Biradicals are perhaps the simplest example of a strongly correlated system: two electrons are distributed in degenerate (or near-degenerate) orbitals yielding a multi-determinate wave function which cannot be expressed in the form of a single Slater determinant. And while many of the most advanced and commonly used electronic structure methods, such as coupled cluster (CC) or density functional theory (DFT) resolve dynamic correlation with reliable accuracy, they fail to account for the strong correlation arising from multireference states[11–13]. Traditional methods that do account for static correlation, such as complete active space self consistent field (CASSCF) calculations in turn fail to resolve the dynamic correlation[14]. It is imperative for new theories to correctly resolve both the static and dynamic components of the total correlation energy[9] to obtain an accurate picture of the electronic structure of biradicals and open shell systems, and to elucidate successfully their experimentally significant properties, such as their spin-state splittings.

In the last two decades many theories have been presented with the aim to calculate accurately the singlet-triplet gaps of biradicaloids and they can generally be divided into two flavors: DFT-based methods and wave function based methods. DFT, which is inherently single-reference, meaning its calculation relies on a single Slater determinant, is known to be notoriously inaccurate at resolving singlet-triplet gaps in diradicals[15]. This is often overcome by the use of an unrestricted formalism, which while leading to improvements in the resolution of spin state gaps, comes at the expense of unphysical spin densities and electronic energies[10, 16, 17]. Multiple theories have been developed to address these issues in DFT, including particle-particle random phase approximation (pp-RPA)[18–21], fractional-spin DFT[22–24], multi-configurational pair-density functional theory (MC-PDFT)[25–27] and spin-flip approaches[28–30]. While these paths have provided for significant improvements, several issues such as the dependence on the chosen functional and lack of correctly bound absolute energies remain. On the wave function end of the spectrum, the most ubiquitous method of CASSCF with a second order Møller-Plesset perturbative correction (CASPT2) suffers from major convergence issues, oftentimes yielding non-physical electronic energies, and inhibitive computational scaling in larger systems[31]. To overcome these issues, Krylov has pioneered spin-flip approaches that may be based on DFT, configuration interaction (CI) or CC calculations[30, 32–34], Piris has developed natural-orbital functional theories[35], and recently Reichman and Friesner have presented an auxiliary-field quantum Monte Carlo approach for the prediction of singlet-triplet gaps that may use CASSCF or unrestricted DFT trial wave functions with great success[36]. Nevertheless, many of the most accurate and up-to-date programs rely on significant data manipulation, e.g. spin coupling or manual state state selection, for accurate calculations, or require highly parallelized computing architectures, and thus remain far from being a ”black-box” method easy to use for non-theoretical researchers.

In this paper we use the anti-Hermitian contracted Schrödinger equation (ACSE) in a spin averaged[37] implementation to resolve accurately the singlet-triplet gaps in multiple biradical systems. The ACSE allows the calculation of the electronic energy as a linear functional of the two-electron reduced density matrix (2-RDM), resulting in favorable polynomial computational scaling compared to wave function based methods[38, 39]. While the ACSE when seeded with a non-correlated initial guess 2-RDM resolves dynamic correlation, use of an initial 2-RDM obtained from a strongly corrrelated CASSCF calculation, allows the calculation of both static and dynamic correlation[40]. The ACSE has been demonstrated to calculate accurately the various ground and excited states, total correlation energies, and dissociation curves or various molecular systems[38–42]. In this paper we implement a spin-averaged implementation of the ACSE, seeded from a CASSCF calculation, to resolve the total correlation energy in the $S = 0$ and $S = 1$ states of a common benchmark set of small main group biradicaloids, and several small organic molecules, namely cyclobutadiene, trimethylenemethane (TMM), naphthalene, and o-, m-, p-benzyne.

4.2 Theory

The N-electron Schroödinger equation may be projected onto the space of all two electron transitions by integrating over the coordinates of all but two electrons, yielding the contracted Schrödinger equation (CSE)[43]:

$$\langle\Psi|\,\hat{\Gamma}^{ij}_{kl}\hat{H}\,|\Psi\rangle = E\,{}^{2}D^{ij}_{kl}\,, \tag{4.1}$$

where $\hat{\Gamma}^{ij}_{kl}$ is a two-body operator whose expectation value yields the elements of the 2-RDM

$$\hat{\Gamma}^{ij}_{kl} = \hat{a}^{\dagger}_{i}\hat{a}^{\dagger}_{j}\hat{a}_{l}\hat{a}_{k}\,, \tag{4.2}$$

and $\hat{H}$ is the Hamiltonian operator

$$\hat{H} = \sum_{ij} {}^1K^i_j \hat{a}^\dagger_i \hat{a}_j + \sum_{ijkl} {}^2V^{ij}_{kl} \hat{a}^\dagger_i \hat{a}^\dagger_j \hat{a}_l \hat{a}_k \,, \tag{4.3}$$

where ${}^1K$ contains the kinetic and nuclear attraction integrals and ${}^2V$ contains the electron-electron repulsion integrals. The CSE can be separated into its Hermitian and anti-Hermitian parts:

$$\langle\Psi| \{\hat{\Gamma}^{ij}_{kl}, (\hat{H} - E)\} |\Psi\rangle + \langle\Psi| [\hat{\Gamma}^{ij}_{kl}, (\hat{H} - E)] |\Psi\rangle = 0 \,, \tag{4.4}$$

where square brackets denote a commutator and curly brackets the anti-commutator. Selection of only the anti-Hermitian part of the CSE yields the ACSE:

$$\langle\Psi| [\hat{\Gamma}^{ij}_{kl}, \hat{H}] |\Psi\rangle = 0 \,. \tag{4.5}$$

While the full CSE and its Hermitian part contain terms of the 2-, 3- and 4-RDM's, the ACSE only depends on the 1-, 2-, and 3-RDM's; explicit expressions of the CSE and ACSE in terms of the RDM's are outlined in references [38, 39]. Furthermore, this dependence on the 3-RDM can be resolved by using an approximate reconstruction in terms of the 2-RDM. Several methods of reconstruction have been published and in this work we use the cumulant reconstruction[44–46].

$${}^3D^{ijk}_{qst} \approx {}^1D^i_q \wedge {}^1D^j_s \wedge {}^1D^k_t + 3\,{}^2\Delta^{ij}_{qs} \wedge {}^1D^k_t \,, \tag{4.6}$$

where

$${}^2\Delta^{ij}_{qs} = {}^2D^{ij}_{qs} - {}^1D^i_q \wedge {}^1D^j_s \,, \tag{4.7}$$

and $\wedge$ denotes the antisymmetric Grassman wedge product, which is defined as:

$${}^1D^i_k \wedge {}^1D^j_l = \frac{1}{2}({}^1D^i_k \, {}^1D^j_l - {}^1D^i_l \, {}^1D^j_k) \,. \tag{4.8}$$

As the 3-RDM terms appear only in the perturbative ${}^{2}V$ part of the Hamiltonian of the ACSE, this approximate reconstruction of ${}^{3}D$ neglects the cumulant 3-RDM part of the expansion, approximating ${}^{3}\Delta^{ijk}_{qst}$ to be zero.

The ACSE has successfully been used to study small open shell singlet and high-spin triplet systems, however, the treatment of triplet and higher spin states employs a rather complicated approach requiring the spin coupling of open-shell molecules to form singlet states[47]. In particular, this approach involved the spin coupling of hydrogen atom(s) to the open shell wave function to create a singlet state and solving the ACSE in terms of its composite 2-RDM to obtain the composite energy, and finally subtracting the energy of the hydrogen atom to obtain the system energy. It requires careful construction of singlet states through coupling of two or more CASSF reference wave functions of different spin states coupled into a singlet wave function by Clebsch-Gordon coefficients and additional post-processing work to obtain the open-shell 2-RDM and energy from the composite system. In this work we present an approach using spin-averaged RDMs, which results in a streamlined computational implementation that requires no further manipulation of RDMs and enables an easy-to-use program.

Various iterations of the ACSE algorithm have been applied to a range of chemical systems, successfully predicting ground- and excited-state energies, dissociation curves and reaction barriers[38–42]. The nature of the result obtained from an ACSE calculation depends on the 2-RDM used to initialize the calculation. While use of an HF solution as the initial guess results in resolution of the dynamic correlation, the calculation may also be seeded with a 2-RDM obtained from a CASSCF calculation, allowing the determination of both dynamic correlation and strong correlation effects[40]. We hence start with a CASSCF calculation in the desired spin state, carried out with the Maple Quantum Chemistry Package[48, 49], obtaining strongly correlated 1- and 2-RDMs which are then used as an initial guess in the ACSE.

While the ACSE requires the 1- and 2-RDM elements in the canonical spin-orbital basis for the $\alpha\alpha$ and $\alpha\beta$ blocks, we obtain initial active space RDMs ${}^1\tilde{D}$ and ${}^2\tilde{D}$ in the spatial orbital basis from a CASSCF calculation (the α and β denote the +1/2 and -1/2 spin states, respectively). The spin-dependent $\alpha\alpha$ and $\alpha\beta$ blocks are then reconstructed from the spatial RDMs according to:

$$ {}^1D^{i}_{j} = {}^1D^{\alpha i}_{\alpha j} = {}^1D^{\alpha i}_{\beta j} = \frac{1}{2}{}^1\tilde{D}^{i}_{j}, \tag{4.9} $$

$$ {}^2D^{\alpha i,\alpha j}_{\alpha k,\alpha l} = {}^2D^{\beta i,\beta j}_{\beta k,\beta l} = \frac{1}{6}({}^2\tilde{D}^{ij}_{kl} - {}^2\tilde{D}^{ji}_{kl}), \tag{4.10} $$

$$ {}^2D^{\alpha i,\beta j}_{\alpha k,\beta l} = {}^2D^{\beta i,\alpha j}_{\beta k,\alpha l} = \frac{1}{6}(2\,{}^2\tilde{D}^{ij}_{kl} + {}^2\tilde{D}^{ji}_{kl}). \tag{4.11} $$

This is followed by reconstruction of the core and virtual elements of ${}^1D$ and ${}^2D$:

$$ {}^1D_{core} = I, {}^1D_{virtual} = 0, \tag{4.12} $$

$$ {}^2D^{\alpha a,\alpha b}_{\alpha c,\alpha d} = {}^2D^{\beta a,\beta b}_{\beta c,\beta d} = {}^1D^{a}_{c}{}^1D^{b}_{d} - {}^1D^{b}_{c}{}^1D^{a}_{d}, \tag{4.13} $$

$$ {}^2D^{\alpha a,\beta b}_{\alpha c,\beta d} = {}^2D^{\beta a,\alpha b}_{\beta c,\alpha d} = {}^1D^{a}_{c}{}^1D^{b}_{d}, \tag{4.14} $$

$$ {}^2D^{\alpha p,\alpha q}_{\alpha s,\alpha t} = {}^2D^{\beta p,\beta q}_{\beta s,\beta t} = {}^2D^{\alpha p,\beta q}_{\alpha s,\beta t} = {}^2D^{\beta p,\alpha q}_{\beta s,\alpha t} = 0, \tag{4.15} $$

where a,b,c,d denote core orbitals and p,q,s,t denote virtual orbitals.

Using the spin-averaged 1- and 2-RDMs, we solve the ACSE via a system of differential equations[50]:

$$ \begin{aligned} E(\lambda+\varepsilon) &= \langle\Psi(\lambda)|\, e^{-\varepsilon S(\lambda)}\hat{H}e^{\varepsilon S(\lambda)}\, |\Psi(\lambda)\rangle \\ &= E(\lambda) + \varepsilon\,\langle\Psi(\lambda)|\,[\hat{H},\hat{S}(\lambda)]\,|\Psi(\lambda)\rangle + O(\varepsilon^2), \end{aligned} \tag{4.16} $$

$$ \frac{dE}{d\lambda} = \langle\Psi(\lambda)|\,[\hat{H},\hat{S}(\lambda)]\,|\Psi(\lambda)\rangle\,, \tag{4.17} $$

$$\frac{d^2D^{ij}_{kl}}{d\lambda} = \langle\Psi(\lambda)|\,[\hat{\Gamma}^{ij}_{kl},\hat{S}(\lambda)]\,|\Psi(\lambda)\rangle\ , \tag{4.18}$$

where the operator $\hat{S}$ is defined as:

$$\hat{S}(\lambda) = \sum_{ijkl} {}^2S^{ij}_{kl}\hat{a}^{\dagger}_i\hat{a}^{\dagger}_j\hat{a}_l\hat{a}_k(\lambda)\,, \tag{4.19}$$

which at each step of λ is chosen to minimize the energy along the gradient:

$${}^2S^{i,j}_{k,l}(\lambda) = \langle\Psi(\lambda)|\,[\hat{\Gamma}^{ij}_{kl},\hat{H}]\,|\Psi(\lambda)\rangle\ . \tag{4.20}$$

An optimal propagation step in λ is determined using a Taylor expansion in approximate form of the 2-RDM

$${}^2D(\lambda+\varepsilon) \approx {}^2D(\lambda) + \varepsilon\,{}^2D^{'}(\lambda) + \frac{\varepsilon^2}{2h}({}^2D^{'}(\lambda+h) - {}^2D^{'}(\lambda))\,, \tag{4.21}$$

where h is a small propagation step, and by minimizing the first derivative of the energy, yielding ε_{opt}:

$$\varepsilon_{\text{opt}} = -\frac{\text{Tr}({}^2K\,{}^2D^{'}(\lambda))}{\text{Tr}({}^2K\,{}^2D^{''}(\lambda))}\,. \tag{4.22}$$

The 2-RDM ${}^2D$ is updated with the optimal step and this procedure is repeated until a critical value in λ is reached where either the energy reaches a minimum or the norm of the residual increases.

4.3 Discussion and Results

4.3.1 Small Main Group Biradicaloid Set

We first evaluate the spin-averaged ACSE by considering a set of small main-group biradicaloids which have been widely used in the literature to benchmark the accuracy of new computational methods at predicting singlet-triplet gaps in biradical systems[22, 25, 30, 33, 36]. The set consists

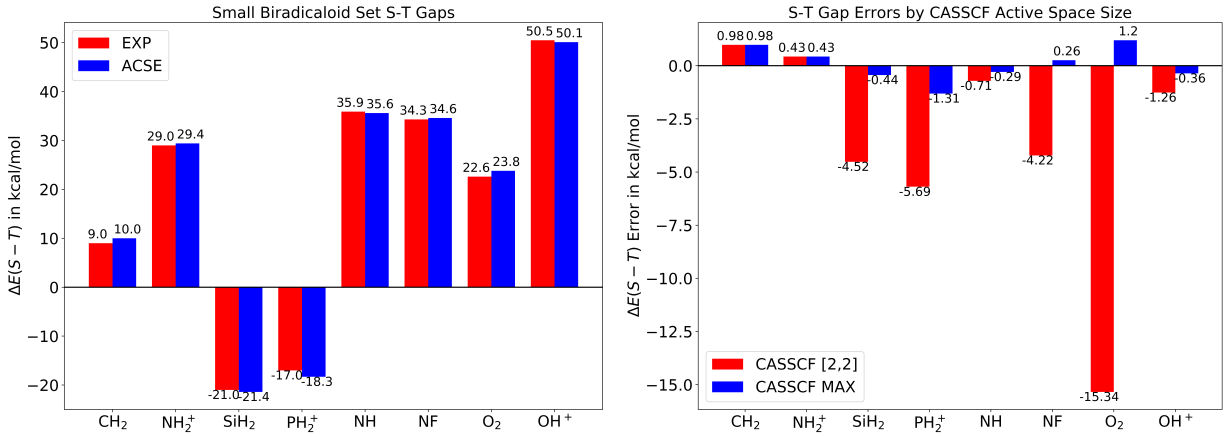

Figure 4.1: Left: Comparison of S-T gaps computed with the converged active-space spin-averaged CASSCF/ACSE method with the cc-pVTZ basis set and experimental values. Experimental results from: OH^+, NH, NF, O_2 [51]; NH_2^+ [52]; CH_2 [53]; PH_2^+[54]; SiH_2[55]. Right: Errors of converged S-T gaps obtained with a minimal [2,2] active space CASSCF guess and the final converged result seeded with the largest active space guess, which corresponds to the gaps shown in the left panel.

of the 8 species OH^+, NH, NF, O_2, NH_2^+, CH_2, PH_2^+, SiH_2, for all of which experimental S-T gap data is available[51–55]. Initial calculations were performed with CASSCF in the Maple Quantum Chemistry Package (QCP)[48, 49] for both singlet and triplet spin states using geometries from reference [25] to obtain seed RDMs for the ACSE calculations. All calculations were performed with the cc-pVTZ basis set[56, 57]. The left hand side of Figure 4.1 shows the results obtained with the CASSCF seeded spin averaged ACSE (CASSCF/ACSE) in comparison to experimental reference values.

The spin-averaged ACSE successfully predicts the singlet-triplet gaps in 6 out of the 8 species with chemical accuracy (error of less than 1 kcal/mol) with the largest errors observed for O_2 (1.2 kcal/mol) and PH_2^+ (1.3 kcal/mol). This large error in O_2 coincides with the system demonstrating particularly slow convergence of the S-T gap as a function of the active space size of the initial CASSCF 2-RDM used to seed the calculation with the minimal [2,2] CASSCF guess yielding in an error of -15.34 kcal/mol. The error improves significantly to 1.9 kcal/mol with a moderately large

[8,8] active space, finally reducing to 1.3 kcal/mol at the largest surveyed active space of [14,14]. This error is in general agreement with results obtained by authors of [36], which shows errors of 1.7 kcal/mol for active spaces as large as [10,15] in AF-QMC with a CASSCF trial wave function. While O_2 proves to be challenging, convergence with respect to the size of the CASSCF active space in all other systems is significantly better, and relatively small active spaces are required to obtain accurate results. The right hand side of Figure 4.1 compares the deviation from experiment for calculations with a minimal [2,2] CASSCF active space to the final converged result. Both CH_2 and NH_2^+ show full convergence with a [2,2] guess, while NH and OH^+ converge to within 1 kcal/mol of the final result, which is achieved with [4,4] and [6,14] active spaces respectively. SiH, PH_2^+ and NF all require larger active spaces for good convergence, however, observed behavior is significantly better than O_2, and final results are reported with [10,20] guesses.

Method	MSE	MAE
ACSE/CASSCF	0.06	0.66
AFQMC/CASSCF[36]	0.83	1.0
AFQMC/U[36]	0.5	1.1
SF-LDA[30]	-0.7	1.7
SF-CIS(D)[33]	1.8	1.9
(V)FS-PBE[22]	4.2	4.3
W2X[25]	3	3.7
pp-B3LYP[18]	-3.5	4.8
CASSCF[25]	2.5	3.0
CASPT2[25]	1.5	2.2
tPBE/MC-PDFT[25]	-5.8	5.9
WABS BLYP[25]	1.0	6.5

Table 4.1: Comparison of mean signed errors (MSE) and mean absolute errors (MAE) in the calculation of S-T Gaps in kcal/mol for the benchmarking set consisting of CH_2, NH_2^+, SiH_2, PH_2^+, NH, NF, O_2, OH^+ with CASSCF/ACSE and various methods reported in the literature. CASSCF/ACSE calculations were carried out with a cc-pVTZ basis set.

The results obtained from the spin-averaged ACSE/CASSCF algorithm compare favorably to other methods reported in the literature, with Table 4.1 showing mean signed errors (MSE) and mean absolute errors (MAE) for the ACSE method and multiple commonly used as well as recently reported methods. The MSE of 0.06 kcal/mol and MAE of 0.66 kcal/mol of this work slightly outperform recently reported AF-QMC/CASSCF (MAE = 0.83 kcal/mol, MSE = 1.0 kcal/mol)[36] values, and provide significantly better results than spin flip or particle-particle random phase approximation based methods.

4.3.2 Small Organic Biradicals

Not only have organic biradical and multiradical compounds attracted significant research interest in the design of molecular magnets, conductors, and the field of spintronics[58–62], they also play important roles in chemical reactions as transition states or reactive intermediates, making their accurate depiction essential for the computational modelling and elucidation of chemical processes[1–6]. Nevertheless, their exact treatment remains a challenge in contemporary electronic structure theory. In this section we investigate several representative small organic biradical systems that have been studied extensively in the literature. This includes the ortho-, meta-, and para- isomers of benzyne, derivatives of which have gained traction in recent years as important intermediates in organic synthesis[63–66], as well as the small four electron biradicals trimethylenemethane (TMM) and cyclobutadiene.

While the three benzyne isomers exhibit singlet ground states, they have a strongly correlated electronic structure arising from their biradical nature. The magnitude of their T-S gap follows an inverse relationship with the degree to which the isomer exhibits diradical character. Experimental data have been reported for the gas phase, with the para isomer exhibiting the smallest adiabatic gap of 3.3 kcal/mol , followed by meta (20.0 kcal/mol) and ortho (38.1 kcal/mol)[67]. Our ACSE/CASSF calculations employ the cc-pVDZ basis set in conjunction with a [4,4] active space. Geometries were obtained from reference [18], producing T-S gaps of 35.79 kcal/mol, 20.66 kcal/mol and 7.49 kcal/mol for the ortho, meta and para isomers respectively. In the cases of all isomers, no gain in accuracy was achieved when using a larger active space to generate the

	ΔE_{T-S}		
	o-	m-	p-
Exp[67]	38.1	20.0	3.3
ACSE	35.79	20.66	7.49
AFQMC/CAS[36]	37.4(6)	20.7(8)	4.5(5)
AFQMC/U[36]	37.6(7)	18.9(9)	2.2(9)
pp-HF[18]	45.6	35.5	4.0
pp-B3LYP[18]	37.4	22.1	0.6
SF-CIS(D)[33]	35.7	19.4	2.1
SF-CCSD(T)[32]	37.3	20.6	4.0
SF-LDA[30]	47.5	29.0	10.5
UB3LYP[29]	29.4	14.2	2.4

Table 4.2: S-T gaps in kcal/mol for the ortho-, meta- and para-benzyne isomers obtained with CASSCF/ACSE and the cc-pVDZ basis set, compared to ZPE corrected experimental gaps and those obtained via several methods reported in the literature.

CASSCF 2-RDM used to seed the ACSE calculation. Increasing the active space from the minimal [2,2] space, which only includes the radical orbitals, to the [4,4] space gave a slight improvement, while any further increases leads to inclusion of molecular orbitals in the active space that show no significant correlation and exhibit occupation numbers of > 0.99 or < 0.01, resulting in divergence away from the experimental results. This is in line with previous observations on the ACSE and its dependence on the initial guess[40, 50], showing that the optimal CASSCF guess should only account for significantly correlated space, allowing the ACSE algorithm to resolve the entirety of the remaining correlation.

Our results are compared with a range of contemporary methods in Table 4.2. The ACSE provides good agreement with experiment in the case of the meta isomer, comparing favorably to the other surveyed methods, and yielding identical results to AFQMC/CAS. The results obtained for the ortho isomer are also satisfactory, being comparable to SF-CIS(D) but producing slightly larger errors than AFQMC/CAS and SF-CCSD(T), which yield gaps of 37.4 kcal/mol and 37.3 kcal/mol respectively. Finally, in the case of the para isomer the ACSE calculation yields an error of 4.2 kcal/mol, which, while small, only outperforms SF-LDA, which displays an error of 7.2 kcal/mol.

		MCQDPT2 [10,10]	ACSE	(dT)[32]	pp-HF[18]	pp-B3LYP[18]	(V)FS-PBE[22]	SF-CIS(D)[33]	SF-LDA[30]	DEA-EOMCC[69]	CASSCF-MkCCSD[70]
ΔE_{T-S}	TMM	16.7	16.60	16	17.1	16.3	21.5	23.6	15.6		
	cyclobutadiene		-7.46	7.2	6.7	6.5				-4.2	-8.1

Table 4.3: S-T gaps in kcal/mol calculated with the CASSCF/ACSE method with a cc-pVDZ basis set for cyclobutadiene and TMM compared with gaps reported in the literature.

The larger error in the para isomer coincides with the greatest contribution of strong correlation to its electronic structure, with the CASSCF reference giving frontier NON for the HONO and LUNO of $\lambda_{\text{HONO}} = 0.610$ and $\lambda_{\text{LUMO}} = 0.390$. The significant multi-reference character results in a particularly large stabilization of the singlet state with respect to the triplet, which in turn is not fully compensated by the additional dynamic correlation recovered by the ACSE, leading to an overestimation of the gap. Additionally, a residual source of error may be the use of the relatively small cc-pVDZ basis set when compared to experiment and calculations using the larger cc-pVTZ and cc-pVQZ basis sets.

In addition to the benzynes we investigate the two small four-electron biradicals TMM and cyclobutadiene. Geometries were obtained from reference [18] and the calculations were carried out with the cc-pVDZ basis set. TMM is a highly reactive radical and the simplest molecule that cannot be described by a Kekule structure[68]. Resulting from the four carbon p-orbitals, four π-orbitals split into one filled orbital, two degenerate orbitals occupied by two electrons, and one unfilled orbital. Obeying Hund's rule, its electronic ground state is an open shell triplet with D_{3h} symmetry, while the first low lying excited state is a singlet that breaks the D_{3h} symmetry and instead assumes a twisted non-planar geometry. The ACSE, seeded with a [4,4] CASSCF guess, predicts a S-T gap of 16.60 kcal/mol, which closely mirrors the results obtained from MCQDPT2 [10,10] (16.7 kcal/mol) and EOM-CCSD(dT) (15.3 kcal/mol). The results are summarized in the first row of Table 4.3.

Analogous to TMM cyclobutadiene has four carbon carbon p-orbitals forming four π-orbitals occupied by four electrons. However, while the orbital picture is identical to TMM, the splitting of the spin states is not — in cyclobutadiene the two unpaired π electrons form a singlet ground state with a triplet excited state, violating Hund's rule. Here we investigate the D_{4h} square symmetric geometry of the molecule, which has previously been theoretically investigated by various methods. It is worth noting that experimentally it has been observed that the singlet is not stable in the D_{4h} geometry due to Jahn-Teller distortion and instead cyclobutadiene adopts a rectangular structure[71]. Using a [12,12] CASSCF guess, the ACSE predicts a triplet ground state with a S-T gap of -7.46 kcal/mol. This result agrees with reference data obtained at the DEA-EOMCC and CASSCF-MkCCSD levels of theory, which yield gaps of -4.2 kcal/mol and -8.1 kcal/mol respectively, while pp-RPA based methods and EOM-CCSD(dT) fail to predict the correct ordering of singlet and triplet states (see second row of Table 4.3). Cyclobutadiene presents a system that benefits from the use of an increased active space, with a [4,4] CASSCF guess producing a S-T gap of -11.33 kcal/mol. This, however, is driven by the role of spectator orbitals in the CASSCF calculation. The [4,4] active space produces degenerate HONO and LUNO populations of $\lambda = 0.5$, while the [12,12] CASSCF converges to non-degenerate populations of $\lambda_{\text{HONO}} = 0.65$ and $\lambda_{\text{LUMO}} = 0.35$, indicating the variation in results can be attributed to major changes in the static correlation across the active spaces in the CASSCF calculation of the singlet state.

4.3.3 Naphthalene

Lastly, we investigate the ability of the spin averaged CASSCF/ACSE method to resolve the S-T gaps in polyacenes. Polyacenes are the building blocks of the narrowest graphene nanoribbons, and due to their tunable electronic properties they are widely studied for their roles in potential semiconducters or field effect transistors[72, 73]. Recent experiments with acene chains up to decacene have shown finite band gaps in the large polymer limit[74], however, electronic structure methods that fail to account for strong correlation such as DFT predict a crossing of the spin states

	ΔE_{T-S}
Exp[76, 77]	64.4
ACSE	67.86
GAS-PDFT[78]	70.6
DMRG[78]	61.3
DMRG-PDFT[78]	67.1
DMRG-ec-MRCISD+Q[78]	62.5
AFQMC/U[36]	68 (1.2)
CCSD(T)/FPA[79]	65.8
pp-B3LYP[18]	66.2

Table 4.4: T-S gap in kcal/mol obtained with CASSCF/ACSE using a [12,12] active space and cc-pVDZ basis set, compared with ZPE corrected experimental value, and a range of data points reported in the literature.

towards a singlet ground state with increased system size at finite ring size[75]. As such acenes remain a prime example for a molecular system that necessitates methods that accurately account for both static and dynamic correlation to hold value as a predictive computational tool. In this section we investigate naphthalene, the smallest member of the polyacene family, to evaluate the ACSE's ability to resolve qualities of the electronic structure of larger organic systems.

Geometries for the singlet and triplet states were obtained from reference [80] and the ACSE calculations were seeded with a 2-RDM obtained from a [12,12] CASSCF calculation. The cc-pVDZ basis set was used for all calculations and the results are summarized and compared to values reported in the literature in Table 4.4. The experimental T-S gap of 64.4 kcal/mol denotes the zero-point energy corrected value, based on the experimentally measured result of 61.0 kcal/mol minus the adiabatic correction energy of -3.4 kcal/mol as reported for B3LYP/6-31G(d)[77]. It is worth noting that experimental data for larger, stable molecules such as naphthalene is obtained under real world laboratory conditions and as such comparison of ab-initio calculations assuming a zero temperature, gas phase environment will always suffer from residual errors. The ACSE/CASSCF value of 67.86 kcal/mol compares favorably to other state of the art methods reported in the literature such as DMRG, PDFT based methods or AFQMC, for which in this case only results seeded with a UDFT guess are available. Overestimation of the gap is in line with the rest of the surveyed methods, with five out of seven yielding a positive deviation from experiment. The spin-free CASSCF/ACSE yields results that show promise for its application in strongly correlated, closed shell organic molecules.

4.4 Conclusions

We have developed a spin-averaging modification to the ACSE, significantly reducing the complexity of state and input preparation, which required coupling to H atoms to yield singlet systems in previous implementations. Using the spin averaging scheme detailed in this article, we can treat open-shell singlets and higher multiplicity states in the same way as closed shell ground states and without additional file or input preparation. To demonstrate the ability of the spin-averaged ACSE to resolve both dynamic and strong correlation, we successfully calculated the singlet-triplet gaps in a small main group biradicaloid benchmark set, as well as several small organic molecules. We show that the spin-averaged ACSE yields results of comparable accuracy to other state-of-the-art methods such as pp-RPA or AFQMC or PDFT reported in the literature. This is a major step in the development of the ACSE into an easily applied computational method to resolve the electronic structure of molecules that require the resolution of both strong and dynamic correlation for an accurate treatment.

Future work is being undertaken to use the spin-averaged ACSE to resolve not only ground states but also excited states of a specified multiplicity, allowing it to resolve spectral information. We also aim to extend the spin-averaged ACSE to include odd-electron count open-shell systems, with applications the spin state splittings and magnetic coupling in transition metal complexes. The latter pose particularly great and relevant challenges to modern quantum chemistry, as they are oftentimes being distinguished by multi-reference ground states with significant dynamical correlation, while being particularly pertinent to large areas of modern synthetic chemistry and materials science[81, 82].

References

(1) Scheschkewitz, D.; Amii, H.; Gornitzka, H.; Schoeller, W. W.; Bourissou, D.; Bertrand, G. *Science* **2002**, *295*, 1880–1881.

(2) Bourissou, D.; Guerret, O.; Gabbaï, F. P.; Bertrand, G. *Chem. Rev.* **2000**, *100*, 39–92.

(3) Bourissou, D.; Guerret, O.; Gabbaï, F. P.; Bertrand, G. *Chem. Rev.* **2000**, *100*, 39–92.

(4) Stuyver, T.; Chen, B.; Zeng, T.; Geerlings, P.; De Proft, F.; Hoffmann, R. *Chem. Rev.* **2019**, *119*, 11291–11351.

(5) Salem, L.; Rowland, C. *Angew. Chem.* **1972**, *11*, 92–111.

(6) Abe, M. *Chem. Rev.* **2013**, *113*, 7011–7088.

(7) Burke, K. *J. Chem. Phys.* **2012**, *136*, 150901.

(8) Jain, A.; Shin, Y.; Persson, K. A. *Nat. Rev. Mater.* **2016**, *1*, 15004.

(9) Grimme, S.; Schreiner, P. R. *Angew. Chem.* **2018**, *57*, 4170–4176.

(10) Perdew, J. P.; Ruzsinszky, A.; Constantin, L. A.; Sun, J.; Csonka, G. I. *J. Chem. Theory Comput.* **2009**, *5*, 902–908.

(11) Raghavachari, K.; Anderson, J. B. *J. Phys. Chem.* **1996**, *100*, 12960–12973.

(12) Benavides-Riveros, C. L.; Lathiotakis, N. N.; Marques, M. A. L. *Phys. Chem. Chem. Phys.* **2017**, *19*, 12655–12664.

(13) Cohen, A. J.; Mori-Sánchez, P.; Yang, W. *J. Chem. Phys.* **2008**, *129*, 121104.

(14) Olsen, J. *Int. J. Quantum Chem.* **2011**, *111*, 3267–3272.

(15) Gräfenstein, J.; Cremer, D. *Phys. Chem. Chem. Phys.* **2000**, *2*, 2091–2103.

(16) Gräfenstein, J.; Kraka, E.; Filatov, M.; Cremer, D. *Int. J. Mol. Sci.* **2002**, *3*, 360–394.

(17) Baker, J.; Scheiner, A.; Andzelm, J. *Chem. Phys. Lett.* **1993**, *216*, 380–388.

(18) Yang, Y.; Peng, D.; Davidson, E. R.; Yang, W. *J. Phys. Chem. A* **2015**, *119*, 4923–4932.

(19) Van Aggelen, H.; Yang, Y.; Yang, W. *Phys. Rev. A* **2013**, *88*, 030501.

(20) Yang, Y.; van Aggelen, H.; Steinmann, S. N.; Peng, D.; Yang, W. *J. Chem. Phys.* **2013**, *139*, 174110.

(21) Zhang, D.; Peng, D.; Zhang, P.; Yang, W. *Phys. Chem. Chem. Phys.* **2015**, *17*, 1025–1038.

(22) Peng, D.; Hu, X.; Devarajan, D.; Ess, D. H.; Johnson, E. R.; Yang, W. *J. Chem. Phys.* **2012**, *137*, 114112.

(23) Ess, D. H.; Johnson, E. R.; Hu, X.; Yang, W. *J. Phys. Chem. A* **2011**, *115*, 76–83.

(24) Su, N. Q.; Li, C.; Yang, W. *Proc. Natl. Acad. Sci. U.S.A* **2018**, *115*, 9678–9683.

(25) Bao, J. L.; Sand, A.; Gagliardi, L.; Truhlar, D. G. *J. Chem. Theory Comput* **2016**, *12*, 4274–4283.

(26) Li Manni, G.; Carlson, R. K.; Luo, S.; Ma, D.; Olsen, J.; Truhlar, D. G.; Gagliardi, L. *J. Chem. Theory Comput.* **2014**, *10*, 3669–3680.

(27) Gagliardi, L.; Truhlar, D. G.; Li Manni, G.; Carlson, R. K.; Hoyer, C. E.; Bao, J. L. *Acc. Chem. Res.* **2017**, *50*, 66–73.

(28) Casanova, D.; Krylov, A. I. *Phys. Chem. Chem. Phys.* **2020**, *22*, 4326–4342.

(29) Shao, Y.; Head-Gordon, M.; Krylov, A. I. *J. Chem. Phys.* **2003**, *118*, 4807–4818.

(30) Bernard, Y. A.; Shao, Y.; Krylov, A. I. *J. Chem. Phys.* **2012**, *136*, 204103.

(31) Pulay, P. *Int. J. Quantum Chem.* **2011**, *111*, 3273–3279.

(32) Manohar, P. U.; Krylov, A. I. *J. Chem. Phys.* **2008**, *129*, 194105.

(33) Slipchenko, L. V.; Krylov, A. I. *J. Chem. Phys.* **2002**, *117*, 4694–4708.

(34) Krylov, A. I. *Chem. Phys. Lett.* **2001**, *350*, 522–530.

(35) Lopez, X.; Ruipérez, F.; Piris, M.; Matxain, J. M.; Ugalde, J. M. *ChemPhysChem* **2011**, *12*, 1061–1065.

(36) Shee, J.; Arthur, E. J.; Zhang, S.; Reichman, D. R.; Friesner, R. A. *J. Chem. Theory Comput.* **2019**, *15*, 4924–4932.

(37) Piris, M. *Phys. Rev. A* **2019**, *100*, 032508.

(38) Mazziotti, D. A. *Phys. Rev. Lett.* **2006**, *97*, 143002.

(39) Mazziotti, D. A. *Phys. Rev. A* **2007**, *75*, 022505.

(40) Mazziotti, D. A. *Phys. Rev. A* **2007**, *76*, 052502.

(41) Mazziotti, D. A. *J. Phys. Chem. A* **2008**, *112*, 13684–13690.

(42) Sand, A. M.; Mazziotti, D. A. *J. Chem. Phys.* **2015**, *143*, 134110.

(43) Mazziotti, D. A. *Phys. Rev. A* **1998**, *57*, 4219–4234.

(44) DePrince, A. E.; Mazziotti, D. A. *J. Chem. Phys.* **2007**, *127*, 104104.

(45) Mazziotti, D. A. *Chem. Phys. Lett.* **1998**, *289*, 419–427.

(46) Mazziotti, D. A. *Int. J. Quantum Chem.* **1998**, *70*, 557–570.

(47) Rothman, A. E.; Foley, J. J.; Mazziotti, D. A. *Phys. Rev. A* **2009**, *80*, 052508.

(48) Maplesoft, a division of Waterloo Maple Inc., Waterloo, Ontario. **2019**.

(49) RDMChem, Chicago, Illinois. **2019**.

(50) Sand, A. M.; Mazziotti, D. A. *J. Chem. Phys.* **2015**, *143*, 134110.

(51) Herzberg G.; Huber, K. *Springer Verlag* **1979**.

(52) Osmann, G.; Bunker, P.; Jensen, P.; Kraemer, W. *J. Mol. Spectrosc.* **1997**, *186*, 319–334.

(53) Gu, J.-P.; Hirsch, G.; Buenker, R.; Brumm, M.; Osmann, G.; Bunker, P.; Jensen, P. *J. Mol. Struct.* **2000**, *517-518*, 247–264.

(54) Berkowitz, J.; Cho, H. *J. Chem. Phys.* **1989**, *90*, 1–6.

(55) Berkowitz, J.; Greene, J. P.; Cho, H.; Ruščić, B. *J. Chem. Phys.* **1987**, *86*, 1235–1248.

(56) Dunning, T. H. *J. Chem. Phys.* **1989**, *90*, 1007–1023.

(57) Woon, D. E.; Dunning, T. H. *J. Chem. Phys.* **1993**, *98*, 1358–1371.

(58) Kawamura, A.; Xie, J.; Boyn, J.-N.; Jesse, K. A.; McNeece, A. J.; Hill, E. A.; Collins, K. A.; Valdez-Moreira, J. A.; Filatov, A. S.; Kurutz, J. W.; Mazziotti, D. A.; Anderson, J. S. *J. Am. Chem. Soc.* **2020**, *142*, 17670–17680.

(59) Gallagher, N. M.; Bauer, J. J.; Pink, M.; Rajca, S.; Rajca, A. *J. Am. Chem. Soc.* **2016**, *138*, 9377–9380.

(60) Yang, K.; Zhang, X.; Harbuzaru, A.; Wang, L.; Wang, Y.; Koh, C.; Guo, H.; Shi, Y.; Chen, J.; Sun, H.; Feng, K.; Ruiz Delgado, M. C.; Woo, H. Y.; Ortiz, R. P.; Guo, X. *J. Am. Chem. Soc.* **2020**, *142*, 4329–4340.

(61) Rajca, A. *Chem. Rev.* **1994**, *94*, 871–893.

(62) Rudebusch, G. E.; Zafra, J. L.; Jorner, K.; Fukuda, K.; Marshall, J. L.; Arrechea-Marcos, I.; Espejo, G. L.; Ponce Ortiz, R.; Gómez-García, C. J.; Zakharov, L. N.; Nakano, M.; Ottosson, H.; Casado, J.; Haley, M. M. *Nat. Chem.* **2016**, *8*, 753–759.

(63) He, J.; Qiu, D.; Li, Y. *Acc. Chem. Res.* **2020**, *53*, 508–519.

(64) Dubrovskiy, A. V.; Markina, N. A.; Larock, R. C. *Org. Biomol. Chem.* **2013**, *11*, 191–218.

(65) Shi, F.; Waldo, J. P.; Chen, Y.; Larock, R. C. *Org. Lett.* **2008**, *10*, 2409–2412.

(66) Sander, W. *Acc. Chem. Res.* **1999**, *32*, 669–676.

(67) Wenthold, P. G.; Squires, R. R.; Lineberger, W. C. *J. Am. Chem. Soc.* **1998**, *120*, 5279–5290.

(68) Dowd, P. *Acc. Chem. Res.* **1972**, *5*, 242–248.

(69) Stoneburner, S. J.; Shen, J.; Ajala, A. O.; Piecuch, P.; Truhlar, D. G.; Gagliardi, L. *J. Chem. Phys.* **2017**, *147*, 164120.

(70) Saito, T.; Nishihara, S.; Yamanaka, S.; Kitagawa, Y.; Kawakami, T.; Yamada, S.; Isobe, H.; Okumura, M.; Yamaguchi, K. *Theor. Chem. Acc.* **2011**, *130*, 749–763.

(71) Bally, T.; Masamune, S. *Tetrahedron* **1980**, *36*, 343–370.

(72) Anthony, J. E. *Angew. Chem.* **2008**, *47*, 452–483.

(73) Anthony, J. E. *Chem. Rev.* **2006**, *106*, 5028–5048.

(74) Shen, B.; Tatchen, J.; Sanchez-Garcia, E.; Bettinger, H. F. *Angew. Chem.* **2018**, *57*, 10506–10509.

(75) Yang, Y.; Davidson, E. R.; Yang, W. *Proc. Natl. Acad. Sci. U.S.A.* **2016**, *113*, E5098–E5107.

(76) Siebrand, W. *J. Chem. Phys.* **1967**, *47*, 2411–2422.

(77) Schriber, J. B.; Hannon, K. P.; Li, C.; Evangelista, F. A. *J. Chem. Theory Comput.* **2018**, *14*, 6295–6305.

(78) Sharma, P.; Bernales, V.; Knecht, S.; Truhlar, D. G.; Gagliardi, L. *Chem. Sci.* **2019**, *10*, 1716–1723.

(79) Hajgató, B.; Huzak, M.; Deleuze, M. S. *J. Phys. Chem. A* **2011**, *115*, 9282–9293.

(80) Ibeji, C. U.; Ghosh, D. *Phys. Chem. Chem. Phys.* **2015**, *17*, 9849–9856.

(81) Boyn, J.-N.; Xie, J.; Anderson, J. S.; Mazziotti, D. A. *J. Phys. Chem. Lett.* **2020**, *11*, 4584–4590.

(82) Sharma, P.; Truhlar, D. G.; Gagliardi, L. *J. Am. Chem. Soc.* **2020**, *142*, 16644–16650.

CHAPTER 5

RESOLVING THE ORBITAL DEPENDENCE OF THE ACSE

Reprinted from an article submitted for publication by J.-N. Boyn and D. A. Mazziotti (2022).

5.1 Introduction

The computational resolution of electronic structure relies on the accurate capture of the correlation energy, which is defined as the difference between the full-configuration-interaction (FCI) and Hartree-Fock (HF) energies. The correlation energy is generally further divided into two components: static or strong correlation arising from a state that may not be described by a single Slater determinant and is hence also termed multi-reference correlation, and the remainder which is defined as dynamic correlation[1–4]. While dynamic correlation is present in all electronic systems and may be well described by many single-reference methods such as coupled cluster (CC), Møller-Plesset perturbation theory (MP)[5] or even density functional theory (DFT)[6, 7], strong correlation only arises in systems exhibiting a degeneracy or near-degeneracy of electronic states[1]. As such, multi-reference correlation plays a particularly important role in processes such as bond dissociation, and in the determination of properties of bi- or multi-radical systems, such as spin state splittings and magnetic couplings in molecules and complexes in the areas of spintronics, photonics or catalysis[8–11].

Multi-reference correlation is commonly resolved with complete active space configuration interaction (CASCI) or CAS self consistent field (CASSCF) calculations, which resolve the strong correlation in a chosen active space[12–14]. However, it has been demonstrated that even in systems dominated by static correlation, experimentally relevant properties, such as singlet-triplet (S-T) gaps or J-coupling parameters may often not be resolved within chemical accuracy without the additional inclusion of dynamic correlation effects[15]. The historically most popular and commonly used method to account for post-CI dynamic correlation CASSCF in combination with second-order many-body perturbation theory (CASPT2) suffers from a variety of shortcomings, including poor computational scaling, and convergence issues arising from the fact that the MP2 correction is not variational, often leading to nonphysical lower bounds to the total electronic energy[16–19]. Consequently, the development of electronic structure methods that account for post-CI dynamic correlation is an area of major research interest and recent developments include algorithms such as quantum Monte-Carlo[20–22], multi-configuration pair-density functional theory (MC-PDFT)[23–27], reduced-density-matrix functional theory (RDMFT)[28–30], incremental FCI (iFCI)[31–33] or CASCI in combination with the anti-Hermitian contracted Schrödinger equation (ACSE)[34, 35].

While FCI yields the exact electronic energy in a chosen basis set and hence is invariant to the molecular orbital (MO) basis, it remains out of reach for systems larger than 18 electrons in 18 orbitals due to exponential computational scaling. As other ab-initio electronic structure methods that aim to resolve the total electronic correlation energy tend to rely on some approximation to truncate the exact Hamiltonian, they exhibit a dependence on the chosen MO basis. Recent research has been performed in the areas of CC and MP theories with the aim of improving their predictive properties via the use of improved molecular orbitals, rather than the commonly used HF reference[36–40]. This includes the implementation of orbital-optimized variants of CC and second-order MP2 (OOMP2), which, while yielding improved results over the HF-reference based implementations, suffer from increased computational scaling, and in the case of OOMP2 three major failures, namely divergence for small MO energy gaps, artificial symmetry restoration and loss of Coulson-Fischer points[41–43]. A contrary approach to the orbital-optimization problem has recently been undertaken by Head-Gordon and coworkers, who demonstrate significant improvements in the prediction of chemical properties in MP3 via the use of OOMP2 and DFT orbitals[44, 45], and in the calculation of vibrational frequencies with CCSD(T) with the use of

DFT orbitals[46].

While research has been undertaken to shine light on the orbital dependence in single-reference methods aimed at resolving dynamic correlation, work aiming at resolving this dependence in multi-reference and post-multi-reference dynamic correlation calculations has been limited[47–54] and common implementations of electronic structure methods aiming to resolve the total correlation energy such as QMC, CASPT2 or MC-PDFT, tend to rely on CASSCF optimized orbitals as their reference. But are orbitals that are optimized to include multi-reference correlation necessarily the best to account for the total correlation or is the restriction of the orbital optimization to an active space representing a small subset of the total molecular orbitals hindering the capture of the complete electronic structure? Specifically, would CASSCF orbitals necessarily provide the best initial guess for the orbitals in a post-CASSCF all-electron correlation SCF method?

In this article we aim to resolve the orbital dependence of CI and post-CI dynamic correlation calculations by using molecular orbitals obtained from KS-DFT, HF, MP2 and CCSD as reference orbitals in CI calculations, which are then used to seed the anti-Hermitian contracted Schrödinger equation (ACSE) to resolve the dynamic correlation. Orbitals obtained from KS-DFT have previously been demonstrated to be more suitable for the construction of electronic states in configuration interaction (CI) calculations compared to HF orbitals[55] and may provide a viable, cost-saving alternative to CASSCF optimization in the quest to resolve the electronic properties of strongly correlated molecules and materials. We apply the CASCI/ACSE algorithm seeded with the various molecular orbitals from the surveyed single-reference methods to three distinct chemical problems dominated by strong correlation effects, namely the dissociation of N_2, the prediction of S-T gaps in a benchmark set of biradicals, and the calculation of the energetic barrier of the isomerization reaction of bicyclobutane to gauche-1,3-butadiene via both the conrotatory and disrotatory transition states.

5.2 Computational Details

To investigate the orbital dependence of the static and dynamic parts of the total electronic correlation energy, molecular orbitals were obtained via self-consistent field (SCF) calculations using various popular single-reference, ab-initio methods. These methods include Hartree Fock (HF), CASSCF, variational 2-RDM CASSCF (V2RDM)[56], DFT[57], as well as, MP2 and CCSD, in which case the natural orbitals are investigated. For the DFT calculations, functionals representing the various rungs of Jacobs-Ladder of functional development were chosen, namely simple LDA[58], and the popular functionals PBE[59, 60], BLYP[61–63], B3LYP[64], M062X[65], ωB97XD[66], MN15[67]. Orbitals from these initial SCF calculations were then used to perform a minimal active space complete active space configuration interaction (CASCI) calculation using the V2RDM method with DQGT conditions (V2-T)[56, 68], obtaining the multi-reference correlation energy in the initial orbitals, as well as the strongly correlated 1- and 2-electron reduced density matrices (RDMs).

We then generate the 1- and 2-electron integrals, namely ${}^1K$ containing the kinetic and nuclear attraction integrals and ${}^2V$ containing the electron-electron repulsion integrals, from the molecular orbitals obtained with the selected single-reference method. These serve as the basis for the ACSE calculations, which is used to calculated the dynamic, post-CI correlation in the given molecular orbital basis. The ACSE arises from the fact that fermions interact pairwise and hence the N-electron Schrödinger equation may be projected onto the space of only two-electron transitions yielding the contracted Schrödinger equation (CSE)[69–71]:

$$\langle\Psi|\,\hat{a}_i^\dagger\hat{a}_j^\dagger\hat{a}_l\hat{a}_k\hat{H}\,|\Psi\rangle = E\;{}^2D^{ij}_{kl}, \tag{5.1}$$

where $\hat{H}$ is the Hamiltonian operator

$$\hat{H} = \sum_{ij} {}^1K^i_j \hat{a}^\dagger_i \hat{a}_j + \sum_{ijkl} {}^2V^{ij}_{kl} \hat{a}^\dagger_i \hat{a}^\dagger_j \hat{a}_l \hat{a}_k \,. \tag{5.2}$$

The CSE can be separated into its Hermitian and anti-Hermitian parts, and selection of only the anti-Hermitian part yields the ACSE:

$$\langle \Psi | \, [\hat{a}^\dagger_i \hat{a}^\dagger_j \hat{a}_l \hat{a}_k, \hat{H}] \, | \Psi \rangle = 0 \,, \tag{5.3}$$

where the square brackets indicate the commutator. Unlike the Hermitian part of the CSE, which depends on the 2-, 3- and 4-RMDs, the highest order terms in the ACSE, which is expanded in more detail in ref[72], depend on only the 2- and 3-RDMs. Furthermore, this dependence may be resolved by using an cumulant reconstruction in terms of the 2-RDM[73, 74]:

$${}^3D^{ijk}_{qst} \approx {}^1D^i_q \wedge {}^1D^j_s \wedge {}^1D^k_t + 3\,{}^2\Delta^{ij}_{qs} \wedge {}^1D^k_t \,, \tag{5.4}$$

where

$${}^2\Delta^{ij}_{qs} = {}^2D^{ij}_{qs} - {}^1D^i_q \wedge {}^1D^j_s \,, \tag{5.5}$$

and $\wedge$ denotes the antisymmetric Grassmann wedge product, which is defined as:

$${}^1D^i_k \wedge {}^1D^j_l = \frac{1}{2}({}^1D^i_k \, {}^1D^j_l - {}^1D^i_l \, {}^1D^j_k) \,. \tag{5.6}$$

As the 3-RDM terms appear only in the perturbative ${}^2V$ part of the Hamiltonian of the ACSE, this approximate reconstruction of ${}^3D$ neglects the cumulant 3-RDM part of the expansion, setting ${}^3\Delta^{ijk}_{qst}$ to be zero.

Using electron integrals and initial guess 1- and 2-RDMs obtained from a lower-level electronic structure calculation of choice, we solve the ACSE via a system of differential equations[75]:

$$\begin{aligned} E(\lambda+\varepsilon) &= \langle\Psi(\lambda)|\, e^{-\varepsilon S(\lambda)}\hat{H}e^{\varepsilon S(\lambda)}\,|\Psi(\lambda)\rangle \\ &= E(\lambda)+\varepsilon\,\langle\Psi(\lambda)|\,[\hat{H},\hat{S}(\lambda)]\,|\Psi(\lambda)\rangle + O(\varepsilon^2)\,, \end{aligned} \tag{5.7}$$

$$\frac{dE}{d\lambda} = \langle\Psi(\lambda)|\,[\hat{H},\hat{S}(\lambda)]\,|\Psi(\lambda)\rangle\,, \tag{5.8}$$

$$\frac{d^2D^{ij}_{kl}}{d\lambda} = \langle\Psi(\lambda)|\,[\hat{a}^\dagger_i\hat{a}^\dagger_j\hat{a}_l\hat{a}_k,\hat{S}(\lambda)]\,|\Psi(\lambda)\rangle\,, \tag{5.9}$$

where the operator $\hat{S}$ is defined as:

$$\hat{S}(\lambda) = \sum_{ijkl} {}^2S^{ij}_{kl}\hat{a}^\dagger_i\hat{a}^\dagger_j\hat{a}_l\hat{a}_k(\lambda)\,, \tag{5.10}$$

chosen at each step of λ to minimize the energy along the gradient:

$${}^2S^{ij}_{kl}(\lambda) = \langle\Psi(\lambda)|\,[\hat{a}^\dagger_i\hat{a}^\dagger_j\hat{a}_l\hat{a}_k,\hat{H}]\,|\Psi(\lambda)\rangle\,. \tag{5.11}$$

The ACSE is propagated in λ until either the energy reaches a minimum or the norm of the residual increases. This algorithm is presented in more detail in Refs. [72, 75].

Seed 1- and 2-RDMs may be obtained from single- or multi-reference electronic structure calculations, minimizing the total electronic energy in the chosen orbital basis of the electron integrals. When provided with a single-reference guess, such as one obtained from a HF calculation, the ACSE has been demonstrated to yield total electronic energies of comparable accuracy to those from CCSD(T)[76]. However, ACSE calculations may also be seeded with initial RDMs from a multi-reference electronic structure calculation, such as CASSCF or CASCI, which yields accurate results even when strong correlation plays a major role[34, 35]. In this case, the ACSE resolves the dynamic correlation on top of the static correlation recovered by the seed RDMs within the orbital basis obtained from the multi-reference calculation. Results have been demonstrated to outperform commonly used CASPT2[77–79], and provide comparable accuracy to MC-PDFT and AF-QMC[80]. All calculations were performed with the Quantum Chemistry Package[81] as implemented in Maple[82].

5.3 Results

5.3.1 Nitrogen Dissociation

To investigate the orbital dependence of the single- and multi-reference parts of the electronic correlation energy, we first consider the dissociation of N_2. Dissociation of N_2 into its two constituent nitrogen atoms provides a classic case of transition from a system dominated by single-reference correlation—N_2 near the equilibrium bond length—to a system dominated by multi-reference correlation as the N-N bond is stretched and the natural occupation numbers (NON) in the [6,6] active space formed by the 6 nitrogen p-based orbitals become more and more fractional until they reach full degeneracy in the dissociated regime.

For our calculations we consider eight data points of N-N bond lengths, R = [0.8, 0.9, 1.0976, 1.2, 1.4, 1.6, 2.0, 2.5] in Å. Calculations use the relatively small 6-31G basis[83] in order to allow comparison to full CI (FCI) data. Once orbitals are obtained via a chosen single-reference method, CASCI calculations in that MO basis set with [6,6] active spaces are carried out to recover the multi-reference correlation in the nitrogen-p-based orbitals. Figure 5.1 shows the dissociation curves obtained from the molecular orbitals of a few select methods, with the left panel showing the CASCI results, and the right panel displaying the ACSE results, as well as, the FCI curve. Furthermore, results of the go-to method for the inclusion of post-multi-reference calculations, CASPT2, are also displayed. It is evident that the recovery of the multi-reference correlation is

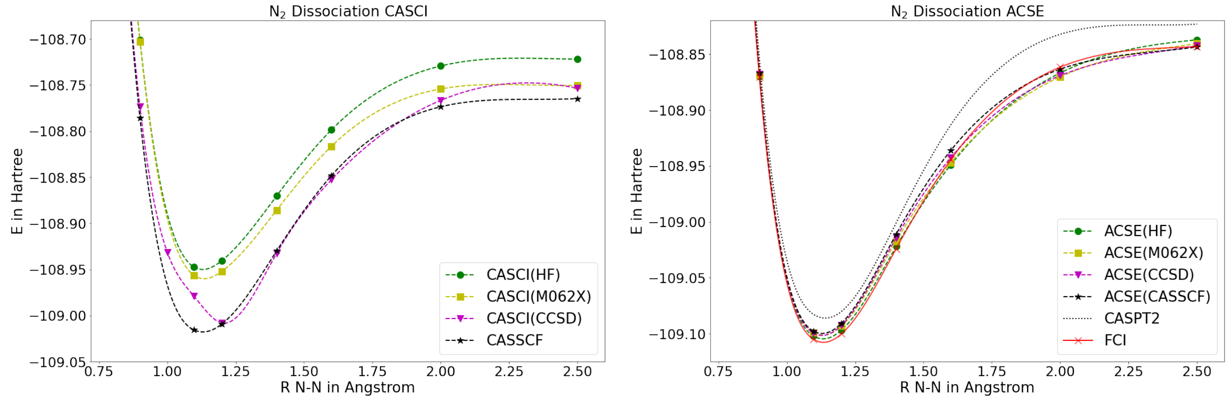

Figure 5.1: Dissociation curves of N2 for (left): [6,6] CASCI calculations; (right): ACSE calculations. All calculations were performed with a 6-31G basis set and the ACSE was seeded with the 2-RDM from the [6,6] CASCI calculations. Curves were constructed from eight points along the N-N dissociation coordinate, [0.8, 0.9, 1.0976, 1.2, 1.4, 1.6, 2.0, 2.5] in Å.

strongly orbital dependent, with large variations in the CASCI curves across the various methods used for orbital optimization. Differences arise not only in terms of the correlation energy recovered across the dissociation coordinate, i.e. in the form of a vertical shift of the curve, but also in its general line shape. This change in line shape is particularly evident in the cases of the HF and CCSD orbitals, which differ significantly from those obtained via DFT. Furthermore, inspection of the ACSE curves shows that while near-exact in the dissociated regime, CASSCF orbitals provide a larger deviation from the FCI curve than any of the displayed single reference methods in the single-reference regime around the equilibrium N-N bond length.

To allow a more in-depth analysis of the optimality of the molecular orbitals from a chosen method in accounting for the different parts of the total electronic correlation energy, we consider the errors of the energies obtained via CASCI relative to the CASSCF results, and the energies obtained via CASCI/ACSE relative to the FCI results. Table 5.1 shows the mean absolute error (MAE) and mean signed error (MSE) versus FCI over the eight N-N bond lengths, as well as, the maximum and minimum errors. The initial results from the orbital optimization calculations split as expected with the wave function based methods providing upper bounds to the FCI energy and

N$_2$ Dissociation Errors in kcal/mol

		HF	MP2	CCSD	CASSCF	CASPT2	V2-T	LDA	PBE	BLYP	B3LYP	M062X	wB97XD	MN15
REF	MAE	225.85	70.41	33.26		13.76		947.85	131.34	201.31	161.51	157.01	160.39	115.91
	MSE	225.85	-67.80	32.19		13.76		947.85	-131.33	-201.31	-161.51	-153.36	-160.39	-104.76
	Δ_{EQM}	148.81	-0.95	5.91		13.99		919.27	-156.14	-222.90	-196.24	-202.00	-203.58	-147.94
	Δ_{DIS}	462.43	-328.34	206.37		12.68		1041.02	-31.83	-108.37	-33.82	14.53	-6.76	44.41
	ΔE_{DIS}	313.62	-327.38	200.45		-1.31		121.75	124.32	114.53	162.42	216.53	196.82	192.35
CAS	MAE	94.03	63.73	60.82	55.49		54.41	84.56	82.99	83.17	83.59	85.30	84.23	85.37
	MSE	94.03	63.73	60.82	55.49		54.41	84.56	82.99	83.17	83.59	85.30	84.23	85.37
	Δ_{EQM}	98.88	59.11	109.01	56.09		55.47	92.54	91.23	91.34	91.90	93.26	92.21	93.54
	Δ_{DIS}	76.19	69.50	48.21	49.41		49.33	54.37	52.38	52.26	53.84	58.40	55.89	55.67
	ΔE_{DIS}	-22.69	10.38	-114.82	-6.68		-6.13	-38.18	-38.85	-39.08	-38.06	-34.87	-36.32	-37.87
ACSE	MAE	2.00	3.05	2.96	3.61		3.02	4.18	4.44	4.82	3.80	2.93	3.48	4.40
	MSE	0.44	3.03	1.77	3.30		1.79	0.98	3.16	3.57	2.59	1.14	2.24	2.69
	Δ_{EQM}	1.84	3.12	3.45	4.52		3.97	5.02	6.62	6.94	5.46	3.73	5.11	6.46
	Δ_{DIS}	3.84	5.24	0.51	-0.14		-0.45	-2.73	0.43	0.61	1.38	1.73	1.54	-0.67
	ΔE_{DIS}	2.01	2.12	-2.94	-4.66		-4.43	-7.76	-6.18	-6.33	-4.08	-2.00	-3.57	-7.13

Table 5.1: Results for the various reference calculations used for the orbital optimization, as well as [6,6] CASCI, and CASCI/ACSE calculations. All calculations were performed with the 6-31G basis set. Errors are relative to the FCI energies and MSE and MAE are calculated over the eight distinct points along the dissociation coordinate; Δ_{eqm} and Δ_{dis} are the errors at $R = 1.0976$ and $R = 2.5$, respectively; and ΔE_{DIS} is the error in the dissociation energy, $E_{DIS} = E_{R=1.0976} - E_{R=2.5}$, with respect to FCI.

DFT yielding lower bounds. The largest positive deviation from FCI results from HF orbitals with a MSE of 225.85 kcal/mol, while the largest negative deviation from DFT orbitals is obtained with the BLYP functional at an MSE of -201.31 kcal/mol. CCSD yields the best results with an MSE of 33.26 kcal/mol, outperforming MP2, which as expected results in unphysical behavior in the dissociated regime and hence large negative deviations from FCI. Use of simple LDA gives rise to unphysical electronic energies with a MAE of 947.85 kcal/mol.

If we consider the contribution of the multi-reference correlation to the total electronic energy, CASSCF calculations using the minimal [6,6] active space give a MSE of 55.49 kcal/mol vs FCI, and on average the correlation recovered in the [6,6] active space accounts for 69.4% of the total correlation energy in the 6-31G basis set across the 8 dissociation points. The CASSCF calculation provides the benchmark result to assess the ability of a chosen method's orbitals to account for multi-reference correlation. As a CASSCF calculation uses orbital rotations to minimize the total energy as a functional of the CI energy in the active space, it yields the variational minimum to the multi-reference correlation that may be recovered in the chosen [6,6] active space and 6-31G basis set, and all CI calculations performed on different sets of orbitals yield upper bounds to this energy. Of the surveyed single-reference methods, the NOs from a CCSD calculation provide the orbitals that best account for static correlation across the N_2 dissociation space and yield the lowest CASCI energy, with a MAE of 60.82 kcal/mol, followed by MP2, which even though giving rise to non-physically low energies in the dissociated regime gives natural molecular orbitals that recover a correct CASCI picture with a MAE of 63.73 kcal/mol. DFT yields better multi-reference-ready orbitals than HF, with variation across the different surveyed DFT functionals being relatively small, ranging from the most correlated orbitals at PBE, MAE of 82.99 kcal/mol, to MN15 at MAE of 85.37 kcal/mol, recovering on average roughly 50% of the total correlation energy.

Application of the ACSE following the converged CASCI calculation in the chosen molecular orbital basis resolves dynamic correlation with accuracy comparable to CCSD with perturbative triple excitations [CCSD(T)], in addition to the multi-reference correlation recovered by the CI. Across all surveyed orbitals the CASCI/ACSE recovers an average of between 97.2% and 99.7% of the total correlation energy, displaying relatively minor dependence on the chosen molecular orbital basis compared to CI and single-reference calculations. Surprisingly, while providing the best multi-reference orbitals, CASSCF does not provide the most optimal orbitals to resolve the total correlation energy, recovering on average 98% of the total correlation energy with a MAE of 3.61 kcal/mol. As such, CASSCF orbitals are outperformed by orbitals obtained with HF, MP2, CCSD, M062X, and wB97XD calculations. Simple HF provides the most optimal orbitals to account for both strong and post-CI dynamic correlation, recovering an average of 99.7% of the FCI energy for MAE of 2.00 kcal/mol. Results from the different DFT functionals vary from an MAE of 2.93 kcal/mol in M06-2X to 4.82 kcal/mol in BLYP. Even in the case of the worst performing DFT functional, BLYP, the MAE increases by only 1.21 kcal/mol over CASSCF. The fact that MSEs are smaller than the MAEs result from the fact that the ACSE may yield a slightly lower bound to the FCI energy in the dissociated regime. ACSE calculations significantly outperform

CASPT2, which only recovers an average of 93.0% of the total correlation energy, for MAE of 13.76 kcal/mol.

Lastly, after considering recovery of the full FCI dissociation curve, we also consider the errors in the reproduction of the FCI dissociation energy, $\Delta E_{\mathrm{DIS}} = E_{\mathrm{DIS,method}} - E_{\mathrm{DIS,FCI}}$, where $E_{\mathrm{DIS}} = E_{R=1.0976} - E_{R=2.5}$. This provides a benchmark for orbitals obtained with a certain method to accurately recover the total energy in the dissociated multi-reference regime and the single-reference regime around the equilibrium bond distance. The observed trends follow those discussed above with large positive errors in the DFT, HF and CCSD reference calculations, which significantly overestimate the bonding energy as they break down as N_2 is dissociated, while MP2 diverges to large negative energies. Considering the CASCI energies, all calculation underestimate E_{DIS}, as correlation is more accurately captured at long bond distances. Now, accounting for mostly static correlation with [6,6] CASCI calculations, CASSCF, and the V2RDM implementation of CASSCF yields the optimal orbitals, followed by MP2 NOs, then HF and finally the various DFT functionals which display only minor variations. CCSD presents an outlier as the CASCI calculation with CCSD NOs at equilibrium suffered from convergence issues. Inspection of the individual errors at the equilibrium and dissociated geometry, Δ_{EQM} and Δ_{DIS}, respectively, reveals the HF result to arise from a favorable cancellation of error, with the energy lying high above the CASSCF and FCI references. Additionally, as indicated by Δ_{EQM} and Δ_{DIS}, the single reference orbitals tend to yield significantly lower errors in the multi-reference, dissociated regime than the dynamically correlated regime around the equilibrium bond length.

Finally, accounting for all-electron correlation with the CASCI/ACSE method, yields ΔE_{DIS} within 10 kcal/mol of the FCI result for all surveyed orbitals. Errors range in magnitude from a minimum of 2.00 kcal/mol with MOs from the M062X DFT functional and 2.01 kcal/mol with HF orbitals to 7.76 kcal/mol with LDA DFT MOs. Only orbitals from HF and MP2 result in an overestimation of E_{DIS}, while all others yield a negative deviation from FCI. Interestingly, CASSCF does not yield the optimal orbitals to resolve the electronic energy accurately in both the equilibrium and dissociated regimes, with deviations from FCI of -4.66 and -4.43 kcal/mol for its wave function and V2RDM implementations, respectively. Indeed, separate consideration of the errors at equilibrium and dissociation bond lengths reveals a relatively large Δ_{EQM} of 4.52 kcal/mol for the CASSCF orbitals, compared to only 1.84 kcal/mol, 3.12 kcal/mol and 3.45 kcal/mol for those obtained with single-reference methods HF, MP2 and CCSD, respectively. Interestingly, for the DFT MOs, Δ_{EQM} is larger than that obtained with CASSCF MOs for all functionals but M06-2X, with generally lower errors in the multi-reference, dissociation regime. The result is that CASSCF/ACSE all-electron correlation calculations with initial CASSCF optimization of the orbitals for the dissociation energy of N_2, where energy differences between a strongly correlated and a dynamically correlated solution are computed, are outperformed by simple CASCI/ACSE calculations using orbitals obtained from HF, MP2, CCSD, as well as the DFT functionals B3LYP, M062X, and wB97XD.

5.3.2 Singlet Triplet Gaps of Main Group Biradicaloids

Biradicals play important roles in a wide range of chemical processes as transition states and intermediates, formed during the breaking and forming of chemical bonds, as well as in the development of new single-molecule magnets and materials for spintronics or molecular qubits[84–86]. Their accurate theoretical description continues to pose a challenge to current developments in electronic structure theory due to the multi-reference character of their open-shell singlet states, requiring the use of methods that account for both static and dynamic correlation to resolve their electronic properties. In this section we investigate the orbital dependence of the singlet-triplet (S-T) gaps for a benchmark set of small main group biradicals OH^+, NH, NF, O_2, NH_2^+, CH_2, PH_2^+, and SiH_2 as calculated with single-reference, CI and post-CI ACSE methods. Singlet-triplet gaps

		HF	MP2	CCSD	V2-T	LDA	PBE	BLYP	B3LYP	M062X	wB97XD	MN15
REF	MAE	20.3	70.7	6.5		21.4	11.5	7.12	7.19	6.62	7.01	4.7
	MSE	20.3	70.7	6.5		21.4	11.5	6.7	7.19	6.62	6.96	3.63
	Δ_{max}	31.1	93.5	13.1		35.7	22.7	16.7	17.1	13.71	16.82	10.9
	Δ_{min}	14.6	26.3	0.12		12.4	3.8	0.03	0.05	0.77	0.10	1.08
CAS	MAE	15.48	14.45	9.39	6.38	11.43	9.75	10.57	10.75	11.85	11.18	10.28
	MSE	10.88	-3.16	-4.18	-0.56	5.16	5.37	4.06	4.95	6.01	4.88	3.96
	Δ_{max}	19.96	45.57	45.57	16.68	25.07	17.54	26.03	23.21	23.37	25.17	25.26
	Δ_{min}	9.74	0.04	0.12	0.04	7.37	4.89	4.88	6.36	8.24	6.37	4.51
	$\bar{R}_S$	0.251	0.212	0.628	0.912	0.855	0.888	0.886	0.851	0.720	0.818	0.866
	$\bar{R}_T$	2.005	2.027	2.037	2.036	2.013	2.013	2.013	2.011	2.009	2.011	2.013
ACSE	MAE	5.44	7.36	3.64	3.16	4.63	5.22	4.37	3.99	4.07	3.99	4.48
	MSE	2.18	12.47	-0.81	-1.28	-3.27	-1.64	-2.98	-2.87	-1.85	-2.43	-3.10
	Δ_{max}	8.71	12.47	9.44	6.25	9.61	12.44	10.34	9.56	9.62	9.47	10.61
	Δ_{min}	0.06	0.05	0.36	0.36	0.14	0.51	0.42	0.21	0.06	0.45	0.58
	$\bar{R}_S$	0.533	0.432	0.835	1.102	1.067	1.116	1.109	1.084	0.968	1.055	1.084
	$\bar{R}_T$	2.189	2.199	2.197	2.200	2.166	2.182	2.180	2.180	2.183	2.183	2.172

Table 5.2: Data for the S-T gaps of the set of eight biradicals, OH^+, NH, NF, O_2, NH_2^+, CH_2, PH_2^+, and SiH_2. All calculations were carried out using the cc-pVTZ basis set, and CASCI and ACSE calculations use a [4,4] active space. MAE and MSE, and maximum and minimum absolute errors, Δ_{max} and Δ_{min}, are calculated relative to experimental reference values obtained from references[87–91]. $\bar{R}_S$ and $\bar{R}_T$ denote the average distance of the NON from the HF solution for the singlet and triplet states, respectively.

of biradicaloids are of particular value as they relate to experimentally relevant properties such as the exchange coupling constant J or their properties in photonics.

We perform calculations on the singlet and triplet states with the cc-pVTZ basis set[92, 93], using a minimal [4,4] active space chosen around the HOMO and LUMO for the CI calculations, allowing for the inclusion of non-trivial correlation in the triplet states and assessing the suitability of the single-reference orbital to yield a suitable CAS guess. The ACSE calculations use a spin-averaged implementation, which has recently been demonstrated to yield highly accurate singlet-triplet gaps for this benchmarking set with converged CASSCF wave functions[94]. The data are presented in Table 5.2. Errors are calculated with respect to the experimental reference values. As expected, none of the single-reference methods yield accurate results, failing to capture the strong correlation of the biradical singlets. MP2 yields extremely inaccurate results with a MAE of 70.7 kcal/mol, while the rest of the surveyed methods range from 6.5 kcal/mol in CCSD (use of perturbative triples correction reduces this to 4.6 kcal/mol) to 21.4 kcal/mol in LDA. HF also yields a large MAE of 20.3 kcal/mol. Across the surveyed DFT functionals we observe a quite significant variation in their ability to calculate the S-T gaps, with MN15 giving the lowest MAE of 4.7 kcal/mol and LDA and PBE giving the largest MAEs of 21.4 kcal/mol and 11.5 kcal/mol, respectively.

As with the dissociation of N_2, of the surveyed methods CCSD natural orbitals yield the most optimal basis to account for multi-reference character in the CASCI calculations, with a MAE of 9.39 kcal/mol, followed by the various DFT functionals, where variation in the CASCI results is less pronounced than in the single-reference calculations. Furthermore, there is no correlation between the accuracy of the CASCI calculation and the reference DFT calculation, with orbitals from the previously best performing MN15 now yielding a MAE of 10.28 kcal/mol, while the second-worst performing PBE returns the best CASCI results with a MAE of 9.75 kcal/mol. Apart from the unreliable MP2 calculations, HF orbitals give the largest MAE of 15.6 kcal/mol. No orbital basis from any method comes close in accuracy to the CASSCF calculations, which yields a MAE of 6.38 kcal/mol. While the MSE is close to zero (-0.56 kcal/mol) in CASSCF, it is of significant, positive magnitude in DFT, ranging from 3.96 kcal/mol in MN15 to 6.01 kcal/mol in M06-2X and HF, while it is negative in MP2 and CCSD. As an additional measure to probe the biradical character in the solutions, we introduce the average distance of the 1-RDM of the CASCI calculation from a closed-shell single-reference 1-RDM, defined as $\bar{R} = \sum_{ij} |\lambda_{HF,i} - \lambda_i|_j / N$, where i runs over all orbitals of the system, N is the number of species in the set, j runs over all its members, λ_i denotes the ith natural occupation number and $\lambda_{HF,i}$ is 2 if the orbital is occupied and 0 if the orbital is virtual.

The inclusion of post-CI dynamic correlation with the spin-averaged ACSE provides significant improvement over single-reference and CASCI results in all cases. While the [4,4] CASSCF optimization does give the best agreement with experiment (MAE of 3.16 kcal/mol), the advantage over the various other orbitals is relatively minor, with MP2 and HF orbitals yielding the largest deviations with MAEs of 7.36 kcal/mol and 5.44 kcal/mol, respectively, and CCSD again yielding the closest agreement with an MAE within 0.5 kcal/mol of CASSCF. The CASCI/ACSE calculations performed with DFT orbitals provide MAEs within 1 kcal/mol of the CASSCF orbitals for all functionals but PBE, which has the largest error at an MAE of 5.22 kcal/mol. Across the surveyed functionals, variation again is minor, meaning while S-T gaps predicted by the individual functionals differ based on empirical fitting, the underlying molecular orbitals obtained in the SCF procedure remain relatively unchanged. Analogous to the N_2 dissociation, the ωB97X-D functional again performs well and provides the molecular orbitals best suited to account for the multi-reference and dynamic correlation in the biradicaloid set, yielding a MAE of 3.99 kcal/mol. In the CASCI/ACSE case the sign of the MSE obtained for the various DFT orbitals agrees with CASSCF, and only HF and MP2 orbitals lead to a positive MSE, while CCSD yields a MSE of small negative magnitude. Again considering $\bar{R}$ as a measure for the recovered total correlation, HF and MP2 which yield the largest MAEs also result in the lowest magnitude of $\bar{R}_S$, 0.533 and 0.432, respectively. However, surprisingly, $\bar{R}_{S,CCSD} = 0.835$ is significantly lower than $\bar{R}_{S,CASSCF} = 1.102$, while DFT orbitals, yield $\bar{R}_S$ values between 0.968 and 1.116, with there being no correlation between $\bar{R}_S$ and MAE. To the contrary, PBE yields greater correlation in the NOs than CASSCF while resulting in the largest MAE of all surveyed functionals.

To resolve the origin of the minor variations across surveyed methods, we plot the deviations from experimental reference values for the individually studied species for CASSCF, HF, CCSD, and M06-2X in Figure 5.2. Inspection of the individual errors in CASCI shows particularly large errors in the calculation of O_2, which has previously been demonstrated to provide a challenge to various electronic structure methods, with AFQMC and ACSE calculations requiring CASSCF wave functions with active spaces as large as [10,15] and [14,14] to yield sub 2 kcal/mol accuracy

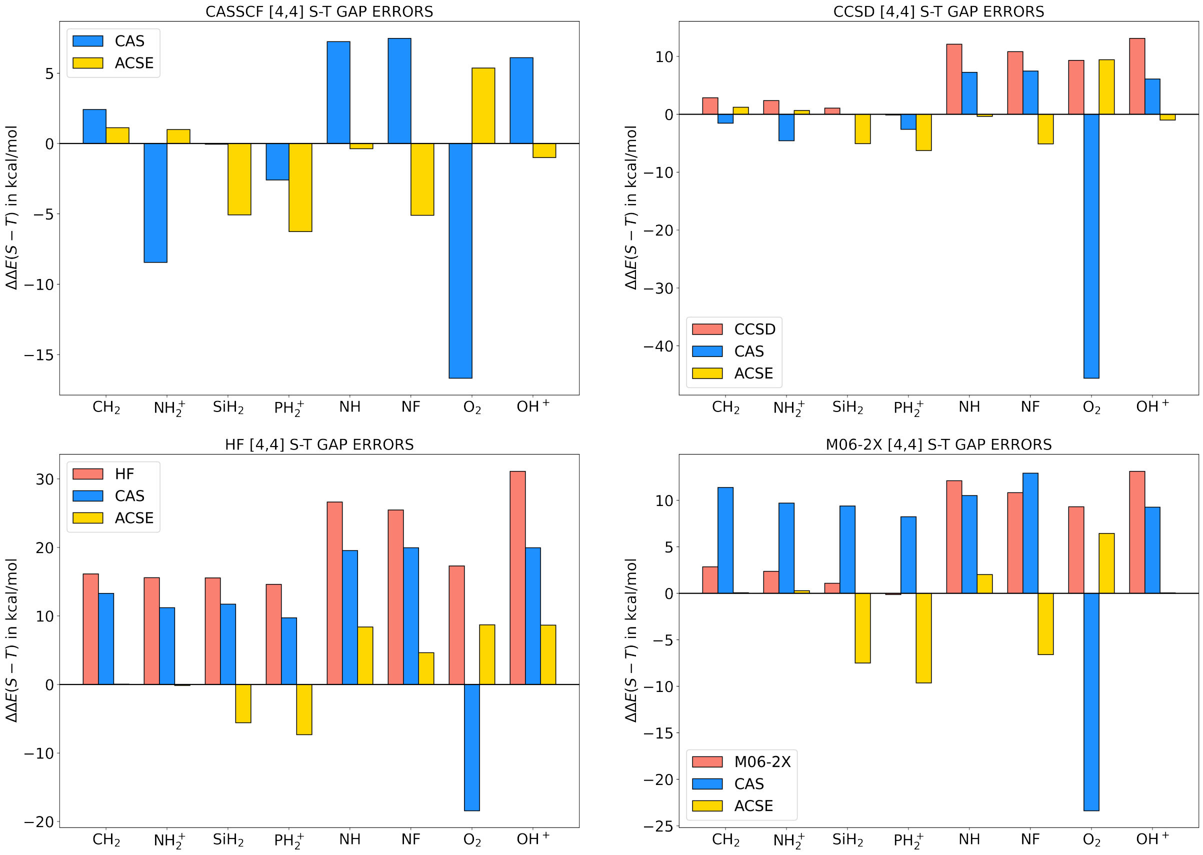

Figure 5.2: Data for the S-T gaps of the biradical set resolved for its individual members for four select methods used for the orbital optimization. Bars indicate the errors of the S-T gap with respect to the experimental reference. Orange bars indicate errors of the single-reference calculation, blue bars the CASCI results based on the single-reference orbitals, and yellow bars the CASCI/ACSE result in the respective single-reference orbital basis. Top row: CASSCF (left), CCSD (right); bottom row: HF (left), M06-2X (right). All data were obtained with a cc-pVTZ basis set and [4,4] active spaces for the CASCI and ACSE calculations.

		M06-L	M06	M06-2X	M06-HF
	% HF	0	27	54	100
REF	MAE	8.65	6.92	6.62	4.25
	MSE	8.65	4.73	6.62	4.22
	Δ_{max}	20.62	15.76	13.71	11.34
	Δ_{min}	0.19	0.75	0.77	0.13
CAS	MAE	10.65	10.77	11.85	14.41
	MSE	4.40	5.10	6.01	4.55
	Δ_{max}	25.00	22.70	23.37	21.39
	Δ_{min}	5.45	7.06	8.24	9.37
	$\bar{R}_S$	0.884	0.838	0.720	0.396
	$\bar{R}_T$	2.014	2.011	2.009	2.005
ACSE	MAE	3.92	4.26	4.07	4.55
	MSE	-2.52	-2.95	-1.85	-0.27
	Δ_{max}	8.79	10.65	9.62	9.72
	Δ_{min}	0.03	0.25	0.06	0.52
	$\bar{R}_S$	1.122	1.072	0.968	0.662
	$\bar{R}_T$	2.190	2.179	2.183	2.177

Table 5.3: Data for the biradical set S-T gaps resolved with orbitals from the members of the MN06 suite of functionals. Calculations were carried out with the cc-pVTZ basis set and CASCI and ACSE data obtained with a [4,4] active space.

for the calculation of its S-T gap[94, 95]. The [4,4] active space successfully resolves its diradical character; however, it significantly overstabilizes the singlet state leading to a large negative deviation from experiment. We observe a particularly strong stabilization of the singlet O_2 state in the CASCI with CCSD molecular orbitals, while the remaining orbitals yield results that are in good agreement with CASSCF, leading to the more negative MSE in the CCSD NO basis. The positive MSE in DFT and HF arises from the fact that, while there is agreement with CASSCF in the case of O_2, the orbitals in all other species lead a to an overestimation of the singlet triplet gap via a relatively less pronounced stabilization of the singlet. Use of the ACSE to include post-CI correlation leads to a significant reduction in the variation of the errors across the different species and methods, with only HF orbitals showing deviations in significant magnitude from the CASSCF/ACSE results, particularly in the cases of NF and OH^+.

Lastly, to provide insight into the effect of exact HF exchange in a chosen DFT functional on the molecular orbitals obtained from the SCF procedure, we compare the results from four M06 functionals with varying degrees of HF exchange: M06-L (0%), M06 (27%), M06-2X (54%), and M06-HF (100%), shown in Table 5.3. Interestingly, the MAE and MSE of the DFT S-T gaps decreases as the HF exchange contribution to the functional increases. While this is contrary to results from large-scale functional benchmarks, which suggest functionals with larger HF exchange contributions yield worse performance on multi-reference interactions[96], the expected trend is observed in the CASCI errors. These consistently increase with the HF exchange fraction, suggesting the inclusion of more exact HF exchange leads to worse multi-reference orbitals in the KS-SCF optimization. Inclusion of post-CI dynamic correlation again results in reduced variation across the functionals, however, showing a trend of increasing MAE with increasing HF exchange in the functional used for the orbital optimization. In fact, the molecular orbitals obtained from a SCF optimization with the 0% HF exchange containing M06L functional yields the lowest MAE, as well as maximum and minimum errors across the data set of all surveyed functionals. Additionally, the decrease in the ability of the functional's orbitals to account for multi-reference character of the singlet state is clearly reflected in the trend observed in the $\bar{R}_S$ values with a steady decrease from a maximum of 1.122 in M06-L to just 0.662 in M06-HF.

While the results obtained from the [4,4] spin-averaged CASSCF/ACSE calculation are comparable to those from CASSCF/MC-PDFT, which yields a MAE of 3.5 kcal/mol[97], the computationally less expensive CASCI/ACSE calculations based on a DFT orbital optimization yield results in line with various methods reported across the literature, such as (V)FS-PBE (MAE = 4.3 kcal/mol)[98], pp-B3LYP (4.8 kcal/mol)[99], W2X (3.7 kcal/mol)[97], or tPBE/MC-PDFT (4.3 kcal/mol)[97].

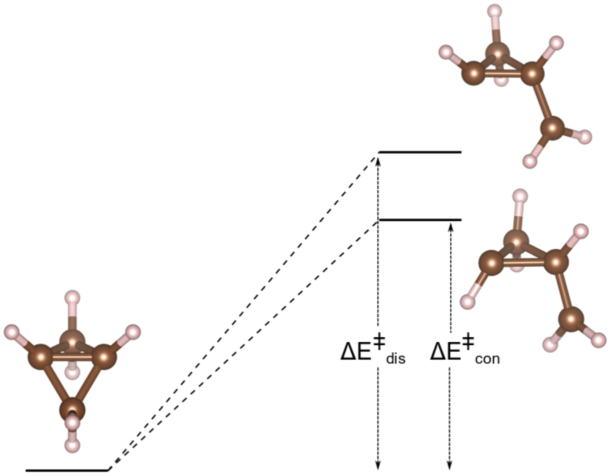

Figure 5.3: Reaction coordinate of the isomerization reaction of bicyclobutane to 1,3-butadiene with the con- and dis-rotatory transition states shown. The conversion to the 1,3-butadiene is not considered.

5.3.3 Transition States of the Bicyclobutane Isomerization Reaction to gauche-1,3-Butadiene

As a final example, we consider the orbital dependence in the use of CI and post-CI methods to model a simple chemical reaction, calculating the energy barrier, $\Delta H^{\ddagger}$, to the isomerization reaction of bicyclobutane to gauche-1,3-butadiene. This isomerization process may proceed via two different transition states arising from conrotatory (CON) and disrotatory (DIS) pathways. The reaction coordinate diagram displaying these is shown in Figure 5.3. Optimized geometries and zero-point and vibrational corrections to the electronic energy were obtained from reference [100], using the MCSCF/6-31G*[101] level of theory, and amounting to 0.0911, 0.0862, and 0.0844 hartrees for bicyclobutane, and the CON and DIS transition states, respectively. Calculations were performed with the previously surveyed methods, CAS orbitals were selected around the HOMO and LUMO, and the results are compared to those obtained from [14,14] CASSCF/ACSE calculations, as well as previously reported ACSE[100], CC(P;Q)[102], and DMC[103] data. The barrier for the CON transition pathway has been experimentally determined to be 40.6 ± 2.5 kcal/mol. The data are shown in Table 5.4.

		CASSCF												
		[4,4]	[14,14]	HF	MP2	CCSD	V2-T	LDA	PBE	BLYP	B3LYP	M062X	wB97XD	MN15
CON	$\Delta H^{\ddagger}$			57.59	48.60	47.53		41.92	42.25	36.75	43.50	53.42	50.30	50.89
	$\Delta H^{\ddagger}_{\text{CAS}}$	37.68	33.70	42.86	39.49	31.16	37.85	45.92	45.23	44.51	43.07	43.25	42.91	42.80
	$\Delta H^{\ddagger}_{\text{ACSE}}$	40.56	40.78	46.56	46.71	43.43	40.74	39.54	42.14	42.49	43.38	43.63	44.01	42.95
	$\lambda_{\text{HONO,CAS}}$	1.701	1.734	1.816	1.846	1.755	1.701	1.782	1.776	1.770	1.776	1.794	1.787	1.785
	$\lambda_{\text{LUNO,CAS}}$	0.299	0.271	0.187	0.155	0.247	0.299	0.220	0.224	0.230	0.225	0.209	0.216	0.218
	$\lambda_{\text{HONO,ACSE}}$	1.669	1.703	1.763	1.800	1.720	1.669	1.722	1.723	1.719	1.726	1.741	1.737	1.732
	$\lambda_{\text{LUNO,ACSE}}$	0.319	0.286	0.228	0.188	0.270	0.319	0.281	0.277	0.280	0.271	0.256	0.261	0.267
DIS	$\Delta H^{\ddagger}$			92.38	68.98	67.51		64.45	64.46	58.18	67.69	80.78	76.36	76.95
	$\Delta H^{\ddagger}_{\text{CAS}}$	46.49	47.25	53.30	53.91	40.07	46.69	51.63	50.21	50.10	49.75	50.62	50.03	49.31
	$\Delta H^{\ddagger}_{\text{ACSE}}$	52.11	51.79	55.93	59.59	54.32	52.33	49.35	51.76	52.43	53.53	53.15	53.53	51.72
	$\lambda_{\text{HONO,CAS}}$	1.364	1.413	1.462	1.612	1.438	1.364	1.434	1.428	1.418	1.420	1.433	1.429	1.428
	$\lambda_{\text{LUNO,CAS}}$	0.636	0.589	0.547	0.398	0.566	0.636	0.573	0.580	0.590	0.588	0.576	0.580	0.581
	$\lambda_{\text{HONO,ACSE}}$	1.345	1.393	1.423	1.574	1.416	1.345	1.399	1.396	1.387	1.390	1.400	1.398	1.395
	$\lambda_{\text{LUNO,ACSE}}$	0.641	0.594	0.567	0.419	0.574	0.641	0.602	0.605	0.612	0.608	0.598	0.601	0.603

Table 5.4: Data for the con- and disrotatory pathways of the isomerization reaction of bicyclobutane. Calculations were carried out with the 6-31G* basis set and CASCI and ACSE calculations utilize a [4,4] active space. Geometries and free energy corrections calculated at the MCSCF/6-31G* level of theory and were obtained from reference[100]. $\Delta H^{\ddagger}$ denotes the transition state barrier including zero point and vibrational corrections amount to -3.087 kcal/mol and -4.221 kcal/mol for the CON and DIS pathways, respectively. λ_{HONO} and λ_{LUNO} denote the occupations of the highest and lowest natural orbitals (HONO and LUNO), respectively.

First considering the conrotatory pathway, variation across the barriers predicted by the single reference methods is significant, ranging from $\Delta H^{\ddagger} = 36.75$ kcal/mol with BYLP to $\Delta H^{\ddagger} = 57.59$ kcal/mol with HF. Within the DFT realm, the obtained results are very sensitive to the choice of functional and lack consistency, with BLYP underestimating $\Delta H^{\ddagger}$ while the remaining functionals overestimate it and variations far exceeding chemical accuracy. Nonetheless, the LDA and PBE functionals predict $\Delta H^{\ddagger}$ values that lie within the experimental bounds of error. It is noteworthy that the MN15 functional which is fitted to perform well in multi-reference problems, gives a large overestimation of $\Delta H^{\ddagger}$ with the predicted 50.89 kcal/mol being far outside the realms of chemical accuracy.

Using a [14,14] active space CASSCF yields $\Delta H^{\ddagger} = 33.70$ kcal/mol, with highest occupied natural orbital (HONO) and lowest unoccupied natural orbital (LUNO) occupation numbers of 1.734 and 0.271, respectively, making the CON transition state the less correlated one. The static correlation from the CASSCF calculation overstabilizes the TS compared to bicyclobutane, resulting in underestimation of $\Delta H^{\ddagger \mathrm{CAS}}$. For our CASCI calculations we use a smaller [4,4] active space ($\Delta H^{\ddagger}_{\mathrm{CAS}} = 37.68$), which reduces the magnitude of this underestimation and is sufficient to resolve the biradical character of the TS, yielding HONO and LUNO occupation numbers of 1.701 and 0.299, respectively. For the CASCI calculations, CCSD again provides the orbitals most optimal to resolve the multireference correlation of the methods surveyed, underestimating the CON barrier, and yielding the smallest deviation from the [14,14] CASSCF result and with $\Delta H^{\ddagger} = 31.16$ kcal/mol—a lower barrier than both [4,4] and [14,14] CASSCF. All other orbitals provide a CASCI energy with a positive deviation from the CASSCF $\Delta H^{\ddagger}$, with MP2 NOs yielding the least correlated solution but the smallest error, followed by HF and finally the various DFT functionals, which yield large $\Delta H^{\ddagger}$s but more correlated solutions than MP2 and HF, showing HONO and LUNO occupations numbers comparable to [4,4] CASSCF.

Using the ACSE to resolve the full correlation energy, both [4,4] and [14,14] CASSCF resolve the CON barrier to near-exact accuracy providing near-identical results of 40.74 kcal/mol and 40.78 kcal/mol, respectively. MP2 NOs provides both the least correlated solution, as well as the largest deviation from the experimental range of $\Delta H^{\ddagger}$, lying 3.61 kcal/mol above this interval. It is closely followed in both error and correlation by HF. Contrary to the results from the S-T gaps and N_2 dissociation, CCSD NOs are now outperformed by the majority of DFT functionals, with only M06-2X, and ωB97XD deviating by more than CCSD's 0.33 kcal/mol from the experimental confidence interval. The LDA, PBE, BLYP and MN15 orbitals all yield $\Delta H^{\ddagger}$ values obtained by the CASCI/ACSE algorithm that lie within the experimental error bound.

The disrotatory TS provides for the more correlated and higher energy isomerization pathway, with [14,14] CASSCF/ACSE yielding a barrier of $\Delta H^{\ddagger} = 51.79$ kcal/mol and LUNO and LUNO occupation numbers of 1.393 and 0.594, respectively. There is no experimental reference data

		M06-L	M06	M06-2X	M06-HF
	% HF	0	27	54	100
CON	$\Delta H^{\ddagger}$	46.72	48.46	53.42	57.46
	$\Delta H^{\ddagger}_{CAS}$	44.87	43.16	43.25	42.66
	$\Delta H^{\ddagger}_{ACSE}$	42.14	43.03	43.63	45.15
	$\lambda_{\mathrm{HONO,CAS}}$	1.785	1.787	1.794	1.806
	$\lambda_{\mathrm{LUNO,CAS}}$	0.215	0.214	0.209	0.198
	$\lambda_{\mathrm{HONO,ACSE}}$	1.732	1.735	1.741	1.755
	$\lambda_{\mathrm{LUNO,ACSE}}$	0.269	0.264	0.256	0.240
DIS	$\Delta H^{\ddagger}$	72.43	74.69	80.78	85.41
	$\Delta H^{\ddagger}_{CAS}$	49.29	49.60	50.62	52.26
	$\Delta H^{\ddagger}_{ACSE}$	51.76	52.57	53.15	53.87
	$\lambda_{\mathrm{HONO,CAS}}$	1.426	1.427	1.433	1.449
	$\lambda_{\mathrm{LUNO,CAS}}$	0.582	0.582	0.576	0.560
	$\lambda_{\mathrm{HONO,ACSE}}$	1.395	1.395	1.400	1.413
	$\lambda_{\mathrm{LUNO,ACSE}}$	0.606	0.604	0.598	0.580

Table 5.5: Data for con- and disrotatory pathways of the bicylobutane isomerization resolved for the members of the MN06 suite of functionals with their varying degrees of exact HF-exchange. Calculations with the 6-31G* basis set and CASCI and ACSE data obtained with a [4,4] active space.

for the DIS pathway, but DMC calculations have yielded a barrier of 58.6 kcal/mol[103], while CR-CC(2,3) predicts a barrier height of 67.5 kcal/mol[102]. Across the various single-reference methods and the CASCI calculations, the trends remain unchanged from the CON pathway, however, with increased errors in the single-reference calculations as the degree of multi-reference correlation in the TS is increased. All CASCI/ACSE calculations with DFT orbitals fall within the ± 2.5 kcal/mol range of the CASSCF[14,14]/ACSE reference, with MN15 and PBE yielding the closest, and near-identical, results. In this more strongly correlated TS, CCSD NOs yield a larger error of 2.53 kcal/mol. As in the CON TS, DFT orbitals yields more fractional NON than those from HF, MP2, and comparable values to CCSD NOs.

Lastly, we again look at the M06 suite of functionals to resolve the influence of HF exchange in the DFT functional. While there is no obvious trend in the barrier height predicted by CASCI based on the various orbitals, $\Delta H^\ddagger$ predicted by the functional and the CASCI/ACSE calculation, as well as, the NONs follow the expected trend with a lower fraction of HF exchange better accounting for the multi-reference correlation in the studied transition states. Consequently, errors in $\Delta H^\ddagger$ and the value of the NON increase across the series from M06-L to M06-HF. The M06-L functional MOs provide a barrier height within the experimental range of error for the CON pathway, yielding identical results to PBE and an only slightly larger error than LDA, while in the DIS pathway M06-L orbitals yield near-exact agreement with [14,14] in both NON and $\Delta H^\ddagger$, providing the best orbitals from any method surveyed.

5.4 Discussion & Conclusions

We have employed CASCI calculations in combination with the ACSE to resolve the orbital dependence on the dynamic and multi-reference parts of the total electronic correlation energy. Considering problems dominated by multi-reference correlation, we show that CASCI calculations display significant dependence on the chosen molecular orbital basis, with coupled cluster natural orbitals yielding the most optimal orbitals to account for multi-reference correlation of the single-reference methods surveyed, and HF yielding the least suitable orbitals, while DFT functionals lie between the two methods. Nonetheless, for the accurate prediction of multi-reference dependent properties through the means of CI calculations only, CASSCF orbital optimization is prudent. Use of a post-CI method to account for dynamic correlation, in this case the ACSE, reduces the orbital dependence of the accuracy in the predicted properties.

Using the ACSE to resolve post-CI dynamic correlation, we survey orbitals from wave function based single-reference, as well as, various popular DFT functionals. While HF orbitals yield good results for the N_2 dissociation, they tend to fail to capture accurately multi-reference character and deliver lackluster results in the CASCI/ACSE scheme for the prediction of biradical S-T gaps and TS barriers. MP2 is plagued by inconsistencies and convergence issues. Natural orbitals obtained from CCSD calculations, however, allow CASCI/ACSE to resolve both dynamic and strong correlation effects in the three case studies accurately, outperforming CASSCF orbitals in the N_2 dissociation, where molecular geometries not dominated by static correlation are considered, most closely mirroring the FCI dissociation curve, and yielding biradical S-T gaps and bicyclobutane isomerization barriers with accuracies close to those achieved with CASSCF orbitals.

The various DFT functionals, which are known to yield widely varying results for different systems and properties based on their parametric fitting, produce orbitals that compared to the results predicted by the functionals themselves, such as S-T gaps or dissociation energies, show much greater consistency. Of the tested functionals, the M06 suite and the ωB97XD functionals provide the best suited orbitals for the CASCI/ACSE calculations, yielding only marginally worse performance than CASSCF and CCSD orbitals. Furthermore, resolving the S-T gaps and bicyclobutane isomerization barriers obtained with the M06 suite functionals shows the most optimal orbitals to account for both multi-reference and dynamic correlation are obtained with the lowest HF-exchange fraction, i.e. the M06-L functional, which yields the best orbitals for the treatment of multi-reference problems of any tested functional. As DFT presents the most ubiquitous electronic structure method across many disciplines in chemistry, physics and materials science, implemented in any commonly used software package, offering inexpensive computational scaling compared to CASSCF or CC methods, it provides a good compromise between computational costs, ease-of-use, and accuracy. Especially, considering the fact that DFT molecular orbitals are already available in most cases through prior geometry optimizations or frequency calculations, they provide a viable option for further ab-initio calculations aimed at resolving electron correlation in many applications, significantly reducing further computational expense while retaining viable accuracy.

This work provides valuable insight into the orbital dependence in the ability of CASCI and post-CI methods to resolve multi-reference and dynamic correlation. We demonstrate that contrary to popular implementations that rely on CASSCF orbital optimizations for the resolution of the total correlation energy, CASSCF may not always provide the optimal molecular orbital basis set to account for the combination of static and dynamic contributions to the electronic energy. Furthermore, improved computational scaling may be obtained through the use of widely available single-reference methods for the optimization of the molecular orbitals. Additionally, if a post-CI method to resolve all-electron correlation were to be implemented in a SCF fashion, undergoing further orbital optimization after the initial CAS seed calculation, performance of an initial CASSCF calculation may be of limited value as compared to a seed with orbitals obtained from the surveyed single-reference methods. Throughout the studied systems we show that the CASCI/ACSE method is a valuable tool in the accurate resolution of the properties of a multi-reference system, and may be used in combination with any single-reference calculation, in particular with DFT, not requiring further CASSCF calculations.

References

(1) Stein, C. J.; von Burg, V.; Reiher, M. *J. Chem. Theory Comput.* **2016**, *12*, 3764–3773.

(2) Pople, J. A.; Binkley, J. S.; Seeger, R. *Int. J. Quantum Chem.* **1976**, *10*, 1–19.

(3) Zhang, D.; Truhlar, D. G. *J. Chem. Theory Comput.* **2021**, *17*, 5733–5744.

(4) Benavides-Riveros, C. L.; Lathiotakis, N. N.; Marques, M. A. L. *Phys. Chem. Chem. Phys.* **2017**, *19*, 12655–12664.

(5) Bartlett, R. J. *Annu. Rev. Phys. Chem.* **1981**, *32*, 359–401.

(6) Cremer, D. *Mol. Phys.* **2001**, *99*, 1899–1940.

(7) Cohen, A. J.; Handy, N. C. *Mol. Phys.* **2001**, *99*, 607–615.

(8) Scheschkewitz, D.; Amii, H.; Gornitzka, H.; Schoeller, W. W.; Bourissou, D.; Bertrand, G. *Science* **2002**, *295*, 1880–1881.

(9) Stuyver, T.; Chen, B.; Zeng, T.; Geerlings, P.; De Proft, F.; Hoffmann, R. *Chem. Rev.* **2019**, *119*, 11291–11351.

(10) Salem, L.; Rowland, C. *Angew. Chem.* **1972**, *11*, 92–111.

(11) Abe, M. *Chem. Rev.* **2013**, *113*, 7011–7088.

(12) Roos, B. O. In *Advances in Chemical Physics*; John Wiley & Sons, Ltd: 1987, pp 399–445.

(13) Olsen, J. *Int. J. Quantum Chem.* **2011**, *111*, 3267–3272.

(14) Siegbahn, P. E. M.; Almlöf, J.; Heiberg, A.; Roos, B. O. *J. Chem. Phys.* **1981**, *74*, 2384–2396.

(15) Pathak, S.; Lang, L.; Neese, F. *J. Chem. Phys.* **2017**, *147*, 234109.

(16) Andersson, K.; Malmqvist, P.-Å.; Roos, B. O. *J. Chem. Phys.* **1992**, *96*, 1218–1226.

(17) Pulay, P. *Int. J. Quantum Chem.* **2011**, *111*, 3273–3279.

(18) Zobel, J. P.; Nogueira, J. J.; González, L. *Chem. Sci.* **2017**, *8*, 1482–1499.

(19) Azizi, Z.; Roos, B. O.; Veryazov, V. *Phys. Chem. Chem. Phys.* **2006**, *8*, 2727–2732.

(20) Ceperley, D.; Alder, B. *Science* **1986**, *231*, 555–560.

(21) Reynolds, P. J.; Ceperley, D. M.; Alder, B. J.; Lester, W. A. *J. Chem. Phys.* **1982**, *77*, 5593–5603.

(22) Austin, B. M.; Zubarev, D. Y.; Lester, W. A. *Chem. Rev.* **2012**, *112*, 263–288.

(23) Li Manni, G.; Carlson, R. K.; Luo, S.; Ma, D.; Olsen, J.; Truhlar, D. G.; Gagliardi, L. *J. Chem. Theory Comput.* **2014**, *10*, 3669–3680.

(24) Gagliardi, L.; Truhlar, D. G.; Li Manni, G.; Carlson, R. K.; Hoyer, C. E.; Bao, J. L. *Acc. Chem. Res.* **2017**, *50*, 66–73.

(25) Gagliardi, L.; Truhlar, D. G.; Li Manni, G.; Carlson, R. K.; Hoyer, C. E.; Bao, J. L. *Acc. Chem. Res.* **2017**, *50*, 66–73.

(26) Ferté, A.; Giner, E.; Toulouse, J. *J. Chem. Phys.* **2019**, *150*, 084103.

(27) Hoyer, C. E.; Ghosh, S.; Truhlar, D. G.; Gagliardi, L. *J. Phys. Chem. Lett.* **2016**, *7*, 586–591.

(28) Yang, W.; Zhang, Y.; Ayers, P. W. *Phys. Rev. Lett.* **2000**, *84*, 5172–5175.

(29) Sharma, S.; Dewhurst, J. K.; Lathiotakis, N. N.; Gross, E. K. U. *Phys. Rev. B* **2008**, *78*, 201103.

(30) Lathiotakis, N. N.; Marques, M. A. L. *J. Chem. Phys.* **2008**, *128*, 184103.

(31) Zimmerman, P. M. *J. Chem. Phys.* **2017**, *146*, 104102.

(32) Zimmerman, P. M. *J. Chem. Phys.* **2017**, *146*, 224104.

(33) Eriksen, J. J.; Gauss, J. Incremental Treatments of the Full Configuration Interaction Problem, 2020.

(34) Mazziotti, D. A. *Phys. Rev. A* **2007**, *76*, 052502.

(35) Rothman, A. E.; Foley, J. J.; Mazziotti, D. A. *Phys. Rev. A* **2009**, *80*, 052508.

(36) Beran, G. J. O.; Gwaltney, S. R.; Head-Gordon, M. *Phys. Chem. Chem. Phys.* **2003**, *5*, 2488–2493.

(37) Fang, Z.; Lee, Z.; Peterson, K. A.; Dixon, D. A. *J. Chem. Theory Comput.* **2016**, *12*, 3583–3592.

(38) Fang, Z.; Vasiliu, M.; Peterson, K. A.; Dixon, D. A. *J. Chem. Theory Comput.* **2017**, *13*, 1057–1066.

(39) Sherrill, C. D.; Krylov, A. I.; Byrd, E. F. C.; Head-Gordon, M. *J. Chem. Phys.* **1998**, *109*, 4171–4181.

(40) Krylov, A. I.; Sherrill, C. D.; Head-Gordon, M. *J. Chem. Phys.* **2000**, *113*, 6509–6527.

(41) Lochan, R. C.; Head-Gordon, M. *J. Chem. Phys.* **2007**, *126*, 164101.

(42) Neese, F.; Schwabe, T.; Kossmann, S.; Schirmer, B.; Grimme, S. *J. Chem. Theory Comput.* **2009**, *5*, 3060–3073.

(43) Lee, J.; Head-Gordon, M. *J. Chem. Theory Comput.* **2018**, *14*, 5203–5219.

(44) Rettig, A.; Hait, D.; Bertels, L. W.; Head-Gordon, M. *J. Chem. Theory Comput.* **2020**, *16*, 7473–7489.

(45) Bertels, L. W.; Lee, J.; Head-Gordon, M. *J. Phys. Chem. Lett.* **2019**, *10*, 4170–4176.

(46) Bertels, L. W.; Lee, J.; Head-Gordon, M. *J. Chem. Theory Comput.* **2021**, *17*, 742–755.

(47) *Chem. Phys. Lett.* **2004**, *395*, 227–232.

(48) Levine, B. G.; Durden, A. S.; Esch, M. P.; Liang, F.; Shu, Y. *J. Chem. Phys.* **2021**, *154*, 090902.

(49) Fales, B. S.; Shu, Y.; Levine, B. G.; Hohenstein, E. G. *J. Chem. Phys.* **2017**, *147*, 094104.

(50) Chattopadhyay, S.; Chaudhuri, R. K.; Mahapatra, U. S. *J. Comput. Chem.* **2015**, *36*, 907–925.

(51) Shu, Y.; Hohenstein, E. G.; Levine, B. G. *J. Chem. Phys.* **2015**, *142*, 024102.

(52) Ronca, E.; Angeli, C.; Belpassi, L.; De Angelis, F.; Tarantelli, F.; Pastore, M. *J. Chem. Theory Comput.* **2014**, *10*, 4014–4024.

(53) Giesbertz, K. *Chem. Phys. Lett.* **2014**, *591*, 220–226.

(54) Ma, Y.; Ma, H. *J. Chem. Phys.* **2013**, *138*, 224105.

(55) Bouř, P. *Chem. Phys. Lett.* **2001**, *345*, 331–337.

(56) Mazziotti, D. A. *Phys. Rev. A* **2002**, *65*, 062511.

(57) Kohn, W.; Sham, L. J. *Phys. Rev.* **1965**, *140*, A1133–A1138.

(58) Hohenberg, P.; Kohn, W. *Phys. Rev.* **1964**, *136*, B864–B871.

(59) Perdew, J. P.; Burke, K.; Ernzerhof, M. *Phys. Rev. Lett.* **1997**, *78*, 1396–1396.

(60) Perdew, J. P.; Burke, K.; Ernzerhof, M. *Phys. Rev. Lett.* **1996**, *77*, 3865–3868.

(61) Becke, A. D. *Phys. Rev. A* **1988**, *38*, 3098–3100.

(62) Lee, C.; Yang, W.; Parr, R. G. *Phys. Rev. B* **1988**, *37*, 785–789.

(63) Miehlich, B.; Savin, A.; Stoll, H.; Preuss, H. *Chem. Phys. Lett.* **1989**, *157*, 200–206.

(64) Becke, A. D. *J. Chem. Phys.* **1993**, *98*, 5648–5652.

(65) Zhao, Y.; Truhlar, D. G. *Theor. Chem. Acc.* **2008**, *120*, 215–241.

(66) Chai, J.-D.; Head-Gordon, M. *Phys. Chem. Chem. Phys.* **2008**, *10*, 6615–6620.

(67) Yu, H. S.; He, X.; Li, S. L.; Truhlar, D. G. *Chem. Sci.* **2016**, *7*, 5032–5051.

(68) Mazziotti, D. A. *Phys. Rev. Lett.* **2012**, *108*, 263002.

(69) Mazziotti, D. A. *Phys. Rev. A* **1998**, *57*, 4219–4234.

(70) Mazziotti, D. A. *Int. J. Quantum Chem.* **1998**, *70*, 557–570.

(71) Mazziotti, D. A. *Phys. Rev. Lett.* **2006**, *97*, 143002.

(72) Mazziotti, D. A. *Phys. Rev. A* **2007**, *75*, 022505.

(73) DePrince, A. E.; Mazziotti, D. A. *J. Chem. Phys.* **2007**, *127*, 104104.

(74) Mazziotti, D. A. *Chem. Phys. Lett.* **1998**, *289*, 419–427.

(75) Sand, A. M.; Mazziotti, D. A. *J. Chem. Phys.* **2015**, *143*, 134110.

(76) Mazziotti, D. A. *Phys. Rev. A* **1999**, *60*, 4396–4408.

(77) Mazziotti, D. A. *J. Phys. Chem. A* **2008**, *112*, 13684–13690.

(78) Foley, J. J.; Rothman, A. E.; Mazziotti, D. A. *J. Chem. Phys.* **2009**, *130*, 184112.

(79) Gidofalvi, G.; Mazziotti, D. A. *Phys. Rev. A* **2009**, *80*, 022507.

(80) Boyn, J.-N.; Mazziotti, D. A. *J. Chem. Phys.* **2021**, *154*, 134103.

(81) RDMChem, Chicago, Illinois. **2019**.

(82) Maplesoft, a division of Waterloo Maple Inc., Waterloo, Ontario. **2019**.

(83) Hehre, W. J.; Ditchfield, R.; Pople, J. A. *J. Chem. Phys.* **1972**, *56*, 2257–2261.

(84) Abe, M. *Chem. Rev.* **2013**, *113*, 7011–7088.

(85) Scheschkewitz, D.; Amii, H.; Gornitzka, H.; Schoeller, W. W.; Bourissou, D.; Bertrand, G. *Science* **2002**, *295*, 1880–1881.

(86) Sun, Z.; Zeng, Z.; Wu, J. *Acc. Chem. Res.* **2014**, *47*, 2582–2591.

(87) Herzberg G.; Huber, K. *Springer Verlag* **1979**.

(88) Osmann, G.; Bunker, P.; Jensen, P.; Kraemer, W. *J. Mol. Spectrosc.* **1997**, *186*, 319–334.

(89) Gu, J.-P.; Hirsch, G.; Buenker, R.; Brumm, M.; Osmann, G.; Bunker, P.; Jensen, P. *J. Mol. Struct.* **2000**, *517-518*, 247–264.

(90) Berkowitz, J.; Cho, H. *J. Chem. Phys.* **1989**, *90*, 1–6.

(91) Berkowitz, J.; Greene, J. P.; Cho, H.; Ruščić, B. *J. Chem. Phys.* **1987**, *86*, 1235–1248.

(92) Dunning, T. H. *J. Chem. Phys.* **1989**, *90*, 1007–1023.

(93) Kendall, R. A.; Dunning, T. H.; Harrison, R. J. *J. Chem. Phys.* **1992**, *96*, 6796–6806.

(94) Boyn, J.-N.; Mazziotti, D. A. *J. Chem. Phys.* **2021**, *154*, 134103.

(95) Shee, J.; Arthur, E. J.; Zhang, S.; Reichman, D. R.; Friesner, R. A. *J. Chem. Theory Comput.* **2019**, *15*, 4924–4932.

(96) Mardirossian, N.; Head-Gordon, M. *Mol. Phys.* **2017**, *115*, 2315–2372.

(97) Bao, J. L.; Sand, A.; Gagliardi, L.; Truhlar, D. G. *J. Chem. Theory Comput* **2016**, *12*, 4274–4283.

(98) Peng, D.; Hu, X.; Devarajan, D.; Ess, D. H.; Johnson, E. R.; Yang, W. *J. Chem. Phys.* **2012**, *137*, 114112.

(99) Yang, Y.; Peng, D.; Davidson, E. R.; Yang, W. *J. Phys. Chem. A* **2015**, *119*, 4923–4932.

(100) Mazziotti, D. A. *J. Phys. Chem. A* **2008**, *112*, 13684–13690.

(101) Hariharan, P. C.; Pople, J. A. *Theor. Chem. Acc.* **1973**, *28*, 213–222.

(102) Lutz, J. J.; Piecuch, P. *J. Chem. Phys.* **2008**, *128*, 154116.

(103) Berner, R.; Lüchow, A. *J. Phys. Chem. A* **2010**, *114*, 13222–13227.

CHAPTER 6

AN ACSE BASED QUANTUM-CLASSICAL HYBRID ALGORITHM

Reprinted with permission from J.-N. Boyn, A. O. Lykhin, S. E. Smart, L. Gagliardi, and D.A. Mazziotti, *Journal of Chemical Physics* **155**, 244106 (2021). Copyright 2021 American Institute of Physics.

6.1 Introduction

Since the advent of density functional theory (DFT) [1], electronic structure theory has assumed an evermore important role in chemical research, ranging from helping researchers rationalize experiment to guiding design in areas extending from molecular synthesis to new materials. While research over the last decades has made incredible progress in developing accurate and black-box methods available for use by both theoreticians and experimentalists, the accurate, as well as computationally tractable treatment of correlated quantum systems continues to pose a major challenge [2]. Quantum simulation of molecular systems offers a novel approach to the problem where a strongly correlated wave function can potentially be prepared and measured at non-exponential cost [3].

In this article we present a novel hybrid quantum-classical algorithm that treats the exponentially scaling part of the calculation—the static (multireference) correlation—on the quantum computer and the non-exponentially scaling part—the dynamic correlation—on the classical computer. While such methods that treat the multireference and dynamic correlation[4, 5] in two separate calculations are common in classical electronic structure theory [2, 6–11], their adaptation to the quantum computer is non-trivial because most techniques require the multireference-correlation part of the calculation to generate a wave function. The measurement of such a wave function on the quantum computer, however, scales exponentially with molecular size [3, 12].

In recent years a variety of hybrid quantum-classical algorithms have been proposed to overcome this hurdle with the inclusion of dynamic correlation in a “perturb-then-diagonalize” fashion, where the dynamic correlation is resolved before the quantum computations and thus no wave function is required for post-processing [2, 13, 14]. Proposals include integration with DFT[3] or the use of classical embedding algorithms, which tackle only a subset of the problem on the quantum computer in combination with dynamical mean-field theory (DMFT) embedding approaches[15–17]. Additionally, Rubin proposed a density matrix embedding theory (DMET) analogue to the DMFT procedure[18], and Yamazaki et al. proposed further implementations using fragment molecular orbital (FMO) and divide-and-conquer (DC) approaches[19]. Other techniques include the down-folding of active-virtual dynamic correlation using unitary coupled-cluster approaches and a variational quantum eigensolver (VQE)[20–22], or a classically constructed transcorrelated Hamiltonian used in combination with a unitary coupled-cluster ansatz[23]. Post quantum computation approaches to the inclusion of dynamic correlation have so far proven more challenging, owing to the dependence of many commonplace methods such as multireference perturbation theory on the wave function or higher order 3- or 4-reduced density matrices (RDMs). One example is the virtual quantum subspace expansion, which perturbs around the singly occupied virtual orbital occupations and can be solved directly from the active space 2-RDM[24, 25].

In the approach presented here, as in most molecular simulations, we avoid the exponential scaling by performing a tomography of only the two-electron reduced density matrix (2-RDM)—more specifically, only the statically correlated part of the 2-RDM [26]. However, in contrast to other methods, we here use the statically correlated 2-RDM as a kernel in two polynomially scaling classical correlation methods to generate a correlated 2-RDM, spanning all of the electrons and orbitals in the calculation, in a “diagonalize-then-perturb” fashion. Importantly, neither method requires computation of the N-electron wave function and the computed, correlated 2-RDM recovers the all-electron correlation energy of a molecule, thereby enabling larger basis sets and realistic comparisons with experimental enthalpies of formation. Although the algorithm is completely general for any 2-RDM-like methods, we test it here with two classical 2-RDM based methods: (*i*) the anti-Hermitian contracted Schrödinger equation (ACSE) theory [27] and (*ii*) multiconfiguration pair-density functional theory (MC-PDFT) [28]. Additionally, unlike the virtual quantum subspace expansion[24, 25], the present approach in combination with the ACSE is size extensive.

We apply the algorithm to resolve the relative energies of the three benzyne isomers to experimental accuracy. The quantum-simulation on IBM superconducting quantum computers is performed with the recently developed quantum ACSE (QACSE), an algorithm that belongs to the family of contracted quantum eigensolvers (CQE) in which a contraction (projection) of the Schrödinger equation is solved for the 2-RDM. While a quantum computer can in theory produce very high quality results at a lower cost than classical methods, NISQ devices exhibit significant noise in their measured quantities such as the 2-RDMs. By using statically correlated 2-RDMs obtained from the QACSE on the IBM quantum computers, we test the ability of the ACSE and MC-PDFT methods to resolve the total energies in the presence of realistic noise profiles of NISQ computers. Importantly, the resulting quantum-classical hybrid algorithm with either ACSE or MC-PDFT for the classical part accurately captures the energies and properties of the benzynes, including the experimental relative energy of the biradical *para*-benzyne.

6.2 Theory

Before we present and discuss results in Section 6.3, we briefly describe the quantum and classical parts of the hybrid algorithm in Sections 6.2.1 and 6.2.3, respectively, which are summarized in Fig. 1.

6.2.1 Contracted Quantum Eigensolver

The active-space 2-RDMs were obtained using a recently developed contracted quantum eigensolver (CQE) algorithm, known as the quantum-ACSE (QACSE) method [26] (details of these quantum calculations are the focus of a separate work [29]). Unlike the variational quantum eigensolvers, the CQE minimizes the residual of a contraction (projection) of the Schrödinger equation onto a few-electron space. In the QACSE method we iteratively define an ACSE-ansatz wave function

$$|\Psi_{n+1}\rangle = e^{\varepsilon A_n}|\Psi_n\rangle \,, \tag{6.1}$$

in which

$$\hat{A}_n = \sum_{ijkl} {}^2A^n_{ij;kl}\hat{a}^\dagger_i\hat{a}^\dagger_j\hat{a}_l\hat{a}_k \tag{6.2}$$

are evaluated as the residuals of the ACSE

$${}^2A^n_{ij;kl} = \langle\Psi_n|\,[\hat{a}^\dagger_i\hat{a}^\dagger_j\hat{a}_l\hat{a}_k,\hat{H}]\,|\Psi_n\rangle \,. \tag{6.3}$$

These residuals are anti-Hermitian and hence, can be readily implemented as unitary operators on a quantum computer. By construction this wave function converges to a solution of the ACSE, which results in the residual vanishing. The two-body nature of the wave function is intrinsically linked to the two-body nature of the ACSE and its residual. The active-space 2-RDM is measured by tomography on quantum computer without explicit construction of the wave function on the classical computer.

Although the QACSE algorithm is in principle exact, in the current era of quantum computing, where only NISQ devices are feasible, several factors must be considered to maximally utilize the present quantum resources. Notably, we truncate elements of ${}^2A$ to reduce the circuit depth. We also use error mitigation which extends the set of 2-RDMs beyond noisy limitations, and then project the 2-RDM onto the 2-positive set of N-representability conditions to ensure our 2-RDM is a good representation of a physical system [30–33]. Obtained RDMs from a quantum computer can have substantial errors depending on the noise characteristics of the quantum device, the system size, the quantum algorithm used, and the amount of correlation energy (common errors range from 0.001 to 0.1 hartrees for small systems currently being studied). More details regarding these calculations can be found in the Methods section in Ref. [29].

6.2.2 Quantum Computation

The 2-RDMs used in the present work were obtained by using quantum devices (ibmq_armonk for the 1-qubit results, and ibmq_bogota and ibmq_santiago, which are 5-qubit devices, for the 3- and 4-qubit results) through the IBM Quantum Experience [34]. We use the PYTHON 3 package QISKIT (v 0.15.0 - v 0.17.0) [35] to interface with the device. The calculations themselves are multifaceted, with significant error mitigation also being required, and we include a brief overview below.

First, we transform the Hamiltonian to the Pauli basis through the Jordan-Wigner transformation, and then we analyze the set of Hamiltonian operators for Pauli type symmetries. These can be related to known quantum chemical (i.e., spin, point-group, etc.) symmetries [36] but in our cases these should be interpreted simply as symmetries of the transformed Pauli basis. Having s symmetries, we can obtain a $2r-s$ qubit representation. For the [4,4] case, we have 8 spin orbitals, mapping to 8 qubits. The 4-qubit case represents 4 symmetries which are tapered from the Hamiltonian. The para-isomer has an exact 3-qubit representation (5 symmetries), whereas meta- and ortho- have errors in the symmetry representations of 0.61 and 0.92 mhartrees, respectively. Note that these errors are significantly less than the external noise related errors on the relevant quantum devices.

Using the residual ${}^2A$ matrix generated from the classical ACSE, we map these elements onto the operator basis and create our test ansatz. We use a first order trotterization to express the $\exp({}^2A)$ operator, which becomes a product of exponential Pauli strings (tensors of Pauli gates).

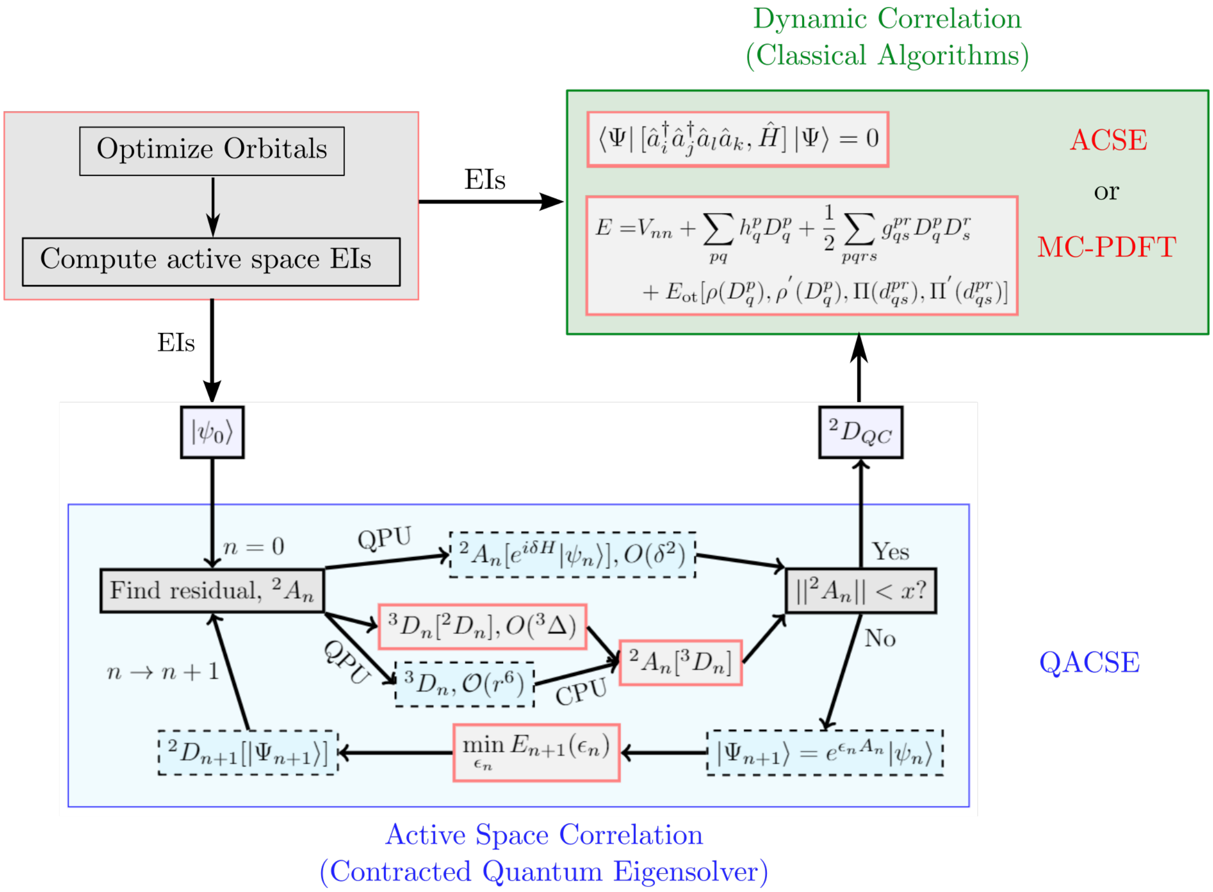

Figure 6.1: Schematic description of the hybrid quantum-classical algorithm employed in this work. Red boxes denote calculations performed on a classical computer while those in blue boxes represent quantum computations. The QACSE algorithm itself can be considered as a hybrid algorithm which possesses corresponding advantages and disadvantages depending on the particular elements which are utilized. For instance, the residual ^2A_n classically requires the 3-RDM, which can be obtained from a 2-RDM with an approximate cumulant $^3\Delta$, or on the quantum computer with $\mathscr{O}(r^6)$ scaling tomography of the 3-RDM. While an $\mathscr{O}(r^4)$ method can be performed solely on the quantum computer with a truncated error in δ, it requires a longer gate sequence which may not be preferable on near-term devices. Given an operator ^2A, we can measure $^2D_{n+1}$ through the preparation of the wave function $|\psi_{n+1}\rangle$, and this process is repeated iteratively until the final 2-RDM $^2D_{\mathrm{QC}}$ is obtained which is used to seed the classical ACSE or MC-PDFT algorithms.

The exponential of an anti-Hermitian Pauli operator can be expressed as sequence of rotated controlled Z gates where the controlled qubits act on a single qubit. Because the pool of operators is quite limited, we simplified likely potential two-body operators for these bases and allowed the ACSE algorithm to choose operators appropriately. Once the gate sequence is prepared, we measure the 2-RDM. We utilized a state preparation technique to counteract readout errors, and then we filtered the diagonal entries so that the trace of the 2-RDM is normalized to the number of electrons. To counter the accumulating effects of noise which occur with an iterative ansatz, we used a limit-preserving correction, which adds a correction matrix to the 2-RDM so that a new step with zero input parameters will give the same energy as the previous step. This attempts to mitigate the increase in energy caused by adding more gates to an ansatz which commonly occurs. Finally, as some of the previous steps can introduce N-representability violations, we used a purification scheme so that the obtained 2-RDM satisfies a set of approximate N-representability conditions. We iterate this procedure until convergence is met or we are unable to decrease the energy of the state. More details regarding these calculations and error mitigation schemes are found in Ref. [29]. For all of these calculations, the error in using an approximate ${}^2A$ can vary depending on the ansatz and the optimization of the step size used.

6.2.3 ACSE and MC-PDFT

To obtain the total electronic energies, we use the classical 2-RDM methods, ACSE and MC-PDFT seeded with the CAS 2-RDM evaluated on the quantum device. On the classical computer the ACSE can be solved by evolving a system of differential equations [37, 38]. Because the ACSE depends upon not only the 2-RDM but also the 3-RDM, the ACSE is indeterminate without a reconstruction of the 3-RDM from the 2-RDM. While in the quantum algorithm this reconstruction occurs implicitly and potentially exactly through the state preparation on the quantum device, in the classical algorithm the 3-RDM is approximately reconstructed from the 2-RDM by its cumulant expansion [39–41]. The classical implementation of the ACSE resolves dynamic correlation with comparable accuracy to CCSD(T) [40], but it may be seeded with a correlated guess 2-RDM from a complete active space (CAS) calculation to resolve the total correlation energy even in the presence of non-negligible static electron correlation [37, 38].

MC-PDFT in turn is an extension of DFT to strongly correlated systems. Seeded with a strongly correlated 2-RDM obtained from a CAS calculation, kinetic and classical Coulomb energies are evaluated and the rest of the energy is non-iteratively computed as a functional of the total electron density, the on-top pair density, and their spatial derivatives using one of the various available functionals:

$$\begin{aligned} E_{\text{MC-PDFT}} =& V_{nn} + \sum_{pq} h^p_q D^p_q + \frac{1}{2} \sum_{pqrs} g^{pr}_{qs} D^p_q D^r_s \\ & + E_{\text{ot}}[\rho(D^p_q), \rho^{'}(D^p_q), \Pi(d^{pr}_{qs}), \Pi^{'}(d^{pr}_{qs})] \, . \end{aligned} \tag{6.4}$$

While the total electron density, ρ, defines the probability of locating a single electron at the given point of space, the on-top pair density, Π, describes the probability of observing two electrons at the same space point. The dependence of the functional upon these densities, conveniently evaluated from 1,2-RDMs, resolves the symmetry dilemma [42] and ensures the correct asymptotic behavior of the total energy at the dissociation limit. In this article we survey translated [28] (tPBE and tBLYP), (ii) fully-translated [43] (ftPBE), and (iii) hybrid [44] (tPBE0) on-top functionals. The ACSE calculations were performed with the Maple Quantum Chemistry Package [45, 46] and MC-PDFT calculations were performed in the PySCF package [47] augmented with the *mrh* addon [48] that enables MC-PDFT features. Note that translation of Kohn-Sham density functionals into the on-top density functionals does not alter the functional form but redefines the spin-densities and their gradients in terms of the total electron density and the on-top pair density.

The quantum ACSE (QACSE) method [26, 29] relies upon the capacity of a quantum computer to efficiently simulate quantum states in potentially two regards. First, the exponential of the $\hat{A}$ operator can be implemented through methods of quantum computation for implementing exponential operators at polynomial cost (see [26, 29]). Then, by performing reduced state tomography, we can measure the 2-RDM of a prepared quantum state at any given iteration. Secondly, we can use an auxiliary state involving the $\exp(i\delta H)$ operator, to find a solution to the ACSE. If this step cannot be carried out accurately on the quantum computer (through noise or limited quantum resources), then we can use the classical solution of the ACSE, which involves a reconstructed 3-RDM. The tomography naively requires $O(r^4)$ measurements, although this can be reduced to $O(r^2)$ through a variety of techniques [49, 50].

Second, elements of the ${}^2A$ matrix can be obtained efficiently through the preparation of an auxiliary state involving a single propagator step. Tomography of the ${}^2A$ matrix scales with the order of the $\hat{A}$ operator, which generally will be $O(r^4)$. In both cases, the use of a quantum computer allows us to extract information directly from the quantum state, circumventing the cost and errors which come from reconstruction [26, 29]. The algorithm iterates between the preparation of the 2-RDM and the A matrix until convergence, which is shown in Fig. 1.

6.3 Results & Discussion

As a benchmarking case of correlated organic molecules, we consider the three structural isomers of benzyne [51–53]. These are obtained by the elimination of two substituents on different positions of the benzene ring, giving rise to ortho-, meta- and para- isomers. While all benzyne isomers are usually drawn as biradical structures, the degree to which they display multi-reference character varies according to the spatial separation between the radical electrons' location on the benzene ring. Figure 6.2 displays the frontier molecular orbitals for each of the three structural benzyne isomers, showing the clear variation in bonding between the ortho, meta, and para geometries.

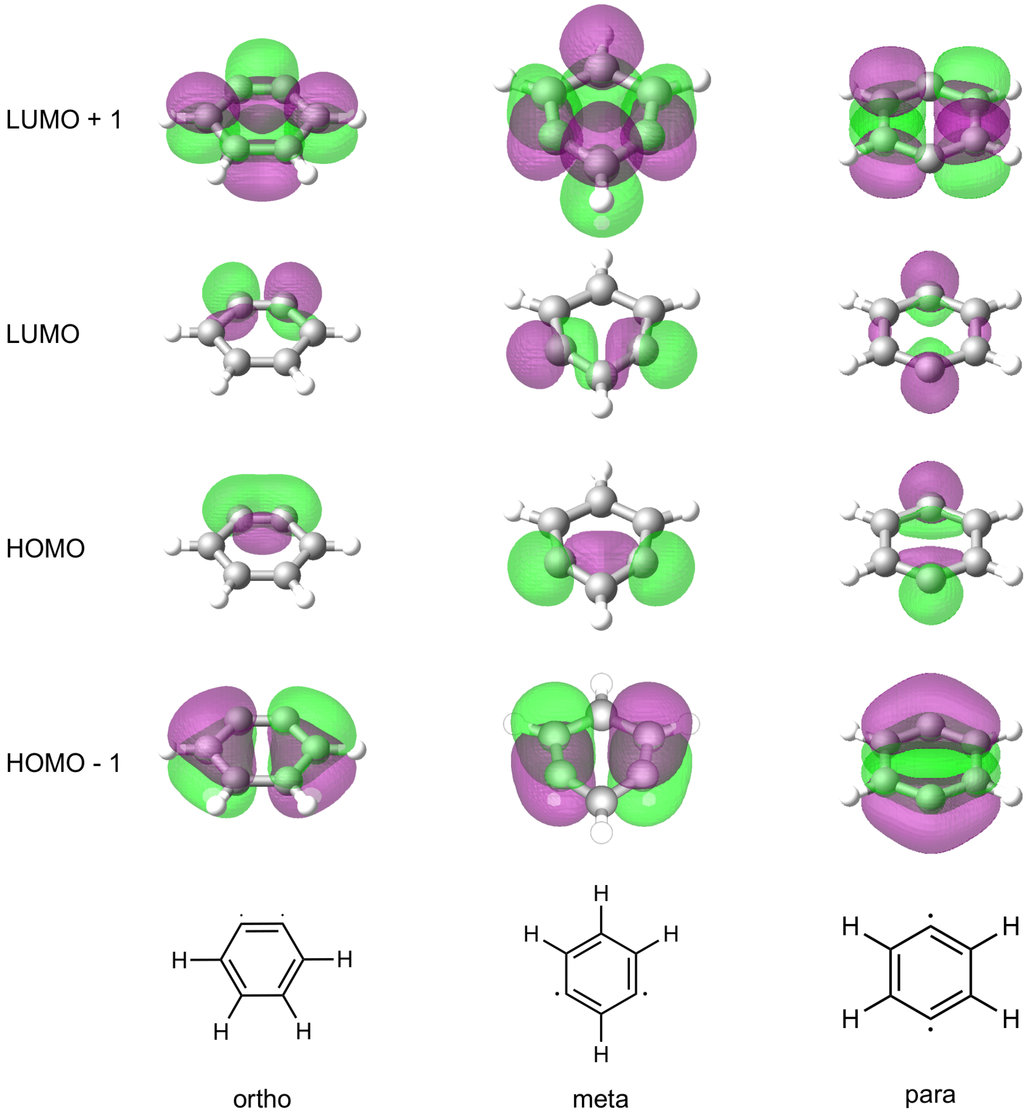

Figure 6.2: HOMO and LUMO for the three structural benzyne isomers as obtained from classical CASSCF calculations in a [4,4] active space with a cc-pVDZ basis set. The biradical character displayed in the frontier MOs increases as the orbital separation between the radical carbon atoms increases. While spatial proximity allows formation of essentially bonding and anti-bonding orbitals in ortho- and meta-benzyne, yielding near-closed-shell character, the larger distance in the para-isomer yields an electronic structure with strong biradical character.

Spatial proximity between the two radical carbon atoms on the benzene ring allows substantial bond formation in the ortho and meta cases, leading to near-closed-shell character, while the para geometry, characterized by large spatial separation between the radical carbons, allows for no overlap between the carbon atomic orbitals, resulting in strong biradical character. The stability of the three isomers correlates with the proximity of the radical carbon atoms, with experimental measurements yielding energies of 15.3 ± 4.31 kcal/mol and 31.2 ± 4.17 kcal/mol, for the meta and para isomers, relative to the ortho structure, respectively [53].

6.3.1 Relative Energies

While the complete active space self-consistent field (CASSCF) and configuration interaction (CASCI) methods capture most of the static correlation, they lack a fraction of dynamic correlation resulting in residual errors in the energies of the ortho-, meta-, and para- isomers. Taking the ortho isomer as a reference, classical CASSCF calculations with the correlation-consistent polarized double-zeta (cc-pVDZ) basis [54] yield relative energies of 15.2 kcal/mol (meta) and 23.5 kcal/mol (para) in a [2,2] active space, which increase to 16.5 kcal/mol (meta) and 29.5 kcal/mol (para) upon moving to a [4,4] active space. We use the $[N_e, N_o]$ active space notation, where N_e is the number of active electrons and N_o denotes the number of spatial orbitals in the active space. The active space MOs are those shown in Figure 6.2 and both MC-PDFT and ACSE calculations do not profit from the use of larger CASSCF active space seeds as the strong correlation in the benzyne systems is contained in two molecular orbitals. Data for larger [6,6] and [8,8] classically seeded calculations are shown in Table 6.1. Using electron integrals obtained from the classical CASSCF calculations, the QACSE has been shown to resolve the relative energies (despite errors in the absolute energies on the order of a few kcal/mol) of the benzyne isomers with comparable accuracy to classical CASSCF calculations, yielding gaps of 13.8 kcal/mol (meta) and 21.7 kcal/mol (para) in the [2,2] active space performed on a 1 qubit device and 17.9 kcal/mol (meta),

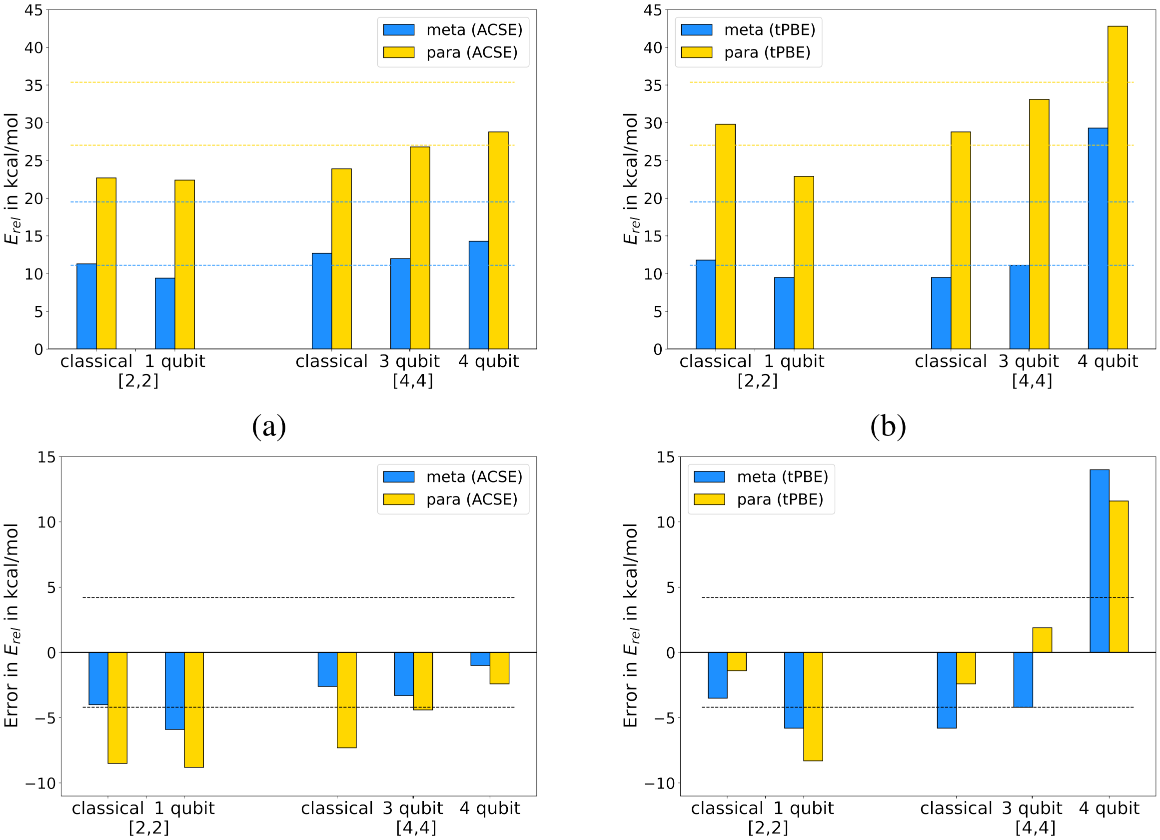

(a) (b)

(c) (d)

Figure 6.3: Top row: Relative energies of the meta and para benzynes calculated with ACSE (a) and MC-PDFT (b). Bottom row: Deviations of the relative energies from the corresponding experimental relative energies of the meta and para benzynes calculated with ACSE (c) and MC-PDFT (d). The ortho isomer serves as the reference to determine energies of meta and para benzynes. On the x-axis, ”classical” refers to the solutions obtained with a CASSCF 2-RDM evaluated on a classical computer, and ”1 qubit”, ”3 qubit”, and ”4 qubit” labels indicate ACSE or MC-PDFT (tPBE functional) calculations seeded with a QACSE 2-RDM measured with 1 qubit, 3 qubits, or 4 qubits, respectively. The active space $[N_e, N_o]$ refers to N_e active electrons distributed in N_o active molecular orbitals. The dashed lines represent uncertainties of the experimental relative energies at the 95% confidence level.

31.0 kcal/mol (para) and 17.6 kcal/mol (meta), 27.8 kcal/mol (para) in a [4,4] active space using 3 and 4 qubit devices, respectively. These results are thoroughly discussed in reference [29] and data are shown in Table 6.2. Having demonstrated the ability to perform sufficiently accurate CAS calculations on a NISQ device and yielding accurate 2-RDMs with the QACSE method, we take the next step in bringing quantum computing to the realm of applicable quantum chemical computation by uniting the QACSE with the 2-RDM dependent MC-PDFT and ACSE methods to recover all electron correlation in a hybrid quantum-classical approach.

		ortho	meta		para	
		E	E	Δ_E	E	Δ_E
ACSE	[2,2]	-230.2683317	-230.2504224	11.3	-230.2323066	22.7
	[4,4]	-230.2682187	-230.2480428	12.7	-230.2302862	23.9
	[6,6]	-230.265173	-230.24655	11.7	-230.2328649	20.3
	[8,8]	-230.2647044	-230.2426574	13.8	-230.2319533	20.6
tPBE	[2,2]	-230.586	-230.567	11.8	-230.539	29.8
	[4,4]	-230.583	-230.568	9.5	-230.537	28.8
	[6,6]	-230.5792657	-230.5630388	10.2	-230.5340164	28.4
	[8,8]	-230.5711622	-230.5557382	9.7	-230.52530	28.8

Table 6.1: Data for ACSE and tPBE calculations fed with classical CASSCF calculations with varying active space sizes.

The 2-RDMs obtained from the QACSE calculations are used to seed the classical ACSE and various MC-PDFT functionals to calculate the total electronic energy of the three different isomers. The meta-ortho and para-ortho energy gaps, obtained with the ACSE and MC-PDFT (tPBE functional) from CASSCF [2,2] and [4,4] calculations on a classical computer (CASSCF), as well as a quantum computer (QACSE CASSCF) with 1 qubit, 3 qubits, or 4 qubits, are displayed in Figure 6.3 (a) and Figure 6.3 (b), while Figure 6.3 (c) and Figure 6.3 (d) show the respective errors in relative energies as compared to experiment. Using the minimal [2,2] active space required to resolve the biradical character, both the ACSE and MC-PDFT seeded with the QACSE 2-RDMs deliver results that yield a lower bound to the gap obtained using the classical CASSCF 2-RDM. Deviations from the classically seeded references are less than 2 kcal/mol in the case of the ACSE and less than 7 kcal/mol for tPBE, yielding errors slightly outside the bounds of the experimental confidence intervals.

A move to the larger [4,4] active space reduces the error of the relative energies in both the underlying classical CASSCF reference and QACSE calculations. Utilizing different symmetry adaptations on the quantum device, the [4,4] QACSE calculations were carried out using either 3 qubits or 4 qubits, with the 4 qubits, producing noisier results. In the post-CASSCF ACSE calculation favorable error cancellation leads to increases in the meta-ortho and para-ortho gaps and correspondingly reduced errors as compared to experiment. The meta-ortho gap is reproduced within the experimental confidence intervals yielding gaps of 12.0 and 14.3 kcal/mol for 3 and 4 qubit 2-RDMs, respectively, while the para-ortho gap of 26.8 kcal/mo in the 3 qubit case lies barely 0.2 kcal/mol outside the experimental interval and is improved to 28.8 kcal/mol with the use of a 4 qubit 2-RDM. It is noteworthy that the meta-ortho gap is captured with significantly greater accuracy by the ACSE than the para-ortho gap.

The trend observed in the ACSE data are reversed in the tPBE calculations and in the classically seeded tPBE calculations the magnitude of relative energies is reduced upon moving from a [2,2] to a [4,4] active space, and the calculated meta-ortho gap lies slightly outside the experimental confidence interval. However, using the 3 qubit QACSE 2-RDM we again observe an increase in the calculated relative energies, which while minor yields relative energies of 11.1 kcal/mol (meta-ortho) and 33.1 kcal/mol (para-ortho) which lie within the experimental bounds of errors. Using the 2-RDM obtained from a 4 qubit NISQ device calculation, the MC-PDFT energies are more prone to errors propagated from noisy 2-RDMs, resulting in significant overestimation of meta-ortho and para-ortho gaps. The sign change in the MC-PDFT relative energies as we move from 3 qubits to 4 qubits occurs because the noise of the 4-qubit QACSE 2-RDM leads to an energy of the ortho isomer that is too low, which overstabilizes that isomer relative to the meta and para isomers.

Absolute energies are discussed in more detail in Section 6.3.2.

		[2,2]		[4,4]		
		classical	1 qubit	classical	3 qubit	4 qubit
EXP	meta			15.3 ± 4.31		
	para			31.2 ± 4.17		
CAS	meta	15.2	13.8	16.5	17.9	17.6
	para	23.5	21.7	29.5	31.0	27.8
ACSE	meta	11.3	9.4	12.7	12.0	14.3
	para	22.7	22.4	23.9	26.8	28.8
tPBE	meta	11.8	9.5	9.5	11.1	30.1
	para	29.8	22.9	28.8	33.1	42.8
ftPBE	meta	12.5	10.5	10.0	10.9	27.8
	para	29.2	23.0	27.7	31.5	40.2
trevPBE	meta	11.4	9.1	9.0	10.6	29.1
	para	29.5	22.6	28.4	32.8	42.6
tBLYP	meta	13.2	10.8	11.0	12.7	31.9
	para	29.6	22.6	28.8	33.2	43.1
tPBE0	meta	12.7	8.4	11.2	18.2	46.6
	para	28.2	16.3	28.9	35.9	53.8

Table 6.2: Energies of the meta and para isomers of benzyne relative to the ortho isomer. Column label ”classical” indicates results obtained using a classical algorithm, in the case of CASSCF calculations, and calculations seeded with a classical CASSCF 2-RDM, in the case of ACSE and MC-PDFT results. ”1 qubit”, ”2 qubit”, and ”3 qubit” indicate the numbers of qubits used for the QACSE calculation. All calculations were performed using a cc-pVDZ basis.

In addition to tPBE we also survey the ftPBE, trevPBE, tBLYP and tPBE0 functionals. The complete data for the meta-ortho and para-ortho energy gaps for all methods are shown in Table 6.2. The choice of the on-top functional does not significantly affect the predicted relative energies of the three benzyne diradicals in MC-PDFT. The energies obtained with the fully-translated functional ftPBE yield the most accurate results; however, they present only slight improvements upon the tPBE, trevPBE and tBLYP results. The hybrid tPBE0 on-top functional is an outlier in the set of surveyed functionals, and it results in large deviations from the experimental energies, particularly in the para-ortho 4-qubit calculations.

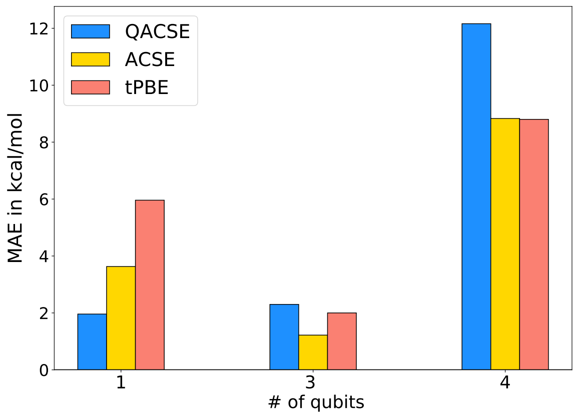

Figure 6.4: MAEs in kcal/mol of the quantum solution with respect to the classical reference over the three isomers for the QACSE CAS, as well as the QACSE 2-RDM seeded ACSE and tPBE functional MC-PDFT calculations. 1 qubit data uses a [2,2] active space while the 3 and 4 qubit data was obtained with a [4,4] active space.

Our data show that efficient error-mitigation in the QACSE algorithm allows us to obtain strongly correlated 2-RDMs on a NISQ device, sufficiently purified so that they may be used to seed ACSE and MC-PDFT calculations to obtain all-electron correlation with near-classical accuracy. While noise increases with the number of qubits used in the quantum computation, in the case of benzyne both the ACSE, as well as MC-PDFT seeded with the NISQ derived 2-RDM allow us to resolve an experimentally verifiable quantity, the relative energies of the three structural isomers, with an accuracy that lies within the bounds of the experimental confidence intervals for a [4,4] CAS calculation implemented with a 3 qubit mapping.

6.3.2 Absolute Energies

To further analyze the impact of the use of NISQ derived QACSE 2-RDMs to seed ACSE and MC-PDFT calculations in a quantum-classical hybrid implementation, we compare the obtained absolute energies to those yielded with a CASSCF seed. Figure 6.4 shows the mean absolute deviations, defined as $MAE = (\sum_{m,o,p} E_{\mathrm{q}} - E_{\mathrm{c}})/3$, where $\sum_{m,o,p}$ runs over the three isomers, E_q indicates the quantum calculation's energy, and E_c indicates the energy derived from the classical

			error in kcal/mol		
			QACSE	ACSE	tPBE
[2,2]	1Q	ortho	3.03	4.39	8.99
		meta	1.64	2.46	6.71
		para	1.21	4.04	2.18
[4,4]	3Q	ortho	1.31	0.08	-3.30
		meta	2.72	-0.62	-1.65
		para	2.83	2.96	1.08
	4Q	ortho	12.36	6.63	-7.52
		meta	13.45	8.25	12.32
		para	10.67	11.59	6.57

Table 6.3: Deviations in kcal/mol from the classical, or classically seeded calculation, $\Delta E = E_q - E_c$, where E_q denotes the QACSE CASCI energy, or the ACSE or tPBE energy when seeded with the QACSE 2-RDM, and Ec denotes the classical CASSCF energy, or the ACSE or tPBE energy obtained with a CASSCF 2-RDM.

reference calculation, for the QACSE, the QACSE/ACSE and QACSE/tPBE calculations of the total electronic energy for the three benzyne isomers. The QACSE calculation yields energies that in these cases are above those from the classical CASCI calculation in the given molecular orbital basis, and as expected, the magnitude of the deviation increases with increasing qubit count and correspondingly greater noise in the quantum device measurements. The deviations for the absolute energies of the individual isomers can be found in Table 6.3.

The same behavior is observed in the QACSE/ACSE calculations, which when seeded with quantum computed 2-RDM yield energies above those from the QACSE/ACSE calculations seeded with classical CASSCF for all but the 3Q meta-benzyne case. In the [2,2] case, the error from the QACSE with an MAE of 1.96 kcal/mol persists in the ACSE solution with its MAE of 2.29 kcal/mol. In contrast, a reduction in errors is observed in the [4,4] calculations. Here, while the error obtained by the QACSE/ACSE calculation for the para isomer remains near-identical to that of the underlying CAS calculation, we yield significantly reduced errors in the ortho and meta isomers. The MAE of 1.22 kcal/mol presents a notable reduction compared to the underlying QACSE which displayed a MAE of 3.41 kcal/mol. While the noisier 4 qubit calculation produces larger deviations from the classical calculations, the errors in the QACSE again do not propagate through to the post-CI ACSE calculation and instead the errors in the underlying QACSE calculation are reduced significantly by ΔMAE = 3.33 kcal/mol in the post-CI result.

Similar trends are observed using MC-PDFT functionals. Here tPBE yields increased errors over the CAS calculation alone when seeded with the [2,2] QACSE 2-RDM, while reduced errors compared to the CAS calculation alone are obtained in the two studied [4,4] settings, with reductions in MAE of 0.3 kcal/mol and 3.36 kcal/mol in the 3 and 4 qubit cases, respectively. Note that in MC-PDFT errors are lowest in the meta and para isomers, while use of the QACSE solution leads to a large negative deviation from the CASSCF/MC-PDFT solution in the ortho case, where a lower bound to the classical solution is obtained. This is observed in both the 3 qubit and 4 qubit [4,4] calculations, but not in the [2,2] 2 qubit case.

6.3.3 Energy Decomposition

Decomposition of the total electronic energy into its 1- and 2-electron components provides further details about the nature of errors introduced via the use of QACSE 2-RDMs obtained on a NISQ device. Figure 6.5 displays the deviations of the 1-electron energy, ΔE_1, 2-electron energy, ΔE_2, and the total energy, ΔE, for the QACSE and QACSE/ACSE calculations. We also consider the QACSE/tPBE results, in which case the total energy may be decomposed into the deviations of the 1-electron, classical coulomb, ΔE_C and on-top (ΔE_{ot}) energies.

The QACSE calculations generally show small deviations for the ortho and para isomers across the 1, 3 and 4 qubit calculations, and relatively large deviations for the meta isomers. While the errors of the individual 1- and 2-electron components are an order of magnitude larger in the meta isomer, the negative ΔE_1 and the positive ΔE_2 compensate each other to yield an overall error in

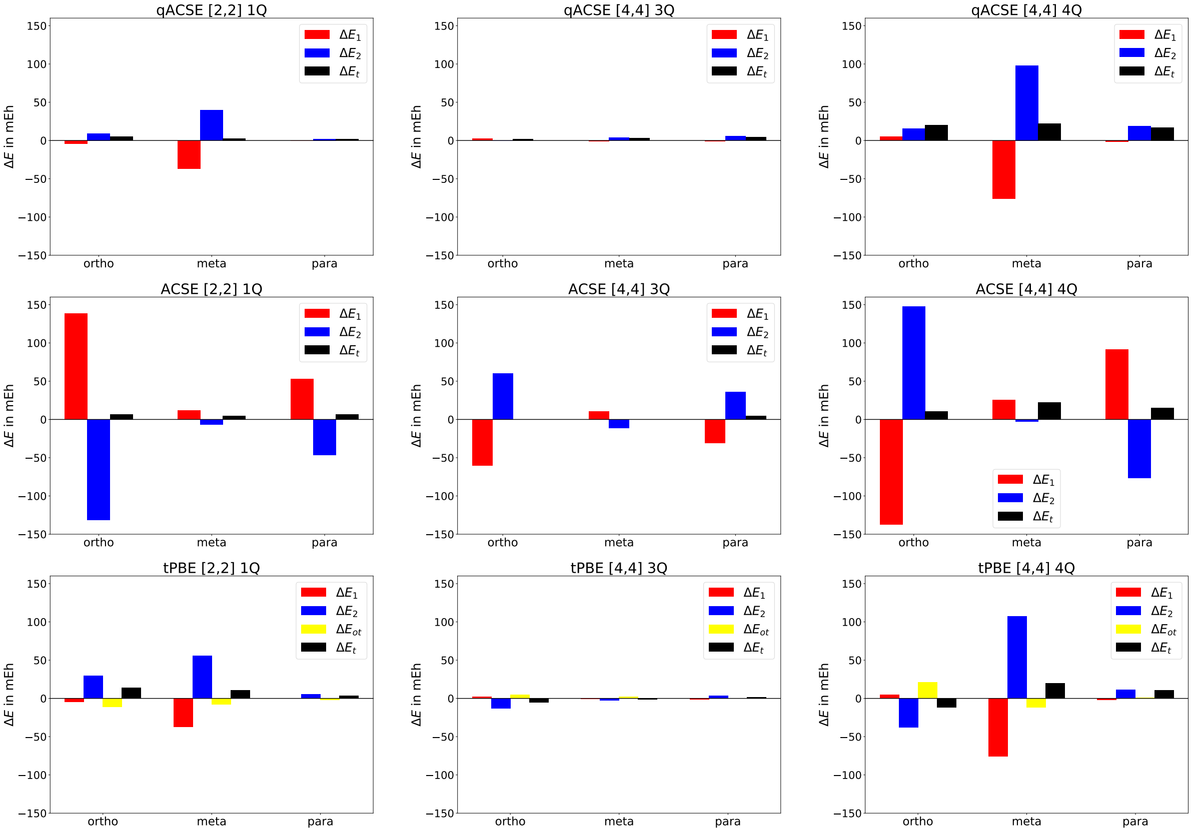

Figure 6.5: Errors in QACSE (top row), ACSE (middle row), and MC-PDFT (lower row) energies obtained with 2-RDMs measured on the quantum computer (mEh). The classical CASSCF are chosen as the reference for the QACSE calculation, and calculations seeded with CASSCF 2-RDMs are the reference for ACSE and MC-PDFT energies. The overall error in the QACSE and ACSE energies ($\Delta E_{\mathrm{QACSE}}$ and ΔE_{ACSE})) is due to deviations in the one-body and two-body terms (ΔE_1 and ΔE_2). The error in MC-PDFT ($\Delta E_{\mathrm{MC\text{-}PDFT}}$) is due to the errors in one-body (ΔE_1), classical Coulomb (ΔE_C), and on-top (ΔE_{ot}) terms.

line with the other isomers.

As MC-PDFT does not involve reoptimization of the 2-RDM, the deviations of the energetic terms of the functional closely mirror those of the underlying QACSE calculation, with deviations in ortho- and para- being small compared to the meta isomer. In the MC-PDFT calculation the two-electron energy is further decomposed into classical Coulomb and on-top correlation components, and correspondingly ΔE_2 in QACSE is mirrored by the sum of ΔE_C and ΔE_{ot}, where ΔE_C tends to mirror the sign of ΔE_2, while it is slightly compensated by a ΔE_{ot} of opposite sign and smaller magnitude. As discussed in the previous section, the only notable deviation from QACSE behavior appears in the [4,4] calculations of the ortho isomer, where we observe a negative deviation from the classical solution, as opposed to the positive one observed in the QACSE. Energy decomposition shows that this is the result of a significant, negative ΔE_C, -12.96 mEh in the 3 qubit case and -38.29 mEh in the 4 qubit calculation, which is not fully compensated by ΔE_{ot}.

The 1- and 2- electron terms in the ACSE calculation behave noticeably different from those of the QACSE and MC-PDFT calculations. The QACSE/ACSE calculations show by far the largest deviations from the classical solution, with the magnitudes of the individual components reaching up to 150 mEh. Additionally, there is a reversal in the previously observed trends and those calculations seeded with the QACSE 2-RDMs most closely mirroring those of CASSCF, i.e. the ortho- and para- isomers, now yield the largest deviations in ΔE_1 and ΔE_2 of the ACSE result, while the previously large deviations in the meta isomer are significantly reduced from the seed QACSE 2-RDM. It is also noteworthy that we observe a general reversal in the signs of ΔE_1 and ΔE_2 from QACSE to QACSE/ACSE. Again we observe favorable cancellation between the deviations in the individual 1- and 2-electron components and the total energies remain close, upper bounds to the CASSCF/ACSE energies.

6.3.4 Orbital Occupation Numbers

Lastly, we consider the impact of the use of a quantum computed 2-RDM on the natural occupation numbers (NON) obtained from the classical dynamical correlation calculations. As MC-PDFT does not reoptimize the 2-RDM and orbital occupations, we only consider the ACSE results. Table 6.4 shows the NON for the CAS and ACSE calculations, for both classical and quantum computations. Generally, a more correlated solution is characterized by more fractional NON. According to deviations of the NON from 0 and 1 with greater deviations indicating more correlation, the quantum CAS (QACSE) results are more correlated than the classical CASSCF results for all three

			CAS		ACSE	
			HONO	LUNO	HONO	LUNO
[2,2]	ortho	classical	0.905	0.095	0.886	0.110
		1 qubit	0.845	0.155	0.833	0.163
	meta	classical	0.855	0.145	0.837	0.156
		1 qubit	0.800	0.200	0.787	0.206
	para	classical	0.615	0.385	0.608	0.386
		1 qubit	0.565	0.435	0.558	0.435
[4,4]	ortho	classical	0.905	0.095	0.888	0.108
		3 qubit	0.925	0.075	0.904	0.092
		4 qubit	0.970	0.025	0.943	0.050
	meta	classical	0.880	0.120	0.859	0.134
		3 qubit	0.880	0.120	0.861	0.133
		4 qubit	0.785	0.215	0.771	0.223
	para	classical	0.615	0.385	0.610	0.384
		3 qubit	0.575	0.425	0.568	0.426
		4 qubit	0.600	0.395	0.593	0.396

Table 6.4: Natural occupation numbers (NON) of the HONO and LUNO orbitals for the CASSCF and QACSE calculations (CAS column) and as well as the QACSE and CASSCF seeded ACSE calculations (ACSE column).

isomers in the [2,2] active space and for the more strongly correlated meta and para isomers in the [4,4] active space. The use of 4 qubits over 3 qubits yields reduced correlation in the ortho isomer and increased correlation in the meta and para isomers. While the dynamic correlation introduced by the post-CI ACSE calculation yields a more correlated solution via the inclusion of core and virtual orbital contributions, the changes in HONO and LUNO occupations that are relevant for the capture of the biradical character displayed by the benzynes are minor compared to the magnitude of the multi-reference character obtained by the QACSE and CASSCF calculations. Consequently, we see a strong dependence on the initial results of the QACSE calculation in the QACSE/ACSE results and as such, computations involving the NISQ device to obtain active space 2-RDMs tend to yield more multi-reference character and more partial HONO and LUNO NON in a post-processing ACSE calculation when compared to the classical reference.

6.4 Conclusions

Realizing the unique position of the ACSE and MC-PDFT as possible post-processing methods to compute all-electron correlation in hybrid quantum-classical algorithms, owing to their dependence on only the 2-RDM rather than the N-electron wave function, we have successfully used them in tandem with a NISQ-CAS calculation, performed with the QACSE contracted quantum eigensolver, to resolve the total electronic correlation energy in the isomers of benzyne. We have demonstrated that 2-RDMs from NISQ devices, after error mitigation with necessary N-representability conditions, allow for the resolution of an experimentally verifiable quantity, the relative energies of the different benzyne isomers, within the bounds of the experimental margins of error in a QACSE/ACSE and QACSE/MC-PDFT hybrid classical-quantum algorithm. Furthermore, we have shown that the errors arising in CAS calculations on NISQ devices are not necessarily amplified in post-correction ACSE and MC-PDFT calculations relying on their 2-RDMs. Instead, in the noisier 3 and 4 qubit calculations we observe a reduction of the error compared to the respective classical analogues when comparing the absolute energies of the CAS and post-CI calculations. Thus classical post-correction calculations of the total correlation energy, as implemented in QACSE/ACSE and QACSE/MC-PDFT, may play an additional role as further sources of error correction in the applications of quantum algorithms.

While we have focused on ACSE and MC-PDFT, other 2-RDM-based methods—methods that require only an input 2-RDM rather than the many-electron wave function or higher RDMs—can also be employed within the general hybrid quantum-classical algorithmic framework proposed here. For example, a recent extension of the quantum subspace expansion (which itself is closely related to the classical methods for extracting excited states from the 2-RDM [55–57]), called the virtual quantum subspace expansion, [24, 25] adds correlation to an initial 2-RDM through single and double excitations. Unlike the ACSE, however, this method is not necessarily size extensive.

With the advances reported in this article we successfully take a first step in bringing NISQ device based hybrid quantum-classical algorithms into the realm of everyday computational chemistry applications. Even as quantum hardware markedly improves, the quantum-classical quantum algorithm presented here, including the 2-RDM-based error mitigation, will be critically important for merging the strengths of quantum and classical computers for accurately simulating the energies and properties of chemically important molecules and materials [2, 3, 8, 13, 58].

References

(1) Kohn, W.; Sham, L. J. *Phys. Rev.* **1965**, *140*, A1133–A1138.

(2) Head-Marsden, K.; Flick, J.; Ciccarino, C. J.; Narang, P. *Chem. Rev.* **2021**, *121*, 3061–3120.

(3) Reiher, M.; Wiebe, N.; Svore, K. M.; Wecker, D.; Troyer, M. *Proc. Natl. Acad. Sci. U.S.A.* **2017**, *114*, 7555–7560.

(4) Zhang, D.; Truhlar, D. G. *J. Chem. Theory Comput.* **2021**, *17*, 5733–5744.

(5) Benavides-Riveros, C. L.; Lathiotakis, N. N.; Marques, M. A. L. *Phys. Chem. Chem. Phys.* **2017**, *19*, 12655–12664.

(6) Roca-Sanjuán, D.; Aquilante, F.; Lindh, R. *Wiley Interdiscip. Rev. Comput. Mol. Sci.* **2012**, *2*, 585–603.

(7) Austin, B. M.; Zubarev, D. Y.; Lester, W. A. *Chem. Rev.* **2012**, *112*, 263–288.

(8) Yanai, T.; Chan, G. K.-L. *J. Chem. Phys.* **2006**, *124*, 194106.

(9) Yanai, T.; Kurashige, Y.; Neuscamman, E.; Chan, G. K.-L. *J. Chem. Phys.* **2010**, *132*, 024105.

(10) Mahapatra, U. S.; Datta, B.; Mukherjee, D. *J. Chem. Phys.* **1999**, *110*, 6171–6188.

(11) Angeli, C.; Pastore, M.; Cimiraglia, R. *Theor. Chem. Acc.* **2007**, *117*, 743–754.

(12) Elfving, V. E.; Broer, B. W.; Webber, M.; Gavartin, J.; Halls, M. D.; Lorton, K. P.; Bochevarov, A. *arXiv:2009.12472* **2020**.

(13) McArdle, S.; Endo, S.; Aspuru-Guzik, A.; Benjamin, S. C.; Yuan, X. *Rev. Mod. Phys.* **2020**, *92*, 015003.

(14) Bauer, B.; Bravyi, S.; Motta, M.; Chan, G. K.-L. *Chem. Rev.* **2020**, *120*, 12685–12717.

(15) Bauer, B.; Wecker, D.; Millis, A. J.; Hastings, M. B.; Troyer, M. *Phys. Rev. X* **2016**, *6*, 031045.

(16) Dhawan, D.; Metcalf, M.; Zgid, D. *J. Chem. Theory Comput.* **0000**, *0*, null.

(17) Keen, T.; Maier, T.; Johnston, S.; Lougovski, P. *Quantum Sci. Technol.* **2020**, *5*, 035001.

(18) Rubin, N. C. *arXiv:1610.06910* **2016**.

(19) Yamazaki, T.; Matsuura, S.; Narimani, A.; Saidmuradov, A.; Zaribafiyan, A. *arXiv:1806.01305* **2018**.

(20) Metcalf, M.; Bauman, N. P.; Kowalski, K.; de Jong, W. A. *J. Chem. Theory Comput.* **2020**, *16*, 6165–6175.

(21) Kowalski, K.; Bauman, N. P. *J. Chem. Phys.* **2020**, *152*, 244127.

(22) Bauman, N. P.; Kowalski, K., 2021.

(23) Motta, M.; Gujarati, T. P.; Rice, J. E.; Kumar, A.; Masteran, C.; Latone, J. A.; Lee, E.; Valeev, E. F.; Takeshita, T. Y. *Phys. Chem. Chem. Phys.* **2020**, *22*, 24270–24281.

(24) Urbanek, M.; Camps, D.; Van Beeumen, R.; de Jong, W. A. *J. Chem. Theory Comput.* **2020**, *16*, 5425–5431.

(25) Takeshita, T.; Rubin, N. C.; Jiang, Z.; Lee, E.; Babbush, R.; McClean, J. R. *Phys. Rev. X* **2020**, *10*, 011004.

(26) Smart, S. E.; Mazziotti, D. A. *Phys. Rev. Lett.* **2021**, *126*, 070504.

(27) Mazziotti, D. A. *Phys. Rev. Lett.* **2006**, *97*, 143002.

(28) Li Manni, G.; Carlson, R. K.; Luo, S.; Ma, D.; Olsen, J.; Truhlar, D. G.; Gagliardi, L. *J. Chem. Theory Comput.* **2014**, *10*, 3669–3680.

(29) Smart, S. E.; Boyn, J.-N.; Mazziotti, D. A. *arXiv:2103.06876* **2021**.

(30) Mazziotti, D. A. *Phys. Rev. Lett.* **2004**, *93*, 213001.

(31) Mazziotti, D. A. *Phys. Rev. Lett.* **2012**, *108*, 263002.

(32) Foley, J. J.; Mazziotti, D. A. *Phys. Rev. A* **2012**, *86*, 012512.

(33) Rubin, N. C.; Babbush, R.; McClean, J. *New J. Phys.* **2018**, *20*, 053020.

(34) IBM Quantum, 2020.

(35) Abraham, H. et al. Qiskit: An Open-source Framework for Quantum Computing, 2019.

(36) Setia, K.; Chen, R.; Rice, J. E.; Mezzacapo, A.; Pistoia, M.; Whitfield, J. D. *J. Chem. Theory Comput.* **2020**, *16*, 6091–6097.

(37) Mazziotti, D. A. *Phys. Rev. A* **2007**, *75*, 022505.

(38) Boyn, J.-N.; Mazziotti, D. A. *J. Chem. Phys.* **2021**, *154*, 134103.

(39) DePrince, A. E.; Mazziotti, D. A. *J. Chem. Phys.* **2007**, *127*, 104104.

(40) Mazziotti, D. A. *Phys. Rev. A* **1999**, *60*, 4396–4408.

(41) Mazziotti, D. A. *Chem. Phys. Lett.* **1998**, *289*, 419–427.

(42) Perdew, J. P.; Savin, A.; Burke, K. *Phys. Rev. A* **1995**, *51*, 4531–4541.

(43) Carlson, R. K.; Truhlar, D. G.; Gagliardi, L. *J. Chem. Theory Comput.* **2015**, *11*, 4077–4085.

(44) Pandharkar, R.; Hermes, M. R.; Truhlar, D. G.; Gagliardi, L. *J. Phys. Chem. Lett.* **2020**, *11*, 10158–10163.

(45) Maplesoft, a division of Waterloo Maple Inc., Waterloo, Ontario. **2019**.

(46) RDMChem, Chicago, Illinois. **2019**.

(47) Sun, Q.; Berkelbach, T. C.; Blunt, N. S.; Booth, G. H.; Guo, S.; Li, Z.; Liu, J.; McClain, J. D.; Sayfutyarova, E. R.; Sharma, S.; Wouters, S.; Chan, G. K.-L. *Wiley Interdiscip. Rev. Comput. Mol. Sci.* **2018**, *8*, e1340.

(48) Hermes, M. R., 2021.

(49) Bonet-Monroig, X.; Babbush, R.; O'Brien, T. E. *Phys. Rev. X* **2020**, *10*, 031064.

(50) Smart, S. E.; Mazziotti, D. A. *Phys. Rev. A* **2021**, *103*, 012420.

(51) Sander, W. *Acc. Chem. Res.* **1999**, *32*, 669–676.

(52) Dubrovskiy, A. V.; Markina, N. A.; Larock, R. C. *Org. Biomol. Chem.* **2013**, *11*, 191–218.

(53) Wenthold, P. G.; Squires, R. R.; Lineberger, W. C. *J. Am. Chem. Soc.* **1998**, *120*, 5279–5290.

(54) Dunning, T. H. *J. Chem. Phys.* **1989**, *90*, 1007–1023.

(55) Mazziotti, D. A. *Phys. Rev. A* **2003**, *68*, 052501.

(56) Greenman, L.; Mazziotti, D. A. *J. Chem. Phys.* **2008**, *128*, 114109.

(57) Hemmatiyan, S.; Sajjan, M.; Schlimgen, A. W.; Mazziotti, D. A. *J. Phys. Chem. Lett.* **2018**, *9*, 5373–5378.

(58) Von Burg, V.; Low, G. H.; Häner, T.; Steiger, D. S.; Reiher, M.; Roetteler, M.; Troyer, M. *arXiv:2007.14460* **2021**.

CHAPTER 7

STRONG CORRELATION IN BIMETALLIC COMPLEXES

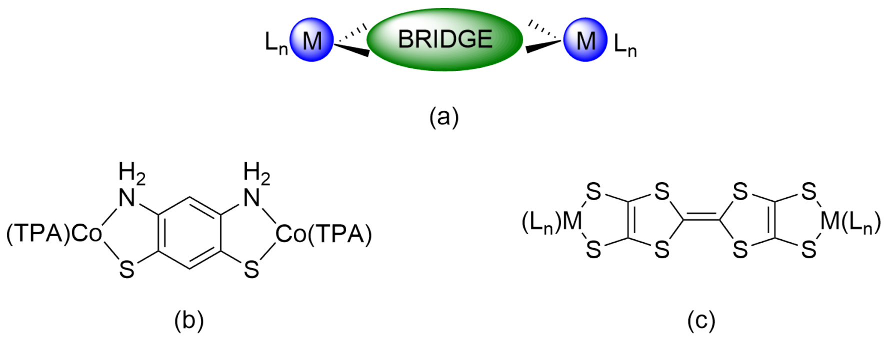

(a)

(b)

(c)

Figure 7.1: (a): Schematic illustration of a metal-ligand-metal bimetallic complex. (b): Quinoid and (c): tetrathiafulvalene-2,3,6,7-tetrathiolate (TTFtt) bridged bimetallics considered in this dissertation.

Bimetallic or binuclear complexes are composed of two metal centers linked by a bridging ligand in a metal-ligand-metal fashion (schematically illustrated in Figure 7.1 (a)) and are valuable targets in several areas of chemistry owing to their tunable magnetic and electronic properties. The first such experimentally characterized complexes were binuclear ruthenium ammines synthesized by Creutz and Taube in 1972[1], and since then a large number of bimetallics of differing metal centers and bridging ligands have been synthesized with popular ligand choices including but not limited to hydroxo[2], phenylene[3] and phosphinidene[4] bridges. In the following parts of this dissertation we will focus on binuclear transition metal complexes bridged by quinoid[5] and tetrathiafulvalene-2,3,6,7-tetrathiolate (TTFtt)[6] ligands, illustrated in Figure 7.1 (b) and (c), respectively.

The electronic structure of bimetallic complexes is characterized by the interaction of the metal center based orbitals with those of the bridging ligand. Generally, they exhibit strongly correlated ground states, with the open-shell nature arising from the degenerate metal-based d-orbital manifolds, which tend to yield multi-configurational electronic states in all but the simplest closed-shell

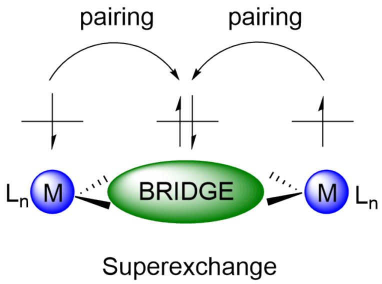

Figure 7.2: Schematic illustration of the superexchange mechanism learding to anti-ferromagnetic coupling in bimetallic complexes. While typically antiferromagnetic, superexchange may also be ferromagnetic depending on the symmetries of the orbitals involved.

d^{10} systems. As such single-reference methods, such as DFT, struggle to accurately capture the electronic and magnetic properties of these complexes. While broken-symmetry approximations have been introduced to allow some DFT treatment via the use non spin-pure singlet states[7, 8], a correct, *ab-initio* simulation of these systems requires the use of multi-configurational methods such as CASSCF, CASPT2 or the ACSE to resolve accurately their spin state splittings, excited states and magnetic properties.

Desirable electronic and magnetic properties arise from the interaction between unpaired electrons localized on the metal centers. This is most commonly rationalized in terms of a superexchange mechanism, where the unpaired spins on the respective metal centers interact with paired spins of the bridging ligand, promoting the overall anti-parallel alignment of electrons across the entire complex and yielding a closed-shell ground state[9–11]. This interaction is schematically displayed in Figure 7.2. It may be quantified in terms of the exchange coupling constant, J, and the Heisenberg-Dirac-Van-Vleck Hamiltonian, $H = -2JS_1S_2$, which in the case of the simplest case of two metal centers each possessing one unpaired electron yields a direct relationship between the singlet-triplet gap and J:

$$E_T - E_S = -2J\,, \tag{7.1}$$

and may be determined computationally, as well as experimentally via magnetic susceptibility measurements. A positive value of J indicates ferromagnetic coupling and a high-spin ground state, while a negative J value indicates anti-ferromagnetic coupling and a low-spin ground state. Exchange via through-space coupling of the two metal centers without involvement of the bridging ligand may provide an alternative pathway to superexchange. Additionally, complexes containing radical bridging ligands have been demonstrated to yield exchange coupling constants of particularly large magnitudes, driven by a direct exchange interaction between the unpaired electrons on the metal centers and the radical bridging ligand[12].

The structure of bimetallic complexes not only allows for coupling of the two terminal metal fragments yielding complex photophysical, magnetic and redox properties, but also the efficient modulation of these via structural or electronic modifications of both the bridging and peripheral ligands[13]. Bimetallics can serve as a donor-bridge-acceptor (D-B-A) system, allowing for photoinduced electron and energy transfer and making them key targets for optoelectronic devices[14], while their luminescence behavior with high quantum yields at tunable emission wavelengths has made them prime candidates for organoelectroluminescence with possible medical and biological applications[15, 16]. Additionally, the intermolecular electron transfer abilities in mixed valence binuclear complexes allow for their use as nanojunctions and molecular switches[17, 18]. Furthermore, the ability to use the bridging ligand to tune the magnetic exchange interactions may be exploited to yield systems with high-spin ground states and large barriers to thermal relaxation of magnetization, which are defined as single molecule magnets (SMM) and present valuable building blocks in spintronics or quantum information storage[11, 12, 19]. Lastly, bimetallic complexes provide building blocks for the synthesis of larger metal organic frameworks or coordination polymers which in turn attract significant research interest as molecular wires or conductors[20–23].

Electronic structure calculations can yield valuable insights into the factors governing the electronic properties of bimetallic complexes, aiding in the elucidation of the quantum mechanics underlying experimentally observed properties, which is essential for the rational design of new compounds. The following sections of this dissertation cover high-level electronic structure calculations carried out on several different bimetallic compounds, resolving their magnetic, electronic and photophysical properties and revealing the key role played by multi-reference correlation effects in these types of complexes.

References

(1) Creutz, C.; Taube, H. *J. Am. Chem. Soc.* **1973**, *95*, 1086–1094.

(2) Ruiz, E.; Alemany, P.; Alvarez, S.; Cano, J. *J. Am. Chem. Soc.* **1997**, *119*, 1297–1303.

(3) Low, P. J. *Coord. Chem. Rev.* **2013**, *257*, Electron Transfer in Coordination Chemistry, 1507–1532.

(4) García, M. E.; García-Vivó, D.; Ramos, A.; Ruiz, M. A. *Coord. Chem. Rev.* **2017**, *330*, 1–36.

(5) Sarkar, B.; Schweinfurth, D.; Deibel, N.; Weisser, F. *Coord. Chem. Rev.* **2015**, *293-294*, 41st International Conference on Coordination Chemistry, Singapore, July 2014, 250–262.

(6) McCullough, R. D.; Belot, J. A. *Chem. Mater.* **1994**, *6*, 1396–1403.

(7) Caballol, R.; Castell, O.; Illas, F.; de P. R. Moreira, I.; Malrieu, J. P. *J. Phys. Chem. A* **1997**, *101*, 7860–7866.

(8) Comba, P.; Hausberg, S.; Martin, B. *J. Phys. Chem. A* **2009**, *113*, 6751–6755.

(9) Anderson, P. W. *Phys. Rev.* **1959**, *115*, 2–13.

(10) Evans, C. E. B.; Naklicki, M. L.; Rezvani, A. R.; White, C. A.; Kondratiev, V. V.; Crutchley, R. J. *J. Am. Chem. Soc.* **1998**, *120*, 13096–13103.

(11) Long, J.; Habib, F.; Lin, P.-H.; Korobkov, I.; Enright, G.; Ungur, L.; Wernsdorfer, W.; Chibotaru, L. F.; Murugesu, M. *J. Am. Chem. Soc.* **2011**, *133*, 5319–5328.

(12) Demir, S.; Jeon, I.-R.; Long, J. R.; Harris, T. D. *Coord. Chem. Rev.* **2015**, *289-290*, Progress in Magnetochemistry, 149–176.

(13) Low, P. J. *Coord. Chem. Rev.* **2013**, *257*, Electron Transfer in Coordination Chemistry, 1507–1532.

(14) Li, G.; Zhu, D.; Wang, X.; Su, Z.; Bryce, M. R. *Chem. Soc. Rev.* **2020**, *49*, 765–838.

(15) Xiao, L.; Chen, Z.; Qu, B.; Luo, J.; Kong, S.; Gong, Q.; Kido, J. *Adv. Mater.* **2011**, *23*, 926–952.

(16) Chaaban, M.; Zhou, C.; Lin, H.; Chyi, B.; Ma, B. *J. Mater. Chem. C* **2019**, *7*, 5910–5924.

(17) Launay, J.-P. *Coord. Chem. Rev.* **2013**, *257*, Electron Transfer in Coordination Chemistry, 1544–1554.

(18) Ward, M. D. *Chem. Soc. Rev.* **1995**, *24*, 121–134.

(19) Mills, D. P.; Moro, F.; McMaster, J.; van Slageren, J.; Lewis, W.; Blake, A. J.; Liddle, S. T. *Nat. Chem.* **2011**, *3*, 454–460.

(20) James, S. L. *Chem. Soc. Rev.* **2003**, *32*, 276–288.

(21) Furukawa, H.; Cordova, K. E.; O'Keeffe, M.; Yaghi, O. M. *Science* **2013**, *341*, 1230444.

(22) Janiak, C. *Dalton Trans.* **2003**, 2781–2804.

(23) Kitagawa, S.; Kitaura, R.; Noro, S.-i. *Angew. Chem. Int. Ed.* **2004**, *43*, 2334–2375.

CHAPTER 8

DIRECT ENTANGLEMENT IN A COBALT-QUINOID DIMER

Reprinted with permission from J.-N. Boyn, J. Xie, J. S. Anderson, and D.A. Mazziotti, *Journal of Physical Chemistry Letters* **11**, 4584-4590 (2020). Copyright 2020 American Chemical Society.

8.1 Introduction

Transition metal dimer complexes have been an area of significant research interest in recent years owing to their wide range of tunability for different applications. Indeed, metal centers bridged by tunable organic ligands have become leading candidates in the development of single molecule magnets (SMM) and extended framework magnetic materials[1–7]. Ideal candidates for SMMs have large relaxation energy barriers leading to consequently large relaxation times[8–10]. Magnetic coupling between metal centers in bridging coordination compounds is thought to be mediated though interactions with the electron density on the bridging ligand: a superexchange mechanism between two paramagnetic metal centers when the ligand is diamagnetic, or a direct exchange interaction when the ligand is paramagnetic[11–16]. Exchange interactions are a quantum mechanical phenomenon that arise from the entanglement of electrons across multiple centers. Formally, quantum entanglement occurs in a pure state when the total wave function cannot be expressed as a product of the wave functions of the entangled centers[17, 18]. Superexchange interactions have been illustrated and studied in transition mental complexes with oxido linkers, where the magnitude of the interaction facilitated via the one atom bridge can be significant[19–25]. Exchange interactions have important implications for the magnetic properties of electronic systems with positive exchange interactions favoring parallel spins and negative exchange energies promoting the pairing of spins.

Since the discovery of the first SMM, $Mn_{12}O_{12}(O_2CMe)_{16}(H_2O)_4$, a Mn cluster compound[19], researchers have been interested in the synthesis of transition metal dimers and clusters bridged by organic ligands with the aim of maximizing the ground-state multiplicity[26, 27]. Recent research has led to the successful synthesis and experimental characterization of a large range of compounds, covering a wide range of transition metal centers, as well as various lanthanide centers[16, 28–31]. Complexes with bis(bidentate) benzoquinoid based ligands with oxygen, sulfur and nitrogen donor atoms have shown particularly promising results[15, 27, 32–42]. The focus of this synthetic work has been the tuning of magnetic exchange interactions in these systems, aiming to yield high spin ground states and large exchange constants J through changes of orbital structure and electron density on the bridging ligand, and more recently by using radical ligands to enable direct exchange coupling[14, 26, 43–46]. However, theoretical and modelling work aimed at elucidating the electronic structure and nature of exchange coupling present in these compounds has been sparse with the little published work mostly relying on density functional theory (DFT) calculations[25, 47–52], which are well known to struggle with strongly correlated systems[53–57].

In this letter we present the synthesis, experimental characterization and computational electronic structure investigation of the novel dimeric complex $[(CoTPA)_2DADT][BF_4]_2$ (TPA: tris(2-pyridylmethyl)amine, DADT: 2,5-diaminobenzene-1,4-bis(thiolate)). The electronic structure is investigated using the active-space variational 2-RDM method (V2RDM)[58–72]. We elucidate the nature of the bonding and exchange in $[(CoTPA)_2DADT]^{2+}$ and provide evidence that, surprisingly, superexchange is not responsible for the magnetic coupling between the two cobalt centers and that exchange is not mediated by the orbitals of the diamagnetic benzoquinoid ligand.

8.2 Results

$[(CoTPA)_2DADT][BF_4]_2$ was synthesized by mixing $(TPA)CoCl_2$ with the hydrochloride salt of DADT and base (Figure 8.1) and was characterized with a suite of methods including single crystal

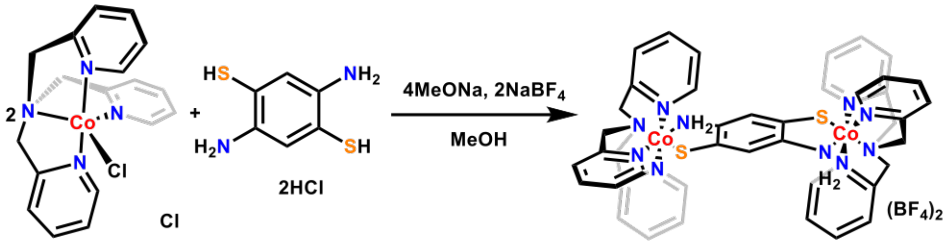

Figure 8.1: Synthesis scheme for $[(CoTPA)_2DADT][BF_4]_2$.

X-ray diffraction (SXRD) and magnetic measurements. Variable temperature magnetic susceptibility superconducting quantum interference device (SQUID) measurements were carried out to probe the magnetic interactions in $[(CoTPA)_2DADT][BF_4]_2$ and determine the electronic ground state. The resulting magnetic susceptibility is shown in the plot of χT vs T in Fig. 8.2. We observe a singlet electronic state for the $[(CoTPA)_2DADT]^{2+}$ complex in the solid state low T limit. Due to possible inter-molecular interactions and zero-field splitting effects, this likely may not reflect the electronic ground state of the molecular species. The decrease in χT from 300K to 100K arises from weak antiferromagnetic exchange coupling between the two high-spin Co centers in the molecular species. Upon initial inspection of the data, we assigned the source of this antiferromagnetic coupling as superexchange interactions mediated by the DADT linker, in accordance with similar assignments in the literature for various transition metal dimers and SMM candidates[14, 16, 25, 33, 36, 37, 39, 43, 45]. Unlike in a direct exchange mechanism between nearest neighbor atoms, in the superexchange mechanism a diamagnetic ligand facilitates antiferromagnetic coupling between the two open-shell transition metal cations. Spins on each metal center are effectively paired through interaction with an electron pair localized on the bridging ligand, enabling exchange coupling over longer distances. This mechanism is schematically illustrated in Figure 8.3. To quantify this antiferromagnetic interaction, we fit the data to the Van Vleck equation according to the spin Hamiltonian $\hat{H} = -2J(\hat{S}_{Co_1} \cdot \hat{S}_{Co_2})$, giving an exchange constant of $J = -2.0(5)\ \mathrm{cm}^{-1}$[73].

For the electronic structure calculations the complex geometry is obtained from the SXRD

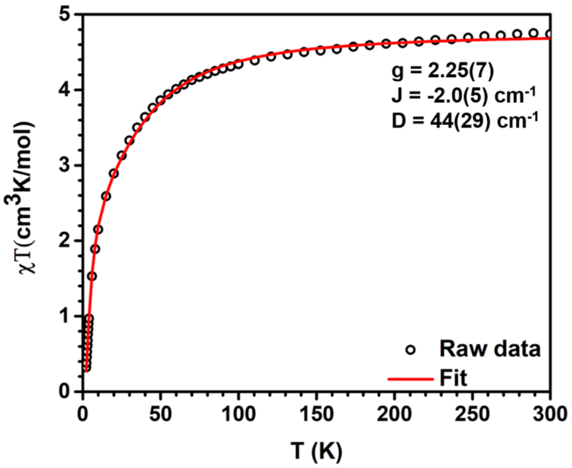

Figure 8.2: Varied-temperature χT data for $[(CoTPA)_2DADT][BF_4]_2$, collected under an applied field of 1000 Oe from 300 to 1.8 K. Red line is the fit as described in the text.

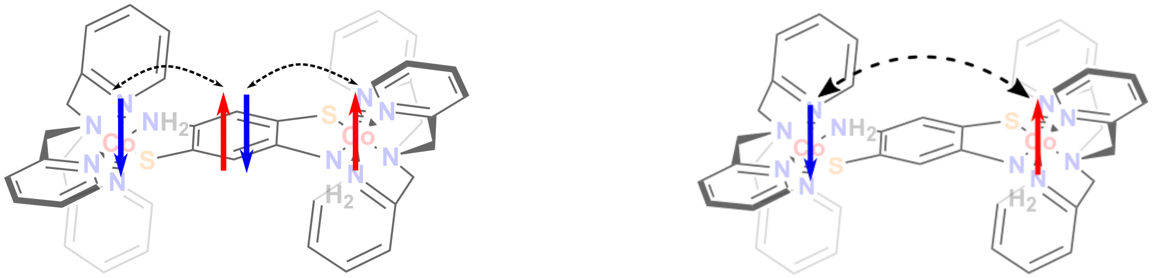

Figure 8.3: Schematic representation of superexchange (left) and EPR-like direct exchange arising from the entanglement of the electrons across the two Co centers (right) in the $[(CoTPA)_2DADT]^{2+}$ complex.

structure and relaxed with DFT using the B3LYP functional in a 6-31G* basis set. Electronic energies and natural orbital occupation numbers (NON) were obtained for the singlet state with V2RDM complete active space self-consistent field (CASSCF) calculations in the Maple Quantum Chemistry Package[74, 75] (QCP) for [12,10], [14,14], [20,20] and [24,24] active spaces with a 6-31G basis set[76] (Table 8.1). A [14,14] active space can be inferred to be sufficient to describe the correlation and electronic structure of this system, and all further V2RDM calculations are performed using this active space.

	[12,10]	[14,14]	[20,20]	[24,24]
E(a.u.)	-5715.73786	-5715.90024	-5716.02253	-5716.10063
λ_{222}	1.99	1.79	1.74	1.76
λ_{223}	1.99	1.78	1.73	1.74
λ_{224}	1.01	1.00	1.00	1.00
λ_{225}	0.99	1.00	1.00	0.97
λ_{226}	0.01	0.56	0.70	0.68
λ_{227}	0.01	0.02	0.07	0.10

Table 8.1: Comparison of energies and NON for different active space size V2RDM CASSCF singlet state calculations carried out in Maple QCP with a 6-31G basis set.

V2RDM calculations in Table 8.2 reveal the spin state splitting and determine the electronic ground state of the isolated molecule. The calculations elucidate the strongly correlated open-shell nature of this system showing significant partial occupations in the frontier NOs and a triplet ground state with a low lying quintet state separated by $\Delta E_{Q-T} = 7.77$ cm^{-1} with inaccessible, high energy singlet and septet states. Assuming the Heisenberg-Dirac-van-Vleck Hamiltonian for localized, weakly interacting electrons can be applied, the triplet-quintet gap corresponds to a J value of $\Delta E_{T-Q} = 4J$ or $J = -1.94$ cm^{-1}. This strongly suggests that the isolated molecule is in a triplet ground state and the experimentally measured antiferromagnetic exchange coupling between the two Co centers can be related to the gap between the triplet ground state and the low lying quintet state. Broken symmetry, unrestricted DFT calculations cannot account for the strong correlation in this system and fail to accurately predict its electronic structure with different functionals giving wildly varying results (displayed in Figure 8.4).

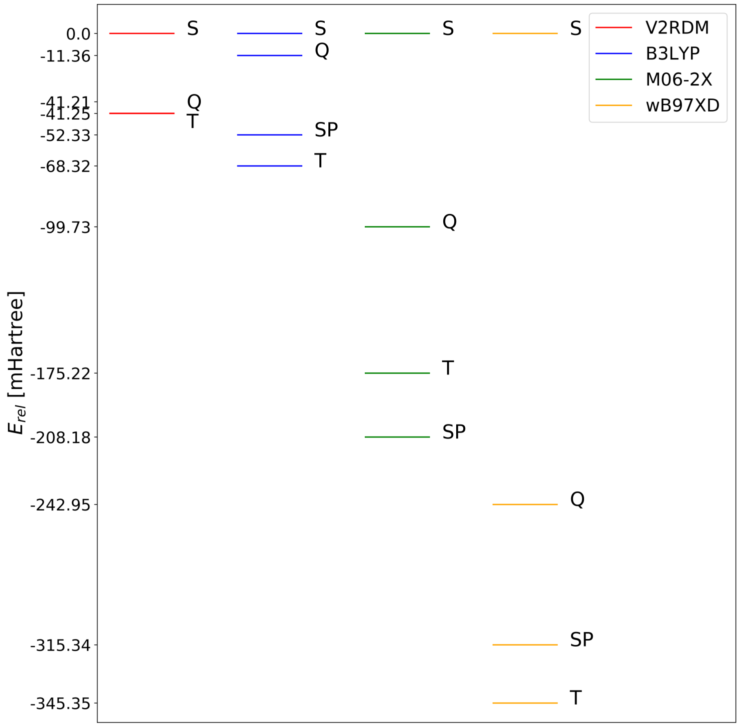

Figure 8.4: Energy splitting of singlet, triplet, quintet and septet spin states as obtained by [14,14] V2RDM CASSCF calculations with a 6-31G basis, and B3LYP, M06-2X and ωB97X-D DFT functionals with a 6-311++G** basis. The high lying V2RDM septet is omitted for clarity.

The nature of the spin state splittings can be rationalized with the help of the NON of the partially occupied frontier NOs and by inspection of the electron density. While the triplet and quintet state exhibit identical NON, singlet and septet states show significant redistribution of electrons within the frontier NOs. In the case of the singlet state we observe an open-shell biradical state and a notable decrease in partial occupancy, suggesting that the destabilization of the singlet by $\Delta E_{S-T} = 9320$ cm^{-1} compared to the triplet ground state arises from a loss of strong correlation. The septet state ($\Delta E_{ST-T} = 25500$ cm^{-1}) requires the unfavorable flipping of an additional spin and population of higher energy orbitals. Knowing the nature of the symmetry breaking in the frontier NOs, we perform DFT calculations at the B3LYP/6-31G* level of theory using a fragment guess approach, yielding $\Delta E_{Q-T} = -2.11$ cm^{-1}. While this splitting is of the correct order of

	Dimer				Capped		
	S	T	Q	ST	S	T	Q
$E_{rel}(\text{cm}^{-1})$	8970	0	7.77	25500	7790	0	196
$\lambda_{220} \mid \lambda_{203}$	1.99	1.99	1.99	1.82	1.98	1.99	1.99
$\lambda_{221} \mid \lambda_{204}$	1.84	1.68	1.67	1.75	1.88	1.68	1.65
$\lambda_{222} \mid \lambda_{205}$	1.79	1.58	1.58	1.75	1.85	1.63	1.61
$\lambda_{223} \mid \lambda_{206}$	1.78	1.50	1.50	1.00	1.85	1.52	1.47
$\lambda_{224} \mid \lambda_{207}$	1.00	1.12	1.12	1.00	1.00	1.08	1.13
$\lambda_{225} \mid \lambda_{208}$	1.00	1.10	1.11	1.00	0.94	1.06	1.12
$\lambda_{226} \mid \lambda_{209}$	0.56	1.00	1.00	1.00	0.45	1.00	1.00
$\lambda_{227} \mid \lambda_{210}$	0.02	0.01	0.01	0.26	0.02	0.01	0.01
$\lambda_{228} \mid \lambda_{211}$	0.01	0.01	0.01	0.25	0.02	0.01	0.01

Table 8.2: Energies relative to the triplet ground state, and NON for the dimeric complex and the capped Co centers. [14,14] V2RDM CASSCF calculations carried out in Maple QCP with a 6-31G basis set.

magnitude, its sign is opposite to that of experimental and V2RDM results, predicting ferromagnetic exchange coupling instead of the observed antiferromagnetic coupling.

We can elucidate the nature of the exchange coupling by examining the frontier NO densities. V2RDM CASSCF minimization leads to a result of severely broken symmetry with all frontier NOs except one localized on one Co center. In the triplet and quintet case, shown in Figure 8.5, this yields a strongly correlated system of one Co center with net spin of $S = 3/2$ and one center with $S = 1/2$. In a superexchange picture the spins on the Co centers would couple by interacting with the electron density on the linker. However, the electron densities in all frontier NOs are highly localized on the two Co centers without contribution from the atomic orbitals of the bridging ligand. Hence, there cannot be an interaction of the unpaired electrons on the Co centers via the bridging ligand's benzene core and antiferromagnetic coupling is not facilitated by a superexchange mechanism. Rather, these results point to an Einstein-Podolsky-Rosen (EPR) like direct exchange mechanism between the unpaired electrons entangled at a distance across the Co centers.

This conclusion is supported by calculations performed on the two Co centers fixed at the same

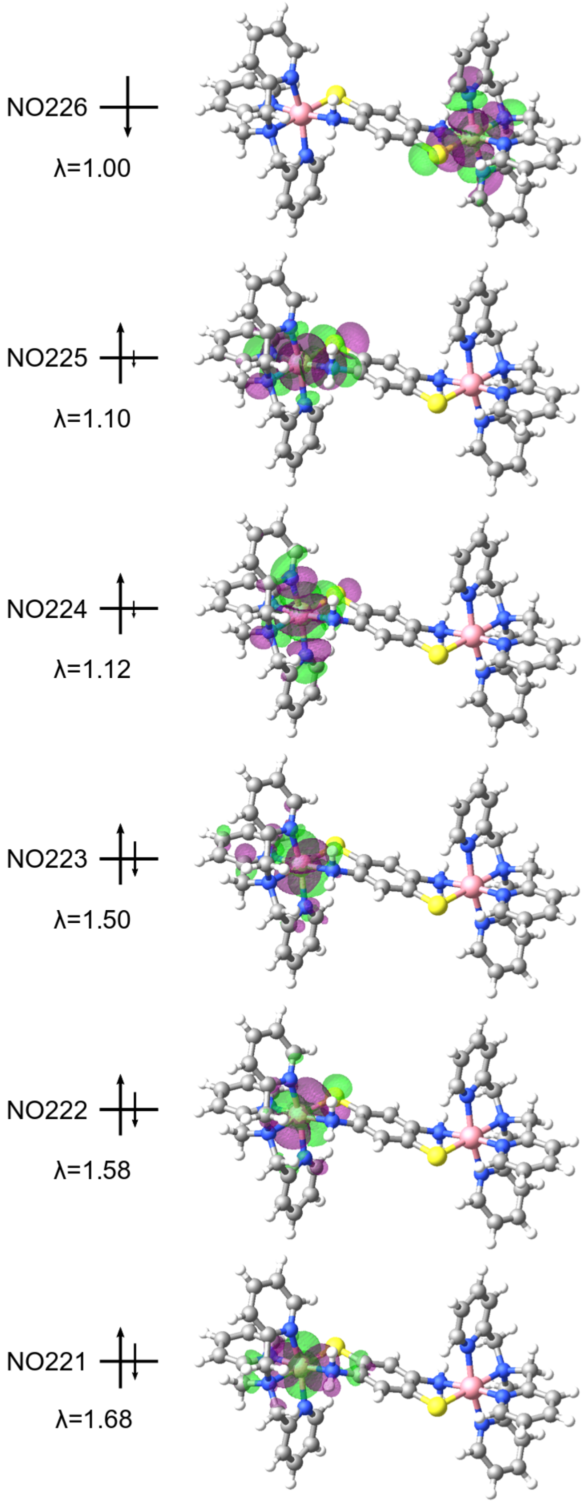

Figure 8.5: NO diagram for the triplet ground state, displaying the electron density in the partially occupied frontier NOs and their NON.

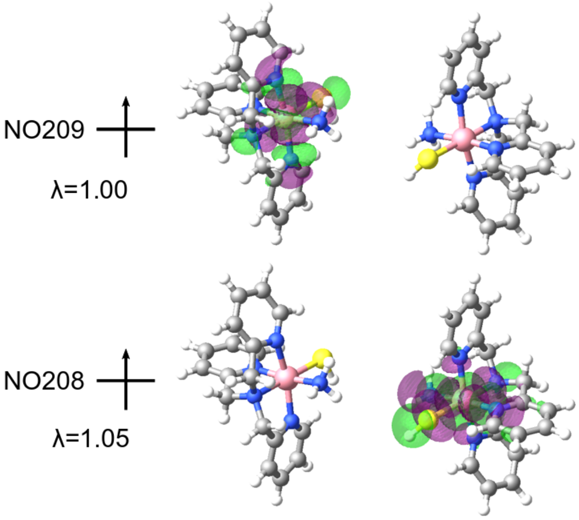

Figure 8.6: Diagram of NOs 208 and 209 for the two Co centers without linker. The frontier NOs remain unchanged by removal of the bridging ligand, suggest a EPR-like direct exchange mechanism, rather than superexchange facilitated by the linker.

Co-Co distances as those in the complex but with the bridging ligand removed and the nitrogen and sulfur atoms coordinated to the Co centers capped with hydrogens (referred to as capped structure). The resulting electronic structure displays similar NON (right hand column of Table 8.2) and the atomic orbitals involved in the frontier NOs remain unchanged upon removal of the linker (Figure 8.6). Calculations on the spin manifold show a triplet ground state with a low lying quintet state, separated by $\Delta E_{Q-T} = 196$ cm^{-1}, and again a higher lying, inaccessible singlet at $\Delta E_{T-S} = 7790$ cm^{-1}. These splittings are very close to the ones obtained for the dimer, in fact removal of the linker increases the exchange coupling constant from $J = -1.94$ cm^{-1} to $J = -48.9$ cm^{-1}. The results are stable with respect to small variations of ±0.3 Å in the distance between the two Co centers. This suggests, that not only is the linker not involved in the exchange mechanism via a superexchange pathway but rather its electron density plays a minimally shielding role, slightly reducing the exchange coupling compared to two Co centers directly entangled at a distance.

While $[(\text{CoTPA})_2\text{DADT}][\text{BF}_4]_2$ exhibits weak exchange coupling, much stronger couplings have been observed in radical bridged complexes[14, 26, 43–46]. To investigate the change to the electronic structure and magnetic exchange mechanism in the case of a radical bridging ligand additional calculations are performed on the vertically ionized species (center columns of Table 8.3). Mulliken charges on the Co centers remain unchanged and as expected ionization occurs from the DADT ligand. In the NO picture this corresponds to the removal of an electron from the inner NOs, yielding 5 approximately singly occupied NOs in all spin states.

The presence of the radical linker substantially changes the frontier orbital picture. While the majority of the NOs remain unchanged from the 2+ state and the system retains broken symmetry, NOs 222 and 226 show significant delocalization of the electron density across the linker, coupling the two cobalt centers (shown for the doublet on the left hand side of Figure 8.7). It becomes clear that in the case of the radical benzoquinoid bridging ligand, the two Co centers are no longer isolated and exchange may be mediated by the electron density on the bridge. V2RDM calculations show a doublet ground state and low lying, accessible quartet and sextet states, separated by $\Delta E_{Q-D} = 12.6$ cm^{-1} and $\Delta E_{S-D} = 223$ cm^{-1}. The octet state is inaccessible ($\Delta E_{O-D} = 20800$ cm^{-1}). In agreement with the experimental observations this shows that involvement of a radical bridging ligand does indeed lead to spin state splittings and consequently exchange couplings of larger magnitude compared to the diamagnetic case, and this stronger interaction is mediated by the atomic orbitals of the linker. This image of radical linker orbital involvement is reinforced by calculations performed on a capped version of the vertically ionized complex (right columns of Table 8.3). In this case the electronic structure differs significantly from the dimer and the NOs resemble those of the 2+ case (the right hand side of Figure 8.7). These results help rationalize recent findings showing radical benzoquinoid ligands to yield significant higher J compared to their neutral counterparts.

	Dimer				Capped		
	D	Q	S	O	D	Q	S
$E_{rel}(\mathrm{cm}^{-1})$	0	12.6	223	25400	0	3270	20800
$\lambda_{220} \mid \lambda_{203}$	1.95	1.95	1.95	1.73	1.95	1.94	1.84
$\lambda_{221} \mid \lambda_{204}$	1.95	1.95	1.95	1.73	1.95	1.94	1.82
$\lambda_{222} \mid \lambda_{205}$	1.15	1.14	1.02	1.00	1.80	1.77	1.49
$\lambda_{223} \mid \lambda_{206}$	1.00	1.01	1.00	1.00	1.71	1.47	1.22
$\lambda_{224} \mid \lambda_{207}$	1.00	1.00	1.00	1.00	0.80	0.99	1.16
$\lambda_{225} \mid \lambda_{208}$	0.98	0.98	0.99	1.00	0.69	0.77	1.00
$\lambda_{226} \mid \lambda_{209}$	0.87	0.88	0.99	1.00	0.05	0.06	0.16
$\lambda_{227} \mid \lambda_{210}$	0.05	0.05	0.05	0.27	0.05	0.05	0.16
$\lambda_{228} \mid \lambda_{211}$	0.05	0.05	0.05	0.27	0.04	0.05	0.15

Table 8.3: Energies relative to the doublet ground state, and NON for the vertically ionized 3+ dimeric complex and the capped Co centers fixed at the dimer geometry but without the bridging ligand. [13,14] V2RDM CASSCF calculations carried out in Maple QCP with a 6-31G basis set.

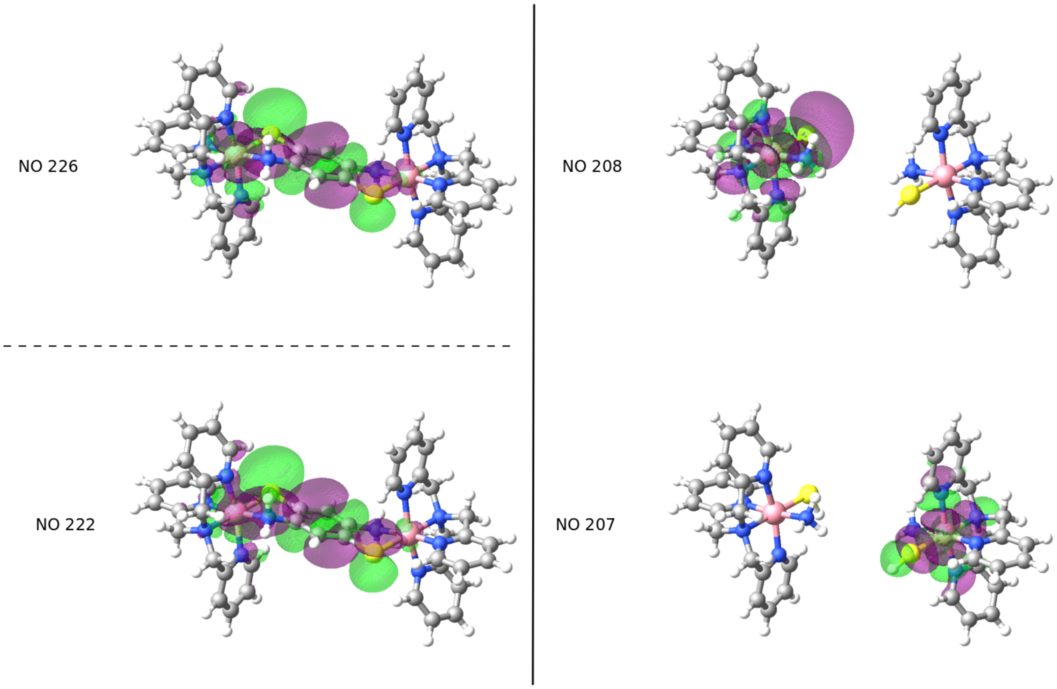

Figure 8.7: Left hand side: NOs 222 and 226 after vertical ionization to the +3 state. In contrast to the +2 complex, localization of the frontier NOs on the Co centers is lost, and the singly occupied frontier NOs show delocalization across the bridging ligand. Right hand side: Frontier NOs 207 and 208 for the capped arrangement after vertical ionization. The frontier NOs resemble those of the +2 state.

8.3 Conclusions

Through the use of large active space CASSCF calculations we render a quantum mechanical picture of the exchange interaction in a novel benzoquinoid bridged cobalt dimer complex, $[(\mathrm{CoTPA})_2\mathrm{DADT}]^{2+}$, allowing us to attribute the experimentally characterized exchange interaction to entanglement rather than the commonly accepted superexchange picture. V2RDM calculations correctly reproduce the experimental exchange constant J, showing a strongly symmetry broken wave function with highly localized singly occupied frontier NOs centered on the Co atoms with no involvement of the benzoquinoid linker, firmly suggesting that superexchange, the commonly accepted mechanism for long distance spin pairing in bridged transition metal and lanthanide complexes and clusters, is not responsible for the antiferromagnetic interaction in this system. Instead, our results suggest an EPR-like, direct exchange mechanism is operating over long distances between the two Co centers in $[(\mathrm{CoTPA})_2\mathrm{DADT}]^{2+}$, illustrated in Figure 8.3. This is further corroborated by V2RDM calculations on the capped Co centers fixed to their positions in the $[(\mathrm{CoTPA})_2\mathrm{DADT}]^{2+}$ complex, revealing no major changes in the electronic structure upon removal of DADT and instead leading to an increase in the magnitude of the exchange coupling, suggesting the presence of the linker may actually shield the exchange interaction between the two metal centers. This is in stark contrast to the electronic structure following vertical ionization, which removes an electron from DADT and yields a radical linker, enabling its participation in the exchange pathway. This is reflected in the frontier NO densities, which are delocalized over both Co centers as well as the linker allowing exchange coupling between the metal centers via the bridge, in line with assignments in the literature.

The work presented here offers compelling evidence that superexchange interactions over long ligand distances may not be a dominant factor in exchange coupling and instead correlation and entanglement may be the chief contributors. The results do, however, confirm a radical linker does, indeed, mediate the exchange interaction between two paramagnetic metal centers. Lastly, this work emphasizes the importance of large active space CASSCF calculations, which allow for symmetry breaking in the wave function and account for strong correlation, in the design of novel complexes with desirable electronic properties, with V2RDM results differing significantly from predictions obtained by traditional DFT functionals. The insight gained from these calculations can be especially useful in cases where the interaction between valence electrons is assumed to play a key role.

References

(1) Bogani, L.; Vindigni, A.; Sessoli, R.; Gatteschi, D. *J. Mater. Chem.* **2008**, *18*, 4750–4758.

(2) Gatteschi, D.; Vindigni, A. In *Molecular Magnets: Physics and Applications*, Bartolomé, J., Luis, F., Fernández, J. F., Eds.; Springer Berlin Heidelberg: 2014, pp 191–220.

(3) Leuenberger, M. N.; Loss, D. *Nature* **2001**, *410*, 789–793.

(4) DeGayner, J. A.; Wang, K.; Harris, T. D. *J. Am. Chem. Soc.* **2018**, *140*, 6550–6553.

(5) Jeon, I.-R.; Negru, B.; Van Duyne, R. P.; Harris, T. D. *J. Am. Chem. Soc.* **2015**, *137*, 15699–15702.

(6) DeGayner, J. A.; Jeon, I.-R.; Sun, L.; Dincă, M.; Harris, T. D. *J. Am. Chem. Soc.* **2017**, *139*, 4175–4184.

(7) Jeon, I.-R.; Sun, L.; Negru, B.; Van Duyne, R. P.; Dincă, M.; Harris, T. D. *J. Am. Chem. Soc.* **2016**, *138*, 6583–6590.

(8) Blagg, R. J.; Ungur, L.; Tuna, F.; Speak, J.; Comar, P.; Collison, D.; Wernsdorfer, W.; McInnes, E. J. L.; Chibotaru, L. F.; Winpenny, R. E. P. *Nat. Chem.* **2013**, *5*, 673.

(9) Murrie, M. *Chem. Soc. Rev.* **2010**, *39*, 1986–1995.

(10) Layfield, R. A. *Organometallics* **2014**, *33*, 1084–1099.

(11) Anderson, P. W. *Phys. Rev.* **1950**, *79*, 350–356.

(12) Powell, A. K. *Nature Chemistry* **2010**, *2*, 351.

(13) Tiron, R.; Wernsdorfer, W.; Foguet-Albiol, D.; Aliaga-Alcalde, N.; Christou, G. *Phys. Rev. Lett.* **2003**, *91*, 227203.

(14) Hua, C.; DeGayner, J. A.; Harris, T. D. *Inorg. Chem.* **2019**, *58*, 7044–7053.

(15) Gaudette, A. I.; Jeon, I.-R.; Anderson, J. S.; Grandjean, F.; Long, G. J.; Harris, T. D. *J. Am. Chem. Soc.* **2015**, *137*, 12617–12626.

(16) Bechlars, B.; D'Alessandro, D. M.; Jenkins, D. M.; Iavarone, A. T.; Glover, S. D.; Kubiak, C. P.; Long, J. R. *Nat. Chem.* **2010**, *2*, 362.

(17) Horodecki, R.; Horodecki, P.; Horodecki, M.; Horodecki, K. *Rev. Mod. Phys.* **2009**, *81*, 865–942.

(18) Huang, Z.; Wang, H.; Kais, S. *J. Mod. Opt.* **2006**, *53*, 2543–2558.

(19) Sessoli, R.; Tsai, H. L.; Schake, A. R.; Wang, S.; Vincent, J. B.; Folting, K.; Gatteschi, D.; Christou, G.; Hendrickson, D. N. *J. Am. Chem. Soc.* **1993**, *115*, 1804–1816.

(20) Lis, T. *Acta Crystallogr. B* **1980**, *36*, 2042–2046.

(21) Caneschi, A.; Gatteschi, D.; Sessoli, R.; Barra, A. L.; Brunel, L. C.; Guillot, M. *J. Am. Chem. Soc.* **1991**, *113*, 5873–5874.

(22) Castro, S. L.; Sun, Z.; Grant, C. M.; Bollinger, J. C.; Hendrickson, D. N.; Christou, G. *J. Am. Chem. Soc.* **1998**, *120*, 2365–2375.

(23) Oshio, H.; Hoshino, N.; Ito, T.; Nakano, M. *J. Am. Chem. Soc.* **2004**, *126*, 8805–8812.

(24) Milios, C. J.; Vinslava, A.; Wernsdorfer, W.; Moggach, S.; Parsons, S.; Perlepes, S. P.; Christou, G.; Brechin, E. K. *J. Am. Chem. Soc.* **2007**, *129*, 2754–2755.

(25) Reger, D. L.; Pascui, A. E.; Smith, M. D.; Jezierska, J.; Ozarowski, A. *Inorg. Chem.* **2012**, *51*, 7966–7968.

(26) Demir, S.; Jeon, I.-R.; Long, J. R.; Harris, T. D. *Coordination Chemistry Reviews* **2015**, *289-290*, 149–176.

(27) Sarkar, B.; Schweinfurth, D.; Deibel, N.; Weisser, F. *Coordination Chemistry Reviews* **2015**, *293-294*, 250–262.

(28) Palii, A.; Aldoshin, S.; Tsukerblat, B. *J. Phys. Chem. C* **2017**, *121*, 27218–27224.

(29) Sessoli, R.; Powell, A. K. *Coordination Chemistry Reviews* **2009**, *253*, 2328–2341.

(30) Long, J.; Habib, F.; Lin, P.-H.; Korobkov, I.; Enright, G.; Ungur, L.; Wernsdorfer, W.; Chibotaru, L. F.; Murugesu, M. *J. Am. Chem. Soc.* **2011**, *133*, 5319–5328.

(31) Novitchi, G.; Costes, J.-P.; Tuchagues, J.-P.; Vendier, L.; Wernsdorfer, W. *New J. Chem.* **2008**, *32*, 197–200.

(32) Tao, J.; Maruyama, H.; Sato, O. *J. Am. Chem. Soc.* **2006**, *128*, 1790–1791.

(33) Heinze, K.; Huttner, G.; Zsolnai, L.; Jacobi, A.; Schober, P. *Chem.: Eur. J.* **1997**, *3*, 732–743.

(34) Carbonera, C.; Dei, A.; Létard, J.-F.; Sangregorio, C.; Sorace, L. *Angew. Chem.* **2004**, *43*, 3136–3138.

(35) Min, K. S.; DiPasquale, A.; Rheingold, A. L.; Miller, J. S. *Inorg. Chem.* **2007**, *46*, 1048–1050.

(36) Guo, D.; McCusker, J. K. *Inorg. Chem.* **2007**, *46*, 3257–3274.

(37) Kumbhakar, D.; Sarkar, B.; Maji, S.; Mobin, S. M.; Fiedler, J.; Urbanos, F. A.; Jiménez-Aparicio, R.; Kaim, W.; Lahiri, G. K. *J. Am. Chem. Soc.* **2008**, *130*, 17575–17583.

(38) Min, K. S.; DiPasquale, A. G.; Rheingold, A. L.; White, H. S.; Miller, J. S. *J. Am. Chem. Soc.* **2009**, *131*, 6229–6236.

(39) Weisser, F.; Huebner, R.; Schweinfurth, D.; Sarkar, B. *Chem.: Eur. J.* **2011**, *17*, 5727–5736.

(40) Schweinfurth, D.; Rechkemmer, Y.; Hohloch, S.; Deibel, N.; Peremykin, I.; Fiedler, J.; Marx, R.; Neugebauer, P.; van Slageren, J.; Sarkar, B. *Chem.: Eur. J.* **2014**, *20*, 3475–3486.

(41) Margraf, G.; Kretz, T.; de Biani, F. F.; Laschi, F.; Losi, S.; Zanello, P.; Bats, J. W.; Wolf, B.; Remović-Langer, K.; Lang, M.; Prokofiev, A.; Assmus, W.; Lerner, H.-W.; Wagner, M. *Inorg. Chem.* **2006**, *45*, 1277–1288.

(42) Park, J. G.; Jeon, I.-R.; Harris, T. D. *Inorg. Chem.* **2015**, *54*, 359–369.

(43) Min, K. S.; DiPasquale, A. G.; Golen, J. A.; Rheingold, A. L.; Miller, J. S. *J. Am. Chem. Soc.* **2007**, *129*, 2360–2368.

(44) Min, K. S.; Rheingold, A. L.; DiPasquale, A.; Miller, J. S. *Inorg. Chem.* **2006**, *45*, 6135–6137.

(45) Jeon, I.-R.; Park, J. G.; Xiao, D. J.; Harris, T. D. *J. Am. Chem. Soc.* **2013**, *135*, 16845–16848.

(46) DeGayner, J. A.; Jeon, I.-R.; Harris, T. D. *Chem. Sci.* **2015**, *6*, 6639–6648.

(47) Shin, K.; Cha, M.; Lee, W.; Kim, H.; Jung, Y.; Dho, J.; Kim, J.; Lee, H. *J. Am. Chem. Soc.* **2011**, *133*, 20399–20404.

(48) Massé, A.; Friederich, P.; Symalla, F.; Liu, F.; Meded, V.; Coehoorn, R.; Wenzel, W.; Bobbert, P. A. *Phys. Rev. B* **2017**, *95*, 115204.

(49) Christian, P.; Rajaraman, G.; Harrison, A.; McDouall, J. J. W.; Raftery, J. T.; Winpenny, R. E. P. *Dalton Trans.* **2004**, 1511–1512.

(50) Baum, A. E.; Lindeman, S. V.; Fiedler, A. T. *Chem. Commun.* **2013**, *49*, 6531–6533.

(51) Pignotti, L. R.; Kongprakaiwoot, N.; Brennessel, W. W.; Baltrusaitis, J.; Luck, R. L.; Urnezius, E. *J. Organomet. Chem.* **2008**, *693*, 3263–3272.

(52) Kar, S.; Sarkar, B.; Ghumaan, S.; Janardanan, D.; van Slageren, J.; Fiedler, J.; Puranik, V. G.; Sunoj, R. B.; Kaim, W.; Lahiri, G. K. *Chem.: Eur. J.* **2005**, *11*, 4901–4911.

(53) Medvedev, M. G.; Bushmarinov, I. S.; Sun, J.; Perdew, J. P.; Lyssenko, K. A. *Science* **2017**, *355*, 49–52.

(54) Burke, K. *J. Chem. Phys.* **2012**, *136*, 150901.

(55) Cohen, A. J.; Mori-Sánchez, P.; Yang, W. *Science* **2008**, *321*, 792–794.

(56) Cohen, A. J.; Mori-Sánchez, P.; Yang, W. *Chem. Rev.* **2012**, *112*, 289–320.

(57) Brittain, D. R. B.; Lin, C. Y.; Gilbert, A. T. B.; Izgorodina, E. I.; Gill, P. M. W.; Coote, M. L. *Phys. Chem. Chem. Phys.* **2009**, *11*, 1138–1142.

(58) Lowdin, P.-O. *Phys. Rev.* **1955**, *97*, 1474–1489.

(59) Mazziotti, D. A. *Chem. Rev.* **2012**, *112*, 244–262.

(60) Mazziotti, D. A. *Phys. Rev. A* **2002**, *65*, 062511.

(61) Mazziotti, D. A.; Erdahl, R. M. *Phys. Rev. A* **2001**, *63*, 042113.

(62) Nakata, M.; Nakatsuji, H.; Ehara, M.; Fukuda, M.; Nakata, K.; Fujisawa, K. *J. Chem. Phys.* **2001**, *114*, 8282–8292.

(63) Mazziotti, D. A. *Phys. Rev. A* **2002**, *65*, 062511.

(64) DePrince, A. E.; Mazziotti, D. A. *J. Chem. Phys.* **2009**, *130*, 164109.

(65) Gidofalvi, G.; Mazziotti, D. A. *J. Chem. Phys.* **2008**, *129*, 134108.

(66) Shenvi, N.; Izmaylov, A. F. *Phys. Rev. Lett.* **2010**, *105*, 213003.

(67) Mazziotti, D. A. *Phys. Rev. Lett.* **2012**, *108*, 263002.

(68) Fosso-Tande, J.; Nguyen, T.-S.; Gidofalvi, G.; DePrince, A. E. *J. Chem. Theory Comput.* **2016**, *12*, 2260–2271.

(69) Mazziotti, D. A. *Phys. Rev. Lett.* **2016**, *117*, 153001.

(70) Schlimgen, A. W.; Heaps, C. W.; Mazziotti, D. A. *J. Phys. Chem. Lett.* **2016**, *7*, 627–631.

(71) Montgomery, J. M.; Mazziotti, D. A. *J. Phys. Chem. A* **2018**, *122*, 4988–4996.

(72) Xie, J.; Boyn, J.-N.; Filatov, A. S.; McNeece, A. J.; Mazziotti, D. A.; Anderson, J. S. *Chem. Sci.* **2020**, *11*, 1066–1078.

(73) Boca, R. *Elsevier, Amsterdam* **1999**.

(74) Maplesoft, a division of Waterloo Maple Inc., Waterloo, Ontario. **2019**.

(75) RDMChem, Chicago, Illinois. **2019**.

(76) Hehre, W. J.; Ditchfield, R.; Pople, J. A. *J. Chem. Phys.* **1972**, *56*, 2257–2261.

CHAPTER 9

INTERPLAY OF ELECTRONIC AND GEOMETRIC STRUCTURE TUNES ORGANIC BIRADICAL CHARACTER IN BIMETALLIC TETRATHIAFULVALENE TETRATHIOLATE COMPLEXES

Reprinted from an article submitted for publication by J.-N. Boyn, L. E. McNamara, J. S. Anderson, and D. A. Mazziotti (2022).

9.1 Introduction

Since first being reported in the early 1970s[1–3], tetrathiafulvalene (TTF) has been established as a valuable building block in multiple areas of chemistry and materials science[4–13]. This includes the use of TTF and its derivatives in organic conductors[6, 10, 13, 14], metal or covalent organic frameworks[15–17], molecular switches[5, 18], coordinating ligands in transition metal and lanthanide chemistry[4, 19–24] and macrocyclic and supramolecular structures[7, 25, 26]. The versatility in its applications arises from its tunable electronic structure, namely its extended π-system that yields low-lying excitations and accessible $1+$ and, more recently, $2+$ oxidation states[14, 27]. Promising applications of TTF-derived compounds include their roles in the development of single molecule magnets (SMM)[21, 23], molecular transistors[28], as well as materials for light harvesting and solar energy conversion[11].

Recently, tetrathiafulvalene tetrathiolate (TTFtt)[29, 30] has found application as a bridging ligand in bimetallic transition metal complexes[27, 31, 32]. Here TTFtt may be utilized as a formal TTFtt^{4-}, TTFtt^{3-} or TTFtt^{2-} ligand, where the TTF-core is in its neutral, $1+$ or $2+$ state, respectively. While radical TTF^{1+} ligands are well studied and have found applications in the development of SMM[21, 23], the TTFtt^{2-} ligand has only recently been shown to yield significant TTF-based organic biradical character as a bridging ligand in transition metal bimetallic complexes[18]. Further TTFtt^{2-} bridged complexes containing different metal centers have been synthesized and demonstrated to display high photoluminescence quantum yield (PLQY)[33], as well as high conductivity in amorphous, glassy coordination polymers[14].

In this article we perform high-level *ab initio* electronic structure calculations on a series of TTFtt^{2-}-bridged bimetallic complexes. Since singlet biradical states are an example of a problem dictated by strong correlation—arising in systems containing degenerate or near-degenerate orbitals that cannot be described by a single Slater determinant, they require computational treatment with a multi-reference theory. Here, we use the complete active space self consistent field (CASSCF) method, allowing us to capture the singlet biradical character of these complexes accurately. Additional accuracy in the calculation of their singlet-triplet gaps is achieved via the inclusion of dynamic correlation effects with N-electron valence state perturbation theory (NEVPT2)[34] and the anti-Hermitian contracted Schrödinger equation (ACSE)[35–45] theory with cumulant reduced-density-matrix reconstruction[46, 47]. Our calculations allow us to elucidate the interplay between both structural and electronic effects governing the trends in the biradical character and T-S gaps of the bimetallic TTFtt^{2-} compounds. As tuneable biradical character[48] is a particularly desirable property for the design of molecular switches[18, 49, 50], qubits[51–53] and spintronics,[54–57] our work will provide valuable insight for future rational design of TTFtt-based molecules and materials.

9.2 Computational Details

The accurate resolution of the singlet biradical character present in the studied systems requires the use of multi-reference methods. Here, we performed [4,4] active space CASSCF calculations with NEVPT2 as implemented in PySCF[58–60], while larger CASSCF calculations with active spaces as large as [24,24] were performed with the variational 2-RDM (V2RDM) method[61–67]

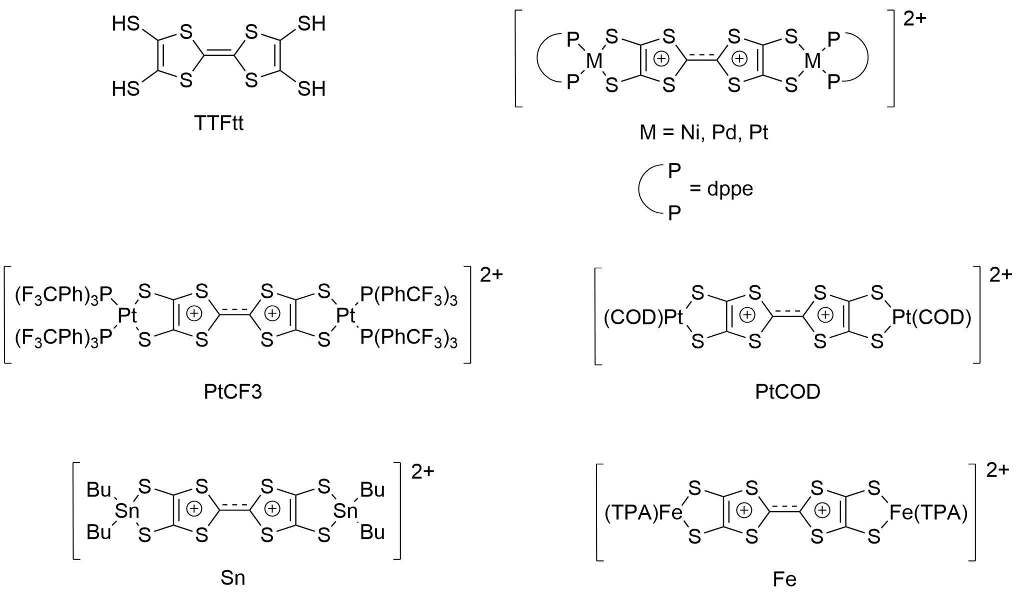

Figure 9.1: Overview of the molecules considered. We refer to the various complexes in the text by the identity of the relevant metal center, and in the case of the two additional platinum complexes with the additional identity of the terminal ligands, i.e. PtCOD and PtCF3.

as implemented in the Maple Quantum Chemistry Package[68, 69]. Additional post-CAS calculations were undertaken on the TTFtt ligand using the ACSE method with the Maple Quantum Chemistry Package, which when seeded with an initial guess from a multi-reference CAS calculation, allows the resolution of the on-top dynamic correlation with an accuracy comparable to that of coupled cluster with singles, doubles and perturbative triples (CCSD(T))[35–37]. Geometry optimizations and frequency calculations were performed using density functional theory (DFT) with the B3LYP[70] and MN15[71] functionals as implemented in Gaussian 16 Revision A.03[72]. The Pople basis sets 6-31G and 6-31G*[73, 74] were used to treat the light atoms H, C, N, P, S, Fe, Ni while the heavy atoms Sn, Pd, Pt were treated using the LANL2DZ[75] and LANL2TZ[76] basis sets. DFT calculations for the fragment analysis were performed with the larger def2-TZVP basis set[77]. Orbital density plots were created using the VESTA program[78].

9.3 Discussion and Results

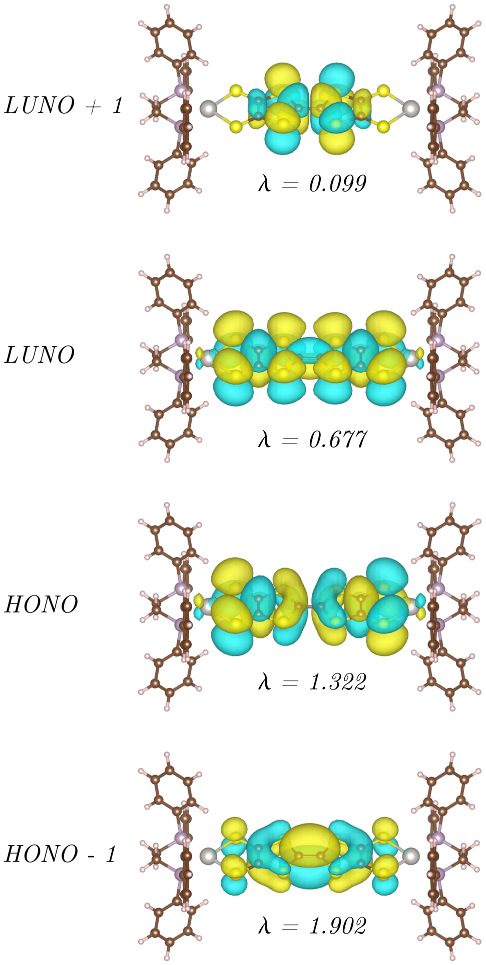

Figure 9.2: Frontier natural orbitals of the PtTTFtt system obtained with [4,4] CASSCF and LAN2LDZ/6-31G basis sets.

To resolve any trends in the biradical character and triplet-singlet (T-S) gaps of bimetallic TTFtt^{2-} bridged complexes, we investigate the electronic structure of a series of complexes which have been recently reported (Pt[33], PtCF3[33], Pd[33], Ni[27], Sn[27], Fe[18]), as well as the newly proposed PtCOD. These compounds are of particular interest in the development of optically addressable molecular qubits or switches and a recent experimental and computational investigation by the authors has shown them to exhibit fluorescent behavior driven by a $\pi^* \rightarrow \pi$ transition of the TTFtt ligand[33]. The chemical structures of all investigated compounds are displayed in

Active Space	[14,14]	[20,20]	[24,24]
ΔE_{T-S}	4.10	2.37	2.00
λE_{LUNO}	0.45	0.46	0.47
λE_{HONO}	1.56	1.57	1.59

Table 9.1: Vertical triplet-singlet gaps and occupations numbers of HONO and LUNO orbitals obtained with V2RDM CASSCF and active spaces of [14,14], [20,20] and [24,24] for the PtTTFtt system. Calculations carried out using the experimental crystal structure geometry and the LANL2TZ/6-31G basis sets.

Basis	LAN2DZ/6-31G	LAN2DZ/6-31G*
$\Delta E_{T-S,CAS}$	7.77	8.01
$\Delta E_{T-S,NEVPT2}$	19.19	20.06
λE_{LUNO}	0.36	0.35
λE_{HONO}	1.64	1.65

Table 9.2: Vertical triplet-singlet gaps and occupation numbers of HONO and LUNO orbitals obtained with [4,4] CASSCF and NEVPT2 for the SnTTFtt system carried out with LAN2DZ/6-31G & LAN2DZ/6-31G* basis sets. Geometry optimized with BS B3LYP & LAN2DZ/6-31G*.

Figure 9.1. First, broken symmetry (BS) DFT geometry optimizations were performed with the B3LYP functional in combination with the LANL2DZ basis set for Pt, Pd, Sn and the 6-31G* basis set for all remaining atoms, relaxing the geometry from the one obtained in the solid state via single crystal X-ray diffraction (XRD). The DFT optimizations were followed by high-level CASSCF and NEVPT2 calculations allowing us to capture accurately the effects arising from both the multi-reference and biradical character and dynamic correlation. A minimal active space comprising 4 electrons distributed in 4 spatial orbitals, [4,4], was chosen for the CASSCF calculations as the strong correlation in these systems has been shown to be limited to two frontier natural orbitals, largely comprised of TTFtt-based π orbitals, that give rise to the biradical character. The active-space natural orbitals of the PtTTFtt system are shown in Figure 9.2. This choice of a limited CASSCF active space is supported by larger V2RDM CASSCF calculations performed on the PtTTFtt system in its XRD geometry using active spaces as large as [24,24], showing no significant changes to the predicted occupations of the highest occupied natural orbital (HONO) and lowest unoccupied natural orbital (LUNO), or the T-S gap (data shown in Table 9.1). The CASSCF and

NEVPT2 calculations utilize the LANL2DZ basis set with its effective core potential for the heavy atoms Pt, Pd, and Sn and the 6-31G basis set for all remaining atoms. Significant changes to natural occupation numbers (NON) and ΔE_{T-S} were not observed with the use of the larger 6-31G* basis set (see Table 9.2).

	Fe	Pt	PtCF3	Ni	Pd	Sn	PtCOD
R(C-C) XRD	1.366	1.399	1.411	1.411	1.421	1.437	
R(C-C) BS	1.371	1.386	1.388	1.390	1.400	1.406	1.409
S^2	0.797	0.541	0.514	0.455	0	0.175	0
$\Delta E_{\text{T-S,CAS}}$	1.14	2.50	3.12	3.50	3.39	7.77	6.09
$\Delta E_{\text{T-S,NEVPT2}}$	2.84	6.67		9.59	8.88	19.19	16.55
$\lambda_{\text{LUNO, S}}$	0.796	0.677	0.630	0.610	0.615	0.359	0.451
$\lambda_{\text{HONO, S}}$	1.203	1.322	1.370	1.390	1.384	1.643	1.550

Table 9.3: Data for the DFT optimized structures. R(C-C) is the length of the central TTF C-C bond with R(C-C) BS obtained from broken-symmetry singlet DFT geometry and R(C-C) XRD obtained from experimental XRD data[18, 27, 33], S^2 is the unrestricted singlet DFT spin contamination in the optimized geometry, $\Delta E_{\text{T-S}}$ denotes the triplet-singlet energy gap, and λ_{HONO} and λ_{LUNO} are the occupation numbers of the HONO and LUNO, respectively.

Table 9.3 displays the vertical T-S gaps for the experimentally surveyed systems and the occupations of their frontier natural orbitals (NOs) based on the BS singlet DFT geometry. The CASSCF/NEVPT2 calculations reveal a significant amount of strong correlation and subsequent biradical character that varies across the different metal centers and ligands. The Fe complex shows the lowest triplet-singlet gap of 2.84 kcal/mol and the correspondingly greatest degree of biradical character with HONO and LUNO occupations of 1.20 and 0.80, respectively. The multi-reference character decreases along the series of Fe $<$ Pt $<$ $PtCF_3$ $<$ Pd $<$ Ni $<$ PtCOD $<$ Sn, with fractionalization of the HONO and LUNO occupations declining to 1.64 and 0.36 in the case of Sn, while the T-S gaps follow the inverse trend and increase across the series to 19.19 kcal/mol in Sn. The trends observed in the NEVPT2 calculations are mirrored by the T-S gaps resolved with CASSCF alone; however, the inclusion of dynamic correlation effects leads to significant stabilization of the singlet state compared to the the triplet and, hence, the gaps predicted by NEVPT2 are of greater magnitude than those calculated from CASSCF.

Inspection of the bond distance between the central TTF C atoms, R(C-C), which follows the trend Fe $<$ Pt $<$ $PtCF_3$ $<$ Ni $<$ Pd $<$ Sn $<$ Pd in the optimized BS geometry, reveals a general correlation between said distance and the calculated $\Delta E_{\text{T-S}}$ and HONO and LUNO occupations. The order of R(C-C) measured via XRD differs only slightly from this, exhibiting the same general order, only switching Pd and Ni, which may be an artifact of the failure of the Pd system to converge to a broken symmetry solution. However, with the exception of Fe there is a general shift to longer R(C-C) lengths in the experimental solid state geometry which suggests that packing and intermolecular interactions arising from the observed π stacking may lead to some minor structural and electronic changes.

Analysis of the frontier NOs reveals that the unpaired electron density is heavily localized in two orbitals of the TTFtt based π-system, with only minimal involvement of metal-centered orbitals. A molecular-orbital diagram for the $PtTTFtt^{2+}$ complex showing the HONO-1 through LUNO+1 orbitals is displayed in Figure 9.2. Additionally, inspection of orbital symmetries reveals the HONO to be of π-antibonding character across the central TTF C-C bond, while the LUNO is of bonding character. The length of the central TTF C-C bond shows variations that closely follow the observed trends in the CASSCF/NEVPT2 calculations: the Fe LT complex displays the shortest C-C distance in both XRD and DFT structures and simultaneously the largest occupation of the π-bonding LUNO, while the Sn analogue displays the longest C-C distance and the greatest π-antibonding HONO occupation.

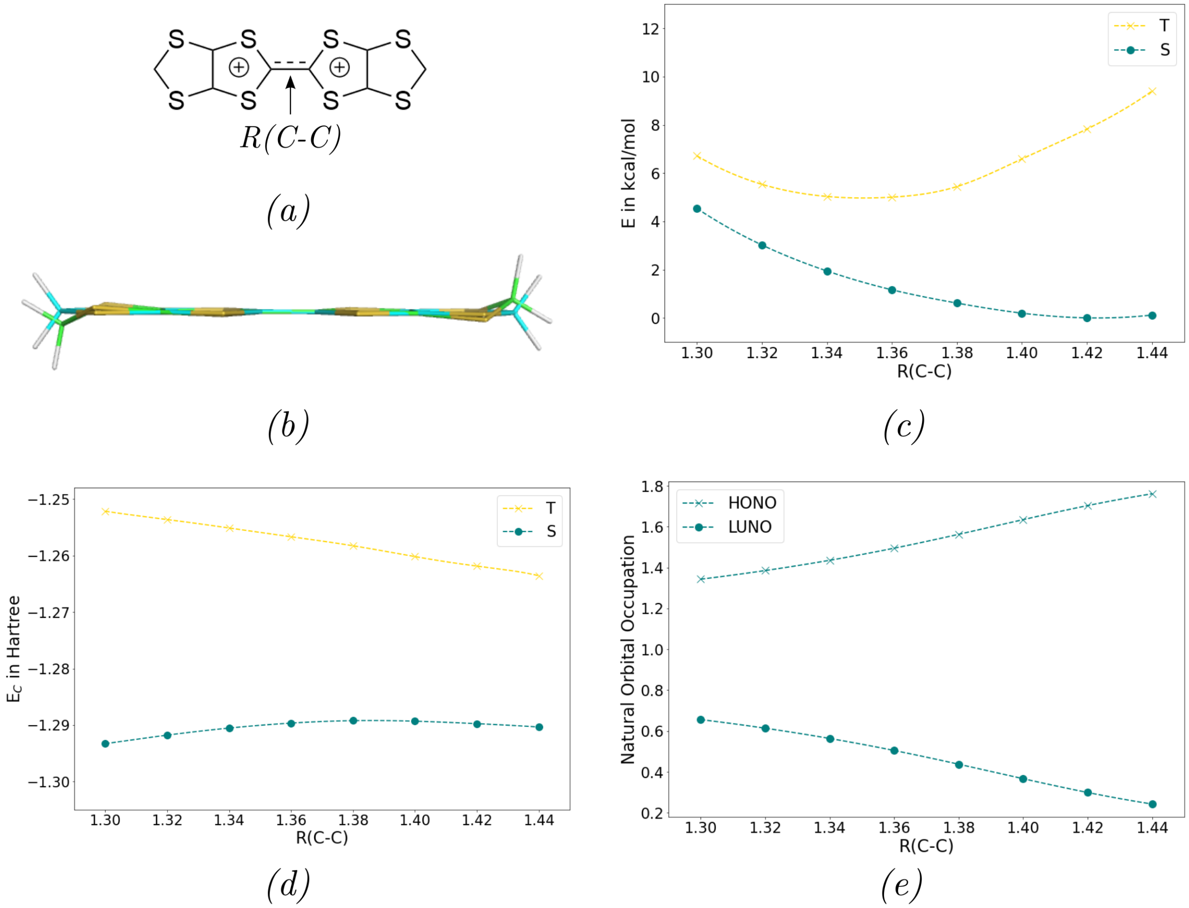

(a)

(b)

(c)

(d)

(e)

Figure 9.3: (a): Structure of the capped TTFtt^{2+} molecule with the central C-C bond, which presents the scan coordinate, indicated. (b): Overlay of the triplet and closed-shell singlet structures at their respective equilibrium geometries with the CH_2 group of the triplet geometry shown in blue and the CH_2 group of the singlet geometry in green. (c): A plot of the ACSE energy of the singlet and triplet states as a function of the central C-C bond length. Geometries at each point are obtained with constrained optimization with the respective multiplicity and the singlet uses broken symmetry. (d): ACSE correlation energies of the singlet and triplet as a function or R(C-C). (e): The HONO and LUNO occupations of the singlet as a function of R(C-C).

9.3.1 Biradical Character Driven Structural Changes to TTFtt

To further investigate how structural changes correlate with the observed biradical character in TTFtt-bridged bimetallics, we performed calculations on CH_2 capped $TTFtt^{2+}$, scanning over the central TTF C-C bond (shown in Figure 9.3 (a)). The smaller size of the capped $TTFtt^{2+}$ allows us to perform high-level ACSE calculations to resolve accurately the effects of both dynamic and multi-reference correlation. As the strong correlation is limited to a set of two frontier π orbitals, the ACSE was seeded with minimal active space [4,4] CASSCF calculations. We utilized the 6-31G basis set and applied the frozen-core approximation.

We investigate C-C distances ranging from 1.30 Å to 1.48 Å in steps of 0.02 Å. For each frozen TTF C-C bond length, the geometry was optimized at the MN15/6-31G* level of theory and both the broken-symmetry singlet and triplet surfaces were evaluated. Figure 9.3 (c) displays the ACSE electronic energy as a function of the C-C bond distance. The data reveals that the structure of $TTFtt^{2+}$ is strongly dictated by its biradical and multi-reference character. The capped $TTFtt^{2+}$ structure shows an equilibrium bond distance of 1.42 Å in the singlet state, which decreases to 1.34 Å in the triplet state. Figure 9.3 (b) displays an overlay of the equilibrium singlet and triplet geometries, showing a clear out-of-plane bending of the terminal S-CH_2-S cap, reducing its overlap with the TTF π system as the biradical character is decreased and the system moves towards being closed-shell. A reduction in R(C-C) results in greater spin contamination in the singlet state and a reduction in the out-of-plane bending. In line with the respective equilibrium bond distances, the vertical T-S gap increases as the bond is stretched.

Further investigation of the total electronic correlation energy (defined as $E_c = E_{\text{ACSE}} - E_{\text{HF}}$, where E_{ACSE} is the ACSE energy and E_{HF} is the Hartree-Fock energy), and HONO and LUNO occupations, which are displayed in Figures 9.3 (d) and (e), respectively, shows a decrease in the magnitude of the correlation energy and a consequent loss of biradical character as the singlet becomes more closed-shell with increasing R(C-C), with the HONO occupation rising from 1.34 at 1.30 Å to 1.76 at 1.48 Å for the broken-symmetry geometry. This trend in the frontier NONs is mirrored by the DFT spin contamination which is reduced with increasing R(C-C) and reaches zero in the long C-C limit of 1.48 Å.

This data strongly suggests that the measurement of the TTF C-C distance by XRD can provide a valuable diagnostic tool in the determination of the degree of biradical character in TTF-based compounds. It may also provide a measure allowing for the comparison or estimation of T-S gaps which scale with increasing C-C distance.

9.3.2 Fragment Orbital Analysis

Lastly, after investigating the correlation between biradical character and TTF C-C bond length we aim to resolve the interaction between the TTFtt^{2-} ligand and the metal fragments. We reoptimized the geometries with spin-restricted DFT to obtain closed-shell geometries, reducing the variations in the structure of the TTFtt^{2-} ligand arising from multi-reference effects, yielding R(C-C)s that vary by only 0.02 Å across the surveyed systems. As expected the use of closed-shell singlet geometries yields lower biradical character and larger T-S gaps; however, the deviations from the broken-symmetry data are minor. The data are displayed in Table 9.4.

To investigate the role of the orbital interaction between the TTFtt^{2-} ligand and the metal fragments in the determination of biradical character and T-S splitting, we perform DFT calculations on separate metal and TTFtt^{2-} fragments in their closed-shell singlet geometry using the B3LYP functional and the larger def2-TZVP basis set for all atoms. The data are displayed in Table 9.4. Analysis of the frontier MO energies of the individual fragments reveals the dominating interaction to be that between the metal fragment based LUMO and the TTFtt^{2-} based HOMO. This interac-

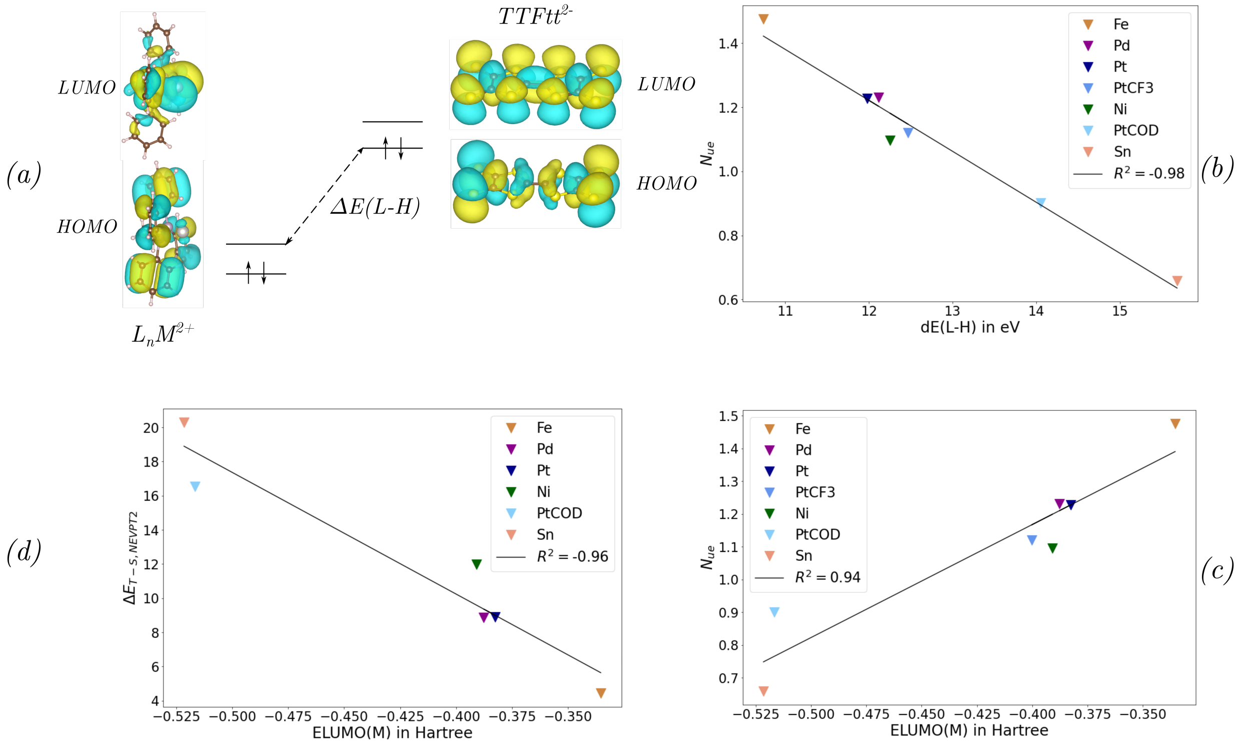

Figure 9.4: Plots showing the scaling of the biradical character with the fragment MO energies in the different TTFtt bridged systems. (a): Diagram of the frontier orbitals of the metal and TTFtt^{2-} fragments, illustrating the interaction between the metal fragment LUMO and the TTFtt^{2-} HOMO. (b): A plot of the biradical character, defined as $N_{ue} = 2 - \lambda_{\text{HONO}} + \lambda_{\text{LUNO}}$, against the energy gap between the metal fragment LUMO and the TTFtt^{2-} HOMO, ΔE_{L-H}. (c): N_{ue} plotted against the energy of the metal fragment LUMO. (d): The NEVPT2 T-S gap, ΔE_{T-S}NEVPT2 of the bimetallic complex plotted against the LUMO energy of the metal fragment.

	Fe	Pd	Pt	$PtCF_3$	Ni	PtCOD	Sn
R(C-C)	1.39	1.40	1.40	1.40	1.40	1.41	1.41
ΔE_{T-S}CASSCF	1.79	3.39	3.39	4.15	4.48	6.09	8.52
ΔE_{T-S}NEVPT2	4.43	8.88	8.91		11.98	16.55	20.29
$\lambda_{\text{LUNO, S}}$	0.74	0.62	0.61	0.56	0.55	0.45	0.33
$\lambda_{\text{HONO, S}}$	1.26	1.38	1.39	1.44	1.45	1.55	1.67
$E_{\text{HOMO, TTF}}$	0.05923	0.05758	0.05782	0.05803	0.05937	0.05746	0.05488
$E_{\text{LUMO,M}}$	-0.33538	-0.38766	-0.38249	-0.40023	-0.39087	-0.51654	-0.5215
ΔE_{L-H}	10.738	12.116	11.981	12.470	12.252	14.056	15.684

Table 9.4: Data for the closed-shell singlet optimized complexes used in the fragment analysis. ΔE_{T-S} denotes the triplet-singlet gap and the λ denote the natural occupation numbers of the bimetallic complex. $E_{\text{HOMO, TTF}}$ and $E_{\text{LUMO,M}}$ denote the energy of the HOMO of the TTFtt^{2-} fragment and the LUMO energy of the metal fragment, respectively, while ΔE_{L-H} denotes the energy difference between these two orbitals.

tion is illustrated in Figure 9.4 (a). We define the number of unpaired electrons in the HONO and LUNO as $N_{ue} = 2 - \lambda_{\text{HONO}} + \lambda_{\text{LUNO}}$, which gives a measure of the biradical character present in a given system, with N_{ue} being equal to 2 in the case of a perfect biradical and 0 in the case of a closed-shell system.

Plotting the orbital energy gap between the metal fragment LUMO and the TTFtt^{2-} HOMO obtained with DFT against N_{ue} from [4,4] CASSCF calculations of the bimetallic complex yields a linear fit with $R^2 = -0.98$ (displayed in Figure 9.4 (b)). Removing the variable of the TTFtt^{2-} LUMO by plotting N_{ue} against the metal fragment LUMO energy (Figure 9.4 (c)) also reveals a linear dependence with a comparable R value of 0.94. This suggests that, bar minor changes to the TTFtt^{2-} orbitals arising from small structural distortions, the degree of biradical character in bimetallic TTFtt^{2-} bridged complexes is determined by the LUMO energy of the terminal metal fragments. As the degree of fractional occupation correlates with the T-S gap, the same trends are observed for $\Delta E_{\text{T-S}}$ with a plot of $\Delta E_{\text{T-S, NEVPT2}}$ against the LUMO energy of the metal fragment shown in Figure 9.4 (d), yielding $R^2 = -0.96$. This data excludes the PtCF3 complex whose size excluded it from NEVPT2 calculations.

While the computational data reveals a near-perfect linear dependence between ΔE_{L-H} of the fragments obtained with DFT and the observed degree of biradical character and $\Delta E_{\text{T-S}}$ calculated with high-level CASSCF and NEVPT2, inspection of the frontier orbitals shows that there is not a good symmetry match between the metal fragment based LUMO and the TTFtt^{2-} HOMO. Instead, inspection of the frontier metal fragment orbitals reveals the LUMO+2 to exhibit the correct π symmetry to ideally interact with the TTFtt^{2-} π system; however unlike in the case of ΔE_{L-H}, analysis of the orbital energies shows no clear correlation with the predicted NONs and T-S gaps. Another more plausible interaction for the trend in biradical character based on chemical intuition would be the interaction of the metal fragment based HOMO with the TTFtt^{2-} LUMO, which would consequently lower the HOMO-LUMO gap in the bimetallic complex. However, inspection of this data again does not yield a good predictive model for the observed NONs and T-S gaps in the bimetallic complexes.

Our fragment analysis reveals a readily implemented one-parameter model that may be used to screen for new terminal ligands and metal centers for the development of bimetallic TTFtt^{2-} bridged complexes with tunable biradical character. Metal fragments with high lying LUNOs yield strongly correlated complexes while those with low energy LUNOs yield closed-shell compounds. Consequently, earlier transition metals, such as Fe(II), yield complexes with strong biradical character and near-degenerate singlet and triplet states, while post-transition metals, such as Sn, yield closed-shell complexes with well separated singlet and triplet states. For a given metal center, the use of strong field ligands and those providing for greater electron delocalization and correspondingly greater splitting of the fragment frontier orbitals yields more fractional occupation of the frontier NOs in the bimetallic complexes, as illustrated by the series Pt $>$ PtCF3 $>$ PtCOD in order of decreasing biradical character. Finally, the biradical character introduced from orbital interactions between the metal and TTFtt^{2-} fragments results in a synergistic geometric change to the TTFtt ligand, with the central C-C bond length being shifted to shorter distances with increasing biradical character, as discussed in the previous section of this article.

9.4 Conclusions

We have performed high-level *ab initio* calculations on a series of recently synthesized and experimentally characterized bimetallic TTFtt-bridged complexes, demonstrating the presence of significant organic TTFtt-based biradical character in their electronic structure that varies with the identity of the metal fragments. To investigate the interplay between biradical character and structural changes to the TTFtt ligand, we performed CASSCF/ACSE calculations on CH_2 capped $TTFtt^{2+}$, revealing correlation between the degree of biradical character and the central TTF C-C bond length. Greater biradical character results in an increase in LUNO occupation accompanied by a corresponding decrease in HONO occupation; as the former is of π bonding character across the central C-C atoms while the latter is π antibonding, an increase in biradical character results in a shorter C-C distance. Comparison with experimental XRD data shows that measurement of this TTF core C-C distance provides a tool for the experimental determination of the multi-reference correlation and biradical character in a given compound and allows for the easy comparison of the biradical properties of TTFtt-bridged species.

Furthermore, we have performed orbital analyses on the different metal and $TTFtt^{2-}$ fragments comprising the various bimetallic systems, revealing a linear dependence of the T-S gap and biradical character of the bimetallic parent compounds on the energy spacing between the metal fragment LUMO and the $TTFtt^{2-}$ based HOMO. As the structural changes to the $TTFtt^{2-}$ ligand are minor compared to the MO changes in the metal fragments, this translates into a linear dependence on the energy of the metal fragment LUNO alone. Consequently, evaluation of fragment MO energies presents a simple one-parameter model for the prediction of biradical character and singlet-triplet splitting exhibited by bimetallic TTFtt bridged complexes, which may be evaluated with DFT at inexpensive computational cost. We demonstrate that increased biradical character may be achieved through the use of higher field ligands or earlier transition metals. Furthermore, since the character of this metal-fragment-based LUNO is largely M-L σ^*, this model provides a very general prediction that stronger sigma donor ligands should lead to more diradical character.

The results presented in this paper provide valuable insight for the rational design of future bimetallic TTFtt linked compounds with desirable properties. Using inexpensive DFT calculations to obtain the orbital energies of metal fragments provides a screening tool in the synthesis of complexes with strong TTFtt based organic biradical character, which are prime candidates in the design of molecular qubits[51, 52] or switches[5, 18], with possible applications in spintronics[54] or quantum information storage[79]. It may also form the basis for the development of future machine learning models for this purpose[80]. Finally, our calculations investigating the correlation between the central TTF C-C bond length and the observed biradical character provide valuable insight into the interplay between structural and electronic effects in this class of compounds and demonstrate that the TTF C-C bond length, which may be experimentally determined via XRD, presents a diagnostic quantity for the degree of organic biradical character present in a given TTFtt based system.

The insight gained from this study informs the design of future TTFtt molecules. Specifically, these findings indicate synthetic chemists can manipulate the TTFtt electronic structure through the manipulation of capping metal orbital energies through selection of different capping ligands. For example, the donor properties of phosphorus-based ligands can be manipulated through different substituents[81, 82]. Thus, these ligands are promising candidates for facile TTFtt electronic structure manipulation, as can be seen when comparing the diradical character and singlet-triplet gaps of Ptdppe and PtCF3.

References

(1) Wudl, F.; Smith, G. M.; Hufnagel, E. J. *J. Chem. Soc. D* **1970**, 1453–1454.

(2) S, H.; G, K.; D, S.; R, Z.; P., C. *Int. J. Sulfur Chem., Part C.* **1971**, 109–122.

(3) Coffen, D. L.; Chambers, J. Q.; Williams, D. R.; Garrett, P. E.; Canfield, N. D. *J. Am. Chem. Soc.* **1971**, *93*, 2258–2268.

(4) Lorcy, D.; Bellec, N.; Fourmigué, M.; Avarvari, N. *Coord. Chem. Rev.* **2009**, *253*, 1398–1438.

(5) Canevet, D.; Sallé, M.; Zhang, G.; Zhang, D.; Zhu, D. *Chem. Commun.* **2009**, 2245–2269.

(6) Martín, N. *Chem. Commun.* **2013**, *49*, 7025–7027.

(7) Jeppesen, J. O.; Nielsen, M. B.; Becher, J. *Chem. Rev.* **2004**, *104*, 5115–5132.

(8) Bryce, M. R. *J. Mater. Chem.* **2000**, *10*, 589–598.

(9) Segura, J. L.; Martín, N. *Angew. Chem. Int. Ed.* **2001**, *40*, 1372–1409.

(10) Bendikov, M.; Wudl, F.; Perepichka, D. F. *Chem. Rev.* **2004**, *104*, 4891–4946.

(11) Martín, N.; Sánchez, L.; Herranz, M. A.; Illescas, B.; Guldi, D. M. *Acc. Chem. Res.* **2007**, *40*, 1015–1024.

(12) Bergkamp, J. J.; Decurtins, S.; Liu, S.-X. *Chem. Soc. Rev.* **2015**, *44*, 863–874.

(13) Fourmigué, M.; Batail, P. *Chem. Rev.* **2004**, *104*, 5379–5418.

(14) Anderson, J.; Xie, J.; Ewing, S.; Boyn, J.-N.; Cheng, B.; Filatov, A.; Ma, T.; Zhao, N.; Itani, R.; Sun, X.; Cho, H.; Patel, S.; Talapin, D.; Park, J.; Mazziotti, D. *Nature Portfolio* **2022**, DOI: `10.21203/rs.3.rs-1281292/v1`.

(15) Narayan, T. C.; Miyakai, T.; Seki, S.; Dincă, M. *J. Am. Chem. Soc.* **2012**, *134*, 12932–12935.

(16) Li, H.; Chang, J.; Li, S.; Guan, X.; Li, D.; Li, C.; Tang, L.; Xue, M.; Yan, Y.; Valtchev, V.; Qiu, S.; Fang, Q. *J. Am. Chem. Soc.* **2019**, *141*, 13324–13329.

(17) Xie, L. S.; Alexandrov, E. V.; Skorupskii, G.; Proserpio, D. M.; Dincă, M. *Chem. Sci.* **2019**, *10*, 8558–8565.

(18) Kawamura, A.; Xie, J.; Boyn, J.-N.; Jesse, K. A.; McNeece, A. J.; Hill, E. A.; Collins, K. A.; Valdez-Moreira, J. A.; Filatov, A. S.; Kurutz, J. W.; Mazziotti, D. A.; Anderson, J. S. *J. Am. Chem. Soc.* **2020**, *142*, 17670–17680.

(19) Soussi, K.; Jung, J.; Pointillart, F.; Le Guennic, B.; Lefeuvre, B.; Golhen, S.; Cador, O.; Guyot, Y.; Maury, O.; Ouahab, L. *Inorg. Chem. Front.* **2015**, *2*, 1105–1117.

(20) Pointillart, F.; le Guennic, B.; Cador, O.; Maury, O.; Ouahab, L. *Acc. Chem. Res.* **2015**, *48*, 2834–2842.

(21) Pointillart, F.; Jung, J.; Berraud-Pache, R.; Le Guennic, B.; Dorcet, V.; Golhen, S.; Cador, O.; Maury, O.; Guyot, Y.; Decurtins, S.; Liu, S.-X.; Ouahab, L. *Inorg. Chem.* **2015**, *54*, 5384–5397.

(22) Shatruk, M.; Ray, L. *Dalton Trans.* **2010**, *39*, 11105–11121.

(23) Cador, O.; Le Guennic, B.; Ouahab, L.; Pointillart, F. *Eur. J. Inorg. Chem.* **2020**, *2020*, 148–164.

(24) Smucker, B. W.; Dunbar, K. R. *J. Chem. Soc., Dalton Trans.* **2000**, 1309–1315.

(25) Bivaud, S.; Goeb, S.; Croué, V.; Dron, P. I.; Allain, M.; Sallé, M. *J. Am. Chem. Soc.* **2013**, *135*, 10018–10021.

(26) Kang, S.; Vignon, S. A.; Tseng, H.-R.; Stoddart, J. F. *Chem. Eur. J.* **2004**, *10*, 2555–2564.

(27) Xie, J.; Boyn, J.-N.; Filatov, A. S.; McNeece, A. J.; Mazziotti, D. A.; Anderson, J. S. *Chem. Sci.* **2020**, *11*, 1066–1078.

(28) Mas-Torrent, M.; Durkut, M.; Hadley, P.; Ribas, X.; Rovira, C. *J. Am. Chem. Soc.* **2004**, *126*, 984–985.

(29) Svenstrup, N.; Rasmussen, K. M.; Hansen, T. K.; Becher, J. *Synthesis (Stuttgart)* **1994**, 809–812.

(30) Rivera, N. M.; Engler, E. M.; Schumaker, R. R. *J. Chem. Soc., Chem. Commun.* **1979**, 184–185.

(31) McCullough, R. D.; Belot, J. A. *Chem. Mater.* **1994**, *6*, 1396–1403.

(32) McCullough, R. D.; Belot, J. A.; Rheingold, A. L.; Yap, G. P. A. *J. Am. Chem. Soc.* **1995**, *117*, 9913–9914.

(33) McNamara, L. E.; Boyn, J.-N.; Melnychuk, C.; Anferov, S. W.; Mazziotti, D. A.; Schaller, R. D.; Anderson, J. S. *Submitted* **2022**.

(34) Angeli, C.; Cimiraglia, R.; Evangelisti, S.; Leininger, T.; Malrieu, J.-P. *J. Chem. Phys.* **2001**, *114*, 10252–10264.

(35) Mazziotti, D. A. *Phys. Rev. Lett.* **2006**, *97*, 143002.

(36) Mazziotti, D. A. *Phys. Rev. A* **2007**, *75*, 022505.

(37) Boyn, J.-N.; Mazziotti, D. A. *J. Chem. Phys.* **2021**, *154*, 134103.

(38) Mazziotti, D. A. *Phys. Rev. A* **2007**, *76*, 052502.

(39) Gidofalvi, G.; Mazziotti, D. A. *Phys. Rev. A* **2009**, *80*, 022507.

(40) Rothman, A. E.; Foley, J. J.; Mazziotti, D. A. *Phys. Rev. A* **2009**, *80*, 052508.

(41) Snyder, J. W.; Mazziotti, D. A. *J. Chem. Phys.* **2011**, *135*, 024107.

(42) Smart, S. E.; Mazziotti, D. A. *Phys. Rev. Lett.* **2021**, *126*, 070504.

(43) Smart, S. E.; Boyn, J.-N.; Mazziotti, D. A. *Phys. Rev. A* **2022**, *105*, 022405.

(44) Boyn, J.-N.; Lykhin, A. O.; Smart, S. E.; Gagliardi, L.; Mazziotti, D. A. *J. Chem. Phys.* **2021**, *155*, 244106.

(45) Boyn, J.-N.; Xie, J.; Anderson, J. S.; Mazziotti, D. A. *J. Phys. Chem. Lett.* **2020**, *11*, 4584–4590.

(46) Mazziotti, D. A. *Chem. Phys. Lett.* **1998**, *289*, 419–427.

(47) Mazziotti, D. A. *Phys. Rev. A* **1998**, *57*, 4219–4234.

(48) Stuyver, T.; Chen, B.; Zeng, T.; Geerlings, P.; De Proft, F.; Hoffmann, R. *Chem. Rev.* **2019**, *119*, 11291–11351.

(49) Buck, A. T.; Paletta, J. T.; Khindurangala, S. A.; Beck, C. L.; Winter, A. H. *J. Am. Chem. Soc.* **2013**, *135*, 10594–10597.

(50) Nakatsuji, S. *Chem. Soc. Rev.* **2004**, *33*, 348–353.

(51) Nakazawa, S.; Nishida, S.; Ise, T.; Yoshino, T.; Mori, N.; Rahimi, R. D.; Sato, K.; Morita, Y.; Toyota, K.; Shiomi, D.; Kitagawa, M.; Hara, H.; Carl, P.; Höfer, P.; Takui, T. *Angew. Chem. Int. Ed.* **2012**, *51*, 9860–9864.

(52) Wedge, C. J.; Timco, G. A.; Spielberg, E. T.; George, R. E.; Tuna, F.; Rigby, S.; McInnes, E. J. L.; Winpenny, R. E. P.; Blundell, S. J.; Ardavan, A. *Phys. Rev. Lett.* **2012**, *108*, 107204.

(53) Timco, G. A.; Carretta, S.; Troiani, F.; Tuna, F.; Pritchard, R. J.; Muryn, C. A.; McInnes, E. J. L.; Ghirri, A.; Candini, A.; Santini, P.; Amoretti, G.; Affronte, M.; Winpenny, R. E. P. *Nat. Nanotechnol.* **2009**, *4*, 173–178.

(54) Zeng, Z.; Shi, X.; Chi, C.; López Navarrete, J. T.; Casado, J.; Wu, J. *Chem. Soc. Rev.* **2015**, *44*, 6578–6596.

(55) Bergenti, I.; Dediu, V.; Prezioso, M.; Riminucci, A. *Philos. Trans. R. Soc. A* **2011**, *369*, 3054–3068.

(56) Zhang, R.; Peterson, J. P.; Fischer, L. J.; Ellern, A.; Winter, A. H. *J. Am. Chem. Soc.* **2018**, *140*, 14308–14313.

(57) Sun, Z.; Zeng, Z.; Wu, J. *Acc. Chem. Res.* **2014**, *47*, 2582–2591.

(58) Sun, Q. et al. *J. Chem. Phys.* **2020**, *153*, 024109.

(59) Sun, Q.; Yang, J.; Chan, G. K.-L. *Chem. Phys. Lett.* **2017**, *683*, Ahmed Zewail (1946-2016) Commemoration Issue of Chem. Phys. Lett., 291–299.

(60) Angeli, C.; Cimiraglia, R.; Malrieu, J.-P. *Chem. Phys. Lett.* **2001**, *350*, 297–305.

(61) Mazziotti, D. A. *Phys. Rev. Lett.* **2004**, *93*, 213001.

(62) Mazziotti, D. A. *Phys. Rev. Lett.* **2004**, *93*, 213001.

(63) Mazziotti, D. A. *Phys. Rev. A* **2002**, *65*, 062511.

(64) Mazziotti, D. A.; Erdahl, R. M. *Phys. Rev. A* **2001**, *63*, 042113.

(65) Mazziotti, D. A. *Phys. Rev. Lett.* **2016**, *117*, 153001.

(66) Mazziotti, D. A. *Phys. Rev. A* **2020**, *102*, 052819.

(67) Schlimgen, A. W.; Heaps, C. W.; Mazziotti, D. A. *J. Phys. Chem. Lett.* **2016**, *7*, 627–631.

(68) Maplesoft, a division of Waterloo Maple Inc., Waterloo, Ontario. **2019**.

(69) RDMChem, Chicago, Illinois. **2019**.

(70) Becke, A. D. *J. Chem. Phys.* **1993**, *98*, 5648–5652.

(71) Yu, H. S.; He, X.; Li, S. L.; Truhlar, D. G. *Chem. Sci.* **2016**, *7*, 5032–5051.

(72) Frisch, M. J. et al. Gaussian 16 Revision A.01, Gaussian Inc. Wallingford CT, 2016.

(73) Hehre, W. J.; Ditchfield, R.; Pople, J. A. *J. Chem. Phys.* **1972**, *56*, 2257–2261.

(74) Kendall, R. A.; Dunning, T. H.; Harrison, R. J. *J. Chem. Phys.* **1992**, *96*, 6796–6806.

(75) Hay, P. J.; Wadt, W. R. *J. Chem. Phys.* **1985**, *82*, 270–283.

(76) Roy, L. E.; Hay, P. J.; Martin, R. L. *J. Chem. Theory Comput* **2008**, *4*, 1029–1031.

(77) Weigend, F.; Ahlrichs, R. *Phys. Chem. Chem. Phys.* **2005**, *7*, 3297–3305.

(78) Momma, K.; Izumi, F. *J. Appl. Crystallogr.* **2011**, *44*, 1272–1276.

(79) Ardavan, A. et al. *npj Quantum Inf.* **2015**, *1*, 15012.

(80) Kulik, H. J. *Wiley Interdiscip. Rev. Comput. Mol. Sci.* **2020**, *10*, e1439.

(81) Tolman, C. A. *J. Am. Chem. Soc.* **1970**, *92*, 2953–2956.

(82) Tolman, C. A. *Chem. Rev.* **1977**, *77*, 313–348.

CHAPTER 10

DIRADICAL PROPERTIES IN TETRATHIAFULVALENE-2,3,6,7-TETRATHIOLATE BIMETALLICS

10.1 Diradical Switching in FeTTFtt

Reprinted in parts with permission from A. Kawamura, J. Xie, J.-N. Boyn, K. A. Jesse, A. J. McNeece, E. A. Hill, K. A. Collins, J. A. Valdez-Moreira, A. S. Filatov, J. W. Kurutz, D. A. Mazziotti, and J. S. Anderson *Journal of the American Chemical Society* **142**, 17670-17680 (2020). Copyright 2020 American Chemical Society.

10.1.1 Introduction

Organic diradicals feature two unpaired electrons which can populate either triplet or open-shell singlet ground states[1]. These unusual species have attracted attention both for their fundamental properties and for applications in organic semiconductors, nonlinear optics, singlet fission, and spintronics[2–5]. Significant progress has been made in generating stable species and in understanding their ground states and electronic structures[6–9]. Tuning or switching diradical character with external stimuli, however, remains challenging[10–15]. This advance is crucial for responsive properties as would be required in spintronics or optical applications. Spin-crossover is a well-known phenomenon in inorganic chemistry[16], particularly in six-coordinate Fe(II) complexes[17–21]. The ability to switch between high-spin ($S = 2$) and low-spin ($S = 0$) states with light (i.e., the LIESST effect)[22–24] or heat makes spin-crossover complexes attractive targets for applications in memory, displays, sensors, and, most relevantly, switches[25]. Combining spin-crossover phenomena with appropriate organic ligands is therefore a compelling strategy for generating switchable diradicals. Merging radical containing ligands with transition metal centers has been an area of active study[26–29]. While several metal-containing organic diradicals have been reported in recent years, these examples are largely limited to transient intermediates or pairs

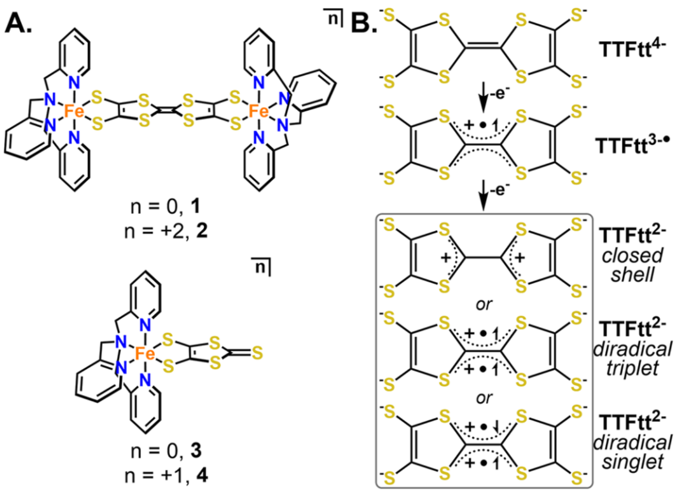

Figure 10.1: (A) Synthesized dinuclear compounds of TTFtt^{n-} and mononuclear dmit^{n-} analogues that serve as half-unit models; (B) Possible redox and spin isomers of TTFtt^{n-} ligands discussed in the text.

of monoradical ligands[30–35]. The viability of spin-crossover modulated diradical character remains untested.

In targeting radical ligands, the archetypal organic electronic material tetrathiafulvalene (TTF) and its derivatives are attractive targets due to their redox activity and electronic properties[36, 37]. Recently, multiple tetrathiafulvalene-2,3,6,7-tetrathiolate (TTFtt^{n-}; n = 4, 3, and 2) complexes have been synthesized[38]. While TTF-based diradicals have not been previously reported, we hypothesized that a compressed π manifold in oxidized TTFtt^{2-} ligands combined with variable π interactions between low- and high-spin Fe centers might enable switchable diradical behavior. Herein, we report the compounds $(\text{FeTPA})_2\text{TTFtt}$ (**1**) (TPA = tris(2-pyridylmethyl)amine) and $[(\text{FeTPA})_2\text{TTFtt}]^{-}[\text{BAr}^{\text{F}}_4]_2$ (**2**) (BAr^{F}_4 = tetrakis[3,5-bis(trifluoromethyl)-phenyl]borate) as well as their monomeric analogues Fe-(TPA)(dmit) (**3**) and $[\text{Fe(TPA)(dmit)}][\text{BAr}^{\text{F}}_4]$ (**4**) (dmit = 1,3-dithiole-2-thione-4,5-dithiolate, Figure 10.1 (A)). Compound **2** represents the first thoroughly characterized example of TTFtt^{n-} ligands coordinated to Fe ions and it exhibits spin-crossover-induced switching of TTFtt^{2-}-based diradical character and is thus an unusual example showing how inor-

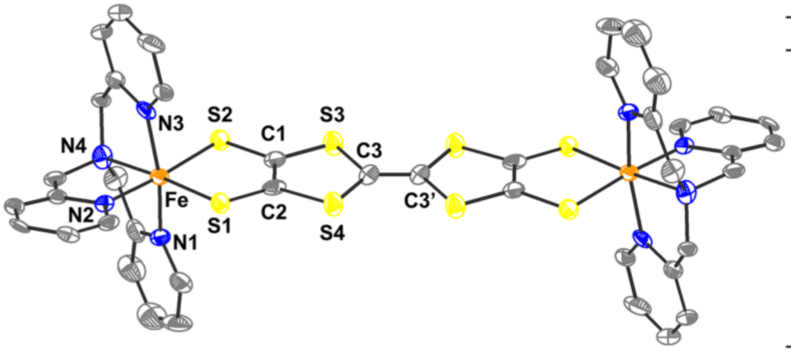

Å	**2-HT**	**2-LT**	Δ (from HT)
Fe–S1	2.368(3)	2.239(2)	−0.129(4)
Fe–S2	2.479(3)	2.289(2)	−0.190(4)
Fe–N1	2.138(8)	1.958(6)	−0.180(10)
Fe–N2	2.168(7)	1.979(6)	−0.189(9)
Fe–N3	2.160(9)	1.976(6)	−0.184(11)
Fe–N4	2.261(8)	2.017(6)	−0.244(11)
C3–C3'	1.408(18)	1.353(15)	−0.05(2)
C3–S3	1.701(11)	1.757(8)	+0.056(14)
C3–S4	1.690(10)	1.719(8)	+0.029(13)

Figure 10.2: Molecular structure for **2** collected at 100 K by SXRD (**2-LT**). H atoms, counterions, and solvent molecules are omitted for clarity, and ellipsoids are shown at 50%. Selected bond length parameters for **2** at 293 K (**2-HT**) and 100 K (**2-LT**)

ganic spin transitions can be used to change organic diradical character.

10.1.2 Experimental Results

The FeTTFtt^{2+} complex was exhaustively characterized. Single-crystal X-ray diffraction reveals significant structural changes between the low temperature (100 K) and room temperature (298 K) measurements. In particular, the bonds between the Fe centers and its ligands (Fe-S and Fe-N) are significantly shortened upon cooling, displaying bond lengths in agreement with those typically observed in low-spin Fe(II) compounds[17, 20]. These temperature dependent structural changes indicate an Fe(II) based spin-crossover process, which has previously been observed in related compounds[17, 24]. Additionally, the central TTF C-C bond is contracted in the LT structure, suggesting involvement of the TTFtt^{2-} ligand in the spin-crossover process.

Further experiments were undertaken to elucidate the temperature driven changes to the electronic structure, with Mössbauer spectroscopy confirming a spin crossover from high spin Fe(II) ($S = 2$) to low spin ($S = 0$) Fe(II) upon cooling. Magnetic susceptibility measurements, displayed in Figure 10.3, reveal two separate regions: high-temperature with high χT and low-temperature

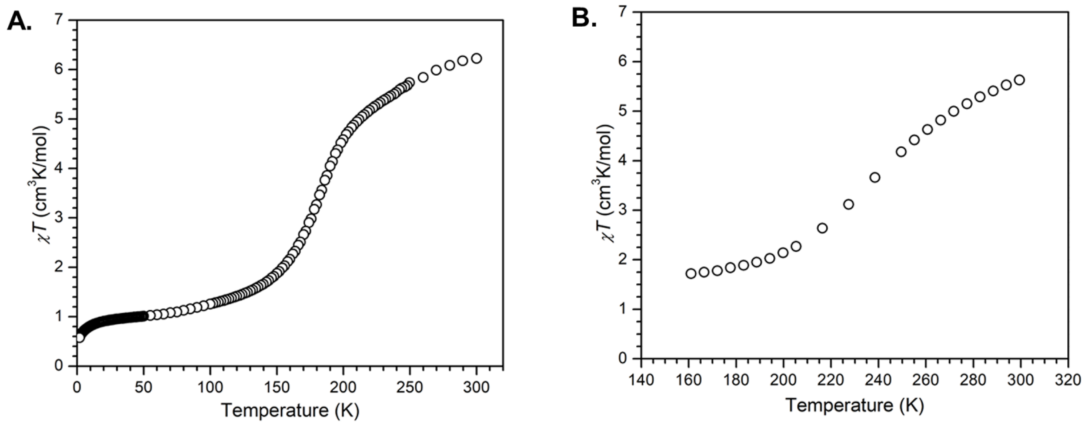

Figure 10.3: (A): Temperature-dependent magnetic susceptibility of **2** in the solid state, collected under an applied field of 0.1 T. (B): Temperature-dependent magnetic susceptibility of **2** in 95% 2-chlorobutane/5% C_6D_6 obtained via the Evans method.

with low χT, separated by spin-crossover. However, the LT measurements continue to show non-zero susceptibility, which due to the fact that the low-spin Fe(II) centers are closed-shell must arise from unpaired spin density on TTFtt^{2-}. This is further corroborated by EPR spectroscopy, which at 15 K in DCM displays an intense signal near $g = 2$, consistent with a $|\Delta m_s| = 1$ transition of an organic $S = 1/2$ or $S = 1$ species and an additional signal at $g = 4$, characteristic of the $|\Delta m_s| = 2$ feature of an organic diradical species with a radical separation in agreement with the distance between the five-center TTF rings. Taken together, the experimental measurements strongly suggest the presence of a TTFtt^{2-} based organic biradical in the **2-LT** structure.

10.1.3 Computational Results

Advanced theoretical techniques were utilized to predict and understand the electronic character of the TTFtt^{2-} ligand. Calculations were performed on **2-LT** using experimental geometries obtained via SXRD. DFT calculations with the B3LYP functional[39] and a 6-311G* basis set[40] as implemented in g16/a.01[41] yielded a triplet ground state with a singlet-triplet gap of $\Delta E(S-T) = 409$ cm^{-1}. The obtained spin density of the triplet state (Figure 10.4) shows the vast majority of the

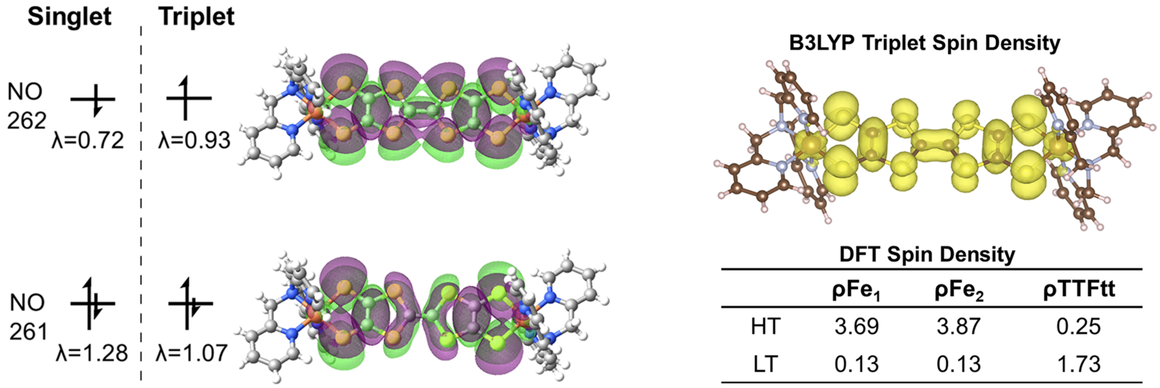

DFT Spin Density

	ρFe_1	ρFe_2	ρTTFtt
HT	3.69	3.87	0.25
LT	0.13	0.13	1.73

(a) (b)

Figure 10.4: (a): Partially occupied frontier NOs and their corresponding NON of **2-LT** from a diradical state [18,20] V2RDM calculation with a 6-31G basis set. (b): Figure: spin density obtained for the triplet state of **2-LT** in DFT with the B3LYP functional and a 6-311G* basis set as implemented in g16/a.01; Table: spin density obtained for the triplet state of **2-LT** and **2-HT** in DFT with the B3LYP functional and a 6-311G* basis set as implemented in g16/a.01. The values for "Fe" includes all density on the FeTPA fragment.

unpaired electron density is localized on the linker with $\rho\text{Fe} = 0.135$ on each FeTPA fragment and $\rho\text{TTFtt} = 1.730$.

Given the fact that DFT is not expected to accurately describe the complex electronic structure of open-shell singlet states, we turned toward advanced theoretical techniques to validate the B3LYP results. Variational two-electron-reduced density matrix (V2RDM) calculations[42–44] were run in the Maple 2019 Quantum Chemistry Package (QCP)[45] with a [18,20] active space and a 6-31G basis set, covering the entire spin manifold of singlet, triplet, quintet, septet, and nonet states. The results predict the ground state of **2-LT** to be a singlet ($\Delta E(S-T) = -373$ cm^{-1}) with strongly correlated, diradical character and frontier natural occupation numbers (NON) of $\lambda_{261} = 1.28$ and $\lambda_{262} = 0.72$ (Figure 10.4 and Table 10.1). Based on the magnetic and spectroscopic data for 2, $\Delta E(S-T)$ should be small, and the magnitude of the computed $\Delta E(S-T)$ from V2RDM is almost certainly overestimated. Inspection of the frontier NOs reveals the diradical to be localized almost exclusively on the TTFtt^{2-} linker with negligible involvement of the Fe d-orbitals, in good agreement with the triplet result from DFT. Hartree-Fock MO coefficients reveal similar distributions. Further calculations were performed to verify that these results were not an artifact of the choice of basis set or orbitals (see Table 10.1).

	[16,14] 6-31G		[14,14] 6-31G*		[16,22] 6-31G*	
	Singlet	Triplet	Singlet	Triplet	Singlet	Triplet
E_{rel}/cm^{-1}	0	210	0	379	0	326
λ_{259}	1.95	1.95	1.92	1.92	1.92	1.92
λ_{260}	1.95	1.94	1.91	1.91	1.90	1.91
λ_{261}	1.25	1.04	1.30	1.06	1.33	1.13
λ_{262}	0.80	1.01	0.71	0.94	0.63	0.85
λ_{263}	0.06	0.06	0.09	0.09	0.09	0.09
λ_{264}	0.06	0.06	0.08	0.09	0.08	0.08

Table 10.1: Energies and NON for [16,14] active space V2RDM calculations with a 6-31G basis set and [14,14] and [16,22] active space calculations with a 6-31G* basis set carried out on the **2-LT** structure.

Additional DFT calculations were performed on the $S = 4$ ground state of **2-HT** (Figure 10.5). In **2-HT** weakening of the interaction between the Fe d-orbitals and the ligand orbitals raises the metal-based orbitals to yield eight singly occupied, Fe-based, frontier NOs. These results show a significant reduction in diradical character in the organic TTFtt^{2-} linker in **2-HT**, as compared to **2-LT**. The unpaired electron density previously localized on the TTFtt^{2-} π system in **2-LT** (ρTTFtt $= 1.730$) is instead in Fe-based NOs in **2-HT**, with ρTTFtt $= 0.25$.

The computational analysis clearly supports the assignment of a TTFtt^{2-}-based, strongly correlated diradical with open shell singlet and triplet states close in energy in **2-LT**. The temperature-driven Fe-based spin transition gives rise to enhanced diradical character on the TTFtt^{2-} core, that is, an increase in the occupancy of the higher-lying NO262 at the expense of decreased occupancy in the lower-lying NO261. The DFT calculations suggest that this arises from the shrinking of the energy gap between the MO261 and MO262 in **2-LT** (19.59 kcal/mol), as compared to the analogous orbitals (MO254 and MO268, respectively) in **2-HT** (26.01 kcal/mol).

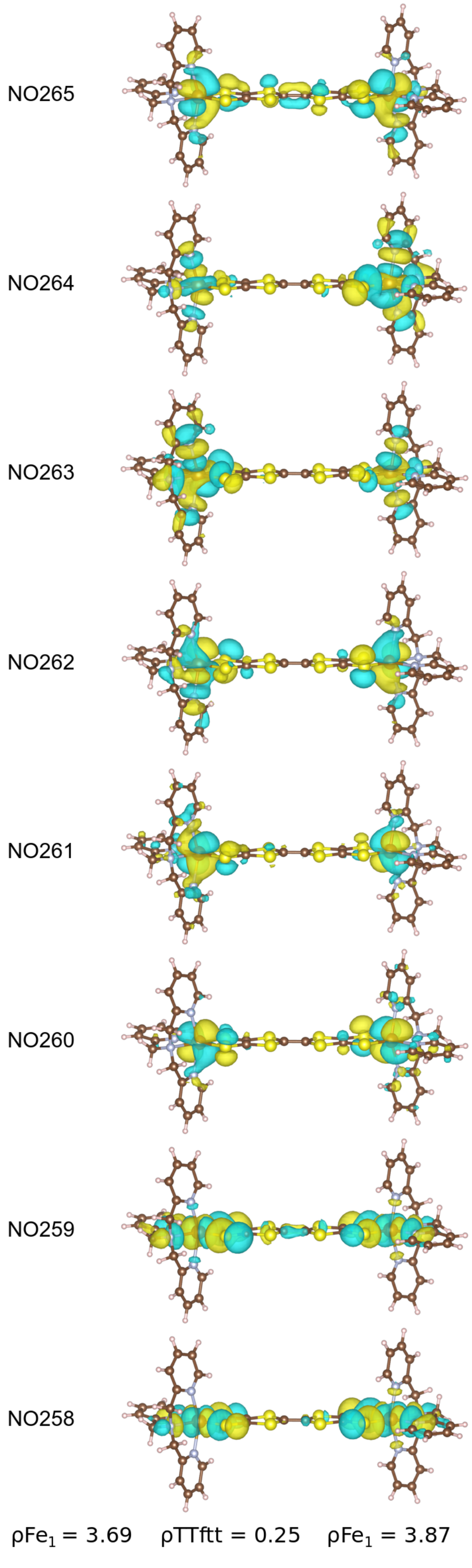

Figure 10.5: Frontier NOs and spin densities obtained for the nonet state of **2-HT** by unrestricted DFT with the B3LYP functional and a 6-311G* basis set as implemented in g16/a.01.

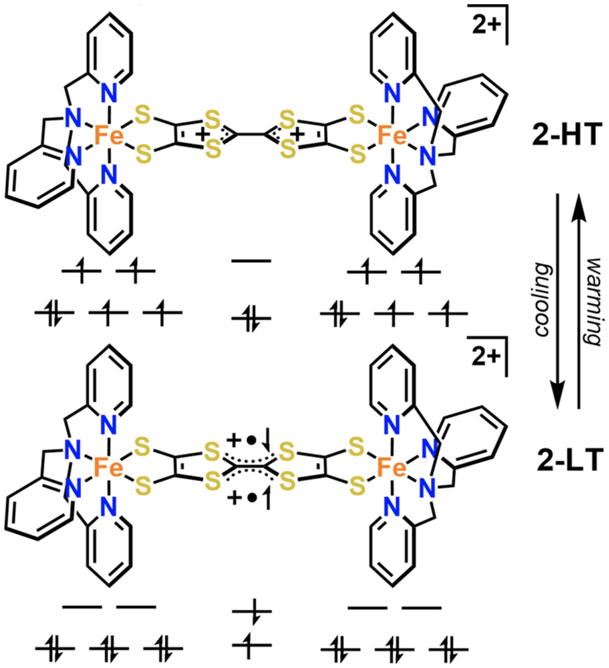

Figure 10.6: Dominant resonance structures for **2-HT** and **2-LT** with qualitative frontier orbital diagrams.

The spin-crossover from **2-HT** to **2-LT** gives rise to enhanced diradical character on the TTFtt^{2-} core. This spin transfer moves electron density from a C-C bonding and C-S antibonding orbital (NO 262 in **2-LT**, NO 268 in **2-HT**) to a C-C antibonding and C-S bonding orbital (NO 261 in **2-LT**, NO 254 in **2-HT**, Figure 10.6). These changes in orbital populations correlate with the observed variations in bond lengths (Figure 10.2) and suggest that there should be bond length changes of similar trend, but of potentially larger magnitude when TTFtt^{2-} undergoes a spin transition as compared to an electron transfer. This is indeed the case when comparing the larger bond length changes of **2** versus those between [(dppeNi)$_2$TTFtt][BAr$^F_4$]$_2$ and [(dppeNi)$_2$TTFtt][BAr$^F_4$][38]. Taken together, all the computational analysis is consistent with the experimental data supporting that an Fe-based spin transition shrinks the gap between TTFtt^{2-}-based orbitals, thereby increasing the organic diradical character.

10.1.4 Conclusions

A family of novel Fe-thiolate compounds with intriguing electronic structures was synthesized and characterized. Theory suggests that **2** shows temperature-dependent Fe-based spin-crossover which decreases orbital energy separations on the TTFtt^{2-} core, generating significant diradical character. This is corroborated by SXRD data illustrating Fe-based spin-crossover alongside distinctive TTFtt^{2-} bond changes. Mössbauer spectroscopy confirms a spin transition at Fe and the assigned Fe(II) oxidation state while variable temperature electronic spectra and magnetic susceptibility support the proposed change from a closed-shell TTFtt^{2-} to a diradical. Finally, the EPR data of **2** reveal signals diagnostic of organic diradicals. Organic diradicals, as seen in **2** at low temperature, are relatively rare in general and are unknown in the well-studied TTF moiety. The reversible modulation of spin between this unusual organic diradical and the Fe centers in **2** represents a fundamentally new form of spin transition and opens the possibility to switch organic diradicals via stimulation of metal-based spin-crossover.

10.2 π-Stacking in Strongly Correlated Highly Conductive Polymers

Reprinted in parts with permission from an article submitted for publication by J. Xie, S. Ewing, J.-N. Boyn, B. Cheng, A. S. Filatov, T. Ma, N. Zhao, R. Itani, X. Sun, H. Cho, S. N. Patel, D. V. Talapin, J. Park, D. A. Mazziotti, and J. S. Anderson (2022), *10.21203/rs.3.rs-1281292/v1*.

Reprinted in parts with permission from J. Xie, J.-N. Boyn, A. S. Filatov, A. J. McNeece, D. A. Mazziotti, and J. S. Anderson, *Chemical Science*, **11**, 1066-1078 (2019). Copyright 2019 Royal Society of Chemistry.

10.2.1 Introduction

Conjugated coordination polymers have attracted recent attention due to promising applications in superconductors[46], energy storage[47–51], thermoelectrics[52–55], spintronics[56–59], and other fields[60–76]. However, delocalized metal–organic systems are still rare and most coordination polymers are limited to architectures constructed with nitrogen and oxygen based ligands[71–80]. Some of the most conductive materials[81–86] in this area have instead used sulfur based linkers which are perhaps best exemplified by dithiolene units that leverage both a better energy match[87–89] between sulfur atoms and metal centers and ligand-based redox activity[57]. Nevertheless, stability and controllable synthetic conditions are still significant challenges associated with the incorporation of dithiolene based linkers. Molecular dithiolene complexes have great utility in addressing these challenges as they allow for a detailed understanding of the properties and reactivity of dithiolene units. Furthermore, molecular dithiolene complexes can be used as transmetalating agents to generate materials in a controlled manner[65, 89].

Of possible dithiolene ligands TTFtt (TTFtt = tetrathiafulvalene-2,3,6,7-tetrathiolate) is attractive as it combines the above mentioned properties of dithiolenes with the favorable electronic properties of tetrathiafulvalene (TTF)[36, 37]. Organic radical salts of TTF and its derivatives are well-known for outstanding electronic properties, being components in organic conductors such as TTF-TCNQ and organic superconductors such as $[\mathrm{TMTSF}]_2[\mathrm{PF}_6]$ (TMTSF: tetramethyltetraselenafulvalene)[90]. While TTF has been incorporated into coordination polymers to improve conductivity[91–94] and enable switching of porosity[95, 96] or magnetism[97, 98], TTFtt has much less precedent in well-defined complexes or materials. Some conductive TTFtt-transition metal chains were reported by IBM Research Laboratory in 1979 with limited characterization data[99]. In 1995, McCullough and coworkers crystalized the first homobimetallic TTFtt complex and the TTFtt unit was proposed as a promising building block for new magnetic, electronic and optical materials[100, 101]. However, there has been little progress towards this end over the fol-

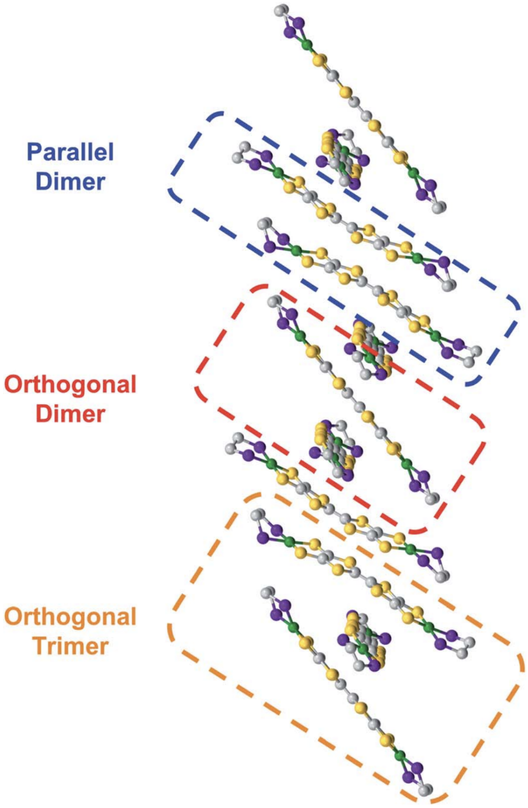

Figure 10.7: Stacking diagram for the twisted polymorph of NiTTFtt$^+$ with phenyl groups, hydrogen atoms, and anions removed for clarity. Ni is shown in green, S in yellow, P in purple, and C in grey. The computationally examined parallel dimer, orthogonal dimer, and orthogonal trimer are indicated.

lowing decades. Only one report of installing TTFtt between fullerene supported Co centers using a decarbonylative process at high temperature has been structurally characterized and limited characterization has been reported on molybdocene fragments bridged by TTFtt[102, 103].

10.2.2 Stacking Properties of TTFtt Bridged Ni Compounds

A novel NiTTFtt$^+$ complex was synthesized and crystallographic analysis revealed a variety of stacking arrangements of the TTF cores. It crystallizes in the in the triclinic space group $P\bar{1}$ with bond lengths typical of those observed in TTF-derivatives in their singly oxidized state[104]. Importantly, NiTTFtt$^+$ forms extended one dimensional chains via weak side-to-side sulfur-sulfur interactions, in addition to significant $\pi - \pi$ stacking. This is in line with known TTF systems and much of the bulk transport properties of TTF based systems arises from their π–π and sulfur–sulfur interactions in the solid state, particularly in single component conductors[36, 37, 90–94, 105–114]. Further analysis of EPR and magnetic moment measurements, which revealed a lower value than expected for the spin-only value of an isolated complex, suggest $\pi - \pi$ interaction driven dimerization or oligomerization is taking place in solution. Additionally, a poorly diffracting alternative polymorph of NiTTFtt$^+$ was isolated and XRD analysis revealed a stacking interaction which has a twist of the TTF cores by a nearly orthogonal 90°. Compared to TTF's usual parallel stacking, this is a rather uncommon structure composed of two different elements: trimers with asymmetric orthogonally crossed interactions and dimers with more typical parallel interactions. The different stacking arrangements are displayed in Figure 10.7.

	Parallel	Orthogonal
E(a.u.)	-16430.761095	-16430.712292
λ_{382}	1.886	1.912
λ_{383}	1.499	1.225
λ_{384}	0.513	0.771
λ_{385}	0.085	0.073
q_1	0.406	0.378
q_2	0.569	0.435
q_3	0.570	0.454
q_4	0.403	0.439

Table 10.2: Energies, NO occupations and Mulliken charges for the two different dimerization geometries. V2RDM calculations with a [18,20] active space and 3-21G basis set.

We then undertook calculations on NiTTFtt$^+$ as a model for the effect of the twisted TTF–TTF interactions. A detailed investigation of the interactions in the dimer and trimer units and, particularly, how the twisting of the TTF–TTF interaction affects their electronic structure, requires large scale CASSCF calculations with extensive active spaces, leading to prohibitively high computational costs with conventional methods. Instead, we employed variational 2-electron reduced density matrix (V2RDM) techniques[115], which have previously been demonstrated to successfully

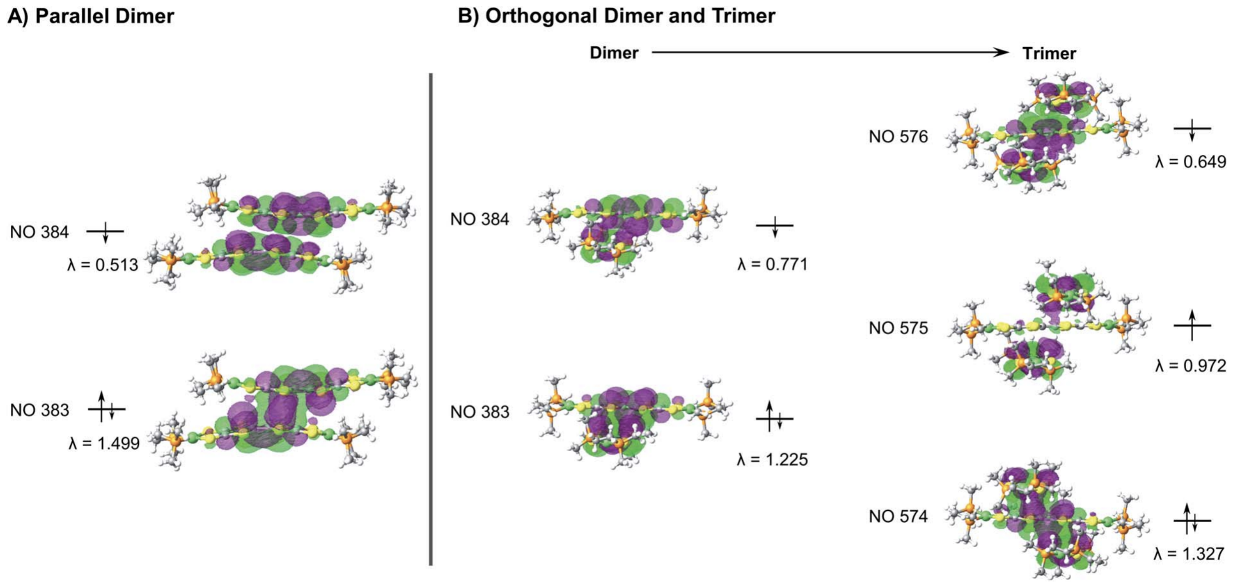

Figure 10.8: Frontier NO occupations and densities for (A) the parallel dimer, showing the splitting into bonding and antibonding orbitals. Data and densities obtained via [18,20] V2RDM calculations with a 3-21G basis set. (B) For the orthogonal dimer and trimer. Good overlap and correspondingly small splitting in the orthogonal dimer give way to a clear splitting into bonding, non-bonding and antibonding frontier NOs upon transitioning to the orthogonal trimer. Data and densities obtained via V2RDM calculations with a 3-21G basis set and [18,20] and [17,20] active spaces for the dimer and trimer respectively.

describe the electronic structure of a variety of strongly correlated large molecules[116]. V2RDM calculations were carried out as implemented in the Maple Quantum Chemistry Package[45]. The phenyl ligands were replaced with methyl groups and [18,20] active space V2RDM calculations with the 3-21G basis set were performed for both geometries with the data shown in Table 10.2. The electronic structures of both arrangements show significant degrees of correlation as demonstrated by partial occupancies in their frontier natural orbitals (NOs). The orthogonal arrangement shows more radical character, with frontier orbital natural occupation numbers (NON) of 1.225 and 0.771 suggesting significant biradical character, compared to 1.499 and 0.513 in the parallel arrangement. Mulliken charges show an effective charge of +1/2 for the Ni centers in both geometries, with a slightly higher cumulative charge of 1.947 in the parallel arrangement compared to 1.706 in the orthogonal system.

Frontier orbital densities, occupations and splittings for the parallel dimer and orthogonal dimer and trimer are shown diagrammatically in Figure 10.8 A and B, respectively. All frontier NOs are localized on the bridging ligand with no involvement of the Ni centers, consistent with experimental results. There are significant differences in the orbital configurations elucidating the variation in frontier NON across the two arrangements. The larger splitting of the NO occupancy in the parallel arrangement clearly arises from better orbital overlap between the two monomers, allowing for greater energetic orbital splitting into NO 384 with significant antibonding character, showing no overlap between the two monomers, and NON 383 with significant bonding character and orbital overlap. In contrast, the orthogonal dimer shows two frontier NOs with very similar densities, both showing significant bonding character and overlap between the two monomers, yielding a smaller splitting and correspondingly greater biradical character.

	Trimer
E(a.u.)	-24645.905214
λ_{573}	1.930
λ_{574}	1.327
λ_{575}	0.972
λ_{576}	0.650
λ_{577}	0.065
q_1	0.442
q_2	0.449
q_3	0.435
q_4	0.434
q_5	0.444
q_6	0.437

Table 10.3: Energies, NO occupations and Ni atom Mulliken charges for the trimer unit. V2RDM calculations were performed with a [17,20] active space and 3-21G basis set.

As the orthogonal dimeric arrangement is actually part of a larger asymmetrically stacked unit, a trimeric unit was run separately in V2RDM using a [17,20] active space and the 3-21G basis set, giving a SCF calculation with 1308 orbitals. Data are shown in Table 10.3. Similar to the dimeric case, the trimer unit exhibits clear radical character and three partially occupied NOs with NON of

1.327, 0.972 and 0.649. Mulliken charges in this arrangement are particularly symmetric with each nickel showing a charge of 0.43 to 0.45 with very little variation between the individual centers. Transitioning from a dimeric to a trimeric unit gives rise to splittings and symmetries in line with a classic Huckel picture with the orbitals splitting into bonding, non-bonding and antibonding. The bonding and antibonding orbitals NO 574 and 576 both show roughly equal distribution of the electron density across all three units within the trimer. NO 574 has good matching of the phases between the orbitals localized on each of the units in the trimer leading to overlap between the orbitals on all units and giving rise to significant bonding character and a NO occupancy of 1.327. Constituent orbitals of NO 576 in contrast constitute a worse matching of the phases, reducing overlap between the individual units and leading to an overall antibonding interaction and a NO occupancy of 0.649. The singly occupied nonbonding NO 575 is localized on the top and bottom molecules with a nodal plane and negligible density on the central unit, leading to an electron entangled across the two isolated top and bottom units within the trimer.

The results from V2RDM CASSCF calculations help rationalize the appearance and stability of the different morphologies in the TTFtt stacks. Packing geometries in both the parallel and orthogonal arrangement allow for good orbital overlap between the individual units. Both morphologies show the frontier natural orbitals form via π–π stacking utilizing orbitals localized on the TTF linkers. The resulting NOs differ slightly between the different morphologies with overlap in the parallel geometry allowing for better splitting into clear bonding and antibonding frontier orbital pairs, reducing radical character. The splitting is less pronounced in the orthogonal dimer; however, as the chain size increases clear splitting into bonding, non-bonding and antibonding frontier orbital pairs is recovered in the trimer. In all cases partial occupancy in the frontier NOs is retained, allowing for radical chain development and electron entanglement across multiple units.

The stacking of the TTFtt-based radicals in NiTTFtt^{+} highlight the key role of strong intermolecular interactions between radicals in the control of morphology. In sum, the stabilization and synthetic access provided by the Sn capped compounds reported here enables the observation of a variety of solid-state interactions of the TTF core. We anticipate that the redox flexibility of these synthons will enable the observation of novel interactions and electronic structures in TTFtt based coordination polymers.

10.2.3 An Intrinsically Glassy Metallic Coordination Polymer Showing Thermally and Aerobically Robust Conductivity

Using molecular design to engender high conductivity in undoped amorphous materials would enable tunable and robust conductivity in many applications, but there are no intrinsically conducting organic materials which maintain high conductivity when completely disordered. Inorganic glassy metals have been discovered but require careful fabrication[117]. Furthermore, the relationship between metallic behavior, which classically requires periodicity giving rise to a well-defined band structure, and geometric disorder in these materials is still unclear[118]. Electron-rich and redox-active tetrathiafulvalene (TTF) motifs feature prominently as molecular building blocks in conducting materials[119]. Appending thiolate groups to TTF to generate tetrathiafulvalene-tetrathiolate (TTFtt) enables the formation of extended coordination polymers that combine the properties of TTF with the rich electronic structures of transition metal dithiolenes[120]. While the promise of these materials has been recognized, their structure, purity, composition, and hence properties are not well-defined due to synthetic challenges[121].

The novel coordination polymer Ni tetrathiafulvalene-tetrathiolate (NiTTFtt) was synthesized (Figure 10.9 (A)) and experimentally characterized. Powder X-ray diffraction (PXRD) data suggests that the material is completely amorphous and that the interchain interactions in NiTTFtt are irregular. Despite its amorphous nature a structural model was built based on experimental data

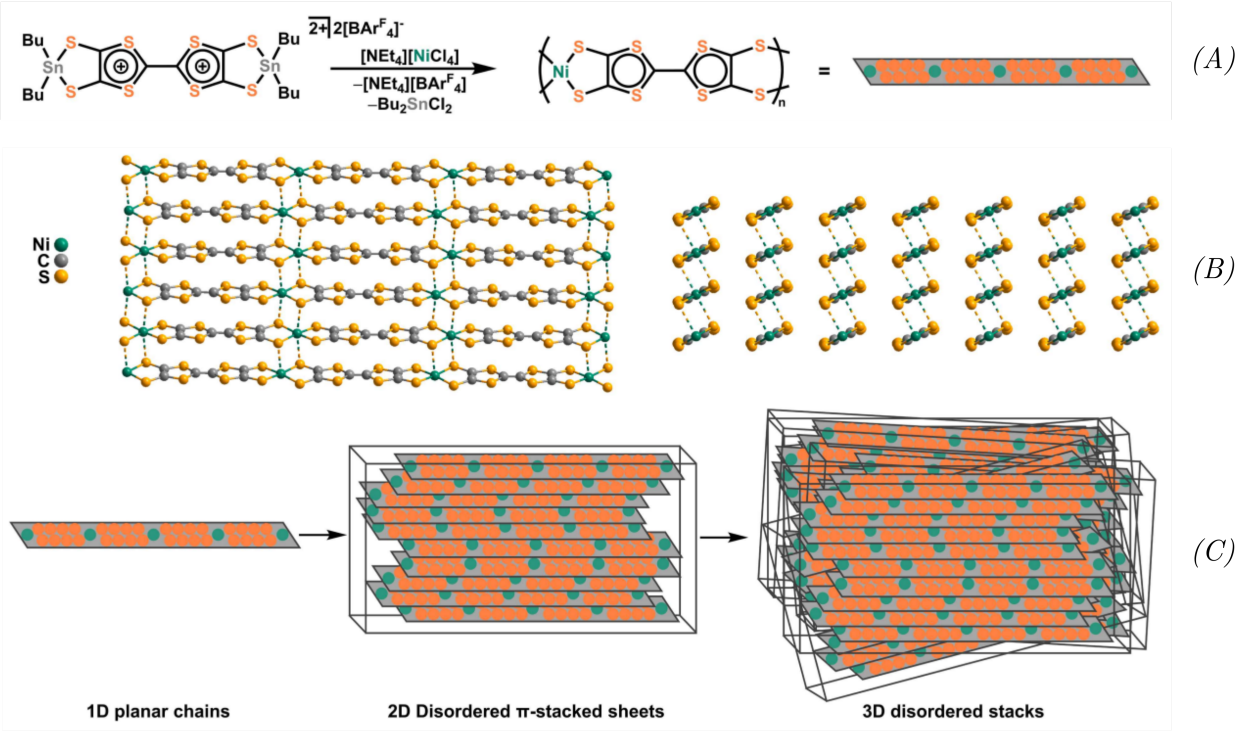

Figure 10.9: Synthesis and structure of NiTTFtt. (A): Synthetic scheme; (B) Modeled structure; (C): Hierarchical structure showing molecularly ordered chains but disordered packing in sheets and stacks.

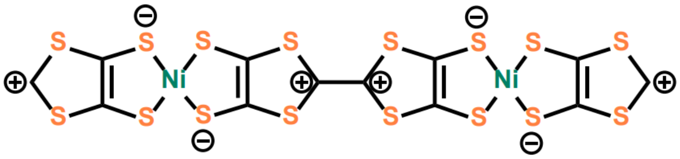

Figure 10.10: The bimetallic fragment of the NiTTFtt polymer used for the molecular model calculations.

(Figure 10.9 (B)) obtained from more crystalline NiTTFtt. This unit cell constrains the model to staggered chain packing and the pairwise distribution function (PDF) data suggests S–S distances of ≈ 3.4-3.7 Å along the π-stack and ≈ 3 and 4 Å side-to-side between chains. These values are similar to those observed in the single-component molecular metal, [Ni(tmdt)2] (tmdt, trimethylene-tetrathiafulvalene-dithiolate)[105], and also support tight packing as previously proposed[122]. Based on this model, the disordered structure of NiTTFtt arises from 1D chains that pack face-to-face to generate disordered 2D sheets which then pack side-to-side to generate a 3D structure (Figure 10.9 (C)). Despite its disordered structure, NiTTFtt exhibits remarkably high electronic conductivity (1280 S/cm) and intrinsically glassy metallic behavior. Its unusual set of structural and electronic features results in remarkably stable organic conductivity which is maintained in air for weeks and at temperatures up to 140°C.

To elucidate the electronic inter-layer interactions allowing for conductivity in the amorphous material, variational 2-RDM (V2RDM) complete active space self consistent field (CASSCF)[115] calculations were carried out on a molecular model based on the PXRD structure (displayed in Figure 10.10). An inter-layer distance of 3.35 Å was chosen based on the average distance measured in the structure. Several calculations were run on the model to investigate the dependence of the electron correlation present in the extended solid based on the orientation of the individual NiTTFtt units. Investigated geometries include: (i) two units symmetrically stacked on top of each other (**top**), (ii) a 1 Å shift parallel along the central TTF C-C bonds (**para**), (iii) a 1 Å shift perpendicular to the central TTF C-C bonds (**perp**), and (iv) a twist by an angle of 10 degrees over the central

	B3LYP/6-31G*			[20,20] V2RDM/6-31G						
	ΔE	ΔH	ΔE_{MO}	ΔE	ΔH	E_c	λ_{385}	λ_{386}	λ_{387}	λ_{388}
top			32.88			-246.43	1.70	1.55	0.41	0.29
para	-6.3	-3.99	20.88	-33.43	-31.64	-291.03	1.56	1.19	0.84	0.42
perp	-4.8	-3.1	26.87	-25.5	-24.9	-259.33	1.60	1.34	0.63	0.20
angle	0.8	2.0	34.54	-10.7	-9.5	-255.60	1.68	1.55	0.44	0.33

Table 10.4: Electronic energy and enthalpy differences (in kcal/mol) of the parallel (para), perpendicular (perp) shifted and 10 degree twisted (angle) structures versus the symmetrically aligned (top) structure. ΔE_{MO} denotes the LUMO-HOMO gap in millihartree, E_c denotes the electronic correlation energy, defined as $E_{V2RDM} - E_{HF}$ in millihartree, and λ_N denotes the occupations of the *N*th natural orbital.

TTF C-C bonds (**angle**).

The results for B3LYP[39]/6-31G*[123] with the GD3BJ[124] dispersion correction and [20,20] active space V2RDM/6-31G calculations are displayed in Table 10.4. DFT calculations show a shallow potential energy surface around the symmetrically aligned structure, with shifts in both the parallel as well as perpendicular directions with respect to the central TTF C-C bonds being favorable, while a 10-degree twist over the on-top aligned TTF C-C bonds is slightly unfavorable. This result agrees with observations made from the X-ray crystal structure of [(Nidppe)$_2$TTFtt][BAr^{F_4}][125], which displays both parallel and perpendicular displacements of the individual NiTTFtt units.

As similar molecular systems containing TTFtt^{2+} units have previously been shown to exhibit multi-reference correlation in their electronic structure, and as such DFT is not sufficient for their description, further analysis was carried out with [20,20] V2RDM calculations. Indeed, our calculations show that all model systems display multi-reference correlation, with the degree of biradical character exhibited depending on the alignment of the two units. Figure 10.11 displays the highest occupied natural orbital (HONO) and lowest unoccupied natural orbital (LUNO) and their occupation numbers (NON) for each of the three studied spatial arrangements. The symmetrically aligned **top** structure exhibits the lowest degree of multi-reference character, however, with

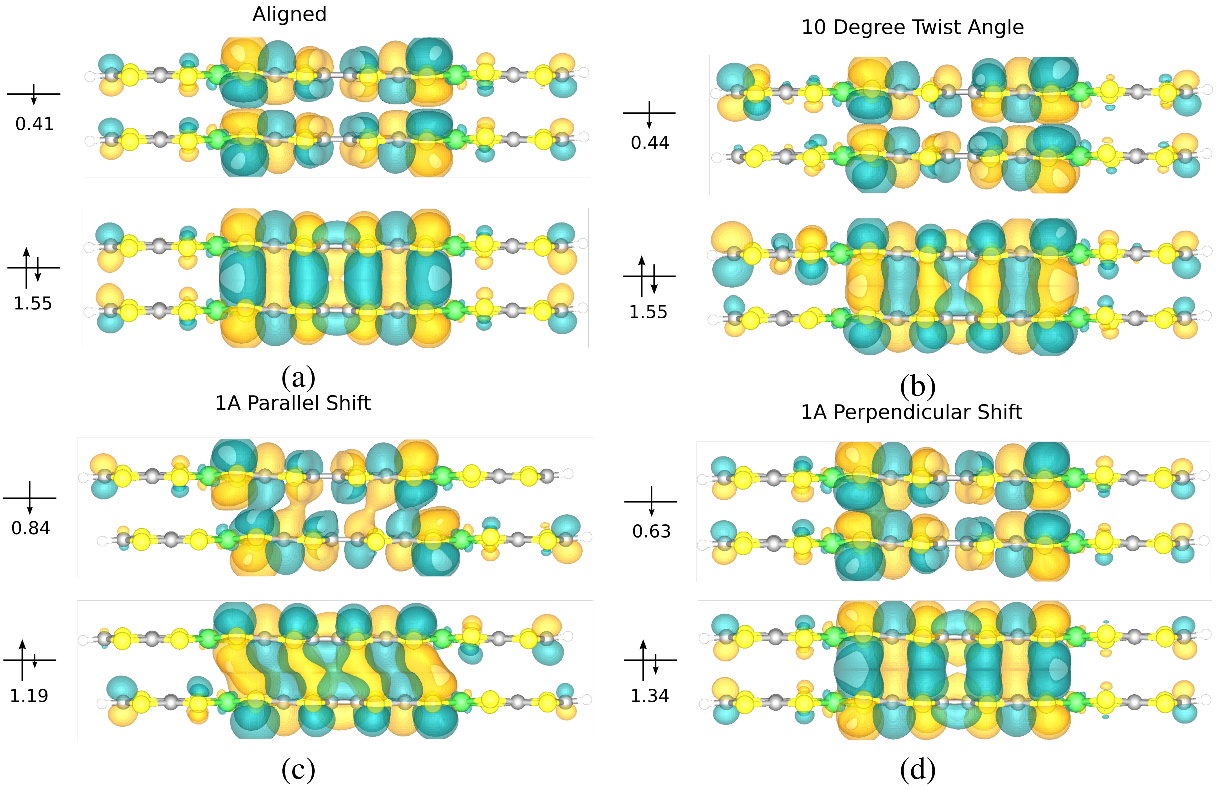

Figure 10.11: Frontier natural orbitals and their occupation numbers for the model system: (a): symmetric stacking (**top**); (b): 10° rotation over the central TTF C-C bond (**angle**); (c): parallel shift by 1Å (**para**); (d): perpendicular shift by 1Å (**perp**).

HONO and LUNO occupations of 1.55 and 0.41, it nonetheless displays a significant amount of strong correlation and biradical character. In this arrangement the HONO and LUNO split into one orbital that is clearly bonding across the π-stack and shows good overlap across the two individual NiTTFtt units, the HONO, and one orbital that is anti-bonding across the π-stack and shows no density bridging the two individual units, the LUNO.

Both parallel, as well as perpendicular displacements of the individual NiTTFtt units result in significant increases in multi-reference correlation. The **para** structure exhibits near-biradical NON of 1.19 and 0.81 for the HONO and LUNO, respectively, and additional significant fractionalization in the HONO-1 and LUNO+1, which display NON of 1.56 and 0.42 as compared to 1.70 and 0.29 in the **top** structure. The **perp** arrangement shows slightly less significant but still noteworthy changes to the HONO and LUNO occupations with $\lambda_{\text{HONO}} = 1.31$ and $\lambda_{\text{LUNO}} = 0.63$. In both cases these changes in the NON are accompanied with corresponding changes to the natural orbitals and in both shift arrangements we observe inter-unit overlap in the LUNO along the π-stacking axis. Lastly, the introduction of a 10-degree twist angle shows no significant changes in the frontier natural orbital occupations and the natural orbital densities. The trends displayed by the NON mirror those of the LUMO-HOMO gaps calculated with DFT; ΔE_{MO} decreases as we shift the NiTTFtt units and fractionalization in the V2RDM HONO and LUNO increases.

This analysis reveals that the molecular fragments of NiTTFtt exhibit significant orbital overlap and strong correlation that is remarkably robust to disorder and the computations explain how metallic character is preserved in amorphous NiTTFtt: periodicity is disrupted by small scale structural disorder, but these defects are not significant enough to disrupt overlap, correlation, and delocalization. These results demonstrate that the use of molecular units that have strong overlap, and subsequently strong electronic delocalization, can lead to metallic character even in completely amorphous materials, and suggest that such organic materials can be composed of complex and tunable molecular building blocks, yielding thermally and aerobically stable organic conductors.

10.3 High Quantum Yield near-IR Flouresence

Reprinted in parts with permission from an article submitted for publication by L. E. McNamara, J.-N. Boyn, C. Melnychuk, S. W. Anferov, D. A. Mazziotti, R. D. Schaller, and J. S. Anderson (2022).

10.3.1 Introduction

Molecular near-infrared (NIR) dyes and lumiphores have gained recent attention due to their promising applications in biological imaging[126–131] and the development of lasers[132], detectors[133], and organic light-emitting diodes (OLEDs)[134]. The NIR region (700 nm - 1700 nm) falls in the tissue transparent window, so NIR emitters are often implemented for in vivo, in vitro, and in intraoperative imaging applications[126–131, 135–137]. For these applications, the main challenges facing current NIR dye development are autofluorescence, scattering, and water overtones[126, 138]. Both auto fluorescence and scattering are dramatically reduced in the NIR II region, but water absorptions at $\sim$ 1400 nm pose a significant obstacle for many NIR dyes which frequently have low photoluminescence quantum yields (PLQY)[126, 138].

The physical underpinnings of emission in the NIR region makes low PLQYs a considerable challenge facing current dye candidates[126, 136, 137, 139]. PLQYs are limited by the energy gap law, which states that nonradiative decay rates exponentially increase for low energy transitions[140, 141]. For molecular organic NIR dyes, these nonradiative rate limits are often dominated by C–H stretching frequencies[126, 140, 141]; however, large conjugated systems are frequently required to enable low-energy absorption and emission, and eliminating higher energy vibrational modes (i.e. C-H groups) poses significant synthetic difficulties.

These limitations on PLQY make the development of efficient NIR dyes challenging. Only two NIR dyes, indocyanine green (ICG) and methylene blue (MB), have been approved by the U.S. FDA, and both emit around 700 nm - 800 nm where autofluorescence and scattering can be problematic[126, 127, 142–144]. In addition to these thiazine and cyanine dyes, donor-acceptor-donor (D-A-D) and polymethine dyes have also been explored to further red-shift emission into the NIR II region[145–147]. While they are often synthetically challenging, such donor-acceptor and D-A-D systems have recently been successfully employed to synthesize the first molecular NIR dyes with emission maxima $\geq$ 1200 nm[148, 149]; however, these dyes exhibit extremely low PLQYs ($\leq$0.05%). Furthermore, efforts to increase the water solubility of large D-A-D systems often result in dramatically decreased PLQYs in aqueous solution. For example, the first water soluble D-A-D dye, CH1055-PEG, exhibited a $\sim$20 fold PLQY decrease in water compared to that of the parent compound (CH1055) in toluene[139].

In addition to D-A-D systems, polymethine dyes are also promising candidates for bright NIR II emission. IR 26 is the brightest commercially available molecular dye with an emission maximum $\geq$1100 nm[142]. While this dye emits around 1130nm in 1,2-dichloroethane, it still exhibits a limited PLQY (0.05%) due to the low emission energy[150]. Aside from poor PLQY values, the molecular size and complexity required to red shift emission into the NIR region poses significant synthetic and solubility challenges[135–137]. The requirement for large conjugated molecular systems makes rationally designing stimuli responsive chromophores, for instance those that turn on or off in specific chemical or electrochemical environments, extremely challenging[135–137]. It would be advantageous to generate a compact and hence modular NIR II emitting moiety with high PLQY that could be tuned for some of these responsive applications.

The recently studied tetrathiafulvalene-2,3,6,7-tetrathiolate (TTFtt) bridged bimetallic com-

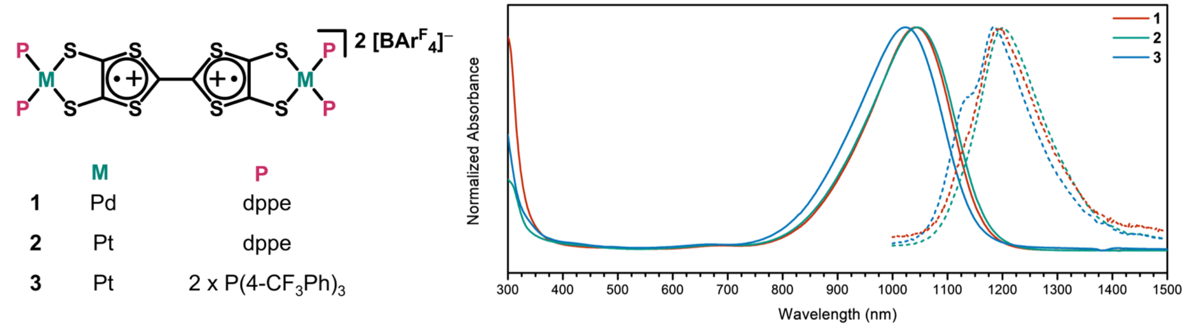

Figure 10.12: Left: TTFtt bimetallic cations discussed in this section. Right: Normalized UV-Vis-NIR (solid) and photoluminescence (dashed) spectra of **1**, **2**, and **3** in DCM at 298 K.

plexes displayed distinct NIR absorbances of the doubly oxidized diradical TTF cores, arising from comparatively weak C–S π-bonding resulting in a compressed π manifold[125, 151]. It is hypothesized that the synthesis of heavy metal analogues of these complexes could result in NIR emission from this π system. The stability, tunability, and modularity of these complexes suggests they are promising new candidates for the development of tunable, responsive, and bright NIR dyes.

10.3.2 Experimental Summary

Three novel diradical TTFtt complexes of Pd and Pt were synthesized and their structures are displayed on the left hand side of Figure 10.12. Photophysical measurements revealed extremely bright emission that arises from the unusual geometric and electronic structure of the TTFtt core. The emission is extremely photostable, persists in ambient conditions and aqueous mixtures, and is redox-switchable for several cycles. As observed in other TTFtt dicationic complexes[125, 151], **1-3** all have intense NIR absorbances at ~1000 nm, which can be assigned to low energy $\pi - \pi$ transitions (right hand side of Figure 10.12). The molar absorptivity of these features is ~80,000 $M^{-1}cm^{-1}$. Such strong absorbance is valuable in capturing a larger fraction of incident light to maximize emissive properties. Despite changing metal centers and ligands, these absorbances are nearly superimposable and shift only minimally across analogues. Upon NIR excitation (900 nm) all three complexes exhibit intense emission centered at $\sim$1200 nm. A minimal hypsochromic shift is apparent in the NIR absorption maximum and photoluminescence (PL) spectra of **3** compared to those of **1** and **2**, however, at 77 K, the PL spectrum of **3** aligns with the other analogues. In general, this photophysical data suggest absorption and emission from the TTF core which is remarkably invariant to the identity of the capping metal/ligand combination.

PLQY measurements show **1** and **2** to have nearly identical PLQY values of $\sim$0.14% (see Table 1), whereas **3** has a notably higher PLQY of 0.43%. These quantum yields distinguish this novel class of dyes as among the brightest monomolecular NIR II lumiphores, with **3** measuring nearly an order of magnitude higher than the commercially available NIR II dye, IR 26. Transient absorption (TA) spectra reveal a broad ground state bleach (GSB) is present at $\sim$1000 nm, with an unusually sharp excited state absorption (ESA) at 1100 nm growing in shortly thereafter. A feature at $\sim$1200 nm grows in at a similar rate to the ESA. This was assigned as a stimulated emission (SE) and the similar lifetime of SE and ESA suggests they correspond to the population of a single excited state. Notably, these three features are consistent across these complexes, suggesting a similar electronic structure despite modification of capping metals and ligands. However, variations arise at longer timepoints of $\sim$ns with both **2** and **3** exhibiting the growth of a low energy ESA at $\sim$1350nm that is notably absent in the TA spectrum of **1**. This feature is potentially indicative of intersystem crossing (ISC), although additional data will need to be acquired to confirm this assignment. Additionally, similarity of aerobic and anaerobic decays, in conjunction with picosecond lifetimes, strongly indicate fluorescence from a singlet excited state. In tandem, the radiative lifetimes for **1**, **2**, and **3** are $\sim$35ns, which are consistent with $\pi - \pi$ transitions. The experimentally determined lifetimes enable the calculation of oscillator strengths which range from 0.47 to 0.86. These values are extremely high, comparable with the best molecular lumiphores, further explaining the bright emission from these complexes.

10.3.3 Electronic Structure

Previous studies suggest that singlet and triplet states are close in energy in TTFtt dicationic complexes[151]. Consistent with this hypothesis, the ^{1}H NMR spectra of **1**, **2**, and **3** appear diamagnetic; however, a significant magnetic moment was detected via Evans method measurements for all three complexes. Furthermore, a strong signal at $g = 2$ suggestive of an organic radical[1] is present in the electron paramagnetic resonance (EPR) spectra of these complexes at both 15 K and 298 K and variable temperature measurements show this signal near $g = 2$ growing in intensity as temperature is increased, suggesting a singlet ground state with thermal population of a triplet excited state. Indeed, the triplet-singlet gaps obtained with V2RDM and density functional theory (DFT) increase across the series **2** $<$ **1** $<$ **3** as the degree of fractional occupation in the highest occupied natural orbital (HONO) and lowest unoccupied natural orbital (LUNO) decreases from $n_{\text{LUNO,S}} = 0.46$, $\lambda_{\text{HONO,S}} = 1.57$ in **2** to $\lambda_{\text{LUNO,S}} = 0.33$, $\lambda_{\text{HONO,S}} = 1.72$ in **3**. Inspection of the frontier natural-orbital densities reveals that the multireference correlation arises from near-degeneracy of the HONO and LUNO, which have Ag and Au symmetries and are π^*-antibonding and π-bonding across the central TTFtt C–C bond, respectively (see Chapter 9 of this dissertation for more details on the V2RDM calculations on those complexes).

		Pt	$PtCF_3$	Pd	Ni	Sn
EXP	GS	1044	1023	1042	1040	914
	TAS	1110	1107	1072	1273	1062
OPT GEO	S	1083	1101	1066	1096	956
	f_S	1.00	1.11	1.01	0.94	0.76
	T	1090	1117	1046	1274	1163
	f_T	0.70	0.78	0.69	0.54	0.55

Table 10.5: B3LYP TD-DFT absorption wavelengths and oscillator strengths for the Ag $\rightarrow$ Au π transition from singlet and triplet ground states.

To elucidate the electronic processes underlying the observed luminescence features in the dicationic TTFtt bimetallics TD-DFT[152] calculations were carried out on **1**, **2**, and **3**, referred to as Pd, Pt and PtCF3, respectively, in this section, as well as the previously discussed NiTTFtt^{2+} and SnTTFtt^{2+} analogues. Geometries were first relaxed from the crystal structures using DFT and then followed by TD-DFT calculations. All calculations utilized the B3LYP functional[39] as implemented in Gaussian 16[41] in combination with a LAN2DZ basis set with ECP for the heavy atoms Pt, Pd and Sn, and a 6-31G* basis set for all other atoms. The SMD model[153] was used to account for solvation effects in the TD-DFT calculations. Data for these calculations are compared those obtained experimentally via UV-Vis spectroscopy in Table 10.5.

	Pt	PtCF$_3$	Pd	Ni	Sn
exp	1202	1187	1193	1202	1045
S	1173	1191	1155	1232	1046
f_S	0.91	1.01	0.96	0.80	0.69
T	1315	1351	1262	DNC	1417
f_T	0.67	0.74	0.66	DNC	0.53

Table 10.6: B3LYP TD-DFT emission wavelengths and oscillator strengths for the Au → Ag π transition from singlet and triplet excited states. No data is available for the triplet state emission of the Ni complex due to non-convergence.

Calculations yield excellent agreement with experimental data, reproducing the measured trends: there is little variation in the absorption wavelength across the Pt, Pd and Ni systems while the Sn system is downshifted by a little more than 100 nm. Deviations from spectroscopic measurements are low and range from 22 nm in the Pd case to 78 nm in the PtCF3 complex. Due to the relatively small singlet-triplet gap in both V2RDM and B3LYP calculations, we calculate transitions from a triplet ground state in addition to those from the broken-symmetry singlet. The T→T (β) transitions are near-degenerate with the singlet transitions in the Pt, PtCF3 and Pd complexes while those in the Ni and Sn complexes are at significantly higher wavelengths as compared to the singlet. Across all systems, the triplet transitions exhibit significantly lower oscillator strengths. The wavelengths of these transitions align well with the excited state absorptions observed in the TAS

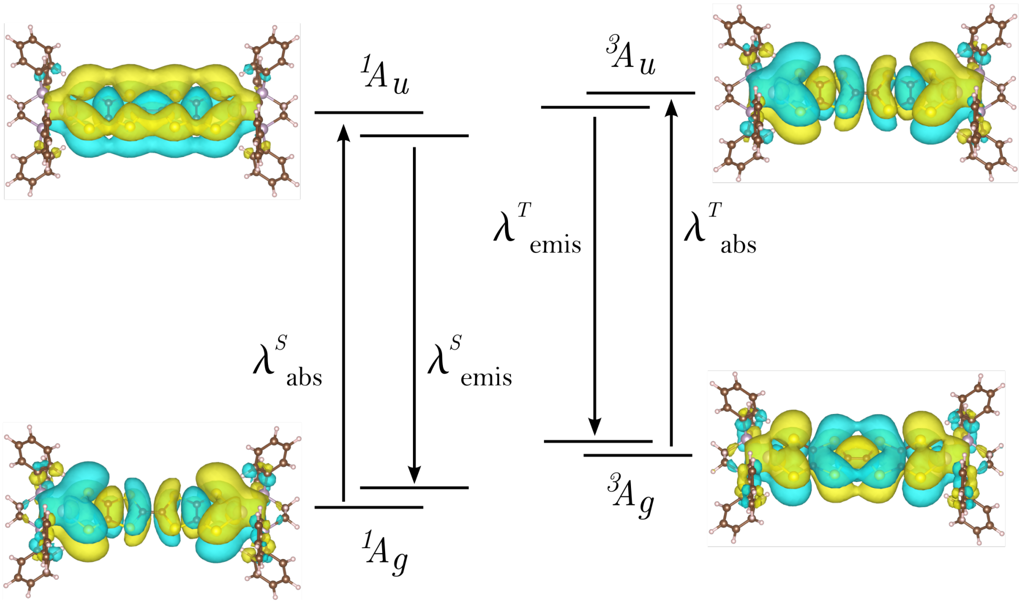

Figure 10.13: Jablonski diagram of the electronic transitions in the TTF-based π-systems resulting in the experimentally observed luminescence behavior. The density plots display NTOs for the PtTTFtt complex obtained at the B3LYP/LANL2DZ/6-31G* level of theory, where the plot aligned with the ground state displays the hole density and the plot aligned with the excited state displays the particle-density of the ground to excited state transition.

spectra, suggesting that ISC and build-up of triplet ground state population may be responsible for the experimentally observed features.

The electronic emission spectra were modelled by performing TD-DFT geometry optimizations on the Au excited states. Again TD-DFT calculations yield excellent agreement with the experimentally measured emission spectra and the trends follow those observed for the absorptions. The data for both the singlet and triplet Au→Ag emissions is displayed in Table 10.6.

The transitions are summarized in the Jablonski diagram displayed in Figure 10.13. This includes orbital analysis of the TD-DFT results for the Pt complex in the form of natural transition orbitals (NTOs) obtained with B3LYP, which reveals these to be a TTF centered $\pi^* \rightarrow \pi$ transitions from the Ag ground state to the Au excited state. Comparison of the Sn and Pt complex NTOs shows the same $\pi^* \rightarrow \pi$ TTFtt-core based transition densities, with only minor differences arising from overlap with the metal center. The NTOs closely mirror the NOs obtained with the V2RDM CASSCF calculations and in comparison to the transition metal analogues the Sn center allows for less interaction with the TTFtt π system, yielding a larger HOMO-LUMO gap, and consequently lower wavelength $\pi^* \rightarrow \pi$ transition. These results, suggest that many different end caps can be included and modified for targeting, switching, stability, or solubility.

10.3.4 Conclusions

The results presented here mark the first report of TTFtt-based luminescence, and the brightness and emission energy of these complexes distinguishes them as an exciting new class of NIR II fluorophores. The compressed TTFtt π manifold allows for strong absorptions and bright emission far into the NIR II region without the need for the extended conjugation typically present in NIR dyes and lumiphores. Additionally, these compounds are a unique example of air and water-stable complexes with organic diradical character, the modulation of which through the alteration of capping metal-ligand combinations allows for electronic structure modification and may enable the rational design of novel lumiphores. Finally, the remarkable photostability and redox switchable behavior presented here provides a promising platform for a wide array of applications. The aforementioned redox tunability and bright NIR II emission suggests this novel class of NIR fluorophores has significant potential to advance biological imaging and sensing technologies.

References

(1) Abe, M. *Chemical Reviews* **2013**, *113*, 7011–7088.

(2) Morita, Y.; Suzuki, S.; Sato, K.; Takui, T. *Nature Chemistry* **2011**, *3*, 197–204.

(3) Kamada, K.; Ohta, K.; Shimizu, A.; Kubo, T.; Kishi, R.; Takahashi, H.; Botek, E.; Champagne, B.; Nakano, M. *The Journal of Physical Chemistry Letters* **2010**, *1*, 937–940.

(4) Smith, M. B.; Michl, J. *Chemical Reviews* **2010**, *110*, 6891–6936.

(5) Schweicher, G.; Garbay, G.; Jouclas, R.; Vibert, F.; Devaux, F.; Geerts, Y. H. *Advanced Materials* **2020**, *32*, 1905909.

(6) Gallagher, N.; Zhang, H.; Junghoefer, T.; Giangrisostomi, E.; Ovsyannikov, R.; Pink, M.; Rajca, S.; Casu, M. B.; Rajca, A. *Journal of the American Chemical Society* **2019**, *141*, 4764–4774.

(7) Tang, S.; Zhang, L.; Ruan, H.; Zhao, Y.; Wang, X. *Journal of the American Chemical Society* **2020**, *142*, 7340–7344.

(8) Fukuzumi, S.; Ohkubo, K.; Ishida, M.; Preihs, C.; Chen, B.; Borden, W. T.; Kim, D.; Sessler, J. L. *Journal of the American Chemical Society* **2015**, *137*, 9780–9783.

(9) Suzuki, S.; Furui, T.; Kuratsu, M.; Kozaki, M.; Shiomi, D.; Sato, K.; Takui, T.; Okada, K. *Journal of the American Chemical Society* **2010**, *132*, 15908–15910.

(10) Su, Y.; Wang, X.; Wang, L.; Zhang, Z.; Wang, X.; Song, Y.; Power, P. P. *Chem. Sci.* **2016**, *7*, 6514–6518.

(11) Wang, J.; Hou, L.; Browne, W. R.; Feringa, B. L. *Journal of the American Chemical Society* **2011**, *133*, 8162–8164.

(12) Zhang, R.; Peterson, J. P.; Fischer, L. J.; Ellern, A.; Winter, A. H. *Journal of the American Chemical Society* **2018**, *140*, 14308–14313.

(13) Trabolsi, A.; Khashab, N.; Fahrenbach, A. C.; Friedman, D. C.; Colvin, M. T.; Cotí, K. K.; Benítez, D.; Tkatchouk, E.; Olsen, J.-C.; Belowich, M. E.; Carmielli, R.; Khatib, H. A.; Goddard, W. A.; Wasielewski, M. R.; Stoddart, J. F. *Nature Chemistry* **2010**, *2*, 42–49.

(14) Schuler, B.; Fatayer, S.; Mohn, F.; Moll, N.; Pavliček, N.; Meyer, G.; Peña, D.; Gross, L. *Nature Chemistry* **2016**, *8*, 220–224.

(15) Yin, X.; Low, J. Z.; Fallon, K. J.; Paley, D. W.; Campos, L. M. *Chem. Sci.* **2019**, *10*, 10733–10739.

(16) Halcrow, M. A., *Spin-Crossover Materials: Properties and Applications*; Wiley-Blackwell: Oxford: 2013.

(17) Batten, S. R.; Bjernemose, J.; Jensen, P.; Leita, B. A.; Murray, K. S.; Moubaraki, B.; Smith, J. P.; Toftlund, H. *Dalton Trans.* **2004**, 3370–3375.

(18) Murray, K. S. *European Journal of Inorganic Chemistry* **2008**, *2008*, 3101–3121.

(19) Tissot, A.; Shepherd, H. J.; Toupet, L.; Collet, E.; Sainton, J.; Molnár, G.; Guionneau, P.; Boillot, M.-L. *European Journal of Inorganic Chemistry* **2013**, *2013*, 1001–1008.

(20) García-López, V.; Waerenborgh, J. C.; Vieira, B. J. C.; Clemente-León, M.; Coronado, E. *Dalton Trans.* **2018**, *47*, 9156–9163.

(21) Shatruk, M.; Phan, H.; Chrisostomo, B. A.; Suleimenova, A. *Coordination Chemistry Reviews* **2015**, *289-290*, Progress in Magnetochemistry, 62–73.

(22) Mathonière, C.; Lin, H.-J.; Siretanu, D.; Clérac, R.; Smith, J. M. *Journal of the American Chemical Society* **2013**, *135*, 19083–19086.

(23) Feng, X.; Mathonière, C.; Jeon, I.-R.; Rouzières, M.; Ozarowski, A.; Aubrey, M. L.; Gonzalez, M. I.; Clérac, R.; Long, J. R. *Journal of the American Chemical Society* **2013**, *135*, 15880–15884.

(24) Arroyave, A.; Lennartson, A.; Dragulescu-Andrasi, A.; Pedersen, K. S.; Piligkos, S.; Stoian, S. A.; Greer, S. M.; Pak, C.; Hietsoi, O.; Phan, H.; Hill, S.; McKenzie, C. J.; Shatruk, M. *Inorganic Chemistry* **2016**, *55*, 5904–5913.

(25) Senthil Kumar, K.; Ruben, M. *Coordination Chemistry Reviews* **2017**, *346*, SI: 42 iccc, Brest– by invitation, 176–205.

(26) Sutter, J.-P.; Fettouhi, M.; Li, L.; Michaut, C.; Ouahab, L.; Kahn, O. *Angewandte Chemie International Edition in English* **1996**, *35*, 2113–2116.

(27) Rose, B. D.; Sumner, N. J.; Filatov, A. S.; Peters, S. J.; Zakharov, L. N.; Petrukhina, M. A.; Haley, M. M. *Journal of the American Chemical Society* **2014**, *136*, 9181–9189.

(28) Thorarinsdottir, A. E.; Harris, T. D. *Chemical Reviews* **2020**, *120*, 8716–8789.

(29) Alexandropoulos, D. I.; Dolinar, B. S.; Vignesh, K. R.; Dunbar, K. R. *Journal of the American Chemical Society* **2017**, *139*, 11040–11043.

(30) Gass, I. A.; Gartshore, C. J.; Lupton, D. W.; Moubaraki, B.; Nafady, A.; Bond, A. M.; Boas, J. F.; Cashion, J. D.; Milsmann, C.; Wieghardt, K.; Murray, K. S. *Inorganic Chemistry* **2011**, *50*, 3052–3064.

(31) Ylijoki, K. E. O.; Lavy, S.; Fretzen, A.; Kündig, E. P.; Berclaz, T.; Bernardinelli, G.; Besnard, C. *Organometallics* **2012**, *31*, 5396–5404.

(32) O'Connor, J. M.; Friese, S. J. *Organometallics* **2008**, *27*, 4280–4281.

(33) Barclay, T. M.; Hicks, R. G.; Lemaire, M. T.; Thompson, L. K. *Inorganic Chemistry* **2001**, *40*, 6521–6524.

(34) Gardiner, M. G.; Hanson, G. R.; Henderson, M. J.; Lee, F. C.; Raston, C. L. *Inorganic Chemistry* **1994**, *33*, 2456–2461.

(35) Paul, N. D.; Rana, U.; Goswami, S.; Mondal, T. K.; Goswami, S. *Journal of the American Chemical Society* **2012**, *134*, 6520–6523.

(36) Wang, H.-Y.; Cui, L.; Xie, J.-Z.; Leong, C. F.; D'Alessandro, D. M.; Zuo, J.-L. *Coordination Chemistry Reviews* **2017**, *345*, Chemical Bonding: ”State of the Art”, 342–361.

(37) Segura, J. L.; Martín, N. *Angewandte Chemie International Edition* **2001**, *40*, 1372–1409.

(38) Xie, J.; Boyn, J.-N.; Filatov, A. S.; McNeece, A. J.; Mazziotti, D. A.; Anderson, J. S. *Chem. Sci.* **2020**, *11*, 1066–1078.

(39) Becke, A. D. *J. Chem. Phys.* **1993**, *98*, 5648–5652.

(40) Krishnan, R.; Binkley, J. S.; Seeger, R.; Pople, J. A. *The Journal of Chemical Physics* **1980**, *72*, 650–654.

(41) Frisch, M. J. et al. Gaussian 16 Revision A.01, Gaussian Inc. Wallingford CT, 2016.

(42) Mazziotti, D. A. *Phys. Rev. Lett.* **2011**, *106*, 083001.

(43) Mazziotti, D. A. *Phys. Rev. Lett.* **2004**, *93*, 213001.

(44) Schlimgen, A. W.; Heaps, C. W.; Mazziotti, D. A. *The Journal of Physical Chemistry Letters* **2016**, *7*, 627–631.

(45) RDMChem, Chicago, Illinois. **2019**.

(46) Huang, X.; Zhang, S.; Liu, L.; Yu, L.; Chen, G.; Xu, W.; Zhu, D. *Angewandte Chemie International Edition* **2018**, *57*, 146–150.

(47) Wang, L.; Han, Y.; Feng, X.; Zhou, J.; Qi, P.; Wang, B. *Coordination Chemistry Reviews* **2016**, *307*, Chemistry and Applications of Metal Organic Frameworks, 361–381.

(48) Sheberla, D.; Bachman, J. C.; Elias, J. S.; Sun, C.-J.; Shao-Horn, Y.; Dincă, M. *Nature Materials* **2017**, *16*, 220–224.

(49) Wada, K.; Sakaushi, K.; Sasaki, S.; Nishihara, H. *Angewandte Chemie International Edition* **2018**, *57*, 8886–8890.

(50) Feng, D. et al. *Nature Energy* **2018**, *3*, 30–36.

(51) Park, J.; Lee, M.; Feng, D.; Huang, Z.; Hinckley, A. C.; Yakovenko, A.; Zou, X.; Cui, Y.; Bao, Z. *Journal of the American Chemical Society* **2018**, *140*, 10315–10323.

(52) Sun, Y.; Sheng, P.; Di, C.; Jiao, F.; Xu, W.; Qiu, D.; Zhu, D. *Advanced Materials* **2012**, *24*, 932–937.

(53) Jiao, F.; Di, C.-a.; Sun, Y.; Sheng, P.; Xu, W.; Zhu, D. *Philosophical Transactions of the Royal Society A: Mathematical, Physical and Engineering Sciences* **2014**, *372*, 20130008.

(54) Sun, Y. et al. *Advanced Materials* **2016**, *28*, 3351–3358.

(55) Sun, L.; Liao, B.; Sheberla, D.; Kraemer, D.; Zhou, J.; Stach, E. A.; Zakharov, D.; Stavila, V.; Talin, A. A.; Ge, Y.; Allendorf, M. D.; Chen, G.; Léonard, F.; Dincă, M. *Joule* **2017**, *1*, 168–177.

(56) Wang, Z. F.; Su, N.; Liu, F. *Nano Letters* **2013**, *13*, 2842–2845.

(57) Kambe, T.; Sakamoto, R.; Kusamoto, T.; Pal, T.; Fukui, N.; Hoshiko, K.; Shimojima, T.; Wang, Z.; Hirahara, T.; Ishizaka, K.; Hasegawa, S.; Liu, F.; Nishihara, H. *Journal of the American Chemical Society* **2014**, *136*, 14357–14360.

(58) Chakravarty, C.; Mandal, B.; Sarkar, P. *The Journal of Physical Chemistry C* **2016**, *120*, 28307–28319.

(59) Liu, L.; DeGayner, J. A.; Sun, L.; Zee, D. Z.; Harris, T. D. *Chem. Sci.* **2019**, *10*, 4652–4661.

(60) Clough, A. J.; Yoo, J. W.; Mecklenburg, M. H.; Marinescu, S. C. *Journal of the American Chemical Society* **2015**, *137*, 118–121.

(61) Dong, R.; Pfeffermann, M.; Liang, H.; Zheng, Z.; Zhu, X.; Zhang, J.; Feng, X. *Angewandte Chemie International Edition* **2015**, *54*, 12058–12063.

(62) Miner, E. M.; Fukushima, T.; Sheberla, D.; Sun, L.; Surendranath, Y.; Dincă, M. *Nature Communications* **2016**, *7*, 10942.

(63) Huang, X.; Yao, H.; Cui, Y.; Hao, W.; Zhu, J.; Xu, W.; Zhu, D. *ACS Applied Materials & Interfaces* **2017**, *9*, 40752–40759.

(64) Miner, E. M.; Wang, L.; Dincă, M. *Chem. Sci.* **2018**, *9*, 6286–6291.

(65) Ji, Z.; Trickett, C.; Pei, X.; Yaghi, O. M. *Journal of the American Chemical Society* **2018**, *140*, 13618–13622.

(66) Tang, Q.; Zhou, Z. *The Journal of Physical Chemistry C* **2013**, *117*, 14125–14129.

(67) Campbell, M. G.; Sheberla, D.; Liu, S. F.; Swager, T. M.; Dincă, M. *Angewandte Chemie International Edition* **2015**, *54*, 4349–4352.

(68) Hendon, C. H.; Rieth, A. J.; Korzyński, M. D.; Dincă, M. *ACS Central Science* **2017**, *3*, 554–563.

(69) Liu, L.; Li, L.; DeGayner, J. A.; Winegar, P. H.; Fang, Y.; Harris, T. D. *Journal of the American Chemical Society* **2018**, *140*, 11444–11453.

(70) Hoppe, B.; Hindricks, K. D. J.; Warwas, D. P.; Schulze, H. A.; Mohmeyer, A.; Pinkvos, T. J.; Zailskas, S.; Krey, M. R.; Belke, C.; König, S.; Fröba, M.; Haug, R. J.; Behrens, P. *CrystEngComm* **2018**, *20*, 6458–6471.

(71) Darago, L. E.; Aubrey, M. L.; Yu, C. J.; Gonzalez, M. I.; Long, J. R. *Journal of the American Chemical Society* **2015**, *137*, 15703–15711.

(72) Jeon, I.-R.; Negru, B.; Van Duyne, R. P.; Harris, T. D. *Journal of the American Chemical Society* **2015**, *137*, 15699–15702.

(73) Jeon, I.-R.; Sun, L.; Negru, B.; Van Duyne, R. P.; Dincă, M.; Harris, T. D. *Journal of the American Chemical Society* **2016**, *138*, 6583–6590.

(74) DeGayner, J. A.; Jeon, I.-R.; Sun, L.; Dincă, M.; Harris, T. D. *Journal of the American Chemical Society* **2017**, *139*, 4175–4184.

(75) Ziebel, M. E.; Darago, L. E.; Long, J. R. *Journal of the American Chemical Society* **2018**, *140*, 3040–3051.

(76) DeGayner, J. A.; Wang, K.; Harris, T. D. *Journal of the American Chemical Society* **2018**, *140*, 6550–6553.

(77) Sheberla, D.; Sun, L.; Blood-Forsythe, M. A.; Er, S.; Wade, C. R.; Brozek, C. K.; Aspuru-Guzik, A.; Dincă, M. *Journal of the American Chemical Society* **2014**, *136*, 8859–8862.

(78) Dou, J.-H.; Sun, L.; Ge, Y.; Li, W.; Hendon, C. H.; Li, J.; Gul, S.; Yano, J.; Stach, E. A.; Dincă, M. *Journal of the American Chemical Society* **2017**, *139*, 13608–13611.

(79) Xie, L. S.; Sun, L.; Wan, R.; Park, S. S.; DeGayner, J. A.; Hendon, C. H.; Dincă, M. *Journal of the American Chemical Society* **2018**, *140*, 7411–7414.

(80) Park, J. G.; Aubrey, M. L.; Oktawiec, J.; Chakarawet, K.; Darago, L. E.; Grandjean, F.; Long, G. J.; Long, J. R. *Journal of the American Chemical Society* **2018**, *140*, 8526–8534.

(81) Kambe, T.; Sakamoto, R.; Hoshiko, K.; Takada, K.; Miyachi, M.; Ryu, J.-H.; Sasaki, S.; Kim, J.; Nakazato, K.; Takata, M.; Nishihara, H. *Journal of the American Chemical Society* **2013**, *135*, 2462–2465.

(82) Huang, X.; Sheng, P.; Tu, Z.; Zhang, F.; Wang, J.; Geng, H.; Zou, Y.; Di, C.-a.; Yi, Y.; Sun, Y.; Xu, W.; Zhu, D. *Nature Communications* **2015**, *6*, 7408.

(83) Maeda, H.; Sakamoto, R.; Nishihara, H. *Langmuir* **2016**, *32*, 2527–2538.

(84) Huang, X.; Li, H.; Tu, Z.; Liu, L.; Wu, X.; Chen, J.; Liang, Y.; Zou, Y.; Yi, Y.; Sun, J.; Xu, W.; Zhu, D. *Journal of the American Chemical Society* **2018**, *140*, 15153–15156.

(85) Dong, R. et al. *Nature Materials* **2018**, *17*, 1027–1032.

(86) Cui, Y.; Yan, J.; Chen, Z.; Zhang, J.; Zou, Y.; Sun, Y.; Xu, W.; Zhu, D. *Advanced Science* **2019**, *6*, 1802235.

(87) Sun, L.; Miyakai, T.; Seki, S.; Dincă, M. *Journal of the American Chemical Society* **2013**, *135*, 8185–8188.

(88) Sun, L.; Campbell, M. G.; Dincă, M. *Angewandte Chemie International Edition* **2016**, *55*, 3566–3579.

(89) Horwitz, N. E.; Xie, J.; Filatov, A. S.; Papoular, R. J.; Shepard, W. E.; Zee, D. Z.; Grahn, M. P.; Gilder, C.; Anderson, J. S. *Journal of the American Chemical Society* **2019**, *141*, 3940–3951.

(90) Bryce, M. R. *Chem. Soc. Rev.* **1991**, *20*, 355–390.

(91) Narayan, T. C.; Miyakai, T.; Seki, S.; Dincă, M. *Journal of the American Chemical Society* **2012**, *134*, 12932–12935.

(92) Sun, L.; Park, S. S.; Sheberla, D.; Dincă, M. *Journal of the American Chemical Society* **2016**, *138*, 14772–14782.

(93) Xie, L. S.; Dincă, M. *Israel Journal of Chemistry* **2018**, *58*, 1119–1122.

(94) Xie, L. S.; Alexandrov, E. V.; Skorupskii, G.; Proserpio, D. M.; Dincă, M. *Chem. Sci.* **2019**, *10*, 8558–8565.

(95) Su, J.; Yuan, S.; Wang, H.-Y.; Huang, L.; Ge, J.-Y.; Joseph, E.; Qin, J.; Cagin, T.; Zuo, J.-L.; Zhou, H.-C. *Nature Communications* **2017**, *8*, 2008.

(96) Souto, M.; Romero, J.; Calbo, J.; Vitórica-Yrezábal, I. J.; Zafra, J. L.; Casado, J.; Ortí, E.; Walsh, A.; Mínguez Espallargas, G. *Journal of the American Chemical Society* **2018**, *140*, 10562–10569.

(97) Wang, H.-Y.; Ge, J.-Y.; Hua, C.; Jiao, C.-Q.; Wu, Y.; Leong, C. F.; D'Alessandro, D. M.; Liu, T.; Zuo, J.-L. *Angewandte Chemie International Edition* **2017**, *56*, 5465–5470.

(98) Su, J.; Hu, T.-H.; Murase, R.; Wang, H.-Y.; D'Alessandro, D. M.; Kurmoo, M.; Zuo, J.-L. *Inorganic Chemistry* **2019**, *58*, 3698–3706.

(99) Rivera, N. M.; Engler, E. M.; Schumaker, R. R. *J. Chem. Soc., Chem. Commun.* **1979**, 184–185.

(100) McCullough, R. D.; Belot, J. A. *Chemistry of Materials* **1994**, *6*, 1396–1403.

(101) McCullough, R. D.; Belot, J. A.; Rheingold, A. L.; Yap, G. P. A. *Journal of the American Chemical Society* **1995**, *117*, 9913–9914.

(102) Matsuo, Y.; Maruyama, M.; Gayathri, S. S.; Uchida, T.; Guldi, D. M.; Kishida, H.; Nakamura, A.; Nakamura, E. *Journal of the American Chemical Society* **2009**, *131*, 12643–12649.

(103) Bellec, N.; Vacher, A.; Barrière, F.; Xu, Z.; Roisnel, T.; Lorcy, D. *Inorganic Chemistry* **2015**, *54*, 5013–5020.

(104) Gao, F.; Zhu, F.-F.; Wang, X.-Y.; Xu, Y.; Wang, X.-P.; Zuo, J.-L. *Inorganic Chemistry* **2014**, *53*, 5321–5327.

(105) Tanaka, H.; Okano, Y.; Kobayashi, H.; Suzuki, W.; Kobayashi, A. *Science* **2001**, *291*, 285–287.

(106) Matsubayashi, G.; Nakano, M.; Tamura, H. *Coordination Chemistry Reviews* **2002**, *226*, 143–151.

(107) Kobayashi, A.; Fujiwara, E.; Kobayashi, H. *Chemical Reviews* **2004**, *104*, 5243–5264.

(108) Okano, Y.; Zhou, B.; Tanaka, H.; Adachi, T.; Ohishi, Y.; Takata, M.; Aoyagi, S.; Nishibori, E.; Sakata, M.; Kobayashi, A.; Kobayashi, H. *Journal of the American Chemical Society* **2009**, *131*, 7169–7174.

(109) Zhou, B.; Idobata, Y.; Kobayashi, A.; Cui, H.; Kato, R.; Takagi, R.; Miyagawa, K.; Kanoda, K.; Kobayashi, H. *Journal of the American Chemical Society* **2012**, *134*, 12724–12731.

(110) Cui, H.; Kobayashi, H.; Ishibashi, S.; Sasa, M.; Iwase, F.; Kato, R.; Kobayashi, A. *Journal of the American Chemical Society* **2014**, *136*, 7619–7622.

(111) Zhou, B.; Ogura, S.; Liu, Q. Z.; Kasai, H.; Nishibori, E.; Kobayashi, A. *Chemistry Letters* **2016**, *45*, 303–305.

(112) Valade, L.; de Caro, D.; Faulmann, C.; Jacob, K. *Coordination Chemistry Reviews* **2016**, *308*, Perspectives in Coordination Chemistry on the Occasion of the 40th anniversary of the LCC-CNRS, Toulouse, France, 433–444.

(113) Silva, R. A. L.; Vieira, B. J. C.; Andrade, M. M.; Santos, I. C.; Rabaça, S.; Lopes, E. B.; Coutinho, J. T.; Pereira, L. C. J.; Almeida, M.; Belo, D. *Molecules* **2018**, *23*.

(114) Zhou, B.; Ishibashi, S.; Ishii, T.; Sekine, T.; Takehara, R.; Miyagawa, K.; Kanoda, K.; Nishibori, E.; Kobayashi, A. *Chem. Commun.* **2019**, *55*, 3327–3330.

(115) Mazziotti, D. A. *Phys. Rev. A* **2002**, *65*, 062511.

(116) Boyn, J.-N.; Xie, J.; Anderson, J. S.; Mazziotti, D. A. *J. Phys. Chem. Lett.* **2020**, *11*, 4584–4590.

(117) Plummer, J. *Nature Materials* **2015**, *14*, 553–555.

(118) Hirata, A.; Kang, L. J.; Fujita, T.; Klumov, B.; Matsue, K.; Kotani, M.; Yavari, A. R.; Chen, M. W. *Science* **2013**, *341*, 376–379.

(119) Kobayashi, Y.; Terauchi, T.; Sumi, S.; Matsushita, Y. *Nature Materials* **2017**, *16*, 109–114.

(120) Eisenberg, R.; Gray, H. B. *Inorganic Chemistry* **2011**, *50*, 9741–9751.

(121) McCullough, R. D.; Belot, J. A. *Chem. Mater.* **1994**, *6*, 1396–1403.

(122) Vogt, T.; Faulmann, C.; Soules, R.; Lecante, P.; Mosset, A.; Castan, P.; Cassoux, P.; Galy, J. *Journal of the American Chemical Society* **1988**, *110*, 1833–1840.

(123) Hariharan, P. C.; Pople, J. A. *Theor. Chem. Acc.* **1973**, *28*, 213–222.

(124) Grimme, S.; Ehrlich, S.; Goerigk, L. *Journal of Computational Chemistry* **2011**, *32*, 1456–1465.

(125) Xie, J.; Boyn, J.-N.; Filatov, A. S.; McNeece, A. J.; Mazziotti, D. A.; Anderson, J. S. *Chem. Sci.* **2020**, *11*, 1066–1078.

(126) Hong, G.; Antaris, A. L.; Dai, H. *Nature Biomedical Engineering* **2017**, *1*, 0010.

(127) Matsui, A.; Tanaka, E.; Choi, H. S.; Winer, J. H.; Kianzad, V.; Gioux, S.; Laurence, R. G.; Frangioni, J. V. *Surgery* **2010**, *148*, 87–95.

(128) Li, B. et al. *Nature Communications* **2020**, *11*, 3102.

(129) Qu, C.; Xiao, Y.; Zhou, H.; Ding, B.; Li, A.; Lin, J.; Zeng, X.; Chen, H.; Qian, K.; Zhang, X.; Fang, W.; Wu, J.; Deng, Z.; Cheng, Z.; Hong, X. *Advanced Optical Materials* **2019**, *7*, 1900229.

(130) Zeng, X.; Xiao, Y.; Lin, J.; Li, S.; Zhou, H.; Nong, J.; Xu, G.; Wang, H.; Xu, F.; Wu, J.; Deng, Z.; Hong, X. *Advanced Healthcare Materials* **2018**, *7*, 1800589.

(131) Antaris, A. L.; Chen, H.; Diao, S.; Ma, Z.; Zhang, Z.; Zhu, S.; Wang, J.; Lozano, A. X.; Fan, Q.; Chew, L.; Zhu, M.; Cheng, K.; Hong, X.; Dai, H.; Cheng, Z. *Nature Communications* **2017**, *8*, 15269.

(132) Wu, J.-J.; Wang, X.-D.; Liao, L.-S. *ACS Photonics* **2019**, *6*, 2590–2599.

(133) Song, Y.; Yu, G.; Xie, B.; Zhang, K.; Huang, F. *Applied Physics Letters* **2020**, *117*, 093302.

(134) Ho, C.-L.; Li, H.; Wong, W.-Y. *Journal of Organometallic Chemistry* **2014**, *751*, 50th anniversary special issue, 261–285.

(135) Zhang, R.; Xu, Y.; Zhang, Y.; Kim, H. S.; Sharma, A.; Gao, J.; Yang, G.; Kim, J. S.; Sun, Y. *Chem. Sci.* **2019**, *10*, 8348–8353.

(136) Sun, C.; Li, B.; Zhao, M.; Wang, S.; Lei, Z.; Lu, L.; Zhang, H.; Feng, L.; Dou, C.; Yin, D.; Xu, H.; Cheng, Y.; Zhang, F. *Journal of the American Chemical Society* **2019**, *141*, 19221–19225.

(137) Lei, Z.; Sun, C.; Pei, P.; Wang, S.; Li, D.; Zhang, X.; Zhang, F. *Angewandte Chemie International Edition* **2019**, *58*, 8166–8171.

(138) Feng, Z.; Tang, T.; Wu, T.; Yu, X.; Zhang, Y.; Wang, M.; Zheng, J.; Ying, Y.; Chen, S.; Zhou, J.; Fan, X.; Zhang, D.; Li, S.; Zhang, M.; Qian, J. *Light: Science & Applications* **2021**, *10*, 197.

(139) Antaris, A. L. et al. *Nature Materials* **2016**, *15*, 235–242.

(140) Englman, R.; Jortner, J. *Molecular Physics* **1970**, *18*, 145–164.

(141) Lin, S. H. *The Journal of Chemical Physics* **1970**, *53*, 3766–3767.

(142) Troyan, S. L.; Kianzad, V.; Gibbs-Strauss, S. L.; Gioux, S.; Matsui, A.; Oketokoun, R.; Ngo, L.; Khamene, A.; Azar, F.; Frangioni, J. V. *Annals of Surgical Oncology* **2009**, *16*, 2943–2952.

(143) Ashitate, Y.; Vooght, C. S.; Hutteman, M.; Oketokoun, R.; Choi, H. S.; Frangioni, J. V. *Molecular Imaging* **2012**, *11*, 7290.2011.00048.

(144) Tummers, Q. R.; Schepers, A.; Hamming, J. F.; Kievit, J.; Frangioni, J. V.; van de Velde, C. J.; Vahrmeijer, A. L. *Surgery* **2015**, *158*, 1323–1330.

(145) Yang, Q.; Ma, H.; Liang, Y.; Dai, H. *Accounts of Materials Research* **2021**, *2*, 170–183.

(146) Yang, Q.; Hu, Z.; Zhu, S.; Ma, R.; Ma, H.; Ma, Z.; Wan, H.; Zhu, T.; Jiang, Z.; Liu, W.; Jiao, L.; Sun, H.; Liang, Y.; Dai, H. *Journal of the American Chemical Society* **2018**, *140*, 1715–1724.

(147) Ding, B.; Xiao, Y.; Zhou, H.; Zhang, X.; Qu, C.; Xu, F.; Deng, Z.; Cheng, Z.; Hong, X. *Journal of Medicinal Chemistry* **2019**, *62*, 2049–2059.

(148) Dou, K.; Feng, W.; Fan, C.; Cao, Y.; Xiang, Y.; Liu, Z. *Analytical Chemistry* **2021**, *93*, 4006–4014.

(149) Fang, Y.; Shang, J.; Liu, D.; Shi, W.; Li, X.; Ma, H. *Journal of the American Chemical Society* **2020**, *142*, 15271–15275.

(150) Semonin, O. E.; Johnson, J. C.; Luther, J. M.; Midgett, A. G.; Nozik, A. J.; Beard, M. C. *The Journal of Physical Chemistry Letters* **2010**, *1*, 2445–2450.

(151) Kawamura, A.; Xie, J.; Boyn, J.-N.; Jesse, K. A.; McNeece, A. J.; Hill, E. A.; Collins, K. A.; Valdez-Moreira, J. A.; Filatov, A. S.; Kurutz, J. W.; Mazziotti, D. A.; Anderson, J. S. *J. Am. Chem. Soc.* **2020**, *142*, 17670–17680.

(152) Bauernschmitt, R.; Ahlrichs, R. *Chem. Phys. Lett.* **1996**, *256*, 454–464.

(153) Marenich, A. V.; Cramer, C. J.; Truhlar, D. G. *J. Phys. Chem. B* **2009**, *113*, 6378–6396.